HYDRO-MECHANICAL BEHAVIOUR OF UNSATURATED AND STRUCTURED LOESS

BAOLIN DAI

PhD

The Hong Kong Polytechnic University

2025

The Hong Kong Polytechnic University

Department of Civil and Environmental Engineering

Hydro-Mechanical Behaviour of Unsaturated and Structured Loess

Baolin DAI

A thesis submitted in partial fulfilment of the requirements for the degree of Doctor of Philosophy

August 2025

CERTIFICATE OF ORIGINALITY

I hereby declare that this thesis is my own work and that, to the best of my knowledge and belief, it reproduces no material previously published or written, nor material that has been accepted for the award of any other degree or diploma, except where due acknowledgement has been made in the text.

_____(Signed)

Baolin DAI (Name of student)

ABSTRACT

Loess is characterised by a metastable and anisotropic structure formed during aeolian depositional history. It is usually unsaturated due to its prevalence in arid and semi-arid regions. Many investigations have demonstrated that soil structure, including that of structured loess, can greatly affect engineering behaviour. Most of the previous studies on structure effects, however, have focused on saturated conditions. The hydro-mechanical behaviour of unsaturated and structured soils remains insufficiently understood.

The principal objectives of this research are to investigate the influence of structure and its evolution on unsaturated soil behaviour. To achieve this, three series of tests were conducted using loess specimens with different initial structures: intact specimens, reconstituted specimens, and compacted specimens with varying compaction dry densities and water contents. First of all, isotropic compression tests with shear wave velocity measurements were performed on saturated specimens to primarily examine the evolution of soil microstructure and anisotropic stiffness under mechanical loading. Then, building on the results, cyclic triaxial shear tests were conducted on unsaturated specimens to investigate micro-macro behaviour under combined mechanical and hydraulic loading. Finally, cyclic hollow cylinder torsional tests were performed on unsaturated specimens to investigate the coupled effects of mechanical, hydraulic, and thermal loads, as well as principal stress rotation (PSR), on the cyclic shear behaviour of structured soils. On the other hand, a bounding surface model was developed to capture the behaviour of unsaturated soils under both monotonic and cyclic loading conditions. The effects of soil structure and anisotropy on the hydro-mechanical response of unsaturated soils are newly incorporated into the model. In parallel, the potential of ground granulated blast-furnace slag (GGBS) as a stabilisation material for mitigating loess collapse was explored.

Experimental results indicate that, during isotropic compression, the initial structure in the intact specimen is stiffer and more orientated than in the compacted and reconstituted specimens, as evident by a larger $G_0/f(e)$ (elastic shear modulus normalised by a void ratio function) and a more evident stiffness anisotropy in the former. The initially stiffer and more orientated structures are also observed in the compacted specimens with a higher dry density and a lower compaction water content. More importantly, it is observed that when the applied stress reaches about 2 to 4 times the yield stress of the initially stiffer specimen, $G_0/f(e)$ becomes smaller than that of the initially softer specimen. This reversal is likely due to more pronounced interparticle contact strengthening and greater pore compression in the latter, as supported by the results of microstructural analysis. This new finding highlights the necessity of considering the important role of soil structure evolution in stiffness.

Under cyclic shearing, the influence of soil structure becomes increasingly complex. In the first cycle, the intact specimen may exhibit either a smaller permanent strain ($\Delta\varepsilon_{z,1}^{p}$) than the compacted specimen (type-I behaviour), attributed to its inherently stiffer soil structure, or a larger $\Delta\varepsilon_{z,1}^{p}$, due to structure degradation-induced additional plastic strain (type-II behaviour). As the number of cycles increases, the intact specimen in type I may have a larger strain increment due to structure degradation. In type II, the compacted specimen may experience a larger strain increment as a result of failure. For compacted loess specimens prepared under different compaction conditions and subsequently adjusted to the same suction, permanent

strain decreases and resilient modulus increases with a higher dry density and a lower compaction water content. These effects of compaction conditions become more pronounced as suction decreases, possibly because the soil skeletons of specimens compacted at higher water contents and lower densities are more sensitive to suction changes. The above results demonstrate the important coupled effects of structure and suction.

Under cyclic shearing with the same change in the principal stress magnitude, specimens subjected to PSR exhibit larger excess PWP and permanent vertical strain, and smaller resilient modulus than those without PSR. These differences are because rotational loading can induce additional deformation in anisotropic soils. More importantly, the extra strain induced by PSR increases with increasing temperature and decreasing suction. When PSR is considered at zero suction, permanent strain increases by 130% and 230% at 5 and 40 °C, respectively. As suction increases to 10 kPa, these increases reduce to 50% and 80%. These coupled effects are likely attributed to the greater influence of PSR at lower overconsolidation ratios.

These new findings highlight that accounting for structure evolution is essential to enhance the reliability of deformation predictions in engineering practice. Specifically, when both compacted and intact soils are involved, it is not always conservative to adopt parameters from the compacted soil, as the strain increment could be smaller in certain cases. Moreover, strict control of compaction conditions is crucial, given their pronounced influence on soil response to cyclic loading, particularly under saturated conditions. Finally, the effects of PSR on resilient modulus should be considered, especially at elevated temperatures and low suctions.

The proposed model newly incorporates the effects of soil structure and anisotropy on both the loading-collapse (LC) curve and the soil water retention behaviour. Experimental results from the literature reveal that the inclination of the normalised LC curve for structured soils can be smaller than, larger than, or equal to that of the reference soils, and these variations are captured within a unified modelling framework. Additionally, the model well represents the increased water retention capacity associated with greater anisotropy, an aspect not incorporated in existing models. The predicted results are well matched with experimental data under both monotonic and cyclic loading, demonstrating that the model effectively captures the effects of structure and anisotropy on the hydro-mechanical behaviour of unsaturated soils.

For loess improvement, it is found that the collapse index of loess decreases with increasing binder content (defined as the mass ratio of lime and GGBS to dry soil), with more pronounced effects observed at higher GGBS-to-binder ratios. For example, as the lime content increases from 0% to 3%, the collapse index decreases from 15.3% (severe collapse) to 4.7% (moderate collapse) for looser specimens. More importantly, substituting 50% of the lime with GGBS further reduces the collapse index to 0.06%, which falls below the lower limit for slight collapse (i.e., 0.1%). These observations indicate that the partial replacement of lime with GGBS can effectively reduce the collapse of loess and satisfy engineering requirements.

The results of this study have enhanced the understanding and modelling of unsaturated loess. These findings may also be applicable, at least qualitatively, to the analysis of other unsaturated and structured soils.

PUBLICATIONS ARISING FROM THE THESIS

1. **Dai, B. L.** and Zhou, C. (2025). Characteristics of permanent strain accumulation and resilient modulus of unsaturated and structured soil under repeated loads. *Journal of Geotechnical and Geoenvironmental Engineering* 151(12):04025157.
2. **Dai, B. L.** and Zhou, C. (2025). Coupled effects of principal stress rotation, temperature, and suction on the cyclic behaviour of unsaturated loess. *Canadian Geotechnical Journal*, 62, 1-16.
3. **Dai, B. L.**, Zhou, C., Mu, Q. Y., and Peng, J. B. (2025). Evolution of structure and anisotropic shear stiffness of compacted loess during compression. *Canadian Geotechnical Journal*, 62, 1-13.
4. **Dai, B. L.**, Zhou, C., Tang, A. M., and Guayacán-Carrillo, L. M. (2024). A bounding surface model for anisotropic and structured soils under saturated and unsaturated conditions. *Computers and Geotechnics*, 173, 106533.
5. Mu, Q. Y., **Dai, B. L.**, and Zhou, C. (2023). A constitutive model for structured soils under saturated and unsaturated conditions. *International Journal for Numerical and Analytical Methods in Geomechanics*, 47(14), 2562-2586.
6. Mu, Q. Y., **Dai, B. L.**, Zhou, C., Meng, L. L., Zheng, J. G., Zhang, J. W., Yu, Y. T., and Liu, Z. H. (2023). A new and simple method for predicting the collapse susceptibility of intact loess. *Computers and Geotechnics*, 158, 105408.
7. **Dai, B. L.**, Zhou, C., Pereira, J. M. and Tang, A. M. (2025). A constitutive model for the mechanical behaviour of saturated frozen soils considering the dual effects of confining pressure. *Computers and Geotechnics* (under review).
8. **Dai, B. L.** and Zhou, C. Coupled effects of compaction conditions and suction on the cyclic behaviour of an unsaturated soil. *Acta Geotechnica* (under review).
9. **Dai, B. L.** and Zhou, C. Collapse susceptibility of lime- and ground granulated blast furnace slag-treated loess. *Engineering Geology* (under review).

ACKNOWLEDGEMENT

First and foremost, I would like to express my deepest gratitude to my chief supervisor, Prof. Chao ZHOU, for his unwavering support, insightful guidance, and continued encouragement throughout this research work. Without his assistance and support, this thesis cannot be completed. His expertise and mentorship have been invaluable to both my academic and personal growth.

I would like to express my sincere appreciation to my co-supervisor, Prof. Qingyi MU, for his valuable insights, constructive feedback, and ongoing support. I am grateful to him for instructing me to develop skills for paper and report writing. I also extend my sincere thanks to my co-supervisor, Prof. Jianhua YIN, for providing access to advanced testing equipment.

Special thanks go to Prof. Anh-Minh TANG and Prof. Jean-Michel PEREIRA for warmly hosting me and providing insightful guidance during my six-month research attachment at École Nationale des Ponts et Chaussées, Institut Polytechnique de Paris. Their rigorous academic attitude greatly inspired me throughout my studies.

In addition, I am deeply grateful to the members of my thesis committee, Prof. Adrian RUSSELL from University of New South Wales, Prof. Yewei ZHENG from Wuhan University, and Prof. Qi ZHAO from Hong Kong Polytechnic University, for their constructive feedback and thoughtful suggestions, which greatly improved the quality of this work.

Many thanks go to my colleagues for their generous assistance and valuable discussions that have supported my research in many ways. I also wish to express my sincere appreciation to the geotechnical laboratory technicians, Mr. Chun Kit LEUNG and Mr. David LEUNG, for their support during the laboratory testing phases.

Finally, I would like to extend my heartfelt thanks to my family for their unwavering love, encouragement, and support throughout the course of my studies.

TABLE OF CONTENTS

ABBREVIATIONS AND NOMENCLATURES

AASHTO	American Association of State Highway and Transportation Officials
AEV	air entry value
ASTM	American Society for Testing and Materials
BBM	Barcelona Basic Model
CDG	completely decomposed granite
CSR	cyclic stress ratio
CL	clay of low plasticity
CSH	calcium silicate hydrate
CSL	critical state line
DTG	derivative thermogravimetry
FCV/SCV	first constitutive variable/second constitutive variable
GGBS	ground granulated blast furnace slag
LC	loading collapse
LCT	Lower Cromer Till
LVDT	linear variable differential transformer
MIP	mercury intrusion porosimetry
NCL	normal compression line
OCR	overconsolidation ratio
PSR	principal stress rotation
PWP	pore water pressure
SD	suction decrease
SEM	scanning electron microscope
SI	suction increase
SM	stereomicroscope
SWRC	soil water retention curve
TG	thermogravimetry
TGA	thermogravimetric analysis

$a,\ b$	parameters used to define the size of the yield (bounding) surface under unsaturated conditions
$a_N,\ b_N,\ k_N$	parameters used to calculate M_R in NCHRP (2004)
$A_G,\ n_G,\ m_G,\ k_G$	parameters used to calculate G_0
$A_{ij},\ n_i,\ n_j$	parameters used to calculate G_{ij}, including A_{hh}, A_{hv}, A_{vh}, n_h, and n_v
c	parameter used to calculate $R(\xi)$
c'	effective cohesion of saturated soils
$C_1,\ C_2$	parameters associated with pore and particle geometries
C_s	swelling index
C_{SA}	parameter used to calculate G_0 in Sawangsuriya et al. (2009b)
C_u	coefficient of uniformity
d	pore diameter
$d\varepsilon_q,\ d\varepsilon_q^e,\ d\varepsilon_q^p$	total, elastic, plastic deviatoric strain increments, respectively
$d\varepsilon_v,\ d\varepsilon_v^e,\ d\varepsilon_v^p$	total, elastic, plastic volumetric strain increments, respectively
$d\varepsilon_{vp}^e,\ d\varepsilon_{vs}^e$	elastic volumetric strain increments induced by stress and suction changes, respectively
$d\varepsilon_{vp}^p,\ d\varepsilon_{vs}^p$	plastic volumetric strain increments induced by stress and suction increases, respectively
$D_p,\ D_s$	fractal dimensions of pore and particle distribution curves, respectively
e	void ratio
e_0	initial void ratio
e_L	void ratio corresponding to the water content at the liquid limit
$E_v,\ E_h$	elastic Young's moduli for loading in the vertical and horizontal directions, respectively
$E_v^u,\ E_h^u$	values of E_v and E_h under undrained conditions, respectively
f	yield (bounding) surface in the $q - p^*$ plane
$f(e)$	void ratio function

$f(s)$	function used to describe the effects of inter-particle normal force imposed by a single water meniscus
f_h	bounding surface in the $S_r - s$ plane
f_l	loading surface in the $q - p^*$ plane
f_u	upscaling function in Lu et al. (2010)
F	frequency
g	plastic potential surface
G	elastic shear modulus
G_0	small-strain shear stiffness
G_{ij}	small-strain shear stiffness in the $i - j$ shear plane, including G_{hh}, G_{hv}, G_{vh}
G_s	specific gravity
h	parameter related to anisotropy effects on the SWRC
I_c	collapse potential
I_e	collapse index
I_v	void index
k_B	parameter used to calculate p_s
K	elastic bulk modulus
L	plastic multiplier
L_{tt}	tip-to-tip distance between two bender elements
m_1, m_2^d, m_2^w, m_3, m_4, m_5	parameters used to define the SWRC of isotropic soils
$m_{1,sc}$, $m_{2,sc}$	parameters used to define the scanning SWRC
M (M_c, M_e)	slope of the critical state line in the $q - p^*$ plane, the subscripts "c" and "e" stand for triaxial compression and extension, respectively
$M_{R,opt}$	resilient modulus at maximum dry density and optimum water content
M_0, k_1, k_2, k_3, k_4	parameters used to calculate M_R

M_R	resilient modulus
n	porosity
$N(s)$ (or $N(\xi)$, $N(\bar{\xi})$)	intercept of the isotropic NCL for isotropic soils at a given moisture condition
$N(N_c,\ N_e)$	parameter used to define the yield (bounding) surface, the subscripts "c" and "e" stand for triaxial compression and extension, respectively
p	mean total stress
p'	mean effective stress
p_n	mean net stress
p^*	mean Bishop's stress
p_{c0}	confining pressure
$P_i,\ P_o$	inner and outer cell pressures, respectively
$p_0(s)$ (or p_0, $p_0(\xi),\ p_0(\bar{\xi})$)	isotropic yield stress for isotropic soils at a given moisture condition or size of the yield (bounding) surface for anisotropic soils at a given moisture condition
$p_0^s(s),\ p_0^r(s)$ (or $p_0^s(\xi),\ p_0^r(\xi)$; $p_0^s(\bar{\xi}),\ p_0^r(\bar{\xi})$)	isotropic yield stresses at a given moisture condition for isotropic structured and reference soils, respectively or sizes of the yield (bounding) surface at a given moisture condition for anisotropic structured and reference soils, respectively
p_l^*	size of loading surface
p_α^*	size of plastic potential surface
p_{at}	atmospheric pressure, taken as 100 kPa
p^c	reference stress at which $e = N(s)$
p_r	reference pressure (1 kPa)
p_s	apparent cohesion for unsaturated soils
q	deviatoric stress
q_{cyc}	cyclic deviatoric stress
r_i, r_o	radii of inner and outer cells, respectively

$R(s)$ (or $R(\xi)$, $R(\bar{\xi})$)	structure parameter at a given moisture condition
R_{res}	parameter used to represent the residual structure elements that remain stable after substantial plastic strain
R_{gas}	universal gas constant
R_p	radius of a spherical particle
s	matric suction
s^*	modified suction in Wheeler et al. (2003b)
s_{ae}, s_{ex}	air entry suction and air expulsion suction, respectively
s_{max}	maximum suction experienced by the soil
s_{res}	suction value corresponding to the residual degree of saturation
s_α	image suction on the main drying or wetting curve
s_r	the last suction reversal occurs
s_M, r_M, β_M	parameters used to calculate G_0 in Mancuso et al. (2002)
S_r	degree of saturation
S_{r0}	initial degree of saturation
S_r^e	effective degree of saturation
S_r^r	residual degree of saturation
$S_{r,opt}$	degree of saturation at maximum dry density and optimum water content
t	time
t_{ij}	travel time of a shear wave that propagates in the i direction and vibrates in the j direction, including t_{hh}, t_{hv}, and t_{vh}
T	temperature in degrees Celsius
T_r	reference temperature (20 °C)
T_q	torque
T_s	surface tension coefficient of the air-water interface
u_a	pore air pressure

u_w	pore water pressure
$\bar{u}_v$	partial pressure of pore water vapour
$\bar{u}_{v0}$	saturation pressure of pore water vapour
v	specific volume
v_{w0}	specific volume of water
w	water content
w_L	liquid limit
w_p	plastic limit
w_{opt}	optimum water content
W	work input to the soil per unit volume
W_v	vertical force
x	parameter used to control the evolution rate of anisotropy
x_E	parameter used to define $f(e)$
$z_1,\ z_2$	parameters used to calculate $\alpha_b(\eta)$
$z_1',\ z_2',\ z_3'$	parameters used to calculate permanent vertical strain
α	inclination of the yield (bounding) surface
$\alpha_b(\eta)$	bounding value of α when soil is loaded under a constant stress ratio
$\bar{\alpha}$	rotational angle of the major principal stress to the vertical direction
α_B	parameter used to define the flow rule in the BBM
$\beta_0,\ \beta_1,\ \beta_2$	parameters used to control structure degradation
$\beta_B,\ r_B$	parameters used to calculate $\lambda(s)$ in the BBM
δ_{ij}	Kronecker's delta
ΔN	inter-particle normal force
ε_z^p	permanent vertical strain
η	stress ratio
η_τ	ratio of $\tau_{z\theta}^{cyc}$ to σ_z^{cyc}
κ	slope of the unloading or reloading line in the $e - \ln p^*$ lane
κ_s	parameter associated with suction change

$\lambda(s)$ (or $\lambda(\xi)$, $\lambda(\bar{\xi})$)	slope of the isotropic NCL for isotropic soils at a given moisture condition
λ_s	parameter used to calculate the elastoplastic strain due to drying
λ_{S_r}	slope of the soil water retention curve in $\ln S_r - \ln s$ plane
λ_G	parameter used in Gallipoli and Bruno (2017)
μ	Poisson's ratio
μ_{hh}	Poisson's ratio relating to the horizontal strain caused by an imposed horizontal strain in the normal direction
μ_{hv}	Poisson's ratio relating to the vertical strain caused by an imposed horizontal strain
μ_{vh}	Poisson's ratio relating to the horizontal strain caused by an imposed vertical strain
μ_{hh}^u, μ_{vh}^u	values of μ_{hh} and μ_{vh} under undrained conditions, respectively
$\mu_1(s, S_r)$, $\mu_2(s, S_r)$	functions of suction and degree of saturation
μ_W, β_W	parameters used to control the evolution rate of anisotropy in Wheeler et al. (2003a)
ξ	bonding variable defined as $f(s)(1 - S_r^e)$
$\bar{\xi}$	bonding variable defined as $f(s)(1 - S_r)$
π	osmotic suction
ρ	bulk density
ρ_d	dry density
$\rho_{d,max}$	maximum dry density
ρ_h, $\bar{\rho}_h$	Euclidian distances in the $S_r - s$ plane
ρ_s, $\bar{\rho}_s$	Euclidian distances in the $q - p^*$ plane
σ	normal stress, refers to the effective vertical stress and the net vertical stress under saturated and unsaturated conditions, respectively
σ_1, σ_2, σ_3	major, intermediate, and minor principal total stresses, respectively

σ_a	axial total stress
σ_r	radial total stress
σ_v'	effective vertical stress
σ_z	vertical total stress
σ_n	net vertical stress
σ_θ	circumferential stress
σ_z^{cyc}	cyclic vertical stress
σ_i', σ_j'	principal effective stresses in the direction i and j, respectively
σ_{ij}	total stress tensor
σ_{ij}'	effective stress tensor
σ_{ij}^*	Bishop's stress tensor
σ^s	suction stress in Lu et al. (2010)
$\tau_{z\theta}$	shear stress
$\tau_{z\theta}^{cyc}$	cyclic shear stress
φ'	effective friction angle
χ	parameter used to define Bishop's stress
χ_1, χ_2, χ_3, χ_4	parameters used to define χ
ψ	total suction
ω	parameter used to incorporate the anisotropy effects on the SWRC
ω_s	parameter used to incorporate structure effects on the flow rule
$\bar{\omega}$	parameter used to link elastic and plastic anisotropies
ω_v	molecular mass of water vapour

LIST OF TABLES

LIST OF FIGURES

CHAPTER 1

CHAPTER 2

CHAPTER 3

CHAPTER 4

CHAPTER 5

CHAPTER 6

CHAPTER 7

CHAPTER 1 INTRODUCTION

1.1 Background

Loess deposits are widely distributed in Asia, Europe, and both North and South America, as shown in Figure 1-1 (Pye, 1995; Li et al., 2020). In China, loess covers approximately 630,000 km^2, accounting for about 6.6% of the country's land area. Engineering activities, such as the construction of high-speed railways, have expanded rapidly in loess regions. However, issues related to the non-uniform and excessive deformation of geo-structures are frequently encountered (Delage et al., 2005; Ma et al., 2017; Sadeghi et al., 2019; Peng et al., 2020; Yates and Russell, 2024). For instance, loess collapse has led to excessive ground movements along the Datong-Xi'an high-speed railway line in northwestern China (Peng et al., 2020) and caused numerous sinkholes near the TGV high-speed railway in northern France (Delage et al., 2005) and near the national Chabahar-Zahedan railway in Iran (Sadeghi et al., 2019), posing significant risks to pavement and embankment safety. Furthermore, as loess is mainly distributed in arid and semi-arid regions (Li et al., 2020), in-situ loess is typically unsaturated and experiences daily and seasonal variations in water content. Therefore, understanding the hydro-mechanical behaviour of unsaturated loess is crucial for improving the serviceability and safety of geo-structures in loess regions.

Loess in the Loess Plateau of China is believed to be wind-transported (Xu and Coop, 2016). Due to its aeolian depositional origin, loess is typically characterised by a metastable and highly porous structure (Muñoz-Castelblanco et al., 2012; Xu and Coop, 2016; Mu et al., 2023b). In addition, it exhibits anisotropic fabric resulting from both its transportation history and the in-situ anisotropic stress state (Ng et al., 2016; Li et al., 2020). This metastable and anisotropic structure is temporarily stabilised by suction. However, loading or infiltration may trigger structure degradation and cause significant settlement or catastrophic failure (Ng et al., 2016). Consequently, understanding the role of structure in the study of structured loess is crucial.

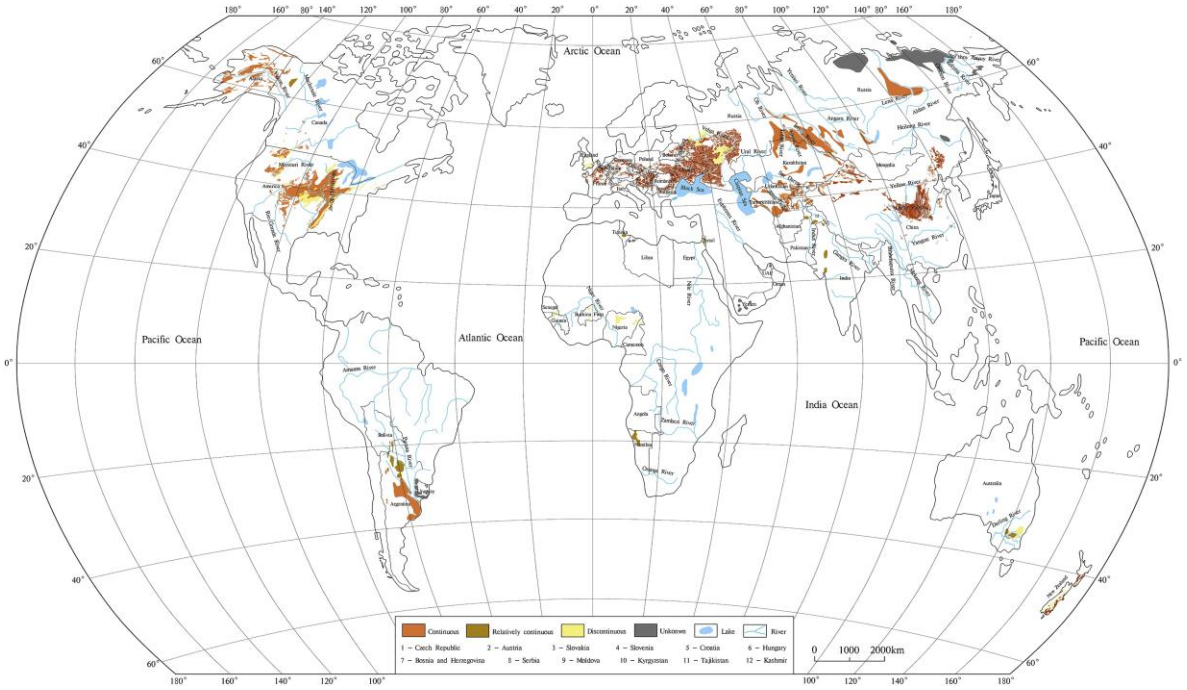

Figure 1-1. Global loess distribution (Li et al., 2020)

So far, many studies have examined the influence of soil structure on soil behaviour (not limited to structured loess) (Viggiani and Atkinson, 1995; Pennington et al., 1997; Ghionna and Porcino, 2006; Wang et al., 2006; Gasparre et al., 2007; Wijewickreme and Sanín, 2008; Song et al., 2017; Wijewickreme et al., 2019; Lu et al., 2020; Jana and Stuedlein, 2021; Stuedlein et al., 2023; Zuo et al., 2024). Most of these studies, however, have focused on saturated conditions. The hydro-mechanical behaviour of unsaturated and structured soils remains insufficiently understood. Several key aspects warrant further investigation. First, the evolution of microstructure on soil behaviour under thermo-hydro-mechanical loads remains unclear. Second, since intact soils in the field are often subjected to dynamic loads (e.g., traffic, wave, and seismic loads), it is essential to investigate the influence of the cyclic behaviour of unsaturated and structured soils. This aspect remains absent in the current literature. Moreover, these dynamic loads involve not only variations in deviatoric stress but also principal stress rotation. The combined effects of principal stress rotation and other factors on the behaviour of structured soils have yet to be fully understood.

Many constitutive models considering the structure effects on soil behaviour have been proposed (Rouainia and Muir Wood, 2000; Baudet and Stallebrass, 2004; Yang et al., 2014a;

Zhou and Ng, 2018), and only some of them have considered unsaturation effects. In the models for unsaturated soil, the loading collapse (LC) curve plays a key role. Experimental data in the literature have demonstrated that the slope of the normalised LC curve for structured soils could be smaller than, larger than, or equal to that of reference soils (Koliji et al., 2009; Arroyo et al., 2013; Mu et al., 2020; Zhang et al., 2020; Mu et al., 2022). However, the existing models were generally proposed for a specific type of structured soil and incorporated only one case of the normalised LC curve. A unified approach that can model these three cases of the LC curve is necessary to capture the behaviour of various structured soils. Furthermore, loess typically exhibits anisotropy resulting from both its aeolian depositional history (inherent anisotropy) and the applied stress conditions (stress-induced anisotropy). Previous studies have shown that anisotropic soils exhibit stronger water retention capacity than isotropic soils (Tse, 2007; Sivakumar et al., 2010; Al-Sharrad, 2013; Zhou and Chen, 2021), which has not been considered in existing models for unsaturated soils.

Finally, during geo-structure construction, loess is commonly stabilised with cement or lime to reduce its collapse potential. The treatment of loess with stabilising additives such as cement and lime has been demonstrated to be an effective method for improving its hydromechanical behaviour (Jefferson et al., 2008; Metelková et al., 2012; Zhang et al., 2017a; Zhang et al., 2018a; Akbari Garakani et al., 2019; Haeri et al., 2019; Zhang et al., 2019b; Guo et al., 2024). Given the energy-intensive and environmentally unsustainable properties of cement and lime, industrial by-products such as ground granulated blast furnace slag (GGBS) are being explored as partial replacements. However, the capacity of GGBS to reduce loess collapsibility has not been investigated, which restricts its application in loess regions.

1.2 Objectives

Given the aforementioned research gaps, the major objectives of this research include the following three parts, with their relationships illustrated in Figure 1-2:

Part A: To investigate the influence of structure and its evolution on soil behaviour under coupled hydro-mechanical loads. This part comprises three main objectives: (i) to examine the

evolution of soil structure during isotropic compression and its effects on anisotropic small-strain shear stiffness of saturated specimens; (ii) to investigate the influence of soil structure on the hydro-mechanical behaviour of unsaturated soils under cyclic loading; and (iii) to investigate the role of principal stress rotation on the cyclic behaviour of unsaturated and structured soils.

Part B: To develop a constitutive model for unsaturated structured and anisotropic soils under both monotonic and cyclic loading conditions.

Part C: To explore the potential of ground granulated blast furnace slag on loess improvement, with particular focus on reducing its collapsibility.

For part A, intact loess, reconstituted loess, and compacted loess with different compaction dry densities and water contents were prepared. To investigate the structure evolution during isotropic compression, stereomicroscope (SM, an optical microscope), scanning electron microscope (SEM), and mercury intrusion porosimetry (MIP) tests were carried out on specimens before and after compression. A suction-controlled test apparatus equipped with bender elements and local linear variable differential transformers (LVDTs) was utilised for measuring small-strain shear stiffness and applying cyclic loads. To apply cyclic loads with principal stress rotation, a dynamic hollow cylinder apparatus was modified to control suction and temperature independently.

For part B, a new constitutive model was proposed to consider the structure and anisotropy effects on the mechanical behaviour. Based on experimental results in the literature, three cases of structure effects on the loading collapse curve are considered. The increase in water retention capacity with an increasing degree of anisotropy is incorporated by a new anisotropy- and void ratio-dependent soil water retention equation.

For part C, loess specimens with various initial dry densities, binder (lime and GGBS) contents, and GGBS-to-binder ratios were prepared. One-dimensional compression tests with wetting at a vertical stress of 200 kPa were conducted. Furthermore, SEM, MIP, and thermogravimetric analysis (TGA) were conducted to investigate the mechanisms underlying

loess modification by lime and GGBS.

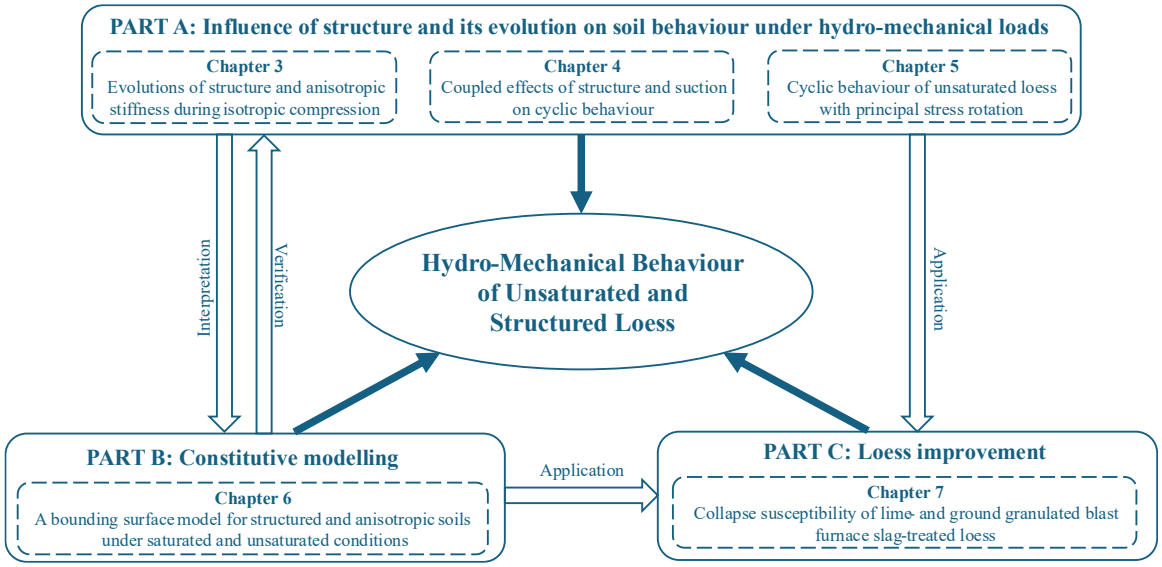

Figure 1-2. Research strategy adopted in this study

1.3 Tested loess in this study

The tested loess was sampled from Xi'an, Shaanxi province of China. Block samples (about 0.25 m × 0.25 m × 0.25 m) were retrieved at a depth of about 1.5 m from an excavated pit and wrapped in thick plastic membranes to preserve the in-situ water content (18.9%), dry density (1.23 g/cm^3) and structure. The particle size distribution, determined through wet sieving and hydrometer analysis (ASTM, 2021a), is shown in Figure 1-3(a), with clay, silt, and sand contents of 13.3%, 84.2%, and 2.5%, respectively. The specific gravity, maximum dry density and optimum water content were determined as 2.67, 1.77 g/cm^3, and 15.2% (see Figure 1-3(b)), respectively. More physical properties are summarised in Table 1-1. This soil is classified as clay of low plasticity (CL) based on the unified soil classification system (ASTM, 2025).

To meet different objectives, intact loess, reconstituted loess, and compacted loess prepared at different compaction dry densities and water contents were investigated. Detailed information is given in the following chapters.

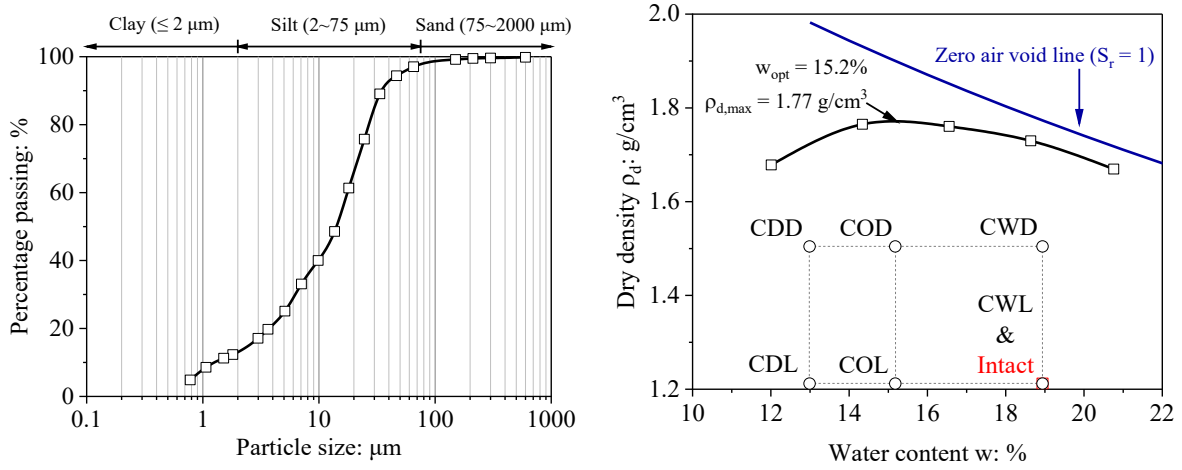

(a) (b)

Figure 1-3. Basic properties of the tested loess: (a) particle size distribution; (b) standard compaction curve and specimen compaction conditions

Table 1-1. Basic properties of the tested loess

Index property	Measured value
Specific gravity, G_s	2.67
In-situ conditions	
In-situ water content w: %	18.9
In-situ dry density ρ_d: g/cm^3	1.23
Standard compaction test (ASTM, 2021b)	
Maximum dry density, $\rho_{d,max}$:g/cm^3	1.77
Optimum water content, w_{opt}: %	15.2
Grain-size distribution: % (ASTM, 2021a)	
Clay fraction (<0.002 mm)	13.3
Silt fraction (0.002 mm - 0.075 mm)	84.2
Sand fraction (0.075 mm - 4.75 mm)	2.5
Atterberg limits (ASTM, 2017)	
Liquid limit, w_L: %	31
Plastic limit, w_p: %	18
Plasticity index: %	13
Unified soil classification system (ASTM, 2025)	CL

1.4 Thesis layout

This thesis includes 8 chapters in addition to this introduction.

In Chapter 2, the basic properties of loess are reviewed. It then presents the effects of unsaturation and anisotropic structure on hydro-mechanical behaviour, including compression and shear responses, small-strain shear stiffness, and cyclic behaviour. Finally, constitutive models considering the effects of unsaturation and anisotropic structure are reviewed.

In Chapter 3, the microstructures of intact, compacted, and reconstituted loess specimens before and after isotropic compression are presented. The effects of soil structure on small-strain shear stiffness and stiffness anisotropy under saturated conditions are analysed.

In Chapter 4, the cyclic responses between intact and compacted specimens, as well as between specimens compacted at different dry densities and water contents are compared.

In Chapter 5, the coupled effects of principal stress rotation, temperature, and suction on the cyclic behaviour of compacted loess are analysed.

In Chapter 6, a new constitutive model for unsaturated structured and anisotropic soils is proposed. The model is validated against extensive data from the literature to examine its performance on capturing the coupled effects of unsaturation, soil structure, and anisotropy.

In Chapter 7, the collapse susceptibility of loess modified by lime and ground granulated blast furnace slag is investigated. Results of MIP, SEM, and TGA are presented to illustrate the mechanisms underlying loess modification by lime and GGBS.

In Chapter 8, major findings from this study are summarised, and recommendations for further research are also presented.

CHAPTER 2 LITERATURE REVIEW

This chapter begins with a review of the basic properties of loess. It then presents the effects of unsaturation and anisotropic structure on hydro-mechanical behaviour, including compression and shear responses, small-strain shear stiffness, and cyclic behaviour. Finally, constitutive models considering the effects of unsaturation and anisotropic structure are reviewed.

2.1 Basic properties of loess

2.1.1 Loess distribution and classification

Loess is a yellowish aeolian sediment, primarily composed of slit-sized particles, and was predominantly deposited during the Quaternary period (Pye, 1995; Li et al., 2020). The global distribution of loess, as illustrated in Figure 1-1, is concentrated in arid and semi-arid regions within the mid-latitudes of both the Northern and Southern Hemispheres. It covers about 16.6% of the land area in Europe, 10.6% in Asia, 6.0% in North America, and 2.6% in South America, amounting to roughly 6% of the Earth's land surface (Li et al., 2020). The thickest and most continuous loess deposits are located in China's Loess Plateau, where the thickness generally ranges from tens to 300 m, with a maximum recorded of 505 m. In contrast, loess deposits in Siberia and Central Asia typically range from several tens of metres to under 200 m in thickness. In other regions, loess thickness generally is less than 20 m in Europe and North America, less than 50 m in South America, less than 20 m in New Zealand, Africa, and the Arabian Peninsula, and less than 3 m in Australia (Li et al., 2020).

Based on gradation curves and Atterberg limits of loess samples taken from the Nebraska-Kansas area, Gibbs and Holland (1960) classified loess into three categories: clayey, silty, and sandy loess, as illustrated in Figure 2-1. Compared to sandy loess, the silty and clayey loess have more fine particles and exhibit higher liquid limits and plasticity indices. This classification method offers a simple yet effective approach for distinguishing loess behaviour and has been widely adopted in subsequent studies (e.g., Jiang et al., 2011; Liu et al., 2016;

Xiao et al., 2022). It should be noted that the properties of loess may fall outside the three regions defined by the gradation curves and Atterberg limits, as this classification provides only a general range rather than strict or exclusive boundaries.

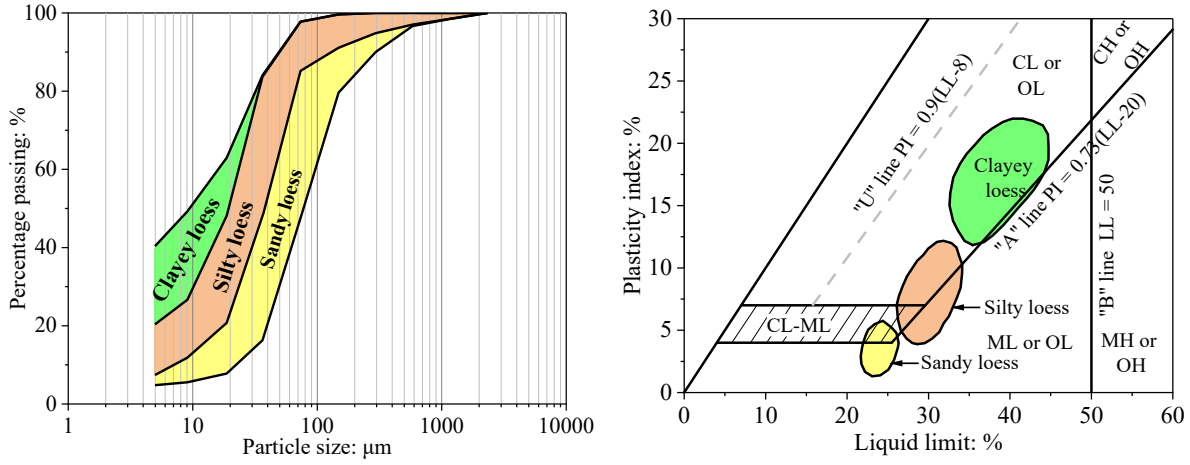

(a) (b)

Figure 2-1. Loess classification based on (a) particle size distribution; (b) Atterberg limits (adapted from Gibbs and Holland, 1960)

2.1.2 Loess modification

Loess is commonly stabilised during geo-structure construction to reduce its collapse potential. The treatment of loess with stabilising additives such as cement and lime has been demonstrated to be an effective method for improving its hydromechanical behaviour (Jefferson et al., 2008; Metelková et al., 2012; Zhang et al., 2017a; Zhang et al., 2018a; Akbari Garakani et al., 2019; Haeri et al., 2019; Zhang et al., 2019b; Guo et al., 2024). The addition of cement or lime results in the formation of new mineral phases, including calcite, calcium silicate hydrates, calcium aluminate hydrates, and calcium aluminate carbonate hydrates (e.g., Metelková et al., 2012; Pei et al., 2015; Guo et al., 2024). These mineral components coat soil particles and fill interparticle voids, resulting in reduced permeability and increased yield stress and shear strength, which significantly improves the performance and durability of earthen structures constructed with treated loess (Jefferson et al., 2008; Sariosseiri and Muhunthan, 2009; Gao et al., 2018; Haeri et al., 2019; Zhang et al., 2019b; Guo et al., 2024). For example, Gao et al. (2018) reported that the saturated hydraulic conductivity of lime-treated loess was lower than that of untreated loess. At a constant dry density, the hydraulic conductivity initially

decreased and then increased as the lime content (by weight) increased from 0% to 12%, with the minimum value observed at 9% lime content. Haeri et al. (2019) showed that adding 3% quicklime (CaO) to untreated loess increased the yield stress by up to 150% and significantly reduced its collapse potential. Guo et al. (2024) reported a substantial increase in unconfined compressive strength from 726 to 3050 kPa when the cement content of loess was increased from 2% to 10% after a 7-day curing period. Jefferson et al. (2008) demonstrated that loess-cement cushion foundations, typically containing 4% to 7% cement (by weight), effectively enhanced the stability of the Kozloduy nuclear power plant. This ground improvement method not only mitigated the risk of loess collapse but also reduced and homogenised settlement across the foundation, thereby improving the long-term performance and safety of the structure.

While cement and lime have been validated as effective stabilising materials, their production processes are energy-intensive and environmentally unsustainable, making their widespread use incompatible with the concept of carbon neutrality (Zhang et al., 2013). Specifically, the production of 1 tonne of Portland cement generally emits approximately 1 tonne of carbon dioxide and consumes around 5000 MJ of energy (Higgins, 2007), and these values are about 0.79 tonne and 3200 MJ for quicklime (Yi et al., 2016). Therefore, industrial by-products such as GGBS are being explored as partial replacements to mitigate these environmental impacts (Yi et al., 2014b). In comparison, the generation of 1 tonne of GGBS results in only 0.07 tonnes of carbon dioxide emissions and requires 1300 MJ of energy (Higgins, 2007), both substantially lower than the corresponding values for Portland cement and quicklime.

As a partial replacement for cement and lime in soil stabilisation, the performance of GGBS has been extensively studied across various soil types (e.g., Kamon and Nontananandh, 1991; Wild et al., 1998; Osinubi, 2006; Obuzor et al., 2011; Yi et al., 2014a; Yi et al., 2014b; Yi et al., 2016; Jia et al., 2019; Cai et al., 2022; Zhao et al., 2024). Obuzor et al. (2011) demonstrated that the addition of lime blended with GGBS reduced the water adsorption rate of Lower Oxford Clay during soaking. Wild et al. (1998) observed that, at a constant binder content, the unconfined compressive strength of kaolinite and Kimmeridge Clay initially

increased and then decreased as the GGBS-to-binder ratio (i.e., the ratio of GGBS to the sum of hydrated lime [$Ca(OH)_2$] and GGBS) increased. The transition ratio, at which peak strength was reached, depended on soil type, binder content, and curing time. A similar trend was also identified by Yi et al. (2014b) for sand and silty clay, and by Parhizkar et al. (2024) for gypsum soil. Although extensive research has been conducted on the applications of GGBS in soil stabilisation, its use in loess modification remains limited. Only a few studies have examined its influence on unconfined compressive strength, where strength was found to increase with increasing GGBS content (Jia et al., 2019; Guo et al., 2022). The capacity of GGBS to reduce loess collapsibility has not been explored, which restricts its application in loess regions.

2.2 Unsaturated soil behaviour

2.2.1 Soil suction

Suction has been commonly considered as one of the fundamental variables for describing the behaviour of unsaturated soils. According to the thermodynamic theory, soil suction can be determined by the measurement of the vapour pressure in equilibrium with the soil water (Aitchison, 1965):

$$\psi = -\frac{R_{gas}(T+273.15)}{v_{w0}\omega_v}\ln\left(\frac{\bar{u}_v}{\bar{u}_{v0}}\right) \tag{2-1}$$

where ψ is the total suction; R_{gas} is the universal gas constant; T is the temperature in degrees Celsius; v_{w0} is the specific volume of water; ω_v is the molecular mass of water vapour; $\bar{u}_v$ is the partial pressure of pore water vapour; $\bar{u}_{v0}$ is the saturation pressure of pore water vapour; and the ratio of $\bar{u}_v/\bar{u}_{v0}$ represents the relative humidity. Total suction is composed of osmotic suction and matric suction (Fredlund and Rahardjo, 1993):

$$\psi = \pi + (u_a - u_w) \tag{2-2}$$

where π is the osmotic suction; u_a and u_w are the pore air pressure and pore water pressure, respectively; and the difference $(u_a - u_w)$ denotes the matric suction s. Osmotic suction is generated by dissolved salts in the soil's pore water. It is equal to the negative gauge pressure required to bring a reservoir of pure water into equilibrium, through a semipermeable

membrane, with a solution of the same chemical composition as the soil water (Krahn and Fredlund, 1972). Matric suction is induced by soil-water interaction, including capillary forces between soil particles and pore water-soil surface adsorptive forces (Philip, 1977; Tuller et al., 1999; Baker and Frydman, 2009; Zhou, 2014). Since this thesis does not involve changes in osmotic suction, the following discussion focuses exclusively on matric suction. Accordingly, the term "suction" is used to denote "matric suction" unless stated otherwise.

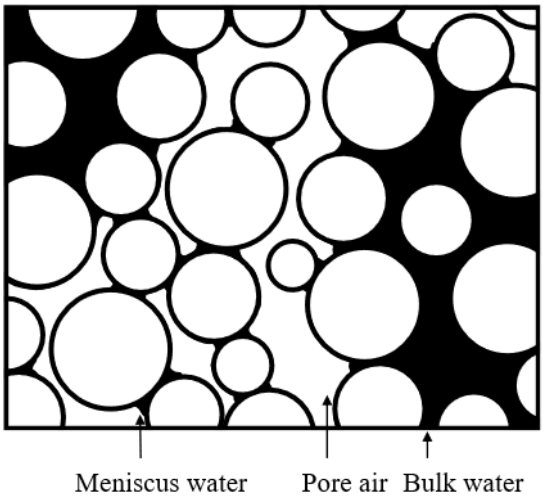

Figure 2-2. Illustration of bulk and meniscus water in an unsaturated soil (Wheeler et al., 2003b)

Soil suction influences the mechanical behaviour of unsaturated soils mainly through two mechanisms (Karube and Kato, 1994; Gallipoli et al., 2003a; Wheeler et al., 2003b): (i) modifying the average soil skeleton stress and (ii) providing additional bonding forces at interparticle contacts. These two mechanisms are closely associated with the distribution of soil water, as shown in Figure 2-2. In unsaturated soils, water can be categorised into adsorptive water, bulk water, and meniscus water (Wheeler and Karube, 1996). Adsorptive water is the thin film of water molecules tightly bound to the surface of soil particles by adsorption forces and can be considered part of the soil skeleton. Bulk water refers to the water that fills the pores in the soil (water-filled voids). Changes in suction within bulk water influence both the normal and tangential forces at interparticle contacts and alter the average soil skeleton stress in a manner analogous to the application of external stress. On the other hand, meniscus water forms at the air-water interface within the soil pores (air-filled voids), creating a meniscus due

to surface tension. The suction within the meniscus water exerts additional normal forces at interparticle contacts, providing stabilisation effects on the soil skeleton (Fisher, 1926; Wheeler et al., 2003b).

Owing to the above two suction mechanisms, two stress state variables are typically required to describe the behaviour of unsaturated soils, as reviewed below.

2.2.2 Stress state variables

Many stress state variables have been proposed to describe the behaviour of unsaturated soils (Bishop, 1959; Coleman, 1962; Jennings and Burland, 1962; Fredlund and Morgenstern, 1977; Khalili and Khabbaz, 1998; Gallipoli et al., 2003a; Lu et al., 2010; Alonso et al., 2013). These stress state variables can be categorised into a single effective stress variable and two constitutive variables (Fredlund and Morgenstern, 1977; Nuth and Laloui, 2008b; Gens, 2010).

2.2.2.1 Single effective stress variable

In earlier studies, researchers attempted to describe unsaturated soil behaviour using a single effective stress variable, analogous to that in saturated conditions (e.g., Bishop, 1959; Coleman, 1962). The single effective stress variable for unsaturated soils was extended from Terzaghi's equation for saturated soils, and any change in soil state could be attributed to changes in the effective stress. A detailed summary of a single effective stress variable was reported by Fredlund and Morgenstern (1977).

One of the most popular single effective stress variables was proposed by Bishop (1959) and is expressed as:

$$\sigma_{ij}^{*} = \left(\sigma_{ij} - u_a\delta_{ij}\right) + \chi s\delta_{ij} \tag{2-3}$$

where σ_{ij}^{*} is the Bishop's stress; σ_{ij} is the total stress; δ_{ij} is the Kronecker's delta, where $\delta_{ij} = 1$ when $i = j$, and $\delta_{ij} = 0$ when $i \neq j$; and χ is a parameter closely associated with suction s and degree of saturation S_r. Various formulations of χ have been proposed in the literature, and several representative forms are given in Table 2-1.

Although adopting a single effective stress variable can well capture the shear strength variation (Khalili and Khabbaz, 1998), certain limitations have been identified when applying this variable to unsaturated soils. On the one hand, calibrating the value of χ is time-consuming (Nuth and Laloui, 2008b). On the other hand, based on the thermodynamic analysis, Houlsby (1997) has proved that at least two stress variables are required to describe the unsaturated soil behaviour fully.

Table 2-1. Typical formulations of χ for the definition of Bishop's stress

Type	Form of χ	Reference
Suction related	$\chi = \begin{cases} 1 & for\ S_r = 1 \\ \left(\frac{\chi_1}{s}\right) s_{ae} & for\ S_r < 1 \end{cases}$	Aitchison (1960) s_{ae} is the air entry suction; χ_1 is a parameter that varies between 0.3 and 0.35
	$\chi = \begin{cases} 1 & for\ s/s_{ae} \le 1 \\ \left(\frac{s}{s_{ae}}\right)^{-\chi_2} & for\ 1 < s/s_{ae} \le 14 \end{cases}$	Khalili and Khabbaz (1998); Khalili et al. (2022) χ_2 is a parameter usually taken as 0.55; extension to high suction was given by Russell and Khalili (2006)
	$\chi = \begin{cases} 1 & for\ s/s_{ae} \le 1 \\ \left(\frac{s}{s_{ae}}\right)^{\chi_3 - 3} & for\ s/s_{ae} > 1 \end{cases}$	Xu (2004) χ_3 is a parameter
Degree of saturation related	$\chi = S_r$	Wheeler et al. (2003b)
	$\chi = (S_r)^{\chi_2/\lambda_{S_r}}$	Mašín (2010) λ_{S_r} is the slope of the SWRC in the $\ln S_r - \ln s$ plane
	$\chi = (S_r)^{\chi_4}$	Vanapalli et al. (1996) χ_4 is a soil-type dependent parameter
	$\chi = S_r^e$	Alonso et al. (2010); Zhou et al. (2012) S_r^e is the effective degree of saturation, and its definition differs among studies

2.2.2.2 Two constitutive variables

Gens (2010) generalised the two constitutive variables into the first constitutive variable (FCV) and the second constitutive variable (SCV), with the general form expressed as:

$$\begin{cases} FCV: \sigma_{ij} - u_a\delta_{ij} + \mu_1(s, S_r)\delta_{ij} \\ SCV: \mu_2(s, S_r)\delta_{ij} \end{cases} \tag{2-4}$$

where $\mu_1(s, S_r)$ and $\mu_2(s, S_r)$ are functions of suction and degree of saturation. Based on the choice of FCV (i.e., the form of function μ_1), Gens (2010) classified the constitutive variables into three classes to examine their influence on the constitutive law.

Class-I: μ_1 = 0. This form is the most straightforward and practical constitutive variable because the stress path can easily be controlled in the experimental tests. Note that the soil is nearly saturated when the suction is higher than zero but lower than the air entry suction. An example is a saturated and heavily overconsolidated soil under undrained shearing, which generates negative pore water pressure during shearing without being unsaturated. Within this suction range, the effective stress should be the total stress minus the pore water pressure (i.e., $\sigma_{ij} - u_w\delta_{ij}$), rather than the total stress minus the pore air pressure (i.e., $\sigma_{ij} - u_a\delta_{ij}$), as obtained by substituting $\mu_1 = 0$ into Equation (2-4). Therefore, the smooth transition between saturated and unsaturated states is not spontaneously ensured in class-I.

Class-II: $\mu_1 = \mu_1(s)$. By incorporating suction into the FCV, the uniqueness of the critical state line under saturated and unsaturated conditions can be observed (Khalili et al., 2004). However, this form of FCV also suffers from some limitations. It is difficult to represent the stress path in conventional laboratory tests.

Class-III: $\mu_1 = \mu_1(s, S_r)$. By considering both suction and degree of saturation, the continuity between saturated and unsaturated conditions is assured, and hydraulic hysteresis is inherently incorporated. However, similar to class-II, a primary disadvantage of this FCV is the difficulty in representing the stress path in experimental tests. Based on the above discussions, typical forms of two constitutive variables are listed in Table 2-2.

Additionally, Lu (2008) argued that should not be considered as a stress variable since stress is defined as force per unit area within a representative elementary volume. However, the area associated with suction pertains to the air-water interface rather than the representative elementary volume. To consider the contribution of suction to effective stress, Lu (2008)

emphasised the need for an upscaling function. Building on this concept, Lu et al. (2010) proposed the effective stress σ'_{ij} as follows:

$$\sigma'_{ij} = \left(\sigma_{ij} - u_a\delta_{ij}\right) - \sigma^s\delta_{ij} \tag{2-5}$$

$$\sigma^s = (u_a - u_w)f_u \tag{2-6}$$

where σ^s is the suction stress; and f_u is an upscaling function.

Table 2-2. Typical formulations of two constitutive variables for unsaturated soils

Type	Typical constitutive variable	References
Class-I	$\begin{cases} FCV: p - u_a \\ SCV: s \end{cases}$	Alonso et al. (1990); Wheeler and Sivakumar (1995); Cui and Delage (1996); Chiu and Ng (2003); Sheng et al. (2008)
Class-II	$\begin{cases} FCV: p - u_a + \chi s \\ SCV: s \end{cases}$	Laloui et al. (2001); Loret and Khalili (2002); Khalili et al. (2008)
Class-III	$\begin{cases} FCV: p - u_a + sS_r \\ SCV: ns \end{cases}$	Wheeler et al. (2003b)
	$\begin{cases} FCV: p - u_a + sS_r \\ SCV: f(s)(1 - S_r) \end{cases}$	Gallipoli et al. (2003a) $f(s)$ is a function of suction
	$\begin{cases} FCV: p - u_a + sS_r \\ SCV: s \end{cases}$	Sheng et al. (2008)
	$\begin{cases} FCV: p - u_a + sS_r^e \\ SCV: S_r^e \end{cases}$	Zhou et al. (2012)
	$\begin{cases} FCV: p - u_a + sS_r^e \\ SCV: sS_r^e \end{cases}$	Alonso et al. (2013)

Note: p is the mean total stress.

From the thermodynamic analysis, Lu et al. (2010) demonstrated that the upscaling function equals the negative effective degree of saturation, allowing the effective stress to be reformulated as:

$$\sigma'_{ij} = \left(\sigma_{ij} - u_a\delta_{ij}\right) + S_r^e(u_a - u_w)\delta_{ij} \tag{2-7}$$

Note that the suction is not a stress variable in the model of Lu et al. (2010) and the suction effects on the soil behaviour are considered through the suction stress term (i.e., σ^s).

2.2.3 Suction effects on mechanical behaviour

2.2.3.1 Compression and shear behaviour

Extensive experimental studies have examined the influence of suction on the compression and shear behaviour of unsaturated soils (e.g., Sivakumar, 1993; Cui and Delage, 1996; Sivakumar and Wheeler, 2000; Mancuso et al., 2002; Lloret et al., 2003; Futai and Almeida, 2005; Sun et al., 2007; Uchaipichat and Khalili, 2009; Alonso et al., 2013; Cheng, 2017; Zheng et al., 2017; Mu et al., 2022). General conclusions regarding suction effects on yield stress, post-yield compressibility, and shear strength are briefly summarised below.

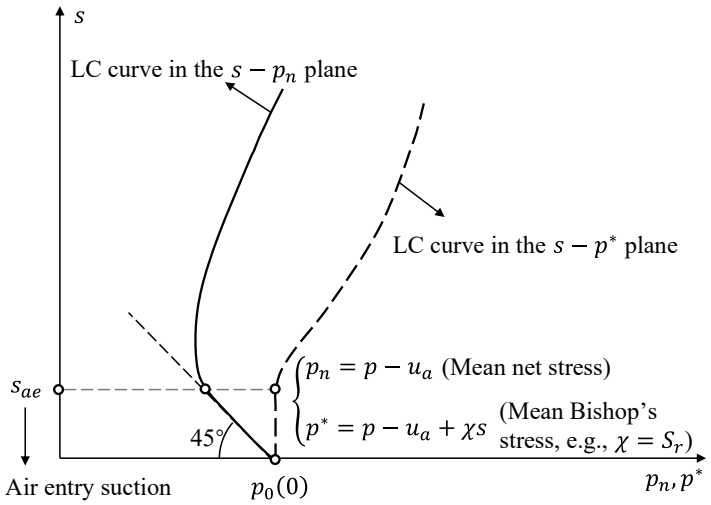

Figure 2-3. Loading collapse curves in the $s - p_n$ and $s - p^*$ planes (adapted from Khalili et al., 2022)

As illustrated in Figure 2-3, the variation in yield stress with suction is highly dependent on the adopted stress state variable. When suction is below the air entry value, the yield stress in terms of mean net stress ($p_n = p - u_a$) decreases with suction, whereas the yield stress in terms of mean Bishop's stress ($p^* = p - u_a + \chi s$, e.g., $\chi = S_r$) remains constant (Sheng et al., 2008; Uchaipichat and Khalili, 2009; Alonso et al., 2013; Khalili et al., 2022). This observation is attributed to the soil remaining nearly saturated within this suction range (i.e., $S_r \rightarrow 1$), thereby resulting in a constant yield stress in terms of mean effective stress ($p - u_w$).

Accordingly, the mean Bishop's yield stress (e.g., $p - u_a + sS_r$), equivalent to the mean effective yield stress under $S_r \to 1$, remains constant. In contrast, the mean net yield stress ($p - u_w - s$) (i.e., the mean effective yield stress minus suction) decreases linearly as suction increases. When suction is higher than the air entry value, the yield stress becomes higher with increasing suction. To support the trend illustrated in Figure 2-3, an experimental observation reported by Uchaipichat and Khalili (2009) is presented in Figure 2-4. It should be highlighted that many experimental studies in the literature do not include compression tests at suctions below the air entry value. Consequently, the decrease in mean net yield stress and the constancy of mean Bishop's yield stress with increasing suction are often not observed.

The observation in Figure 2-3 can be well explained by the suction mechanisms outlined in the "2.2.1 Soil suction" section. When suction remains below the air entry value ($s < s_{ae}$), it influences soil behaviour predominantly by modifying the average soil skeleton stress (e.g., mean Bishop's stress). In this range, the second mechanism, providing additional bonding forces at interparticle contacts, is negligible due to the absence of sufficient meniscus water, thereby leading to a constant mean Bishop's yield stress. In contrast, both suction mechanisms contribute once suction exceeds s_{ae}, resulting in increased yield stress with increasing suction.

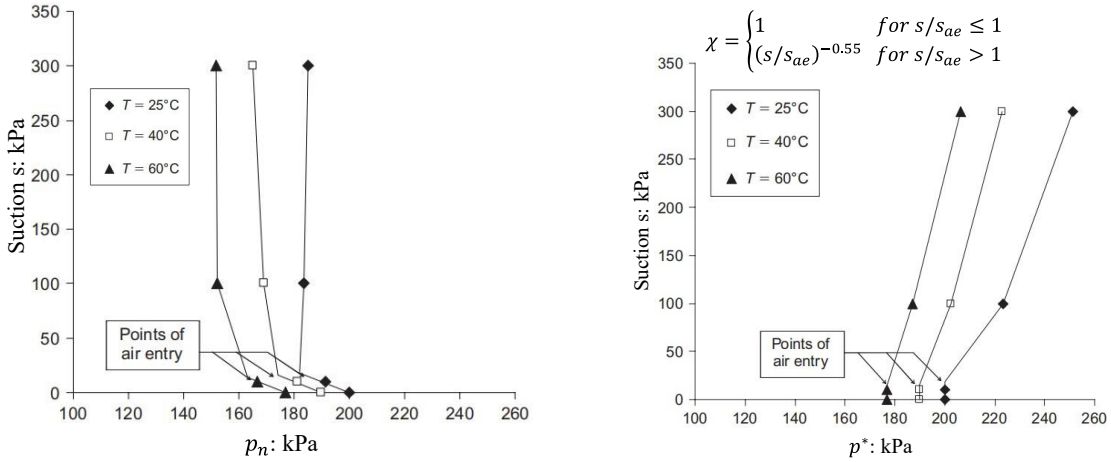

(a) (b)

Figure 2-4. Measured LC curves under different planes: (a) $s - p_n$ plane; (b) $s - p^*$ plane (Uchaipichat and Khalili, 2009)

The influence of suction on post-yielding compressibility, denoted as $\lambda(s)$, exhibits divergent trends in the literature. With increasing suction, $\lambda(s)$ has been reported to either

increase (e.g., Chiu and Ng, 2003; Futai and Almeida, 2005; Mu et al., 2022), decrease (e.g., Cui and Delage, 1996; Mancuso et al., 2002; Vassallo et al., 2007), or exhibit a non-monotonic variation (e.g., Sivakumar, 1993; Estabragh et al., 2004; Sivakumar et al., 2010). For example, Chiu and Ng (2003) observed an increase in $\lambda(s)$ for compacted silt from 0.09 to 0.18 as suction increased from 0 to 150 kPa. In contrast, Mancuso et al. (2002) reported a decrease in $\lambda(s)$ for compacted silty sand as suction increased from 0 to 300 kPa. Additionally, Estabragh et al. (2004) found that $\lambda(s)$ for loosely compacted low-plasticity clay initially increased with suction changed from 0 to 100 kPa, then decreased as suction increased to 300 kPa. The increase in compressibility with increasing suction could be attributed to the formation of more compressible macropores during drying. In contrast, the reduction in compressibility is likely due to the stiffer soil skeleton at a higher suction, which governs soil behaviour (Zhou et al., 2012). Furthermore, a non-monotonic compressibility trend may result from the competing effects of macropore formation and skeleton stiffening. These findings suggest that expressing the compressibility as a function of suction is difficult to normalise the compression behaviour of unsaturated soils.

The shear strength of unsaturated soils generally increases linearly with suction when suction remains below the air entry value. Beyond the air entry suction, the rate of shear strength increase diminishes, with strength approaching a maximum value (Gan and Fredlund, 1996; Vanapalli et al., 1996; Khalili and Khabbaz, 1998). This is because the shear strength of unsaturated soils is strongly correlated to the Bishop's stress, with shear strength $\tau = c' + (\sigma - u_a + \chi s)\tan\phi'$, where c' is the effective cohesion under saturated conditions, and ϕ' is the effective friction angle (Alonso et al., 2010). When suction is below the air entry value (i.e., S_r and χ are close to 1), the increase in suction is equivalent to an increase in Bishop's stress and consequently shear strength. However, once suction exceeds the air entry value, the degree of saturation decreases and χ becomes less than 1, thereby reducing the contribution of suction to Bishop's stress and diminishing its influence on shear strength.

2.2.3.2 Small-strain shear stiffness

The stress-strain response of soils is highly non-linear, with shear stiffness decreasing significantly as strain increases, often by several orders of magnitude (see Figure 2-5). Based on its relative magnitude, the shear strain can be categorised into three ranges (Atkinson, 2000; Clayton, 2011): very small-strains (≤ 0.001%), small-strains (from 0.001% to 1%), and large strains (> 1%). The shear stiffness at very small strains remains constant and is referred to the small-strain shear stiffness G_0, which can be determined using bender elements or resonant column tests. In the small-strain range, stiffness decreases significantly with increasing strain and it can be measured using local strain measurement devices such as Hall-effect transducers (Ng and Yung, 2008) or local LVDTs (Clayton, 2011). At strains exceeding approximately 1%, stiffness is usually an order of magnitude smaller than G_0 and continues to decrease until failure (Viggiani and Atkinson, 1995). Large strain behaviour is generally captured through conventional tests such as the triaxial shear test.

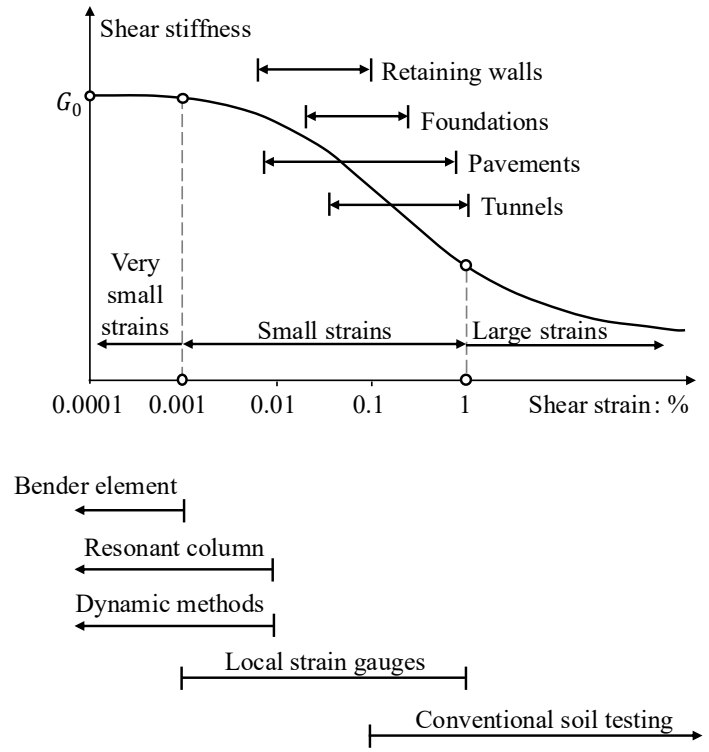

Figure 2-5. Variation of shear stiffness with deviatoric strain (adapted from Atkinson, 2000)

Figure 2-5 illustrates that the strain levels experienced by many geotechnical structures (such as foundations, pavements, and tunnels) under working conditions typically fall within

the small-strain range. Therefore, understanding soil behaviour at very small and small strains is critical for evaluating the performance of geo-structures under service states. Over the past several decades, extensive research has been conducted on the small-strain behaviour of saturated and unsaturated soils. Findings indicate that stiffness at small strains is significantly influenced by suction.

Experimental evidence indicates that G_0 generally increases with suction, attributed to increased average skeleton stress (e.g., mean Bishop's stress) and the stabilisation effects of suction (Mancuso et al., 2002; Mendoza and Colmenares, 2006; Vassallo et al., 2007; Ng and Yung, 2008; Sawangsuriya et al., 2009b; Biglari et al., 2012; Hoyos et al., 2015; Ng et al., 2017).

Furthermore, G_0 is highly dependent on hydraulic hysteresis (Vassallo et al., 2007; Ng et al., 2009; Heitor et al., 2015b). Ng et al. (2009) examined the effects of drying-wetting cycles on the stiffness of completely decomposed tuff (clayey silt). For a given suction, G_0 was consistently larger during wetting than drying. Similarly, Heitor et al. (2015b) found that, under the same suction, the stiffness of compacted silty sand was larger along the wetting path than the drying path, and the difference diminished with successive drying-wetting cycles (see Figure 2-6).

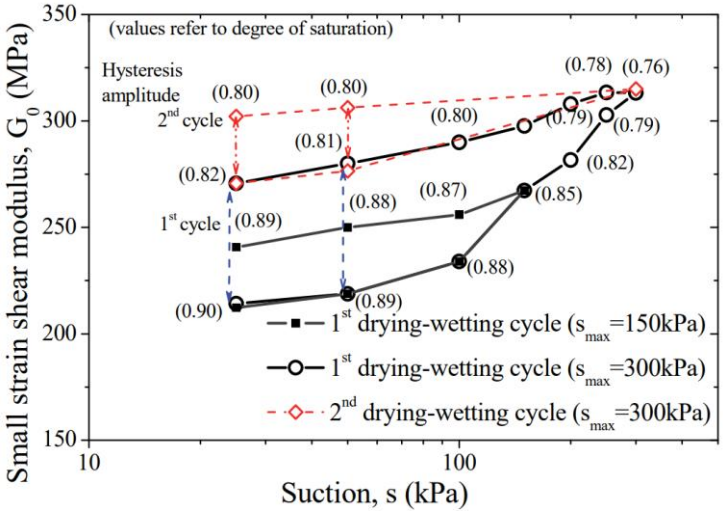

Figure 2-6. Variation of small-strain shear stiffness during drying-wetting cycles (Heitor et al., 2015a; Heitor et al., 2015b)

Ng and Xu (2012) investigated the influence of suction history on G_0 of clayey silt. They

found that, at a given suction, specimens that had previously experienced a higher maximum suction exhibited a larger stiffness, consistent with observations by Vassallo et al. (2007) for clayey silt and Heitor et al. (2015b) for silty sand (see Figure 2-6). Furthermore, Ng and Xu (2012) demonstrated that the specimens that experienced the same maximum suction but underwent different suction paths had similar G_0. The findings of Ng and Xu (2012) suggest that, aside from differences in water content, another major reason for the larger G_0 observed during the wetting path compared to the drying path is the exposure of the specimen to a higher maximum suction, which may cause significant volumetric contraction.

In addition to experimental investigations, many semi-empirical equations have been proposed to calculate the small-strain shear stiffness under various stress states. For saturated soils under isotropic compression, the general form describing the dependence of G_0 on mean effective stress, void ratio, and overconsolidation ratio (OCR) is given as follows (Hardin, 1978; Atkinson, 2000):

$$\frac{G_0}{p_r} = A_G f(e) \left(\frac{p'}{p_r}\right)^{n_G} OCR^{m_G} \tag{2-8}$$

where A_G, n_G, and m_G are model parameters; $f(e)$ is a void ratio function (see Table 2-3 for typical formulations); and p_r is the reference pressure, typically taken as 1 kPa.

Table 2-3. Void ratio functions $f(e)$ for the calculation of G_0 (Mitchell and Soga, 2005)

$f(e)$	Reference
$(2.174 - e)^2/(1 + e)$	Hardin and Richart (1963)
$(2.973 - e)^2/(1 + e)$	
e^{-x_E}	Lo Presti et al. (1997) x_E is a model parameter
$(1 + e)^{-x_E}$	Shibuya et al. (1997): $x_E = 2.4$ Oztoprak and Bolton (2013): $x_E = 3$
$(4.4 - e)^2/(1 + e)$	Marcuson and Wahls (1972)
$(7.32 - e)^2/(1 + e)$	Kokusho et al. (1982)
$1/(0.3 + 0.7e^2)$	Hardin and Blandford (1989)
$e^{-(0.28C_u + 0.98)}$	Senetakis et al. (2012) C_u is the coefficient of uniformity obtained from particle size distribution curve
$e^{-0.419C_u}$	Senetakis et al. (2013)

It has been demonstrated that G_0 can be determined using any two of the three variables (i.e., p', e, and OCR), since the third can be derived from the isotropic compression curve (e.g., Houlsby and Wroth, 1991; Rampello et al., 1997). Moreover, laboratory tests on various soil types have shown that the OCR term in Equation (2-8) becomes redundant when an appropriate void ratio function is employed (e.g., Jamiolkowski et al., 1995; Viggiani and Atkinson, 1995; Shibuya et al., 1997). Consequently, Equation (2-8) can be simplified as:

$$\frac{G_0}{p_r} = A_G f(e) \left(\frac{p'}{p_r}\right)^{n_G} \tag{2-9}$$

For saturated soils under anisotropic stress conditions, it is well established that G_0 is primarily governed by the effective principal stresses within the shear plane and is nearly unaffected by the stress normal to that plane (Roesler, 1979; Hardin and Blandford, 1989; Stokoe et al., 1995; Bellotti et al., 1996). Accordingly, Equation (2-9) has been adapted for anisotropic stress conditions as:

$$\frac{G_{ij}}{p_r} = A_{ij} f(e) \left(\frac{\sigma_i'}{p_r}\right)^{n_i} \left(\frac{\sigma_j'}{p_r}\right)^{n_j} \tag{2-10}$$

where A_{ij} is a model parameter associated with the $i-j$ shear plane on which the stiffness G_{ij} is measured; n_i and n_j are model parameters related to the influence of σ_i' and σ_j', respectively; and σ_i' and σ_j' represent the principal effective stresses acting within the shear plane. Experimental data have shown that both stresses σ_i' and σ_j' exert comparable effects on G_{ij}, implying that the value of n_i is close to that of n_j (Viggiani and Atkinson, 1995; Bellotti et al., 1996). Therefore, Equation (2-10) can be rewritten as:

$$\frac{G_{ij}}{p_r} = A_{ij} f(e) \left(\frac{\sigma_i' \sigma_j'}{p_r^2}\right)^{(n_i+n_j)/2} \tag{2-11}$$

In unsaturated soils, the calculation of G_0 typically incorporates suction and degree of saturation (e.g., Cho and Santamarina, 2001; Mancuso et al., 2002; Mendoza et al., 2005; Sawangsuriya, 2006; Takkabutr, 2006; Ng and Yung, 2008; Sawangsuriya et al., 2009b; Khosravi et al., 2010; Biglari et al., 2011; Hoyos et al., 2011; Khosravi, 2011; Khosravi and McCartney, 2012; Ghayoomi et al., 2013; Heitor et al., 2013; Oh and Vanapalli, 2014; Wong

et al., 2014; Zhou et al., 2015; Dong et al., 2016; Vahedifard et al., 2020; Biglari et al., 2021). It is worth noting that the review of G_0 for unsaturated soils mainly focuses on the isotropic stress state, as the consideration of anisotropic stress states is similar to that in saturated soils.

Among the previously proposed equations, several incorporate the effects of unsaturation on G_0 using suction alone as the governing parameter (e.g., Mancuso et al., 2002; Ng and Yung, 2008). For instance, based on experimental evidence showing an S-shaped increase of G_0 with suction, Mancuso et al. (2002) proposed the following equation:

$$\begin{cases} G_0 = A_G \left(\frac{p_n+s}{p_r}\right)^{n_G} OCR^{m_G} \quad for\ s \le s_M \\ G_0 = (G_0)_{s=s_M}\{[1-r_M]\exp[-\beta_M(s-s_M)]+r_M\} \quad for\ s > s_M \end{cases} \tag{2-12}$$

where s_M is a suction closely related to the air entry value; r_M is the ratio of stiffness at infinite suction to that at s_M; β_M is a parameter governing the rate of stiffness increase with suction; and the subscript "M" indicates that the parameters are specific to Mancuso et al. (2002).

However, incorporating only suction cannot consider the effects of hydraulic hysteresis. Therefore, equations incorporating both suction and degree of saturation have been proposed (e.g., Khosravi and McCartney, 2012; Heitor et al., 2013; Oh and Vanapalli, 2014; Zhou et al., 2015). For example, Zhou et al. (2015) proposed an equation for unsaturated soils that incorporates the effects of hydraulic hysteresis on G_0:

$$G_0 = A_G(1+e)^{-3}\left[\left(\frac{p-u_a+sS_r}{p_r}\right)^{0.5} + n_G\bar{\xi}^{0.5}\right] \tag{2-13}$$

where $\bar{\xi} = f(s)(1-S_r)$ is a bonding variable; and $f(s)$ is a function used to describe the effects of interparticle normal force (ΔN) imposed by a single water meniscus, defined as ΔN at a suction of s normalised by ΔN at zero suction. The term $(1-S_r)$ accounts for the number of water meniscus per unit soil volume in a simplified approach. Therefore, the variable $\bar{\xi}$ (i.e., production of $f(s)$ and $(1-S_r)$) represents a measurement of the interparticle bonding provided by the water meniscus. $f(s)$ can be calculated with the following equation

(Fisher, 1926):

$$f(s) = \frac{3T_s}{R_p s}\frac{\left(\sqrt{9+8R_p s/T_s}-3\right)\left(\sqrt{9+8R_p s/T_s}+1\right)}{16} \quad (2\text{-}14)$$

where T_s is the surface tension of the air-water interface (72.8 mN/m at 20 °C); and R_p is the radius of the spherical particles. In Equation (2-13), the difference in S_r between drying and wetting paths leads to distinct G_0 values, thereby accounting for the influence of hydraulic hysteresis. More formulations for G_0 under unsaturated conditions are presented in Table 2-4.

Table 2-4. Typical formulations of G_0 for unsaturated soils under isotropic stress state

Type	Equation	Reference
Without hydraulic hysteresis	$\begin{cases} G_0 = A_G\left(\frac{p_n+s}{p_r}\right)^{n_G} OCR^{m_G} \quad for\ s \le s_M \\ G_0 = (G_0)_{s=s_M}\{[1-r_M]\exp[-\beta_M(s-s_M)]+r_M\}\ for\ s > s_M \end{cases}$	Mancuso et al. (2002)
	$G_0 = A_G e^{-x}\left(\frac{p_n}{p_r}\right)^{n_G}\left(1+\frac{s}{p_r}\right)^{k_G}$	Ng and Yung (2008) k_G is a model parameter
With hydraulic hysteresis	$G_0 = \frac{A_G}{0.3+0.7e^2}(p_n)^{n_G} + C_{SA}s(S_r)^{k_G}$	Sawangsuriya et al. (2009b) C_{SA} is a parameter
	$G_0 = \frac{A_G}{0.3+0.7e^2}[p_n + s(S_r)^{k_G}]^{n_G}$	Sawangsuriya et al. (2009b)
	$G_0 = A_G f(e)\left(\frac{p_n+sS_r}{p_r}\right)^{n_G}$	Ghayoomi et al. (2013)
	$G_0 = A_G(1+e)^{-3}\left[\left(\frac{p-u_a+sS_r}{p_r}\right)^{0.5} + n_G\bar{\xi}^{0.5}\right]$	Zhou et al. (2015)
	$G_0 = \frac{A_G}{0.3+0.7e^2}\left[\frac{p_n+s(S_r^e)^{k_G}}{p_r}\right]^{n_G}$	Vahedifard et al. (2020)

2.2.3.3 Cyclic behaviour

In engineering practice, soils are commonly subjected to cyclic stresses from sources such as earthquake loads, traffic loads, and wave loads. Understanding soil behaviour under these conditions is essential for the serviceability and safety of geo-structures, including soil slopes, pavements, and marine infrastructures. In this section, the responses of unsaturated soils

subjected to cyclic loading are reviewed.

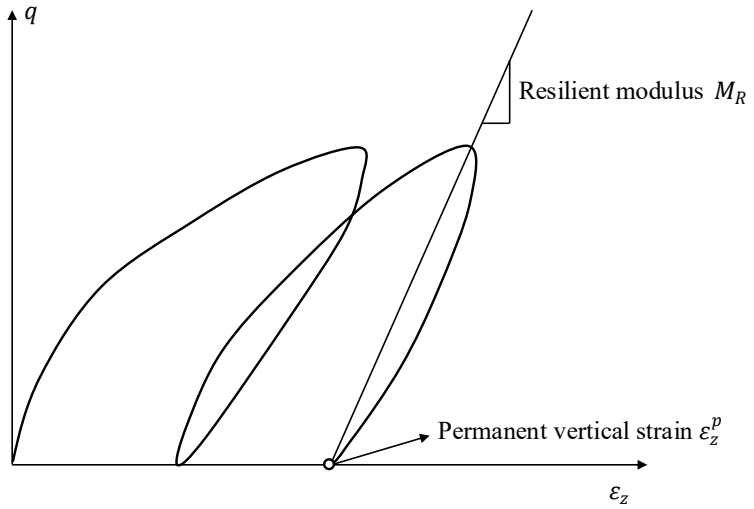

Figure 2-7. Definitions of permanent strain and resilient modulus

Previous studies on the cyclic behaviour of unsaturated soils have primarily focused on the accumulation of permanent vertical strain (i.e., ε_z^p) and variation of resilient modulus (i.e., M_R). As illustrated in Figure 2-7, permanent vertical strain refers to the irreversible deformation that accumulates in the soil after each loading cycle, while resilient modulus is defined as the ratio of the applied cyclic deviatoric stress (i.e., q_{cyc}) to the recoverable strain in the soil (Brown, 1996). To study the suction effects on cyclic behaviour, some studies prepared soil specimens under different water contents and conducted cyclic tests at their as-compacted states (e.g., Khoury and Zaman, 2004; Sivakumar et al., 2013; Zhang et al., 2019a). However, their specimen preparation method resulted in differences not only in initial suction but also in soil fabric among specimens (Delage et al., 1996; Sivakumar and Wheeler, 2000; Alonso et al., 2013), making it challenging to examine the effects of suction on cyclic behaviour. Consequently, it is preferable to prepare specimens under an identical compaction condition and then specimens are dried or wetted to states with different suctions before the application of cyclic stresses.

Yang et al. (2008b) compacted specimens at the optimum water content and performed suction-controlled cyclic tests on two types of unsaturated low-plasticity clay. For one soil type, the resilient modulus consistently increased with increasing suction under various levels of cyclic deviatoric stress. However, for the second type, a decrease in resilient modulus with

increasing suction was observed when cyclic deviatoric stress was less than 34 kPa. Ng and Zhou (2014) examined the effects of suction on permanent vertical strain and resilient modulus in unsaturated silt. As illustrated in Figure 2-8, their results showed a substantial reduction in permanent vertical strain and a notable increase in resilient modulus with increasing suction. Specifically, the permanent vertical strain decreased by up to 90%, while the resilient modulus increased by as much as 200% as suction was increased from 0 to 60 kPa. The smaller permanent vertical strain and larger resilient modulus at a higher suction have been widely observed in the literature, such as Ng et al. (2013) for silt, Han and Vanapalli (2016) for low-plasticity clayey silt and low-plasticity clays, Chen et al. (2018) and Su and Cui (2022) for fine-coarse soil mixtures, and Azizi et al. (2023) for clayey sand.

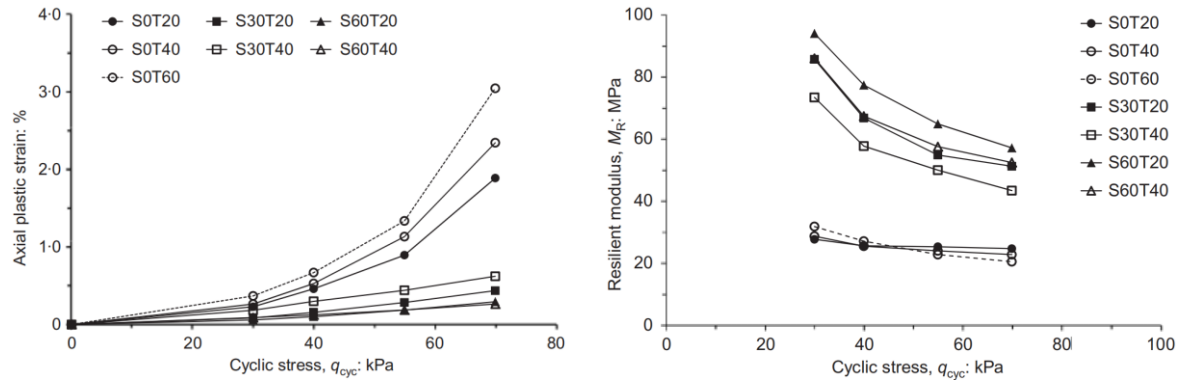

(a) (b)

Figure 2-8. Influence of suction (S) and temperature (T) on cyclic behaviour: (a) permanent vertical strains; (b) resilient moduli (Ng and Zhou, 2014)

The cyclic behaviour of unsaturated soils is also strongly influenced by hydraulic hysteresis. Ng et al. (2013) conducted cyclic tests on unsaturated silt under drying and wetting curves. Under the same suction, the resilient modulus along the wetting path was larger than that along the drying path, with a relative difference of about 20% at a suction of 150 kPa and a cyclic deviatoric stress of 30 kPa. The difference in resilient modulus became negligible when cyclic deviatoric stress exceeded 40 kPa under the same suction. Azizi et al. (2023) investigated the effects of hydraulic cycles on the cyclic behaviour of clayey sand. Their findings indicated that, under the same suction and cyclic deviatoric stress, specimens subjected to more drying-wetting cycles may exhibit either smaller or larger permanent vertical strains. The seemingly contradictory observations were attributed to the different degrees of saturation before and after

drying-wetting cycles. Under the same suction, specimens subjected to more hydraulic cycles may exhibit either higher or lower degrees of saturation. Consequently, variations in S_r lead to distinct average skeleton stresses and bonding forces between soil particles (the two suction mechanisms described in section 2.2.1) and result in different strain accumulation responses. The results of Azizi et al. (2023) highlight that both suction and degree of saturation are necessary to fully capture the effects of hydraulic hysteresis on the cyclic behaviour of unsaturated soils.

However, the aforementioned studies on the influence of suction on cyclic behaviour have primarily focused on soil response under cyclic vertical stress, without accounting for the principal stress rotation that occurs under repeated traffic loads. So far, extensive experimental tests have been conducted to investigate the deformation behaviour of subgrade soil under repeated traffic loads (Chan and Brown, 1994; Gräbe and Clayton, 2009,2014; Xiao et al., 2014; Cai et al., 2015; Guo et al., 2016; Qian et al., 2016; Cai et al., 2017; Cai et al., 2018; Guo et al., 2018; Qian et al., 2019a; Blackmore et al., 2020; Fedakar et al., 2021). It has been revealed that the PSR has deleterious impacts on soil behaviour (Gräbe and Clayton, 2009). Under the same cyclic deviatoric stress, the permanent vertical strain was generally larger, and the modulus was smaller when considering PSR than the case without PSR. For example, Xiao et al. (2014) found that under the same cyclic deviatoric stress, the application of PSR resulted in a 23% increase in permanent strain for a low-plasticity clay. Gräbe and Clayton (2014) observed a 20% to 26% reduction in resilient modulus (the ratio of cyclic deviatoric stress to recoverable vertical strain) when PSR is considered for silty sand and clayey sand. The PSR may affect cyclic behaviour with suction in a coupled approach for different mechanisms. For instance, variations in suction can either stabilise or weaken the soil skeleton, thereby influencing the additional deformation induced by PSR. Therefore, it is essential to investigate the impact of PSR on cyclic behaviour through suction-controlled tests.

As the resilient modulus is a critical parameter in pavement design (AASHTO, 2020), many semi-empirical equations have been proposed to account for the unsaturation effects (Heath et al., 2004; NCHRP, 2004; Liang et al., 2008; Sawangsuriya et al., 2009a; Ba et al.,

2013; Khoury et al., 2013; Ng et al., 2013; Han and Vanapalli, 2015,2016; Su et al., 2022; Azizi et al., 2023). These equations can generally be categorised into three groups based on the adopted stress variables: (i) suction-based (e.g., Heath et al., 2004; Ng et al., 2013); (ii) degree of saturation-based (e.g., NCHRP, 2004; Khoury et al., 2013); and (iii) combined suction and degree of saturation-based approaches (e.g., Han and Vanapalli, 2015; Azizi et al., 2023).

A representative suction-based equation for resilient modulus, proposed by Ng et al. (2013), is expressed as follows:

$$M_R = M_0 \left(\frac{p_{c0}}{p_r}\right)^{k_1} \left(1 + \frac{q_{cyc}}{p_r}\right)^{k_2} \left(1 + \frac{s}{p_{c0}}\right)^{k_3} \quad (2\text{-}15)$$

where M_0, k_1, k_2, and k_3 are model parameters; and p_{c0} is the confining pressure. The suction-based equation is adapted from the formulation by Ng and Yung (2008), originally proposed for calculating small-strain shear stiffness. While it can be conveniently applied to interpret results from suction-controlled cyclic tests, it does not account for the effects of hydraulic hysteresis on resilient modulus.

With respect to the degree of saturation, the National Cooperative Highway Research Program (NCHRP, 2004) developed an equation to predict change in modulus with moisture content as follows:

$$\log\left(\frac{M_R}{M_{R,opt}}\right) = a_N + \frac{b_N - a_N}{1+\exp[\ln(-b_N/a_N) + k_N(S_r - S_{r,opt})]} \quad (2\text{-}16)$$

where $M_{R,opt}$ is the resilient modulus at maximum dry density and optimum water content; a_N, b_N, and k_N are model parameters; $S_{r,opt}$ is the degree of saturation at maximum dry density and optimum water content; and the subscript "N" refers to parameters defined in NCHRP (2004). Using the available literature data and assuming a maximum ratio of $M_R/M_{R,opt}$ of 2.5 for fine-grained materials and 2 for coarse-grained materials, NCHRP (2004) recommended the following values for the model parameters: for coarse-grained materials: a_N = -0.3123, b_N = 0.3000, and k_N = 6.8157; for fine-grained materials: a_N = -0.5934, b_N = 0.4000, and k_N = 6.1324. One advantage of the degree of saturation-based equation for resilient modulus is its practicality in engineering applications, as the degree of saturation can

be readily measured in the field.

To consider the influence of hydraulic hysteresis, many researchers have developed their equations using both suction and degree of saturation. Based on the suction mechanisms, Azizi et al. (2023) proposed the following equation for resilient modulus:

$$M_R = \left(\frac{p-u_a+sS_r}{p_r}\right)^{k_1}\left(1+\frac{q_{cyc}}{p_r}\right)^{-k_2} + M_0\exp\left(k_3\bar{\xi}\right) \quad (2\text{-}17)$$

In Equation (2-17), the effects of suction on average skeleton stress are captured by the first term on the right-hand side, while its contribution to additional bonding forces is represented by the last term. Furthermore, since the degree of saturation varies after drying-wetting cycles, the influence of hydraulic hysteresis is inherently incorporated. Based on a comparison between experimental data and model calculations, Azizi et al. (2023) demonstrated that Equation (2-17) performs well in capturing the resilient modulus of unsaturated soils.

Overall, soil suction has a significant influence on the mechanical properties of unsaturated soils, and hydraulic hysteresis plays a critical role in unsaturated soil behaviour. The two suction mechanisms, modifying the average skeleton stress and providing additional bonding forces between soil particles, effectively explain the observed behaviour of unsaturated soils.

2.3 Influence of soil structure and anisotropy on soil behaviour

Soil structure, defined as a combination of fabric (arrangement of particles) and cementation bonding (Mitchell and Soga, 2005), exerts a substantial influence on the hydro-mechanical behaviour of soil. The investigation of structure effects typically involves a comparison between structured soils and reference states, such as intact versus reconstituted or compacted soils (Burland, 1990; Liu and Carter, 2002), or soils prepared under different compaction conditions, including compaction dry density (or compaction effort) and water content (Tarantino and De Col, 2008; Oualmakran et al., 2016). Intact soils typically possess inherent structures resulting from natural deposition processes and complex stress-strain

histories (Burland, 1990). Additionally, soils prepared under different compaction conditions exhibit distinct particle arrangements (Delage et al., 1996; Alonso et al., 2013). For example, Delage et al. (1996) found that Jossigny silt compacted at the dry of optimum water content exhibited an aggregated structure. In contrast, a matrix-type structure (i.e., silt particles enveloped by clay grains) was identified in the specimen compacted at the wet of optimum. This section presents the influence of soil structure on mechanical properties, including compression curve, shear strength, small-strain shear stiffness, and cyclic behaviour. In addition, anisotropic soil behaviour is reviewed as structured soils are typical anisotropic due to their depositional history.

2.3.1 Structure effects on mechanical behaviour

2.3.1.1 Compression and shear behaviour

By conducting tests on intact (structured) and reconstituted (or compacted) soils (reference), the influence of soil structure on compression behaviour has been investigated by many researchers (e.g., Burland, 1990; Anagnostopoulos et al., 1991; Callisto and Calabresi, 1998; Jiang et al., 2011; Haeri, 2016; Xu and Coop, 2016; Ng et al., 2019; Mu et al., 2022). As illustrated in Figure 2-9, structured soils usually have a higher yield stress and can sustain a higher void ratio at a given stress state than reference soils. When the applied stress exceeds the yield stress of the structured soil, plastic deformation alters the soil fabric and damages the interparticle cementation bonds, resulting in structure degradation (Kavvadas and Amorosi, 2000; Baudet and Stallebrass, 2004; Zhou and Ng, 2018). This degradation increases the post-yielding compressibility and causes a gradual convergence of the compression curves of structured and reference soils.

Moreover, the LC curve, a fundamental characteristic of unsaturated soils, is also significantly influenced by soil structure. As illustrated in Figure 2-10, the inclination of the normalised LC curve for a structured soil can be either smaller (i.e., case-I) or larger (i.e., case-II) than that of the reference state. Case-I is generally observed in soils containing a significant number of cementitious materials, like artificially cemented soils (e.g., Arroyo et al., 2013).

The bonding effects play a dominant role, as compared to the influence of unsaturation. Case-II often corresponds to natural soils without strong bonding but with significant fabric effects. One example is intact loess, in which most clay particles accumulate around the contacts between silt particles (e.g., Muñoz-Castelblanco et al., 2012; Ng et al., 2017). The stiffening effects of clay particles on the soil skeleton are sensitive to the moisture condition (e.g., Mu et al., 2022). Additionally, the normalised LC curve of some soils is insensitive to soil structure (i.e., case-III) (e.g., Mu et al., 2020).

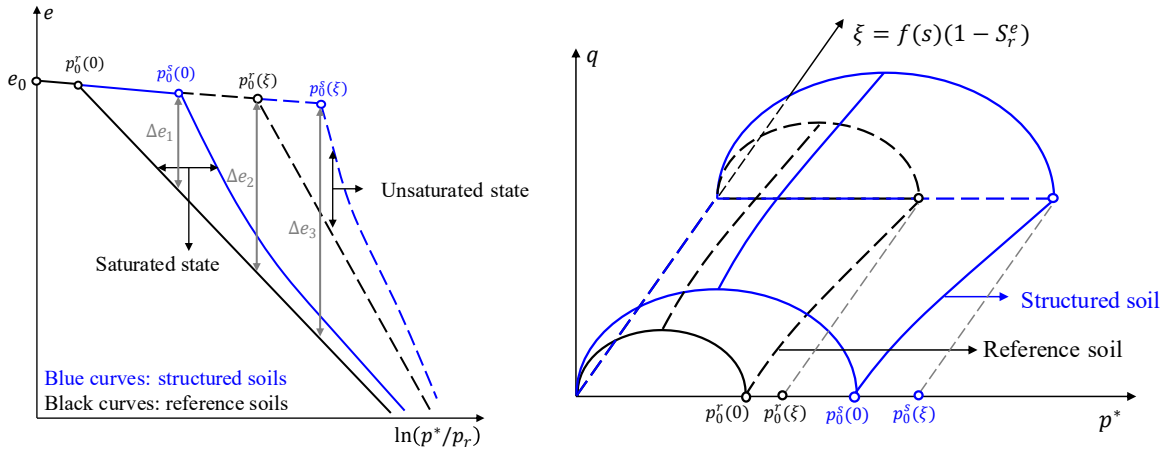

Figure 2-9. Influence of soil structure on (a) isotropic compression curve; (b) yield surface

During shearing, Liu and Carter (2002) found that a structured soil was more contractive (i.e., a larger value of $d\varepsilon_v^p/d\varepsilon_q^p$) than the corresponding reference soil. A similar phenomenon can also be identified for structured soils under unsaturated conditions (Haeri et al., 2017). Furthermore, previous studies have suggested that structured soils behave similarly to reference soils after experiencing significant plastic deformation (Kavvadas and Amorosi, 2000; Liu and Carter, 2002; Yan and Li, 2011; Zhou and Ng, 2018). This implies that the critical state line is identical for both structured and reference soils, even though their stress-strain curves during shearing differ substantially. Conversely, based on microstructural analysis by Fearon and Coop (2000), Baudet and Stallebrass (2004) suggested that some structure elements persisted in structured soils even under large strains, implying the existence of stable fabrics in structured soils. Accordingly, at a given stress state, the void ratio of structured soils remains consistently higher than that of reference soils, even after experiencing significant plastic deformation.

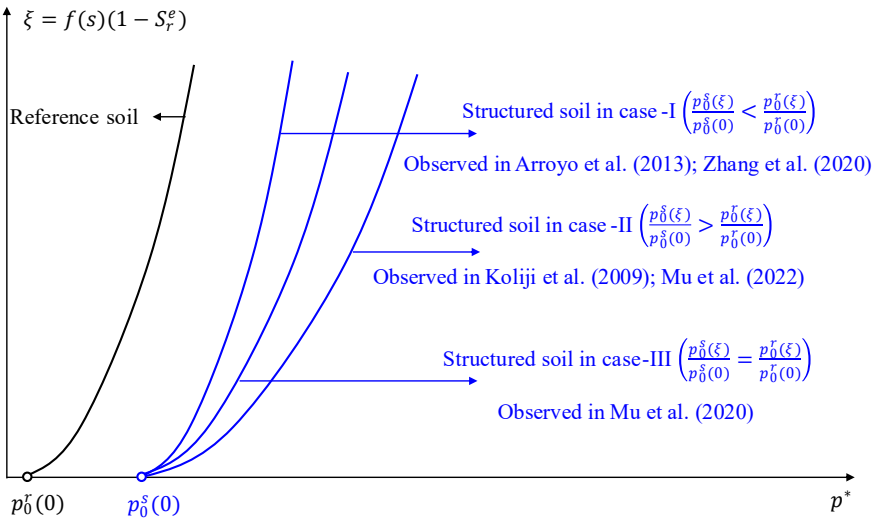

(a)

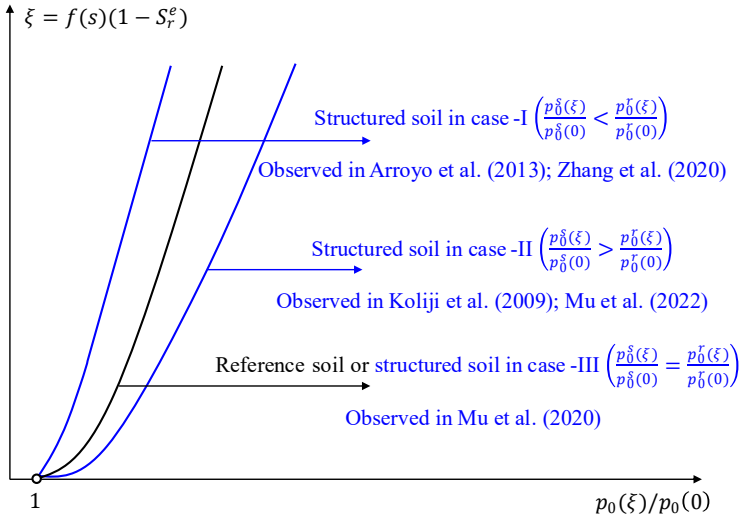

(b)

Figure 2-10. Influence of soil structure on yield stress: (a) LC curves; (b) normalised LC curves

Compaction conditions are known to have significant impacts on soil microstructure and compression behaviour (Delage et al., 1996; Sivakumar and Wheeler, 2000; Watabe et al., 2000; Mancuso et al., 2002; Estabragh et al., 2004; Tarantino and Tombolato, 2005; Koliji et al., 2010b; Alonso et al., 2013; Heitor et al., 2013; Yokohama et al., 2014; Heitor et al., 2015b; Zhang et al., 2018b; Ng and Peprah-Manu, 2023). For the influence of compaction dry density, Sivakumar and Wheeler (2000) observed that at a given compaction water content and suction, the densely compacted speswhite kaolin exhibited a higher yield stress than the loosely compacted one. The difference in void ratio between looser and denser specimens decreased

with increasing mean stress, align with the trend reported by Watabe et al. (2000) for silty sand. Xu and Coop (2017) found that the convergence of compression curves for loosely and densely compacted loess (a low-plasticity clay) is influenced by the compaction water content. For loess compacted at zero water content (i.e., dry compaction) and subsequently saturated, the void ratio difference between loosely compacted and densely compacted specimens became negligible as stress increased. However, the compression curves of saturated looser and denser specimens did not converge when compacted at a water content of 12%, even at vertical stresses above 10 MPa. the looser specimen maintained a higher void ratio at a given stress, with a Δe of about 0.10. Todisco et al. (2018) observed similar behaviour in Leighton Buzzard quartz sand, with a Δe of around 0.05, and they attributed this to the presence of strong microscale fabrics that were difficult to break down. Overall, it can be concluded that densely compacted specimens exhibit a higher yield stress than loosely compacted ones, whereas the convergence of compression curves at higher stresses appears to be dependent on other factors, such as soil type and specimen preparation method. Moreover, the LC curve has been shown to depend on compaction dry density. Estabragh et al. (2004) found that the yield stress of the loosely compacted low-plasticity clay was more sensitive to suction changes than that of the densely compacted specimen. Increasing suction from 0 to 100 kPa resulted in a 70% increase in yield stress for the looser specimen, whereas the increase was about 40% for the denser one, diminishing the difference in yield stress between the two compaction states at a higher suction.

For the influence of compaction water content, Sivakumar and Wheeler (2000) observed that speswhite kaolin compacted at a lower water content exhibited a higher void ratio at a given stress state. Conversely, Watabe et al. (2000) reported that silty sand compacted at a lower water content may have a lower void ratio under otherwise identical conditions. Oualmakran et al. (2016) investigated the compression behaviour of clayey silt prepared at the dry and wet of optimum water contents. It was found that both the yield stress and post-yielding compressibility $\lambda(s)$ increased as the compaction water content decreased. The compression curves for specimens compacted at different water contents tended to converge at higher stresses, consistent with observations by Tarantino and De Col (2008) for speswhite kaolin and

Ge et al. (2024) for loess (a low-plasticity clay). In contrast, Mancuso et al. (2002) revealed that silty sand compacted at a lower water content exhibited a smaller $\lambda(s)$, resulting in a higher void ratio as mean stress increased. These findings indicate that the effects of compaction water content on the compression curve are highly soil-type dependent, making it difficult to establish a general trend. Additionally, several studies reported that the yield stresses of specimens compacted at lower water contents were more sensitive to suction changes, indicating a more inclined LC curve (Sivakumar and Wheeler, 2000; Mancuso et al., 2002; Alonso et al., 2013).

During triaxial shearing, Wheeler and Sivakumar (2000) revealed that compaction conditions significantly influenced the stress-strain curves of speswhite kaolin but had a limited impact on the critical state. The specimens compacted under different dry densities and water contents reached an identical critical state line in the stress plane. Consistently, Santucci de Magistris and Tatsuoka (2004) (testing silty sand) and Tarantino and Tombolato (2005) (testing speswhite kaolin) found that the ultimate shear strength envelope was not affected by compaction conditions.

2.3.1.2 Small-strain shear stiffness

To date, several researchers have investigated the effects of soil structure on the small-strain shear stiffness (G_0) under saturated conditions (Viggiani and Atkinson, 1995; Pennington et al., 1997; Gasparre et al., 2007; Song et al., 2017; Zuo et al., 2024). Viggiani and Atkinson (1995) investigated the variation of G_0 with mean effective stress for intact and reconstituted London clay. Their results showed that G_0 of intact specimens was significantly larger than that of reconstituted specimens, but the difference diminished as mean effective stress increased. Similarly, Pennington et al. (1997) reported that the G_0 of intact Gault clay was considerably larger than that of reconstituted Gault clay at a given stress state. In contrast, Song et al. (2017) observed nearly identical G_0 values for saturated intact and compacted loess (a low-plasticity clay) under isotropic compression. Wang et al. (2022) studied the G_0 of saturated intact and compacted granite with mean effective stress ranging from 50 to 900 kPa.

They found that the intact specimen initially had approximately 15% smaller G_0 than the compacted specimen at a mean effective stress of 50 kPa. However, G_0 of the intact specimen became larger than that of the compacted specimen at stress above 300 kPa. Macari and Hoyos (1996) also reported a similar trend, where intact specimens had smaller G_0 at the initial state but exhibited larger G_0 than compacted specimens with increasing stress.

Additionally, compaction conditions have also been shown to significantly influence the G_0 of saturated soils. For the influence of compaction dry density, Wang et al. (2022) reported that the G_0 of saturated compacted granite (a gravelly sand) increased by approximately 20% as the dry density increased from 1.60 to 1.92 g/cm^3. The increase in G_0 with increasing compaction dry density was also found by Ge et al. (2024) for low-plasticity clay. Wang et al. (2021) studied the G_0 of saturated loess under mean effective stress ranging from 40 to 1200 kPa. At a stress of 40 kPa, the denser specimen had 20% larger G_0 than the looser specimen but the difference became negligible as stress exceeded 400 kPa although their void ratios were different (Δe = 0.05). The looser and denser specimens had identical G_0 but different void ratios was also observed for Leighton Buzzard sand (Todisco et al., 2018). For the influence of compaction water content, Mancuso et al. (2002) found that saturated silty sand compacted at the wet of optimum water content had approximately 50% and 20% smaller G_0 than the specimen compacted at the optimum water content, at mean effective stresses of 1 and 400 kPa, respectively. Conversely, Ge et al. (2024) investigated the G_0 of saturated low-plasticity clay and found that the specimen compacted at a lower water content exhibited a smaller G_0 even when the void ratio was the same.

The above results suggest that the G_0 is affected by soil structure, but inconsistent structure effects are identified. For example, intact specimens could have larger, similar, or smaller G_0 compared to their reconstituted or compacted counterparts. Under otherwise identical conditions, specimens compacted at lower water contents may show either smaller or larger G_0 those compacted at higher water contents. These findings remain valid when stiffness is normalised using a void ratio function (i.e., $G_0/f(e)$). However, possible explanations for the inconsistent structure effects on stiffness are still absent.

Furthermore, the variation of G_0 with suction is influenced by soil structure. Ng et al. (2017) observed that the increase in G_0 with suction was less pronounced in intact loess (a low-plasticity clay) than in compacted loess. Heitor et al. (2015b) investigated the evolution of G_0 with suction for silty sand compacted at different dry densities and water contents. At a given compaction water content, the increase in G_0 with increasing suction was more pronounced in specimens compacted at lower dry densities. Consequently, the difference in G_0 between looser and denser specimens decreased during the drying process. On the other hand, Heitor et al. (2015b) reported that at a given compaction dry density and suction, G_0 exhibited a non-monotonic variation with compaction water content. The specimen compacted at a water content of 12% displayed the largest G_0 and was more sensitive to suction variations compared to those compacted at 10% and 14%. Mancuso et al. (2002) observed that as suction increased from 0 to 400 kPa, the G_0 of silty sand increased by 50% to 85% for specimens compacted at the optimum water content, and by 40% to 165% for those compacted at the wet of optimum, depending on the applied mean net stress. Sawangsuriya et al. (2009b) measured the G_0 of clayey sand compacted at different water contents. For specimens compacted at higher water contents, G_0 was found to be smaller, while the rate of increase in G_0 with suction was more evident. For example, G_0 increased by about 30% with suction increasing from 20 to 200 kPa for the specimen compacted at the dry of optimum, whereas this value was approximately 100% for the specimen compacted at the wet of optimum under the same suction variation. These observations highlight the significant role of soil structure on the variation of small-strain shear stiffness with suction.

2.3.1.3 Cyclic behaviour

Intact soils are commonly found in pavements constructed in cuts or on-grade (i.e., without filling or cutting) (Christopher et al., 2006). For instance, according to the pavement design guideline in China (JTG/T3610, 2019), the construction of highway subgrades typically involves compacting a soil layer with a thickness of 0.8 meters. Beyond this depth, the subgrade soil remains in its natural, undisturbed state. Previous studies have demonstrated that understanding the structure effects on cyclic behaviour is important for pavement design

(Delage et al., 2005; Karam et al., 2009). For example, field monitoring data from Huang (2019) indicated that intact soils beneath 1.7 m of road surface were subjected to repeated traffic loads of approximately 20 kPa, and their deformation is critical to the long-term serviceability of pavements. In addition, intact soils near the pavement are also subjected to repeated traffic loads. Karam et al. (2009) indicated that the cyclic instability of intact loess under repeated traffic loads contributed to the formation of sinkholes near the Northern French TGV railway line, posing significant risks to its safety.

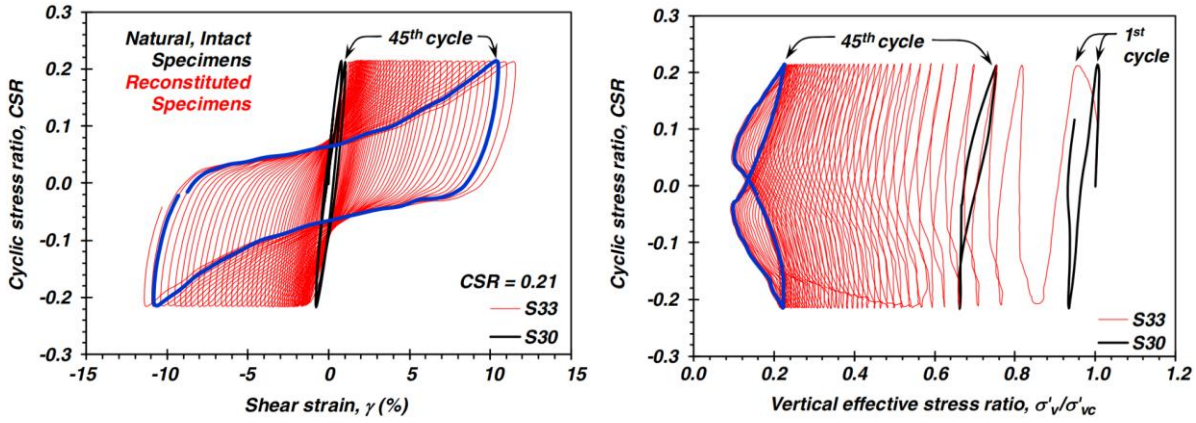

(a) (b)

Figure 2-11. Comparison of cyclic responses between intact and reconstituted alluvial plastic silt under saturated and overconsolidated (OCR = 1.8) conditions: (a) stress-strain curves; (b) effective stress paths (Jana and Stuedlein, 2021)

The influence of soil structure on cyclic behaviour under saturated conditions has also been extensively investigated, primarily in the context of soil liquefaction (Ghionna and Porcino, 2006; Wang et al., 2006; Wijewickreme and Sanín, 2008; Wijewickreme et al., 2019; Lu et al., 2020; Jana and Stuedlein, 2021; Stuedlein et al., 2023). Jana and Stuedlein (2021) conducted cyclic tests on saturated intact and reconstituted alluvial plastic silt. It was found that, under the overconsolidated state, the intact specimen exhibited a smaller permanent strain and greater resistance to cyclic loading than the reconstituted specimen (see Figure 2-11). In contrast, Wijewickreme and Sanín (2008) reported different results for normally consolidated saturated silt. Their results showed that the intact specimen had a slightly larger excess pore water pressure (PWP) than the reconstituted specimen at the first and second cycles. Afterwards, the excess PWP of the intact specimen became smaller than that of the reconstituted specimen.

These phenomena indicate that the structure effects on cyclic behaviour depend on the stress state. In the overconsolidated state, the saturated intact specimen exhibits smaller excess PWP and permanent strain than the reconstituted specimen, whereas the opposite trend may occur when the intact specimen is normally consolidated.

While previous studies mainly focused on saturated soils, subgrade soils in the pavements are typically in unsaturated states (Alonso and Gens, 1994; Ng et al., 2024), so it is essential to investigate the influence of soil structure on cyclic behaviour under unsaturated conditions. So far, some cyclic tests have been conducted on unsaturated soils using either intact or compacted specimens (e.g., Cui et al., 2007; Karam et al., 2009; Ng et al., 2013; Sivakumar et al., 2013; Han and Vanapalli, 2016; Blackmore et al., 2020; Azizi et al., 2023). For example, Cui et al. (2007) investigated the cyclic behaviour of unsaturated intact loess under various water contents. It was observed that, at a given number of cycles, both permanent strain and volumetric strain were larger at a higher water content. Karam et al. (2009) consistently revealed that unsaturated intact loess exhibited greater resistance to cyclic loading at a lower water content. Ng et al. (2013) investigated the cyclic behaviour of unsaturated compacted silt under various suctions. Their results showed that resilient modulus increased by up to one order of magnitude when the suction increased from 0 to 250 kPa. However, the aforementioned studies have not compared the behaviour of unsaturated intact and compacted specimens, leaving the structure effects on cyclic behaviour under unsaturated conditions not understood.

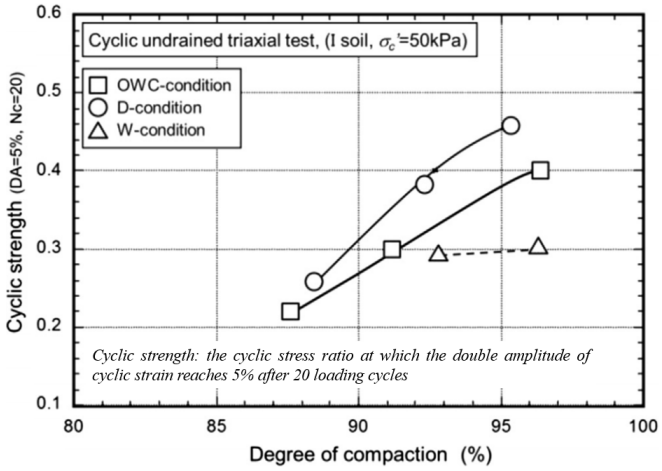

Figure 2-12. Influence of compaction conditions on cyclic behaviour of saturated sandy silt (Yokohama et al., 2014)

Moreover, previous studies have demonstrated that the cyclic behaviour of saturated compacted soils highly depends on the compaction states. For instance, Yokohama et al. (2014) conducted cyclic undrained triaxial tests on saturated sandy silt prepared under different compaction conditions. Their findings indicated that at a given dry density, specimens compacted at the dry of optimum exhibited greater resistance to cyclic loading compared to those compacted at the wet of optimum. Additionally, denser specimens demonstrated greater stability than looser ones when compacted at the same water content, as shown in Figure 2-12. Under unsaturated conditions, Sivakumar et al. (2013) compacted kaolin under various compaction conditions and performed constant water content cyclic tests on those specimens at their as-compacted states. The results manifested that an increase in compaction dry density significantly reduced the development of permanent vertical strain, and a higher compaction water content resulted in more evident strain accumulation with the number of cycles. Similar findings were observed by other researchers, such as Duong et al. (2013) for different types of clayey gravel and Zhang et al. (2024) for high-plasticity clay. In contrast, Xu et al. (2024) observed that, at the same dry density, red mudstone (a well-graded gravel) compacted at the optimum water content exhibited lower permanent strains than those compacted at either dry or wet of optimum water content. However, these studies applied cyclic loads to specimens in their as-compacted states, so these specimens have differences not only in soil structure but also in soil suction. It is challenging to distinguish the impact of compaction conditions on cyclic behaviour from the suction effects. Consequently, more experimental studies are required to investigate the influence of soil structure (both inherent and compaction condition-induced) on cyclic behaviour under a suction-controlled manner.

2.3.2 Anisotropic soil behaviour

Soil typically exhibits anisotropic behaviour due to its directional depositional history (inherent anisotropy) or the application of anisotropic stress (stress-induced anisotropy), implying that the hydro-mechanical behaviour of soil is direction-dependent. Studies have shown that anisotropy can significantly influence the serviceability analysis of geo-structures. For example, Simpson et al. (1996) demonstrated that the calculated tunnel settlement aligned

with measured data when stiffness anisotropy was considered, while assuming isotropic stiffness led to an underestimation of the maximum settlement by approximately 70%. The following discussion presents the yield surface, small-strain shear stiffness, and water retention behaviour of cross-anisotropic (i.e., transversely isotropic) soils, a common anisotropic state in geotechnical practice.

2.3.2.1 Yield surface of anisotropic soils

For anisotropic soils, it is well established that the yield surface is not symmetric about the mean stress axis (Dafalias, 1986a; Cui and Delage, 1996; Wheeler et al., 2003a; Jiang and Ling, 2010; Al-Sharrad, 2013). By accounting for the influence of soil anisotropy on plastic dissipation work, Dafalias (1986a) proposed an inclined yield surface for saturated and anisotropic soils, as presented in Figure 2-13. The corresponding formulation is given as follows:

$$f = (q - \alpha p')^2 - (M^2 - \alpha^2)p'(p_0 - p') = 0 \tag{2-18}$$

where p_0 represents the size of the yield surface under saturated and anisotropic conditions and denotes the isotropic yield stress under saturated and isotropic conditions; and α is the inclination of the yield surface, which evolves with plastic deformation. When α is equal to zero, the soil is isotropic, and the yield surface is identical to that of the Modified Cam-Clay model.

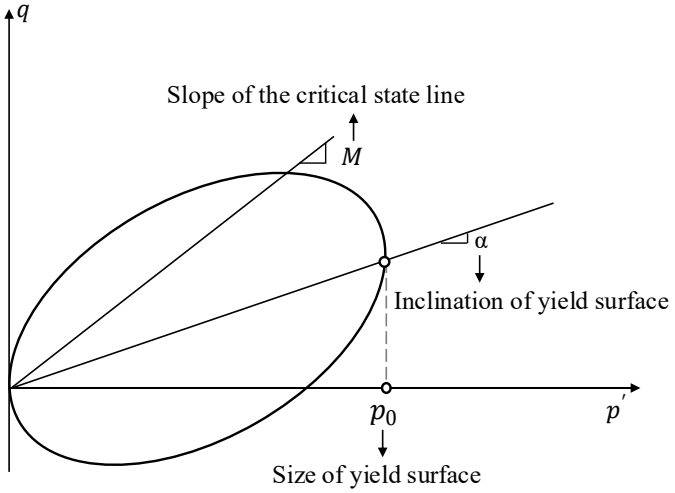

Figure 2-13. Yield surface for a saturated and anisotropic soil (Dafalias, 1986a)

At the critical state, some researchers have assumed a non-zero α (e.g., Wheeler et al., 2003a; Dafalias and Taiebat, 2013; Gao and Zhao, 2015), consistent with observations of persistent anisotropic fabric and stiffness at the critical state (Ng et al., 2009; Li and Dafalias, 2012; Wang et al., 2020; Zuo et al., 2024). In contrast, others have adopted an isotropic fabric (i.e., α is zero) based on the thermodynamic framework, suggesting that free energy cannot accumulate indefinitely upon critical state failure (e.g., Chen and Yang, 2020; Sitarenios and Kavvadas, 2020; Yu and Yang, 2023). To date, whether soil fabric at the critical state is isotropic or anisotropic remains unresolved and still a debatable issue.

Moreover, by measuring yield stress under various stress paths and suctions, it has been observed that the inclination of the yield surface is nearly independent of suction (see Figure 2-14) (Cui and Delage, 1996; Al-Sharrad, 2013; Al-Sharrad et al., 2017). This indicates that the parameter α can be considered constant across different moisture conditions. By analysing data from 17 intact clays, Jiang and Ling (2010) demonstrated that the inclined yield surface can well capture the yield behaviour of intact soils. These findings suggest that yield surface developed for saturated and reconstituted soils can be extended to describe the yield behaviour of unsaturated and structured soils.

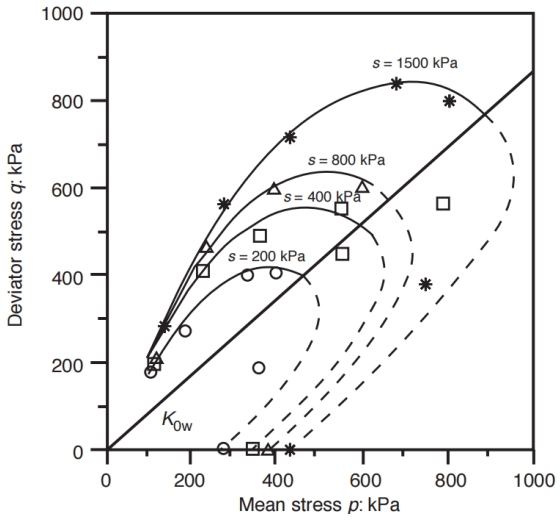

Figure 2-14. Suction effects on the inclination of the yield surface (Cui and Delage, 1996)

2.3.2.2 Anisotropic small-strain shear stiffness

To evaluate stiffness anisotropy, shear wave velocities are measured along different shear

planes (Pennington et al., 1997; Gasparre et al., 2007; Ng and Yung, 2008; Clayton, 2011; Zuo et al., 2024), including G_{hh}, G_{hv}, and G_{vh}. In this notation, the first subscript denotes the direction of shear wave propagation, while the second indicates the direction of wave polarisation. For cross-anisotropic soils, G_{hv} and G_{vh} are equal as they both represent shear stiffness in the vertical plane. Consequently, stiffness anisotropy can be determined by comparing either G_{hh} with G_{hv} or G_{hh} with G_{vh}.

Stiffness anisotropy has been widely observed in intact soils, with a larger stiffness in the horizontal plane (G_{hh}) than in the vertical plane (G_{hv}) (e.g., Jovičić and Coop, 1998; Li et al., 2012; Zuo et al., 2024), or in a reverse trend with G_{hv} larger than G_{hh} (e.g., Landon and DeGroot, 2006; Liu et al., 2023). This anisotropy is strongly influenced by the soil's inherent structure. Pennington et al. (1997) observed that intact Gault clay exhibited more pronounced stiffness anisotropy than compacted specimens. Similarly, Zuo et al. (2024) reported that during isotropic compression, the stiffness anisotropy G_{hh}/G_{hv} in the intact loess (a low-plasticity clay) was approximately 1.27, whereas in the compacted loess, it was 1.01. Furthermore, Jovičić and Coop (1998) found that the reconstituted London clay, when subjected to the same stress history as the intact clay, showed comparable stiffness anisotropy to the intact specimen. This finding suggested that plastic strain history plays a significant role in developing inherent anisotropy.

Stress-induced stiffness anisotropy has also been reported in many studies (e.g., Ng and Yung, 2008; Ng et al., 2009; Choo et al., 2011). For example, Ng and Yung (2008) observed that one-dimensional compaction during specimen preparation induced anisotropic stiffness in clayey silt, with G_{hh} larger than G_{hv}. By conducting constant stress ratio loading on reconstituted Lucera clay, Mitaritonna et al. (2014) concluded that a complete modification of stress-induced stiffness anisotropy (e.g., from anisotropic to isotropic) can be achieved when the applied stress was four times higher than the yield stress, as illustrated in Figure 2-15. However, previous studies have primarily focused on soils compacted under a given state, and the influence of compaction conditions on stiffness anisotropy remains unclear. Hasan and Wheeler (2014) examined the effect of compaction procedures on stiffness anisotropy and

reported that the stiffness G_{hh} could be either larger (in dynamic compaction) or smaller (in static compaction) than the stiffness G_{hv}. Nevertheless, their results were limited to the as-compacted state, and the influence of suction cannot be eliminated during the interpretation of the results. More experimental studies are needed to investigate the effects of compaction conditions on stiffness anisotropy.

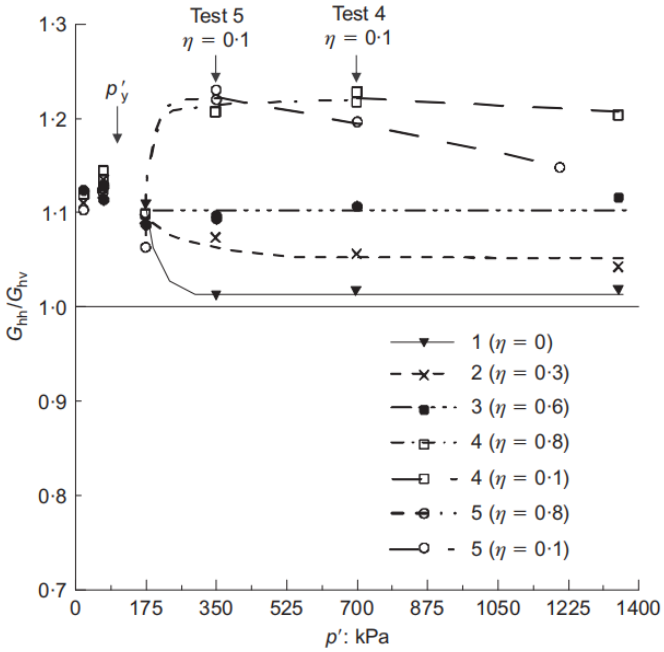

Figure 2-15. Influence of stress ratio on stiffness anisotropy (Mitaritonna et al., 2014)

Furthermore, previous studies have revealed that the stiffness anisotropy G_{hh}/G_{hv} may be influenced by suction (Ng and Yung, 2008; Ng et al., 2009; Ng and Xu, 2012; Kaewsong, 2017). Ng and Yung (2008) found that G_{hh}/G_{hv} of clayey silt increased slightly as suction increased. For example, G_{hh}/G_{hv} increased from 1.03 to 1.08 as suction increased from 0 to 200 kPa at a mean net stress of 200 kPa, indicating a more evident stiffness anisotropy. Similarly, Ng et al. (2009) reported that G_{hh}/G_{hv} of clayey silt increased during drying and decreased during wetting, with the soil exhibiting greater anisotropy after one drying-wetting cycle (see Figure 2-16). Kaewsong (2017) observed that after a drying-wetting cycle, compacted loess became less anisotropic, whereas intact loess exhibited more pronounced anisotropy. In contrast, Ng and Xu (2012) found that G_{hh}/G_{hv} in silt remained nearly constant across different suctions and drying-wetting cycles. These divergent findings indicate inconsistent trends in the influence of suction on stiffness anisotropy, which contrasts with the

influence of suction on the inclination of yield surface, known to remain nearly constant across different suctions (Cui and Delage, 1996; Al-Sharrad et al., 2017).

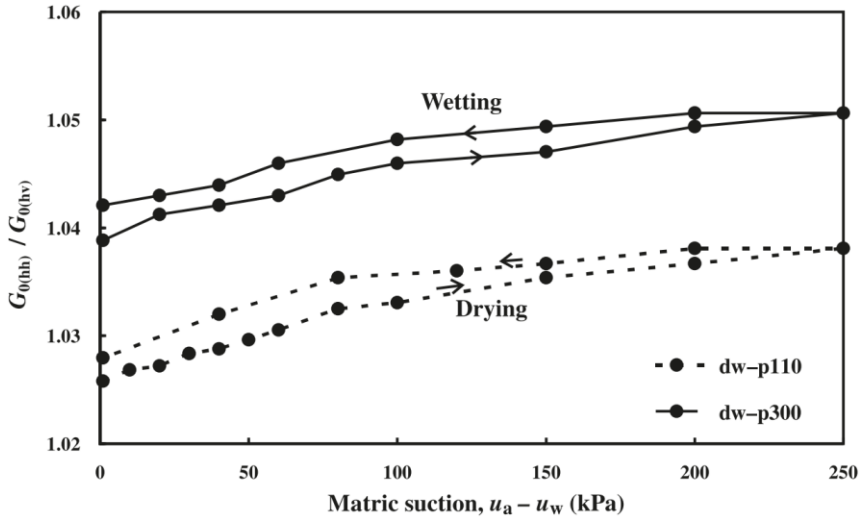

Figure 2-16. Variations of stiffness anisotropy during drying-wetting cycles (Ng et al., 2009)

2.3.2.3 Influence of soil anisotropy on water retention ability

Previous studies have demonstrated that water retention behaviour differs between isotropic and anisotropic soils (Tse, 2007; Sivakumar et al., 2010; Al-Sharrad, 2013). Sivakumar et al. (2010) investigated the water retention behaviour of isotropically and anisotropically compressed speswhite kaolin during wetting. Their results showed that, at the same initial void ratio, anisotropic specimens exhibited a higher degree of saturation than isotropic specimens at a given suction. Tse (2007) examined the soil water retention curves (SWRCs) of completely decomposed granite (CDG, a poorly graded sand) under the same mean net stress but different stress ratios. Results showed that the specimen subjected to a higher stress ratio had a higher air entry suction. Beyond this air entry value, anisotropically loaded specimens exhibited higher degrees of saturation than isotropically loaded specimens under the same suction, with a percentage difference of up to 30%. Similar observations were also reported by Habasimbi and Nishimura (2018).

To explain the influence of anisotropy on water retention capacity, Zhou and Chen (2021) demonstrated that anisotropic soils tend to develop more elongated pores compared to isotropic soils. For a given degree of saturation and void ratio, elongated pores induce higher suction

than rounded pores, as described by the Young-Laplace equation (Ng et al., 2024). Consequently, anisotropic soils exhibit stronger water retention capacity than isotropic soils at the same void ratio. Based on this observation, Zhou and Chen (2021) proposed a model correlating pore elongation with water retention behaviour, indicating that a more anisotropic fabric corresponds to a higher degree of saturation.

2.4 Models considering the effects of unsaturation, structure, and anisotropy

2.4.1 Models on unsaturation effects

As discussed in section 2.2, the behaviour of unsaturated soils is significantly affected by pore water distribution. Consequently, the elastoplastic models for unsaturated soils can be categorised into two types: uncoupled and coupled with hydraulic hysteresis.

2.4.1.1 Models uncoupled with hydraulic hysteresis

The first complete elastoplastic model for unsaturated soils is the Barcelona Basic Model proposed by Alonso et al. (1990). It is formulated in the triaxial stress state with mean net stress p_n, deviatoric stress q, and suction s.

In the BBM, elastic volumetric strains consist of components induced by changes in both stress and suction. Upon unloading or reloading at a constant suction, the elastic volumetric strain is given by

$$d\varepsilon_{vp}^{e} = \frac{\kappa}{1+e}\frac{dp_n}{p_n} \tag{2-19}$$

where κ is the slope of the unloading or reloading line in the $e - \ln p_n$ plane. Similarly, the elastic volumetric strain upon drying or wetting at a constant stress is determined as follows:

$$d\varepsilon_{vs}^{e} = \frac{\kappa_s}{1+e}\frac{ds}{s+p_{at}} \tag{2-20}$$

where κ_s is a parameter associated with suction change; and p_{at} is the atmospheric pressure, taken as 100 kPa. When both stress and suction vary, the elastic strain $d\varepsilon_v^e$ is obtained by the summation of Equations (2-19) and (2-20):

$$d\varepsilon_v^e = \frac{\kappa}{1+e}\frac{dp_n}{p_n} + \frac{\kappa_s}{1+e}\frac{ds}{s+p_{at}} \tag{2-21}$$

The elastic deviatoric strain is calculated as follows:

$$d\varepsilon_q^e = \frac{dq}{3G} \tag{2-22}$$

where G is the elastic shear modulus.

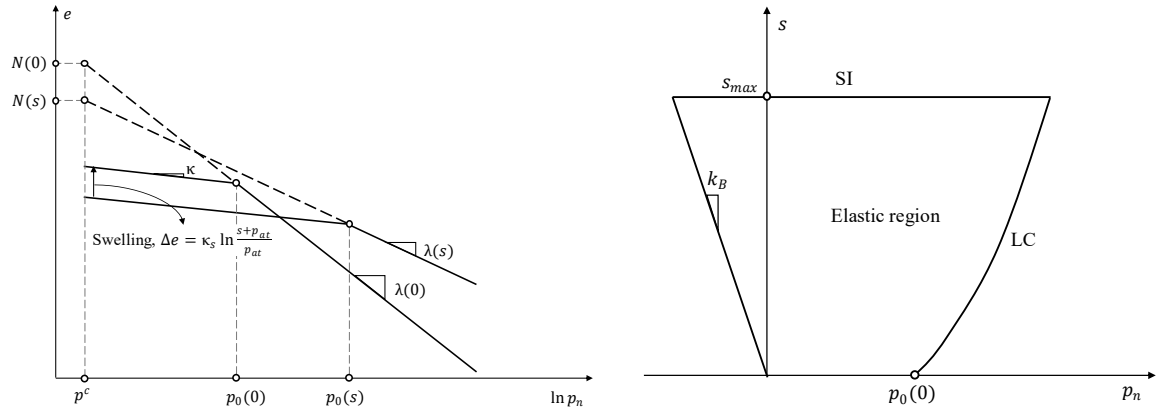

(a) (b)

Figure 2-17. Isotropic compression behaviour in the BBM: (a) compression curves for saturated and unsaturated soils; (b) SI and LC curves (adapted from Alonso et al., 1990)

Consistent with elastic components, plastic volumetric strains in the BBM are also associated with increases in both stress and suction. As illustrated in Figure 2-17(a), the isotropic normal compression line (NCL) under a constant suction is expressed as:

$$e = N(s) - \lambda(s)\ln\frac{p_n}{p^c} \tag{2-23}$$

where $N(s)$ and $\lambda(s)$ are the intercept and slope of the NCL at a given suction, respectively; and p^c is the reference stress at which $e = N(s)$. To calculate $N(s)$, it is assumed that when the mean net stress equals the reference stress p^c, the saturated state can be achieved from an unsaturated state via a wetting path involving only elastic swelling. Accordingly, the following equation can be derived from Equation (2-20):

$$N(s) = N(0) - \kappa_s \ln\frac{s+p_{at}}{p_{at}} \tag{2-24}$$

Furthermore, $\lambda(s)$ is assumed to decrease with increasing suction, indicating reduced

compressibility. The value of $\lambda(s)$ is calculated as follows:

$$\lambda(s) = \lambda(0)[(1 - r_B)\exp(-\beta_B s) + r_B] \quad (2\text{-}25)$$

where r_B is a parameter related to the minimum compressibility; and β_B is a parameter controlling the reduction rate of $\lambda(s)$ with increasing suction.

Based on the compression behaviour described from Equations (2-19) to (2-25), the increase of mean net yield stress with increasing suction can be derived as follows:

$$\frac{p_0(s)}{p^c} = \left[\frac{p_0(0)}{p^c}\right]^{\frac{\lambda(0)-\kappa}{\lambda(s)-\kappa}} \quad (2\text{-}26)$$

where $p_0(s)$ is the mean net yield stress at a given suction. The curve described by Equation (2-26) is defined as the LC curve, as it explains the wetting-induced collapse phenomenon. As shown in Figure 2-17, wetting leads to swelling when the stress state is above the LC curve, whereas wetting-induced collapse occurs when the stress state reaches the LC curve. The plastic volumetric strain due to yielding on the LC curve is calculated as follows:

$$d\varepsilon_{vp}^{p} = \frac{\lambda(0)-\kappa}{1+e}\frac{dp_0(0)}{p_0(0)} \quad (2\text{-}27)$$

where $p_0(0)$ is the value of $p_0(s)$ under saturated conditions. It should be noted that the LC curve defined in Equation (2-26) does not account for the reduction in mean net yield stress with increasing suction when suction is below the air entry value, as illustrated in Figure 2-3. Further modifications to the LC curve have been proposed in subsequent studies (e.g., Sheng et al., 2008; Alonso et al., 2013).

To describe the drying-induced plastic strain, a suction increase (SI) curve is defined as shown in Figure 2-17(b):

$$s = s_{max} \quad (2\text{-}28)$$

where s_{max} is the maximum suction experienced by the soil. Plastic strain is induced when suction increases and reaches the SI curve, with the corresponding plastic volumetric strain expressed as follows:

$$d\varepsilon_{vs}^{p} = \frac{\lambda_s - \kappa_s}{1+e}\frac{ds_0}{s_0 + p_{at}} \tag{2-29}$$

where λ_s is a parameter describing the drying-induced elastoplastic strain. Given the assumption that the positions of the LC and SI curves are governed by the total plastic volumetric strain (i.e., $d\varepsilon_v^p = d\varepsilon_{vp}^p + d\varepsilon_{vs}^p$), the hardening laws are given by

$$\frac{dp_0(0)}{p_0(0)} = \frac{1+e}{\lambda(0) - \kappa} d\varepsilon_v^p \tag{2-30}$$

$$\frac{ds_0}{s_0 + p_{at}} = \frac{1+e}{\lambda_s - \kappa_s} d\varepsilon_v^p \tag{2-31}$$

Furthermore, a linear increase in apparent cohesion with increasing suction is adopted as follows (see Figure 2-17):

$$p_s = k_B s \tag{2-32}$$

where p_s is the apparent cohesion; and k_B is a parameter. Note that the region below the line described in Equation (2-32) is inadmissible, as it is assumed that the soil skeleton cannot sustain a tensile stress higher than its apparent cohesion.

In the triaxial stress space, the yield surface is formulated as (see Figure 2-18):

$$q^2 - M^2(p_n + p_s)(p_0(s) - p_n) = 0 \tag{2-33}$$

where M is the slope of the critical state line (CSL) in the $q - p_n$ plane.

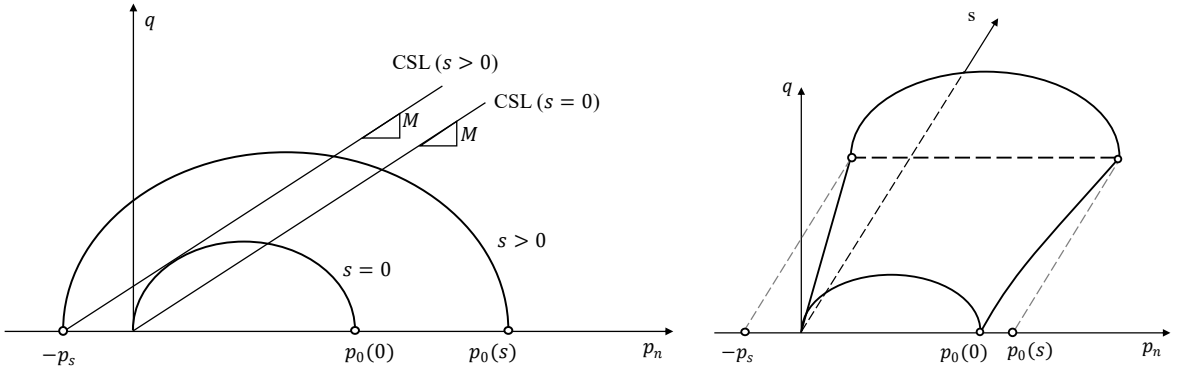

(a) (b)

Figure 2-18. Yield surface for triaxial stress state: (a) $q - p_n$ plane; (b) $q - p_n - s$ space (adapted from Alonso et al., 1990)

The BBM employs a non-associated flow rule:

$$\frac{d\varepsilon_q^p}{d\varepsilon_{vp}^p} = \frac{2q\alpha_B}{M^2(2p_n+p_s-p_0(s))} \tag{2-34}$$

where $d\varepsilon_q^p$ is the plastic deviatoric strain; and α_B is a parameter chosen to ensure zero lateral strain under K_0 consolidation. Therefore, α_B is determined using the following equation:

$$\alpha_B = \frac{M(M-9)(M-3)}{9(6-M)}\frac{1}{1-\kappa/\lambda(0)} \tag{2-35}$$

Using a framework similar to the BBM, many models have been proposed for unsaturated soils with mean net stress and suction (e.g., Gens and Alonso, 1992; Josa et al., 1992; Wheeler and Sivakumar, 1995; Cui and Delage, 1996; Chiu and Ng, 2003). For instance, Gens and Alonso (1992) proposed a model for unsaturated expansive clays, incorporating interactions between microstructure and macrostructure. Josa et al. (1992) introduced a nonlinear NCL to account for the maximum collapse of unsaturated soils. Wheeler and Sivakumar (1995) modified some equations in the BBM based on the experimental findings from unsaturated speswhite kaolin. Cui and Delage (1996) adopted an inclined yield surface to capture the behaviour of anisotropically consolidated soils. Chiu and Ng (2003) developed a state-dependent model incorporating the influence of void ratio, stress state, and suction on soil dilatancy.

However, the aforementioned models do not incorporate the influence of hydraulic hysteresis on mechanical behaviour. Some important aspects, such as irreversible volume changes caused by drying-wetting cycles at a constant mean net stress (in addition to irreversible deformation during the first cycle), cannot be captured (Wheeler et al., 2003b). To address these limitations, models incorporating the SWRC and hydraulic hysteresis have been developed (e.g., Gallipoli et al., 2003a; Wheeler et al., 2003b; Russell and Khalili, 2006; Sheng et al., 2008; Zhou et al., 2012; Pedrotti and Tarantino, 2019).

2.4.1.2 Models coupled with hydraulic hysteresis

One of the first models for unsaturated soils considering hydraulic hysteresis was

proposed by Wheeler et al. (2003b) using the mean Bishop's stress p^* ($p - u_a + \chi s$ with $\chi = S_r$) and a modified suction s^* ($s^* = ns$). This set of constitutive variables partially presents the coupling between hydraulic and mechanical behaviour. On the one hand, variations in S_r due to the drying-wetting cycles lead to changes in mean Bishop's stress, thereby influencing the mechanical response of unsaturated soils. On the other hand, compression-induced changes in porosity n (or void ratio e) alter the modified suction, resulting in different water retention characteristics.

The yield curves in the model of Wheeler et al. (2003b) are illustrated in Figure 2-19. Three curves, LC, SI, and suction decrease (SD), are defined to describe yield behaviour during compression, drying, and wetting, respectively. The evolutions of these curves are fully coupled, such that the movement of one curve results in coordinated movements of the others. For example, plastic volumetric strain generated during isotropic compression under a constant suction will lead to an outward shift of the LC curve and simultaneous upward shifts of the SI and SD curves, attributable to a reduction in porosity (i.e., a decrease in ns). Similarly, drying or wetting processes induce changes in the LC curve due to variations in suction and degree of saturation (reflected in changes in $p - u_a + sS_r$).

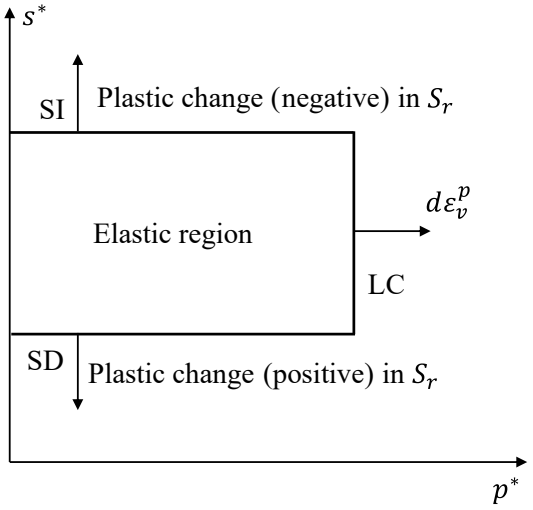

Figure 2-19. Yield curves in the $s^* - p^*$ plane for the model of Wheeler et al. (2003b)

Gallipoli et al. (2003a) proposed an alternative approach to incorporate the effects of hydraulic hysteresis on mechanical behaviour. Suction effects are considered through the following two constitutive variables:

$$p^* = p - u_a + sS_r \tag{2-36}$$

$$\bar{\xi} = f(s)(1 - S_r) \tag{2-37}$$

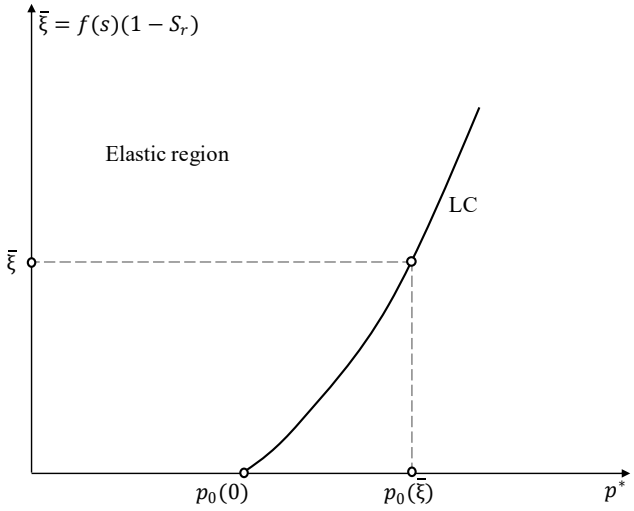

Figure 2-20. LC curve in the $\bar{\xi} - p^*$ plane for the model of Gallipoli et al. (2003a)

The mean Bishop's stress p^* accounts for suction effects by modifying the soil skeleton stress, while the bonding variable $\bar{\xi}$ considers the suction-induced additional bonding force at interparticle contacts. An important aspect of the model proposed by Gallipoli et al. (2003a) is that it employs a single LC yield curve in the $\bar{\xi} - p^*$ plane, as shown in Figure 2-20. This simplification does not limit the model's ability to account for hydraulic hysteresis, as both suction and degree of saturation influence the mean Bishop's stress p^* and bonding variable $\bar{\xi}$. For example, during drying-wetting cycles, changes in these variables can bring the stress state to the LC curve, thereby resulting in irreversible deformation.

Sheng et al. (2008) proposed a constitutive model for unsaturated soils that incorporates hydraulic hysteresis using mean net stress and suction. The corresponding yield curves in the $s - p_n$ plane are illustrated in Figure 2-21, where the LC, SI, and SD curves account for loading, drying, and wetting, respectively. Note that while the hysteresis in the SWRC is incorporated in Sheng et al. (2008), the mechanical response is solely governed by the current suction, without distinguishing between drying and wetting paths.

Sheng et al. (2008) demonstrated that the LC curve in the $s - p_n$ plane follows a 45° line for suction below the air entry value (see section 2.2.3). This behaviour arises because the soil

remains nearly saturated (S_r is close to 1) in this suction range, resulting in a constant mean effective yield stress $(p - u_w)$. Consequently, the mean net yield stress $(p - u_w - s)$ decreases linearly with increasing suction. In contrast, the mean Bishop's stress $(p - u_a + sS_r)$ converges to the mean effective stress $(p - u_w)$ when the soil is saturated. Therefore, the LC curve in the $s - p^*$ plane is a vertical line for suction below the air entry value. Notably, this vertical line collapses into a single point in the model of Gallipoli et al. (2003a), as the bonding variable $\bar{\xi}$ becomes zero under saturated conditions.

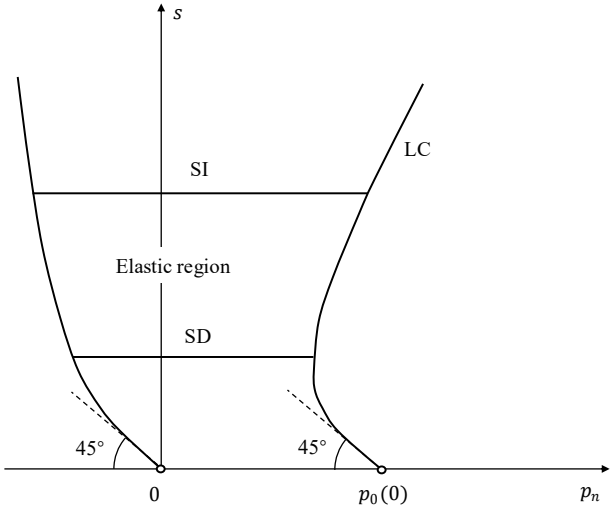

Figure 2-21. Yield curves in the $s - p_n$ plane for the model of Sheng et al. (2008)

In additional to the aforementioned studies, many other models have been proposed to incorporate hydraulic hysteresis into the constitutive behaviour of unsaturated soils (e.g., Khalili and Zargarbashi, 2010; Zhou et al., 2012; Alonso et al., 2013; Zhou et al., 2015; Gallipoli and Bruno, 2017; Pedrotti and Tarantino, 2019). For example, Zhou et al. (2012) employed the mean Bishop's stress ($p^* = p - u_a + sS_r^e$) and the effective degree of saturation (S_r^e) as constitutive variables to capture the nonlinear variation of soil compressibility under a constant suction. To describe the behaviour of unsaturated soils compacted at different water contents, Alonso et al. (2013) developed a model with the mean Bishop's stress ($p^* = p - u_a + sS_r^e$) and a modified suction (sS_r^e), where the effective degree of saturation is related to the ratio of microstructural void ratio to total void ratio. Gallipoli and Bruno (2017) demonstrated that the NCL for unsaturated soils can be unified into a single line when the stress variable is expressed as $S_r^{\lambda_G/\lambda(0)}(p - u_a + sS_r)$, where λ_G is a model parameter and $\lambda(0)$ is

the slope of the unified compression line (equals to the slope of the NCL under saturated conditions).

2.4.1.3 Models for soil water retention behaviour

The SWRC is essential for developing a complete model of unsaturated soils that accounts for hydraulic hysteresis. It describes the relationship between moisture conditions (e.g., degree of saturation or water content) and suction. Many models have been formulated to capture the water retention behaviour, which can generally be classified into two types: (i) those that assume a unique relationship between moisture conditions and suction, and (ii) those that incorporate the influence of additional factors, such as void ratio or stress state.

Van Genuchten (1980) proposed a simple equation to describe soil water retention behaviour, which is widely used and formulated as follows:

$$S_r = \left[1 + \left(\frac{s}{m_1}\right)^{m_2}\right]^{-m_3} \tag{2-38}$$

where m_1, m_2, and m_3 are model parameters.

Assuming that adsorption and desorption are governed by the pore size distribution, Fredlund and Xing (1994) proposed the following equation:

$$S_r = \left[1 - \frac{\ln(1+s/s_{res})}{\ln(1+10^6/s_{res})}\right]\left\{\ln\left[\exp(1) + \left(\frac{s}{m_1}\right)^{m_2}\right]\right\}^{-m_3} \tag{2-39}$$

where s_{res} is the suction value corresponding to the residual degree of saturation.

Experimental results indicate that the degree of saturation is influenced not only by suction but also by stress state and void ratio (e.g., Sivakumar, 1993; Ng and Pang, 2000b), which cannot be captured by Equations (2-38) and (2-39). Many equations have been developed to express the degree of saturation as a function of both suction and void ratio (Romero and Vaunat, 2000; Gallipoli et al., 2003b; Nuth and Laloui, 2008a; Tarantino, 2009; Gallipoli, 2012; Hu et al., 2013; Gallipoli et al., 2015). For example, Gallipoli et al. (2003b) extended the model of Van Genuchten (1980) to account for the influence of void ratio:

$$S_r = \left[1 + \left(\frac{se^{m_1}}{m_2}\right)^{m_3}\right]^{-m_4} \tag{2-40}$$

where m_1, m_2, m_3, and m_4 are model parameters. Gallipoli (2012) demonstrated that the product $m_1 m_3 m_4$ should be 1, as a unique relationship between water content and suction (independent of void ratio) exists in the low saturation range.

In these void ratio-dependent water retention models, stress effects on the SWRC are implicitly assumed to be represented by changes in void ratio. However, Zhou and Ng (2014) suggested that stress influences both void ratio and pore structure, making this assumption overly simplistic. Consequently, they proposed a stress state-dependent water retention model as follows:

$$S_r = \left[1 + \left(\frac{se^{m_1}}{m_2(1+p_n/p_r)^{m_3}}\right)^{m_4}\right]^{-m_5} \tag{2-41}$$

where m_1, m_2, m_3, m_4, and m_5 are model parameters. Stress effects on the SWRC are considered through two components: the void ratio part e^{m_1} and the pore structure-correlated part $(1 + p_n/p_r)^{m_3}$.

The above two types of models can be readily extended to incorporate hydraulic hysteresis, as the main drying and wetting curves share a similar mathematical formulation and the major difference is their air entry values. Accordingly, Gallipoli (2012) proposed a hysteretic water retention model as follows:

$$\begin{cases} S_r = \left[1 + \left(\frac{se^{m_1}}{m_2^d}\right)^{m_3}\right]^{-m_4} \\ S_r = \left[1 + \left(\frac{se^{m_1}}{m_2^w}\right)^{m_3}\right]^{-m_4} \end{cases} \tag{2-42}$$

where m_2^d and m_2^w are model parameters employed to simulate the main drying and wetting curves, respectively.

As suction and void ratio change, the soil state may deviate from the main curve to the scanning curve. Gallipoli (2012) assumed that when the soil state is on the scanning curve, any infinitesimal changes in suction or void ratio will produce only reversible changes in the degree

of saturation. The variation of the degree of saturation with suction and void ratio in the scanning curve is calculated as follows:

$$\frac{\partial \ln S_r}{\partial \ln s} = -m_{1,sc} m_{2,sc} (1 - S_r^{1/m_{1,sc}}) \tag{2-43}$$

$$\frac{\partial \ln S_r}{\partial \ln e} = -(1 - S_r^{1/m_{1,sc}}) \tag{2-44}$$

where $m_{1,sc}$ and $m_{2,sc}$ are model parameters introduced to define the scanning water retention curves. To ensure that all scanning paths remain within the attainable region bounded by the main drying and wetting curves, the condition $0 \leq m_{1,sc} m_{2,sc} \leq m_3 m_4$ must be satisfied. Alternatively, the scanning curve can be simulated using bounding surface theory, wherein the adsorption (or desorption) rate increases as the soil state approaches the main wetting (or drying) path (e.g., Gallipoli et al., 2015; Zhou et al., 2015).

While the aforementioned models can effectively capture soil water retention behaviour, they are largely empirical and phenomenological. Consequently, some researchers have sought to derive water retention models from the pore size distribution curve obtained through MIP testing (e.g., Russell and Buzzi, 2012; Hu et al., 2013; Russell, 2014; Cheng et al., 2019; Jimenez and Russell, 2023). For example, using fractal theory, Russell and Buzzi (2012) and Russell (2014) linked the main drying and wetting curves to particle and pore geometries, including size distributions, shapes, volumes, and surface areas, as follows:

$$\begin{cases} S_r = 1 \quad for\ s \leq s_e \\ S_r = \left(\frac{s}{s_e}\right)^{\alpha_R} \quad for\ s > s_e \end{cases} \tag{2-45}$$

where s_e is the suction separating the saturated and unsaturated states, which corresponds to the air entry suction s_{ae} during drying and the air expulsion suction s_{ex} during wetting; and α_R is a parameter controlling the adsorption/desorption rate. The three parameters, s_{ae}, s_{ex}, and α_R, are determined from the following equation:

$$\begin{cases} s_{ae} = C_1 e^{-D_s} \\ s_{ex} = C_1 C_2 e^{-D_s} \\ \alpha_R = 3 - D_p \end{cases} \quad (2\text{-}46)$$

where C_1 and C_2 are parameters related to pore and particle geometries; D_p and D_s are the fractal dimensions of pore and particle size distributions, respectively. A particle/pore size distribution is considered fractal when the number of particles/pores larger than a given size is proportional to that size in a power law, with the exponent representing the fractal dimension (Russell and Buzzi, 2012). Accordingly, water retention behaviour and the associated hysteresis can be related to pore and particle properties using Equation (2-46) within the framework of fractal theory. Using a similar approach, pore and particle information has also been correlated with other key soil characteristics, such as compression curves (Russell, 2011) and hydraulic conductivity functions (Yang et al., 2014b).

2.4.2 Models on structure effects

2.4.2.1 Models for saturated and structured soils

Many constitutive models for structured soils under saturated conditions have been developed within the critical state framework. To account for structure effects, these models primarily address: (i) the characterisation of soil structure; (ii) structure degradation due to plastic deformation; and (iii) the influence of soil structure on the shearing behaviour.

The characterisation of soil structure typically involves quantifying the differences between structured and reference soils. Various approaches have been proposed, such as the ratio of the yield stress of structured soils to that of reference soils at the same initial void ratio (Rouainia and Muir Wood, 2000; Baudet and Stallebrass, 2004; Zhou and Ng, 2018); the difference in void ratios between structured and reference soils at the same stress state (Liu and Carter, 1999,2000,2002; Ouria, 2017); the ratio between the slopes of the NCLs of structured and reference soils (Yang et al., 2014a); and the ratio of the unconfined shear strength of structured soils to that of reference soils (i.e., sensitivity) (Thakur and Degago, 2012). For

example, Zhou and Ng (2018) defined the soil structure parameter as follows:

$$R(0) = p_0^s(0)/p_0^r(0) \tag{2-47}$$

where $R(0)$ is a structure parameter at saturated conditions, with a value larger than or equal to 1; $p_0^s(0)$ and $p_0^r(0)$ are isotropic yield stresses of saturated structured and reference soils, respectively; and the zero in the bracket represents the fully saturated state.

Structure degradation under mechanical loading is commonly linked to the accumulation of plastic strain (Baudet and Stallebrass, 2004; Zhou and Ng, 2018). Several models assume that, following significant irreversible deformation, structured soils behave similarly to reference soils (Rouainia and Muir Wood, 2000; Liu and Carter, 2002; Yan and Li, 2011). Consequently, the structure degradation suggests that:

$$\frac{dR(0)}{R(0)-1} = -\beta_1\sqrt{(1-\beta_0)\left(d\varepsilon_v^p\right)^2 + \beta_0\left(d\varepsilon_q^p\right)^2} \tag{2-48}$$

where β_0 is a positive parameter smaller than 1, governing the relative contribution of plastic volumetric and deviatoric strains on structure degradation; and β_1 is a positive parameter controlling the rate of structure degradation. Some studies distinguish the effects of volumetric and deviatoric plastic strains on structure degradation (e.g., Kavvadas and Amorosi, 2000; Rouainia and Muir Wood, 2000; Koliji et al., 2010a), while others assume equal contributions by setting β_0 = 0.5 in Equation (2-48) (e.g., Baudet and Stallebrass, 2004; Zhou and Ng, 2018). Moreover, Equation (2-48) suggests that $R(0)$ decreases with increasing plastic strain and evolves towards 1, implying a transition in the behaviour of structured soils toward that of reference soils.

Baudet and Stallebrass (2004) claimed that some structure elements persist even at large strains based on the microstructural analysis of Fearon and Coop (2000), suggesting the presence of stable fabrics in structured soils. Consequently, Equation (2-48) is modified as:

$$\frac{dR(0)}{R(0)-R_{res}} = -\beta_1\sqrt{(1-\beta_0)\left(d\varepsilon_v^p\right)^2 + \beta_0\left(d\varepsilon_q^p\right)^2} \tag{2-49}$$

where R_{res} is a parameter representing the residual structure elements that remain stable after

substantial plastic strain.

In addition, the structure effects on shear behaviour have been studied. Liu and Carter (2002) demonstrated that soil structure affects dilatancy by comparing the shearing responses of intact and reconstituted clay. Intact soils exhibited larger plastic volumetric strain increments than reconstituted soils under the same plastic deviatoric strain increment. This behaviour was captured using a structure-dependent flow rule (Liu and Carter, 2002):

$$\frac{d\varepsilon_v^p}{d\varepsilon_q^p} = \frac{M^2-\eta^2}{2(1-\omega_s\Delta e_s)\eta} \tag{2-50}$$

where η is the stress ratio; ω_s is a parameter characterising the influence of soil structure on the flow rule, constrained by $0 < 1-\omega_s\Delta e_s < 1$; and Δe_s is the difference in void ratio between structured and reference soils at a given stress.

2.4.2.2 Models for unsaturated and structured soils

To date, several constitutive models for structured soils under unsaturated conditions have been proposed (Alonso and Gens, 1994; Yang et al., 2008a; Koliji et al., 2010a; Pereira et al., 2014; Bruno et al., 2020; Moghaddasi et al., 2021; Rotisciani et al., 2021). A crucial consideration in developing such models is accounting for the influence of soil structure on the LC curve, which is a key component in unsaturated soil behaviour.

Alonso and Gens (1994) extended the BBM to simulate the mechanical behaviour of unsaturated and structured soils. The isotropic yield stress of structured soils at a specific suction is calculated as the product of a suction-related structure parameter and the isotropic yield stress of saturated reference soils (i.e., the product of $R(s)$ and $p_0^r(0)$), supplemented by an extra term accounting for capillary forces. During loading, the value of $R(s)$ decreases towards 1 due to plastic strain-induced structure degradation, and the LC curve of structured soils tends to converge with that of reference soils.

Yang et al. (2008a) developed a model for unsaturated and structured soils under cyclic loading with mean net stress and suction. Following the BBM approach for reference soils, the LC curve was obtained using the isotropic yield stress of structured soils under saturated

conditions (i.e., $p_0^s(0)$):

$$\frac{p_0^s(s)}{p^c} = \left[\frac{p_0^s(0)}{p^c}\right]^{\frac{\lambda(0)-\kappa}{\lambda(s)-\kappa}} \tag{2-51}$$

where $p_0^s(s)$ is the isotropic yield stress of structured soils at a given suction. A similar approach for modelling the LC curve of structured soils was adopted by Pereira et al. (2014).

Koliji et al. (2010b) proposed a model for unsaturated and structured soils with mean Bishop's stress and suction. They found that the yield stress of structured soils is more sensitive to moisture changes than that of reference soils. At the same suction, the yield stress of structured soils was calculated by the production of the yield stress of reference soils and a suction-dependent structure parameter (i.e., the product of $R(s)$ and $p_0^r(s)$). Upon loading, $R(s)$ evolves towards 1, and structure soils exhibit behaviour similar to that of reference soils after substantial plastic strains, similar to the approach of Alonso and Gens (1994).

Recently, a model for unsaturated and structured soils was developed by Moghaddasi et al. (2021) using mean Bishop's stress and effective degree of saturation. They assumed that the difference in yield stress between structured and reference soils is independent of moisture conditions. Accordingly, the LC curve of structured soils was obtained by simply translating the LC curve of reference soils. This assumption was also adopted by Rotisciani et al. (2021) in their model development.

As illustrated in Figure 2-10, the slope of the normalised LC curve for structured soils could be smaller than (i.e., case-I), larger than (i.e., case-II), or equal to (i.e., case-III) that of reference soils. However, the existing models were generally proposed for a specific type of structured soil and incorporated only one case of the normalised LC curve. Therefore, a unified approach that can model these three cases (case-I/II/III) of the LC curve is necessary to capture the behaviour of various structured soils. Moreover, some studies have investigated the influence of soil structure on wate retention behaviour(e.g., Vanapalli et al., 1999; Ng et al., 2016; Yates and Russell, 2023). However, existing models do not explicitly account for the effects of soil structure on the SWRC, due to the scarcity of experimental data on the impacts

of structure degradation.

2.4.3 Models of anisotropy effects

2.4.3.1 Models for saturated and anisotropic soils

Modelling anisotropic soils requires the consideration of both the elastic and plastic anisotropies. Love (1927) demonstrated that a general formulation of elastic anisotropy involves 21 independent parameters, rendering it impractical for application in soil mechanics. Therefore, some simplifications have been adopted to capture the essential elastic behaviour (e.g., Graham and Houlsby, 1983; Hueckel and Tutumluer, 1994; Lashkari, 2010; Castro and Sivasithamparam, 2017). A widely adopted simplification assumes that soil is cross-anisotropic (or transversely isotropic), and therefore only seven parameters are required to describe the elastic anisotropy. For a cross-anisotropic material where the isotropic plane is horizontal, the seven parameters are: E_v and E_h (Young's moduli for loading in the vertical and horizontal directions, respectively), μ_{vh} (Poisson's ratio relating to the horizontal strain caused by an imposed vertical strain), μ_{hv} (Poisson's ratio relating to the vertical strain caused by an imposed horizontal strain), μ_{hh} (Poisson's ratio relating to the horizontal strain caused by an imposed horizontal strain in the normal direction), G_{hv} (or equivalently G_{vh}) and G_{hh} (shear moduli in the vertical and horizontal planes, respectively). Furthermore, it has been proved that (Clayton, 2011)

$$\frac{\mu_{hv}}{E_h} = \frac{\mu_{vh}}{E_v} \tag{2-52}$$

$$G_{hh} = \frac{E_h}{2(1+\mu_{hh})} \tag{2-53}$$

Therefore, only five of the above seven parameters are necessary. The elastic stress strain relationship can be described as follows:

$$\begin{bmatrix} d\varepsilon_{11} \\ d\varepsilon_{22} \\ d\varepsilon_{33} \\ d\varepsilon_{12} \\ d\varepsilon_{31} \\ d\varepsilon_{23} \end{bmatrix} = \begin{bmatrix} 1/E_v & -\mu_{vh}/E_v & -\mu_{vh}/E_v & 0 & 0 & 0 \\ -\mu_{vh}/E_v & 1/E_h & -\mu_{hh}/E_h & 0 & 0 & 0 \\ -\mu_{vh}/E_v & -\mu_{hh}/E_h & 1/E_h & 0 & 0 & 0 \\ 0 & 0 & 0 & 1/2G_{vh} & 0 & 0 \\ 0 & 0 & 0 & 0 & 1/2G_{vh} & 0 \\ 0 & 0 & 0 & 0 & 0 & (1+\mu_{hh})/E_h \end{bmatrix} \begin{bmatrix} d\sigma'_{11} \\ d\sigma'_{22} \\ d\sigma'_{33} \\ d\sigma'_{12} \\ d\sigma'_{31} \\ d\sigma'_{23} \end{bmatrix} \tag{2-54}$$

In drained conditions, the following sets of parameters can be selected: (i) E_v, E_h, μ_{vh}, μ_{hv}, G_{vh}; (ii) E_v, E_h, μ_{vh}, G_{hh}, G_{vh}; (iii) E_v, E_h, μ_{vh}, μ_{hh}, G_{vh}; or (iv) E_v, μ_{hv}, μ_{hh}, G_{hh}, G_{vh}. The selection of a parameter set is arbitrary. Clayton (2011) emphasised that the strain energy of an elastic material should also be positive, and therefore the following restrictions must be satisfied:

$$-1 \leq \mu_{hh} \leq 1 \tag{2-55}$$

$$\frac{E_v}{E_h}(1-\mu_{hh}) - 2\mu_{vh}^2 \geq 0 \tag{2-56}$$

For undrained conditions, the volumetric strain should be zero and thus the following equations should be satisfied:

$$\mu_{vh}^u = 0.5 \tag{2-57}$$

$$\mu_{hh}^u = 1 - \frac{E_h^u}{2E_v^u} \tag{2-58}$$

Consequently, fewer parameters are required for describing transversely isotropic soils under undrained conditions (e.g., E_v^u, E_h^u and G_{vh}).

For plastic anisotropy, its effects are typically represented by an inclined yield surface. A widely adopted yield surface for anisotropic soils proposed by Dafalias (1986a) is expressed as follows:

$$f = (q - \alpha p')^2 - (M^2 - \alpha^2)p'(p_0 - p') = 0 \tag{2-59}$$

An essential feature of Equation (2-59) is that the yield surface is tangentially horizontal at its intersection with the CSL, regardless of the value of α. Therefore, an associated flow rule can be employed to satisfy the critical state condition.

Another key aspect of plastic anisotropy is the evolution of the yield surface, governed by hardening laws that include a volumetric hardening law for p_0 and a rotational hardening law for α. In early studies, some models assumed that α will evolve only with plastic volumetric strain (e.g., Banerjee and Yousif, 1986; Whittle and Kavvadas, 1994). This assumption will

induce the absence of a unique CSL in the $e - \ln p'$ plane, which is physically unreasonable (Wheeler et al., 2003a; Dafalias and Taiebat, 2013). Therefore, both plastic volumetric and deviatoric strains should be incorporated into the rotational hardening formulation of α. The widely adopted hardening laws for p_0 and α proposed by Wheeler et al. (2003a) are given as follows:

$$\begin{cases} dp_0 = \frac{(1+e)p_0}{\lambda-\kappa} d\varepsilon_v^p \\ d\alpha = \mu_W \left[\left(\frac{3\eta}{4} - \alpha \right) \langle d\varepsilon_v^p \rangle + \beta_W \left(\frac{\eta}{3} - \alpha \right) \left| d\varepsilon_q^p \right| \right] \end{cases} \tag{2-60}$$

where μ_W is a parameter controlling the evolution rate of α; β_W is a parameter controlling the relative effectiveness of plastic deviatoric and volumetric strains on the target value $\alpha_b(\eta)$; $\alpha_b(\eta)$ is the bounding value of α when the soil is loaded along a constant stress ratio η (see Figure 2-22); and the Macaulay bracket $\langle \quad \rangle$ indicates that $\langle d\varepsilon_v^p \rangle = d\varepsilon_v^p$ for $d\varepsilon_v^p \geq 0$, and $\langle d\varepsilon_v^p \rangle = 0$ for $d\varepsilon_v^p < 0$.

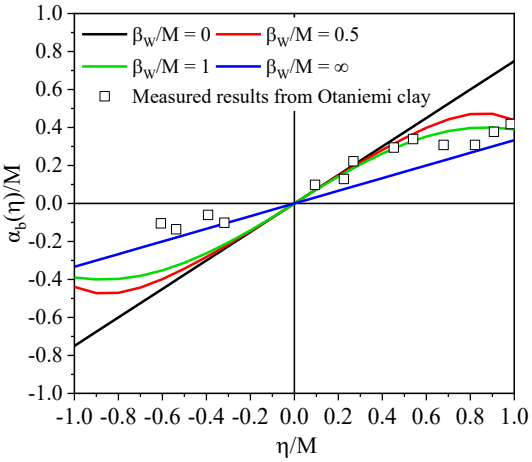

Figure 2-22. Equilibrium values of α for stress paths with constant stress ratio (adapted from Wheeler et al., 2003a)

More available rotational hardening laws were presented by Dafalias and Taiebat (2013), with one representative example provided as follows:

$$d\alpha = p_r \frac{p'}{p_0} \langle L \rangle x [\alpha_b(\eta) - \alpha] \tag{2-61}$$

where L is the plastic multiplier; and x is a model parameter. The value of $\alpha_b(\eta)$ is determined by

$$\alpha_b(\eta) = \pm\frac{M}{z_1}\left[1 - \exp\left(-z_2\left|\frac{\eta}{M}\right|\right)\right] \tag{2-62}$$

where z_1 and z_2 are model parameters; and the sign "±" takes positive and negative for $\eta \geq 0$ and $\eta < 0$, respectively.

Furthermore, constraints on the evolution of α are necessary to prevent unrealistic predictions (Dafalias and Taiebat, 2013,2014):

(i) The value of α should always be lower than M to avoid excessive rotation of the yield and plastic potential surfaces. This restriction is justified by the absence of observed cases where $\alpha \geq M$, and by the requirement that $\alpha < M$ ensures the existence of real solutions for certain yield surface formulations (e.g., the yield surface described by Equation (2-59)).

(ii) The ratio $\alpha_b(M)/M$ should be independent of mean effective stress p' and Lode angle θ to ensure the uniqueness of the CSL ($\alpha_b(M)$ is the value of $\alpha_b(\eta)$ when $\eta = M$).

(iii) A constraint must be introduced to prevent a negative increment in plastic deviatoric strain under loading paths where $\eta > \alpha$. For example, the flow rule in Wheeler et al. (2003a) is given by:

$$\frac{d\varepsilon_v^p}{d\varepsilon_q^p} = \frac{M^2-\eta^2}{2(\eta-\alpha)} \tag{2-63}$$

To maintain a positive $d\varepsilon_q^p$, it is essential to ensure $\alpha_b(\eta) < \eta$ in Equation (2-63).

Given the fact that both elastic and plastic anisotropies originate from the orientated microstructure, some studies have attempted to establish a relationship between G_{hh}/G_{hv} and α. Using experimental data from clay, Amorosi et al. (2021) derived an empirical relationship between elastic and plastic fabric tensors for cross-anisotropic soils. In triaxial stress space, this formulation can be simplified as follows:

$$\frac{G_{hh}}{G_{hv}} = \frac{1+(1/3)\bar{\omega}\alpha^2}{1-(2/3)\bar{\omega}\alpha^2} \tag{2-64}$$

where $\bar{\omega}$ is a parameter linking elastic and plastic anisotropies. Amorosi et al. (2021) demonstrated that the value of $\bar{\omega}$ is larger for clays with higher plasticity indices. Equation

(2-64) provides a practical method to estimate plastic anisotropy from stiffness anisotropy, or vice versa.

2.4.3.2 Models for unsaturated and anisotropic soils

The first model for unsaturated and anisotropic soils was proposed by Cui and Delage (1996) using mean net stress and suction as stress variables. The LC curve was determined following the approach in the BBM (Alonso et al., 1990). Cui and Delage (1996) demonstrated that the inclination of the yield surface could be considered independent of suction, which was subsequently adopted in later models.

Stropeit et al. (2008) proposed a model for unsaturated and anisotropic soils with mean net stress and suction. The yield surface was formulated as follows:

$$f = (q - \alpha p_n)^2 - (M^2 - \alpha^2)(p_n + p_s)(p_0(s) - p_n) = 0 \quad (2\text{-}65)$$

where α is independent of suction, consistent with Cui and Delage (1996). The LC curve was determined based on the BBM (Alonso et al., 1990), while the flow rule and the volumetric and rotational hardening laws were identical to those in Wheeler et al. (2003a). This model was further modified by other researchers to improve its capacity (D'Onza et al., 2010; Al-Sharrad and Gallipoli, 2014; Al-Sharrad and Gallipoli, 2016).

Based on experimental evidence, Al-Sharrad (2013) observed that the inclination of the yield surface remained nearly unchanged under varying suctions. They extended the model of Wheeler et al. (2003b) to consider the anisotropic effects on the mechanical behaviour of unsaturated soils with mean Bishop's stress and a modified suction s^* (i.e., ns). To ensure the uniqueness of the CSL, two alternative flow rules were introduced: (i) a non-associated flow rule with a constant N value in Equation (2-59) and (ii) an associated flow rule where N equals M at the critical state.

The aforementioned models primarily focus on the mechanical behaviour of unsaturated soils without explicitly accounting for the SWRC. To address this limitation, Romero and Jommi (2008) proposed a model using mean Bishop's stress and degree of saturation. By

incorporating hydro-mechanical coupling, the model allowed for the evolution of anisotropy in response to drying-wetting cycles.

Building upon the work of Romero and Jommi (2008), Vecchia and Romero (2013) developed a model for unsaturated and anisotropic soils with mean Bishop's stress and degree of saturation. The model incorporated hydraulic hysteresis and multiscale interactions, with the SWRC formulated to capture the distinct contributions of micro and macropores. Additionally, the evolution rate of α was assumed to increase with higher water contents.

Sitarenios and Kavvadas (2020) proposed a model for unsaturated and anisotropic soils with mean Bishop's stress and effective degree of saturation. Unlike the previously discussed models, the yield surface in their formulation becomes symmetric about the mean stress axis at the critical state (i.e., isotropic fabric).

By comparing the SWRCs of isotropic and anisotropic soils, Zhou and Chen (2021) concluded that anisotropy enhances the water retention capacity. However, the influence of anisotropy on the SWRC has not been incorporated into existing models for unsaturated soils. Moreover, no current models explicitly link the anisotropic effects on water retention behaviour to either elastic anisotropy (G_{hh}/G_{hv}) or plastic anisotropy (α).

2.5 Summary

As the distribution of loess is concentrated in arid and semi-arid regions, it is necessary to investigate the coupled effects of soil structure and suction on soil behaviour. Experimental data in the literature demonstrated that the slope of the normalised LC curve for structured soils could be smaller than (i.e., case-I), larger than (i.e., case-II), or equal to (i.e., case-III) that of reference soils (Koliji et al., 2009; Arroyo et al., 2013; Mu et al., 2020; Zhang et al., 2020; Mu et al., 2022). However, the existing models were generally proposed for a specific type of structured soil and incorporated only one case of the normalised LC curve. A unified approach that can model these three cases (case-I/II/III) of the LC curve is necessary to capture the behaviour of various structured soils. Furthermore, previous studies have shown that anisotropic soils possess a stronger water retention capacity than isotropic soils (Tse, 2007;

Sivakumar et al., 2010; Al-Sharrad, 2013; Zhou and Chen, 2021), which has been considered in existing models for unsaturated soils.

The soil stiffness at very small-strains (0.001% or less) and small-strains (from 0.001% to 1%) are important for predicting ground movements and the performance of many earth structures such as pavements under working conditions (Atkinson, 2000; Clayton, 2011). Previous results suggest that the small-strain shear stiffness G_0 is affected by soil structure, but inconsistent structure effects are identified. For example, intact specimens could have larger, similar, or smaller G_0 compared to their reconstituted or compacted counterparts. Under otherwise identical conditions, specimens compacted at lower water contents may show either smaller or larger G_0 those compacted at higher water contents. Possible explanations for the inconsistent structure effects on stiffness are still absent.

Soil structure also significantly affects the cyclic behaviour of soil. In the overconsolidated state, the saturated intact specimen exhibits smaller excess PWP and permanent strain than the reconstituted specimen, whereas the opposite trend may occur when the intact specimen is normally consolidated. At a given dry density, specimens compacted at the dry of optimum exhibited greater resistance to cyclic loading compared to those compacted at the wet of optimum. Additionally, denser specimens demonstrated greater stability than looser ones when compacted at the same water content. Nevertheless, previous studies mainly focused on saturated soils, although soil in the field is usually unsaturated.

Previous studies on the influence of suction on cyclic behaviour have primarily focused on soil response under cyclic vertical stress, without accounting for the PSR. It has been revealed that the PSR has deleterious impacts on soil behaviour (Gräbe and Clayton, 2009). Under the same cyclic deviatoric stress, the permanent vertical strain was generally larger, and the modulus was smaller when considering PSR than the case without PSR. The PSR may affect cyclic behaviour with suction in a coupled approach for different mechanisms. For instance, variations in suction can either stabilise or weaken the soil skeleton, thereby influencing the additional deformation induced by PSR. Therefore, it is essential to investigate

the impact of PSR on cyclic behaviour through suction-controlled tests.

Loess is commonly stabilised with cement or lime during geo-structure construction to reduce its collapse potential. The treatment of loess with stabilising additives such as cement and lime has been demonstrated to be an effective method for improving its hydromechanical behaviour (Jefferson et al., 2008; Metelková et al., 2012; Zhang et al., 2017a; Zhang et al., 2018a; Akbari Garakani et al., 2019; Haeri et al., 2019; Zhang et al., 2019b; Guo et al., 2024). Given the energy-intensive and environmentally unsustainable properties of cement and lime, industrial by-products such as GGBS are being explored as partial replacements. However, the capacity of GGBS to reduce loess collapsibility has not been explored, which restricts its application in loess regions.

CHAPTER 3 EVOLUTIONS OF STRUCTURE AND ANISOTROPIC SHEAR STIFFNESS DURING ISOTROPIC COMPRESSION

This chapter presents the structure evolution during isotropic compression and its effects on the small-strain shear stiffness of saturated loess. Both intact loess, reconstituted loess, and compacted loess with different compaction dry densities and water contents are examined. During isotropic compression, shear stiffnesses in the horizontal and vertical planes were measured throughout isotropic compression. Additionally, SM, SEM, and MIP tests were conducted before and after compression to analyse structure evolution. The results obtained from this chapter are also useful for understanding the cyclic behaviour of loess in the following two chapters.

3.1 Specimen preparation, test apparatus, test program, and test procedures

3.1.1 Specimen preparation

Both intact, compacted, and reconstituted specimens with 76 mm in diameter and height were prepared. The sampling and specimen preparation procedures are shown in Figure 3-1. For each intact specimen, a cube of about 100 mm × 100 mm × 100 mm was first cut from the block sample. The cube was carefully trimmed on a lathe into a cylinder with a diameter of 76 mm, and then the top and base were cut to attain a height of 76 mm. According to the null-type axis translation technique (Fredlund and Rahardjo, 1993), the initial suction is about 50 kPa.

To prepare compacted specimens, the disturbed soil was oven-dried and crushed with a rubber hammer, then sieved using a 2 mm sieve. Note that all soil particles passed the 2 mm sieve, and no particle was removed. Afterwards, de-aired water was sprayed over the soil powder step by step. Between each step, the soil was thoroughly mixed with water, and any clod was broken up to achieve uniform water distribution. As the target water content was obtained, the soil was sieved again with a 2 mm sieve and kept in sealed plastic bags for 24

hours for moisture equalisation. Afterwards, the soil mixture was statically compacted by five layers in a split mould. The under-compaction method was utilised to minimise excessive compaction of the lower layers (Ladd, 1978).

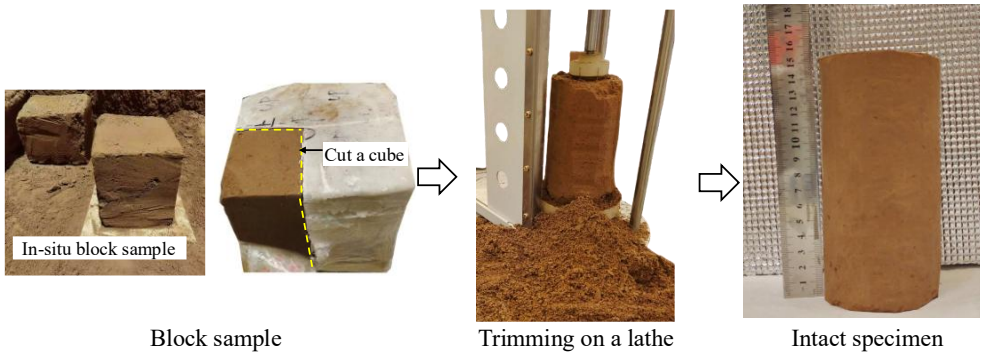

Block sample　　Trimming on a lathe　　Intact specimen

(a)

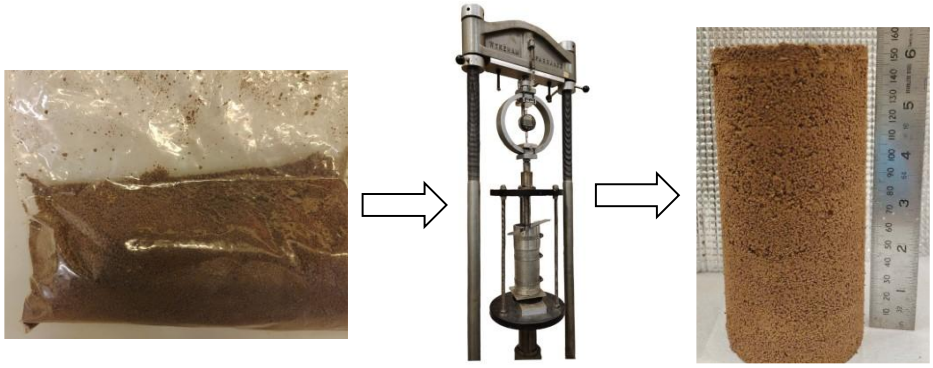

Soil mixture　　Compaction within a split mould　　Compacted specimen

(b)

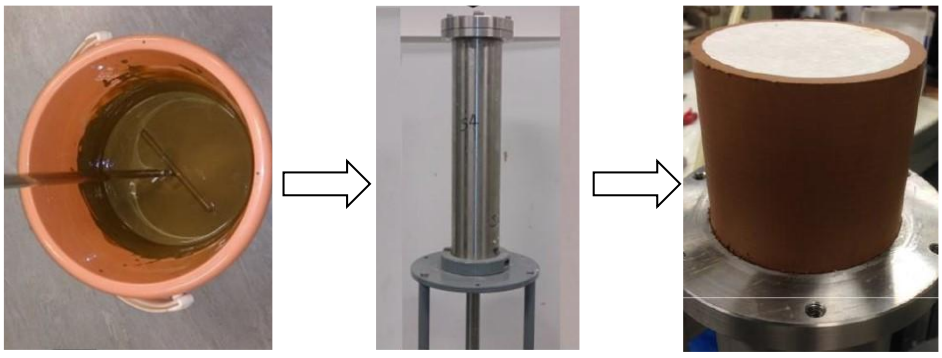

Slurry　　Consolidation　　Extrusion

(c)

Figure 3-1. Illustrations of sampling and specimen preparation procedures: (a) intact specimen; (b) compacted specimen; (c) reconstituted specimen

The reconstituted specimen was prepared from a slurry composed of oven-dried loess powder and de-aired water at a water content of 46.7%, equivalent to 1.5 times the liquid limit.

The slurry was consolidated in a one-dimensional consolidometer with a diameter of 76 mm. Vertical stress was applied in 10 kPa increments up to 40 kPa, each held for 24 hours, to strengthen the specimen and allow for bender element installation. Upon completion of consolidation, the specimen was carefully extruded and trimmed to the desired dimensions.

For microstructural analysis, small cubic samples (approximately 10^{-6} m^3 in volume) were carefully extracted from the central region of the specimens before and after compression. Dehydration was conducted using the freeze-drying technique to preserve the soil fabric. The samples were first immersed in liquid nitrogen, then placed in a freeze dryer to remove frozen water through sublimation mechanism. After 24 hours of drying, the cubes were used for microstructural investigations.

3.1.2 Test apparatus

A modified triaxial apparatus (Ng and Yung, 2008; Ng et al., 2009) was employed to perform isotropic compression tests, as shown in Figure 3-2. Volumetric changes and axial strains were continuously recorded using Global Digital System volume controllers and linear variable differential transformers, respectively. Two pairs of bender elements, integrated with shear wave generation and measurement systems, were used to determine shear wave velocity and small-strain shear stiffness. The bender elements were installed at the mid-height of each specimen using silicon grommets.

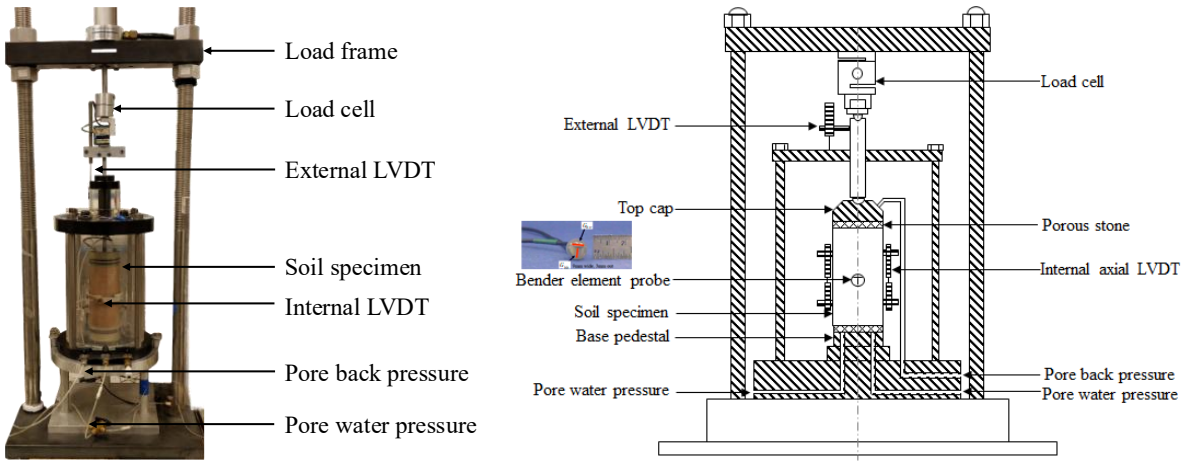

(a) (b)

Figure 3-2. Triaxial apparatus: (a) overview; (b) schematic diagram

The SM, SEM, and MIP tests were conducted using Nikon SMZ1270, VEGA3 TESCAN, and PoreMaster 33, respectively. The magnification ranges for the SM and SEM were from 6× to 48× and from 30× to 50 000×, respectively. In the MIP test, the maximum intrusion pressure reached approximately 230 MPa. A contact angle of 140° was assumed, and the pore throat diameters were calculated based on the methodology outlined by Romero and Simms (2008).

3.1.3 Test program

Two series of isotropic compression tests were conducted, as summarised in Table 3-1.

Table 3-1. Test program for isotropic compression tests

Test series	Test ID[*1]	Vertical stress applied during preparation	Initial water content: %	Initial dry density: g/cm^3	Initial void ratio
I	Intact	--	18.9	1.23	1.17
	Compacted (CWL)	35	18.5	1.23	1.17
	Reconstituted	40	30.8	1.46	0.83
II	CDL	220	13.5	1.19	1.22
	CDD	500	13.3	1.50	0.78
	COL	130	15.3	1.20	1.22
	COD	250	15.6	1.50	0.78
	CWL[*2]	35	18.5	1.23	1.17
	CWD	170	18.6	1.52	0.75

[*]Notations:
1. In the test ID: “C” indicates compacted specimens; the letters “D”, “O”, and “W” following “C” represent compaction at the dry of optimum, optimum, and wet of optimum water contents, respectively; and the final letters “L” and “D” denote loosely and densely compacted states, respectively.
2. The CWL specimen in series II is identical to the compacted specimen used in series I.

Series I examined the stiffness evolution of intact, compacted, and reconstituted loess specimens. Isotropic compression tests, with measurements of small-strain shear stiffness, were conducted on intact and compacted specimens prepared with identical initial dry density and water content. A reconstituted specimen was also tested as a reference. Series II explored the influence of compaction conditions. The initial states of compacted specimens are illustrated in Figure 1-3(b). Three water contents (13.0%, 15.2% and 18.9%) and two dry densities (1.21

and 1.52 g/cm^3) were considered. These three water contents correspond to the dry of optimum, optimum, and wet of optimum conditions ("D", "O", and "W" in Table 3-1), respectively. The loosely and densely compacted states ("L" and "D" in Table 3-1) represent 70% and 85% degrees of compaction, respectively.

As shown in Table 3-2, SM, SEM, and MIP tests were conducted to examine the structure effects on stiffness evolution. The first series focused on the differences among intact, compacted, and reconstituted loess. In the second series, CWD and CDD specimens were compared to reveal the influence of compaction water content, while CWD and CWL specimens were used to investigate the influence of compaction dry density. SM and SEM were employed to observe particle arrangements at relatively low (e.g., 10×) and high (e.g., 1000×) magnifications, respectively. The microstructure of each specimen was examined before and after compression.

Table 3-2. Test program for microstructure investigations

Test series	Test ID	Soil state	Analysis method
I	Intact	Before and after compression	SEM and MIP
	Compacted (CWL)	Before and after compression	SEM and MIP
	Reconstituted	Before and after compression	SEM and MIP
II	CDD	Before and after compression	SM, SEM, and MIP
	CWL	Before and after compression	SEM and MIP
	CWD	Before and after compression	SM, SEM, and MIP

3.1.4 Test procedures

After setup in the triaxial cell, specimens were saturated by applying a back pressure of 150 kPa, with B values greater than 0.98. Following saturation, isotropic compression was carried out in stages of 8, 16, 30, 50, 100, 200, 300, and 400 kPa. Upon reaching equilibrium at each stress level, travel times of shear waves were determined using the peak-to-peak method (Lee and Santamarina, 2005). Both t_{hh} and t_{hv} were measured using horizontally embedded bender elements. For t_{hh}, the shear wave propagated and vibrated in the horizontal direction, whereas for t_{hv}, the wave propagated horizontally and vibrated in the vertical direction. Shear stiffness was then calculated as follows:

$$\begin{cases} G_{hh} = \rho \left(\frac{L_{tt}}{t_{hh}}\right)^2 \\ G_{hv} = \rho \left(\frac{L_{tt}}{t_{hv}}\right)^2 \end{cases} \tag{3-1}$$

where ρ is the bulk density; and L_{tt} represents the tip-to-tip distance between two bender elements. For the analysis, stiffness values both with and without normalisation by the void ratio function (i.e., G_{hv} and $G_{hv}/f(e)$, with $f(e) = e^{-1.3}$) are both presented. The findings remain valid when alternative void ratio functions, such as $(2.17 - e)^2/(1 + e)$ (Iwasaki and Tatsuoka, 1977; Liu et al., 2019a) and $(1 + e)^{-3}$ (Oztoprak and Bolton, 2013; Zhou et al., 2015), are employed.

Following the test program outlined in Table 3-2, the compressed specimens were unloaded, dismantled from the triaxial cell, and sectioned into small cubes for SM, SEM, and MIP analyses. Note that the volumetric strain during unloading was relatively small (approximately 3%), indicating minimal disturbance and suggesting that the structure features of the specimens remained representative of their compressed state.

3.2 Isotropic compression behaviour

Figure 3-3(a) compares the compression curves of intact, compacted, and reconstituted specimens. The intact specimen exhibits a higher isotropic yield stress (35 kPa) than the compacted specimen (1 kPa), indicating that the former's structure is more resistant to external loads. After yielding, the intact specimen shows greater compressibility than the compacted and reconstituted specimens, as the degradation of its structure induces additional plastic strain (Burland, 1990; Liu and Carter, 2002). As plastic strain accumulates, the structure effects on compression behaviour diminish, as evidenced by the gradual convergence of the compression curves for the intact, compacted, and reconstituted specimens.

Figure 3-3(b) illustrates the influence of compaction water content and dry density on isotropic compression curve. The yield stress increases with decreasing compaction water content. Specimens compacted at lower water contents can sustain higher void ratios at a given

stress, which is attributed to structure differences arising from varying compaction water contents, as explained later. As expected, the denser specimen exhibits a higher yield stress than the looser specimen at the same compaction water content. The compression curves for looser and denser states become nearly parallel once the applied stress exceeds the yield stress. Within the considered stress range, the tested loess displays transitional mode behaviour, in which the normal compression lines of specimens with different initial densities do not converge to the same void ratio. In this study, the difference in void ratio (Δe) is approximately 0.15 (Martins et al., 2001). Transitional behaviour in saturated loess has also been reported in previous studies, such as Lee (2004) (Δe = 0.05) and Xu and Coop (2017) (Δe = 0.1). One postulation for this behaviour is that strong microscale fabrics are difficult to break down (Todisco et al., 2018).

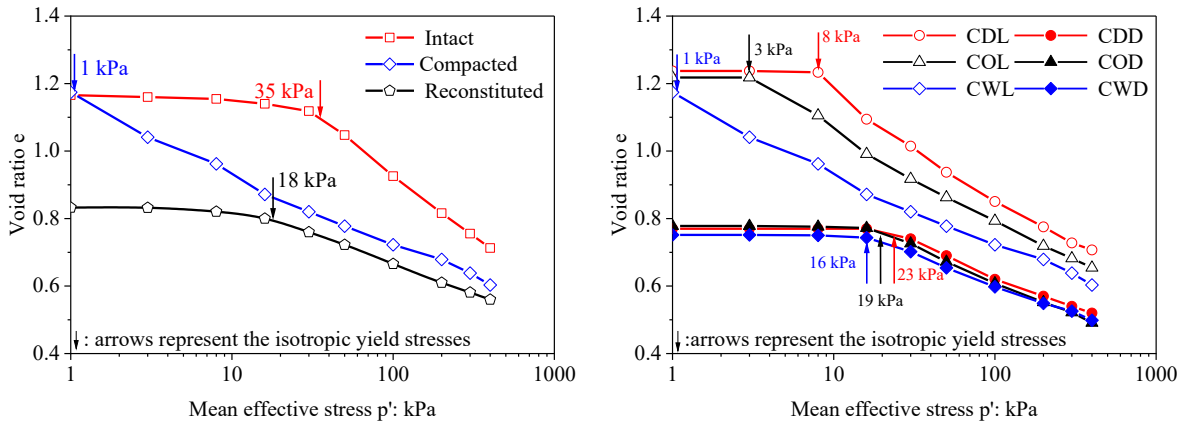

(a) (b)

Figure 3-3. Isotropic compression curves: (a) comparison of intact, compacted, and reconstituted; (b) influence of compaction conditions

3.3 Anisotropic stiffness characteristics

3.3.1 Comparisons of intact, compacted, and reconstituted specimens

Figure 3-4 shows the stiffnesses and stiffness anisotropies of intact, compacted, and reconstituted specimens from the tests in series I. As shown in Figure 3-4(a) and (b), the stiffness of all specimens increases with increasing stress but at different rates. The intact specimen has approximately twice larger $G_{hv}/f(e)$ than the compacted and reconstituted specimens at p' = 3 kPa. The trend is reversed when stress is 400 kPa, where $G_{hv}/f(e)$ of

the intact specimen becomes about 10% and 25% smaller than those of the compacted and reconstituted specimens, respectively. Similar values of $G_{hv}/f(e)$ are observed between the intact and compacted specimens, as well as between the intact and reconstituted specimens at a stress of approximately 100 kPa (roughly three times the isotropic yield stress of the intact specimen). At this stress level, significant plastic deformation has occurred, and the initial structure has been substantially altered in all specimens. This structure evolution accounts for the observed trend reversal, which is further examined in the subsequent structure analysis.

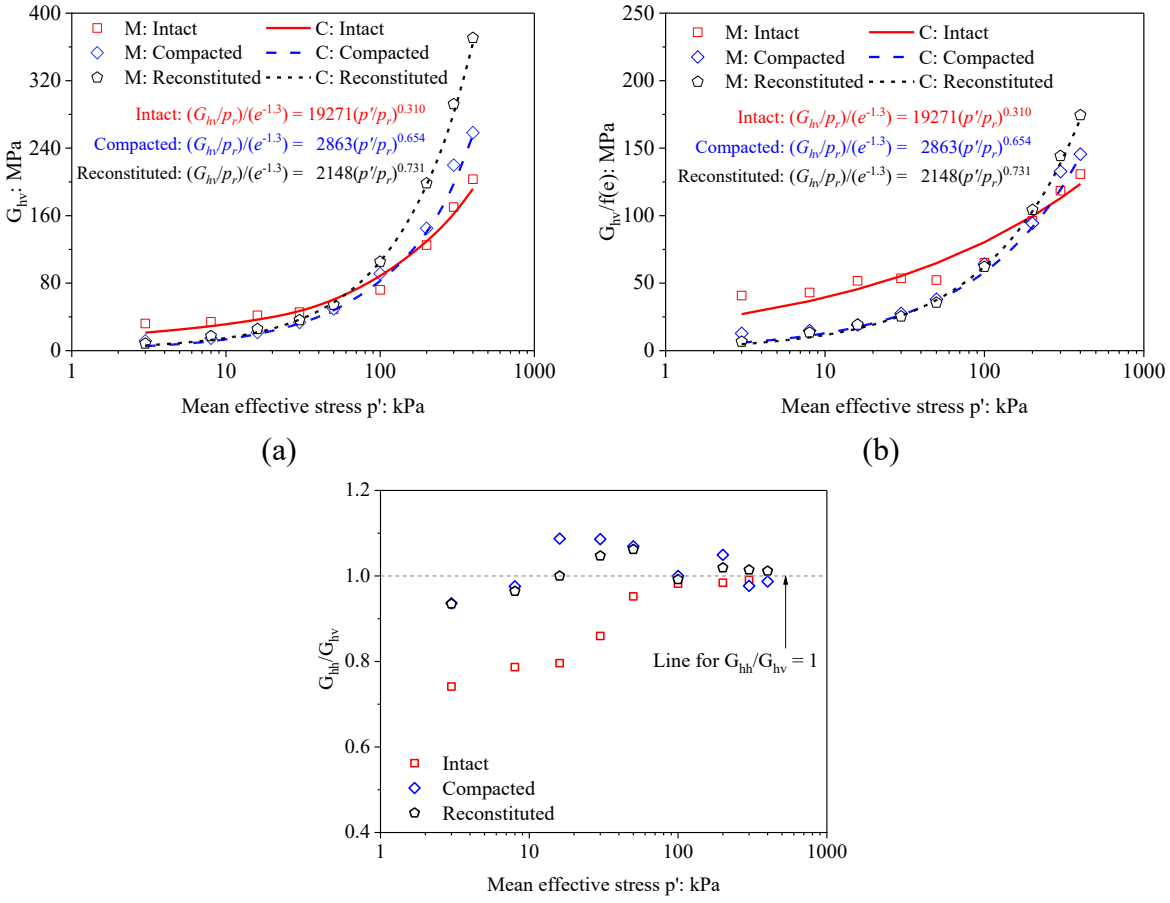

Figure 3-4. Stiffnesses and stiffness anisotropies of intact, compacted, and reconstituted specimens (M/C: measured/computed): (a) stiffnesses; (b) normalised stiffnesses; (c) stiffness anisotropies

Stiffness anisotropy, quantified by the ratio of G_{hh}/G_{hv}, is presented in Figure 3-4(c). The stiffness anisotropy is insignificant for the compacted and reconstituted specimens (with G_{hh}/G_{hv} of about 0.95), likely due to the relatively low vertical stress (approximately 40 kPa) applied during one-dimensional compaction or consolidation. In contrast, the intact specimen

displays clear stiffness anisotropy, with G_{hh}/G_{hv} remaining around 0.8 when the applied stress is below the yield stress (35 kPa). This anisotropic behaviour is likely attributed to the directionally oriented particles or aggregates formed during aeolian deposition (Zuo et al., 2024). After yielding, the stiffness ratio progressively approaches unity. Isotropic stiffness is observed when the stress exceeds 100 kPa, indicating that the initially oriented particles or aggregates have transitioned to a more isotropic configuration.

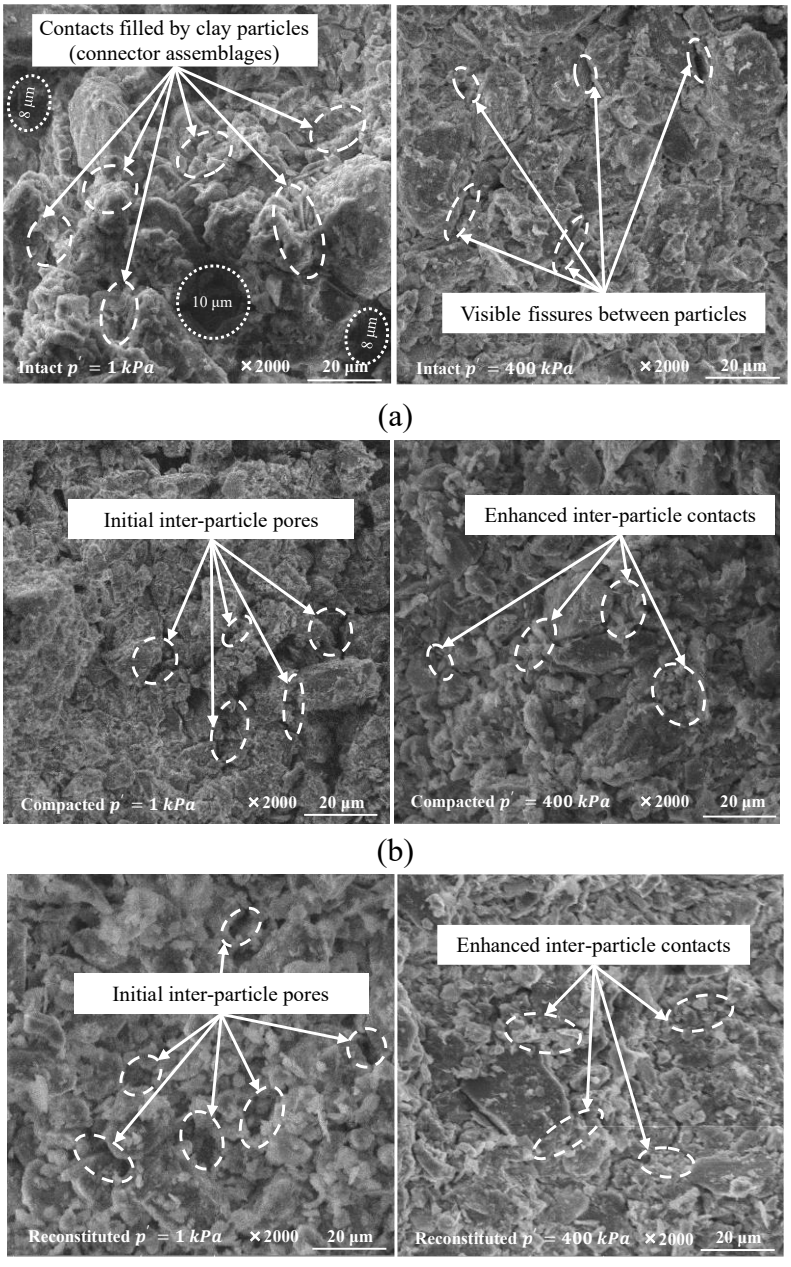

Figure 3-5. SEM results before and after compression: (a) intact specimen; (b) compacted specimen; (c) reconstituted specimen

Figure 3-5 presents SEM images of intact, compacted, and reconstituted specimens before and after compression. Prior to compression, Figure 3-5(a) shows that connector assemblages (i.e., clay particles) are well identified between silt particles in the intact specimen. The connector assemblages increase the contact area and stiffen the soil skeleton (Ng et al., 2017; Mu et al., 2020). After compression, these connector assemblages are damaged and abundant micro-fissures are observed, as shown in Figure 3-5(a). In contrast, Figure 3-5(b) and (c) show that the compacted and reconstituted specimens initially exhibit many pores between silt particles, suggesting softer particle contacts compared to the intact specimen. At the post-compression state, these interparticle pores are compressed and the interparticle contacts are strengthened with increasing stress.

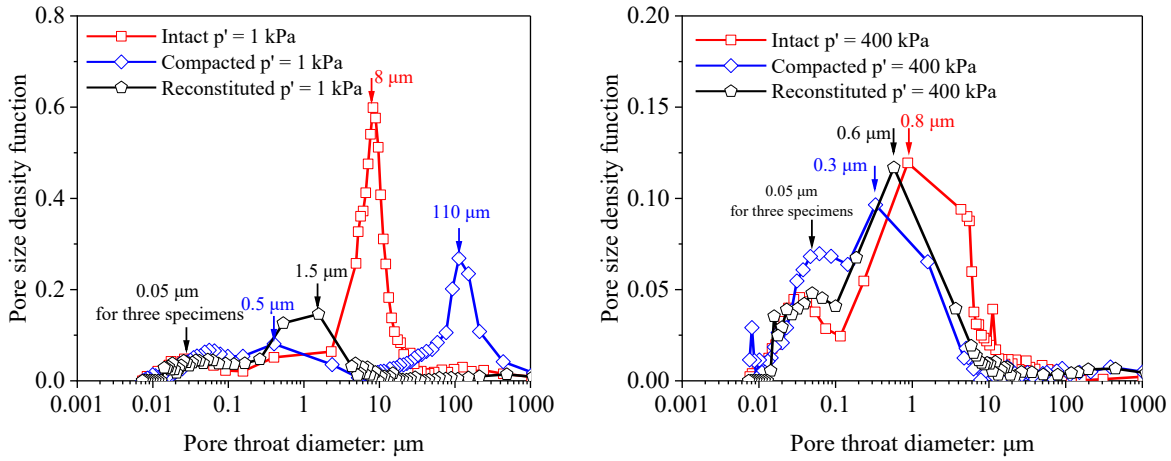

(a) (b)

Figure 3-6. MIP results of intact, compacted, and reconstituted specimens: (a) before compression; (b) after compression

Figure 3-6 shows the pore size distributions of intact, compacted, and reconstituted specimens. Prior to compression, the intact specimen exhibits a dominant pore diameter of approximately 8 μm, which aligns with the SEM observations showing numerous pores around 10 μm in size. The compacted specimen displays extra-large pores with diameters around 110 μm, which is consistent with Zhan et al. (2014), who reported that loess particles tended to aggregate and formed soil clods and inter-clod pores under high compaction water contents. After compression, all specimens show a marked reduction in both the dominant pore diameter and associated intensity. Among the three, the intact specimen retains the largest dominant pore

diameter (0.8 μm), compared to 0.3 μm for the compacted and 0.6 μm for the reconstituted specimens, indicating that the pores in the intact specimen underwent less compression.

Previous studies have demonstrated that interparticle contact is the primary factor influencing small-strain shear stiffness (e.g., Cascante and Santamarina, 1996). Prior to compression, the presence of stiffer interparticle contacts formed by connector assemblages in the intact specimen is responsible for its larger $G_{hv}/f(e)$ than the compacted and reconstituted specimens. As compression progresses, all specimens experience significant reductions in dominant pore diameter and intensity, leading to increased values of $G_{hv}/f(e)$ with increasing stress. At the post-compression state, the damaged connector assemblages (Figure 3-5(a)) and less compressed pores (Figure 3-6(b)) in the intact specimen result in smaller $G_{hv}/f(e)$ than the compacted and reconstituted specimens, where the interparticle contacts are strengthened by stress (see Figure 3-5(b) and (c)).

3.3.2 Influence of compaction dry density on stiffness evolution

Figure 3-7 shows the influence of compaction dry density on stiffness and normalised stiffness. Before compression, the G_{hv} of denser specimens is about 140%, 100%, and 60% larger than that of looser specimens compacted at the dry of optimum, optimum, and wet of optimum water contents, respectively. As stress increases, the G_{hv} of looser and denser specimens progressively become almost identical, although different void ratios are still observed (see Figure 3-3). The results that looser and denser specimens have nearly identical stiffness were also reported by Todisco et al. (2018) for Leighton Buzzard quartz sand (Δe = 0.1) and Wang et al. (2021) for loess (Δe = 0.05). Such behaviour may be related to the parallel nature of the isotropic compression curves of looser and denser specimens (i.e., transitional behaviour), as shown in Figure 3-3(b). A plausible explanation is that the initial fabric, which contributes to the non-converging compression response, also governs stiffness magnitude, thereby resulting in nearly identical G_{hv}. Consequently, due to their similar G_{hv} and different void ratios at the post-compression state, the $G_{hv}/f(e)$ of looser specimens is larger than that of denser specimens, as shown in Figure 3-7.

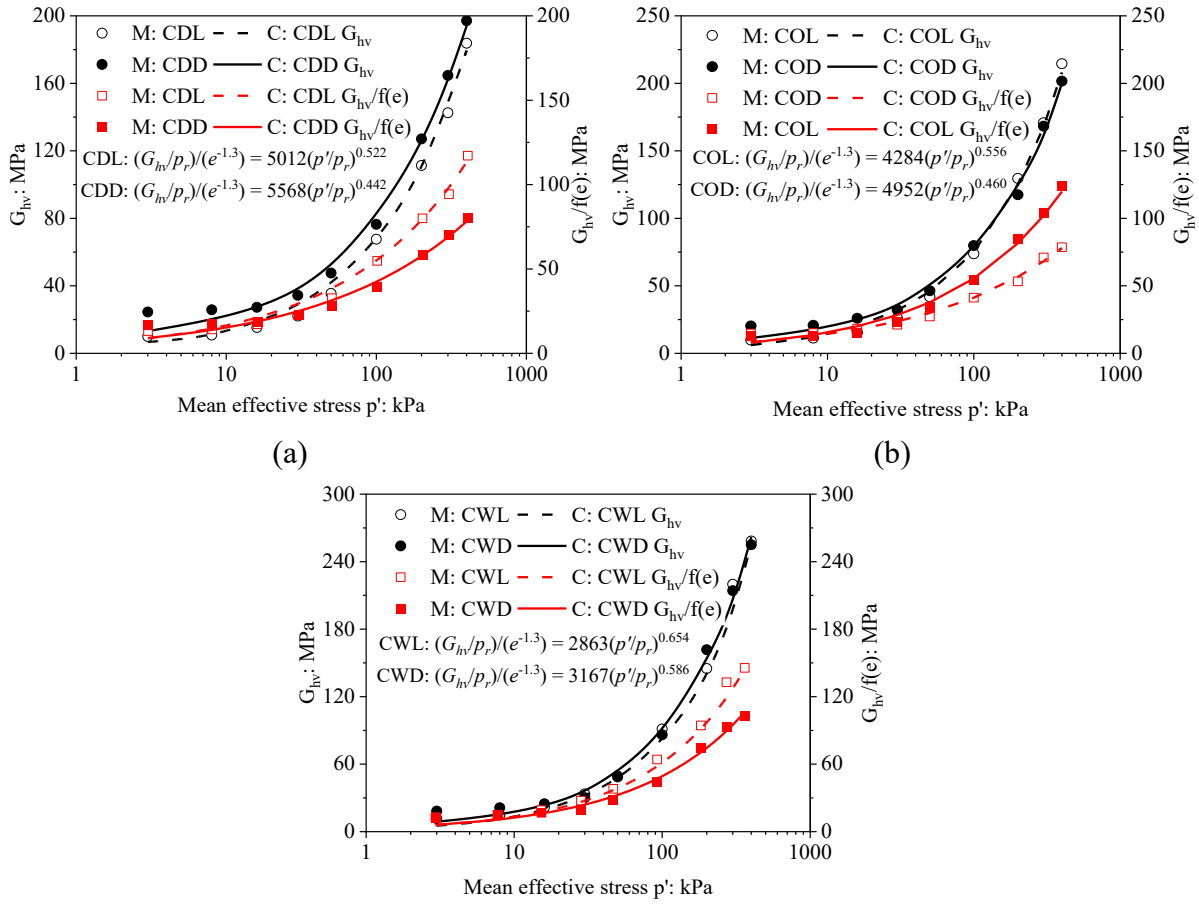

Figure 3-7. Influence of compaction dry density on stiffness and normalised stiffness (M/C: measured/computed): (a) dry of optimum; (b) optimum; (c) wet of optimum

Figure 3-8 presents the SEM results of specimens CWL and CWD, with three images captured from random locations for each specimen. Before compression, silt particles are coated by clay particles, and abundant interparticle pores are observed. These interparticle pores are compressed, and interparticle contacts are enhanced after compression. A comparison of the post-compression SEM images reveals that the particle contacts in the looser (CWL) and denser (CWD) specimens are similar. Figure 3-9 shows the MIP results of specimens CWL and CWD. Prior to compression, both specimens exhibit multi-modal pore size distributions. The dominant pores (around 100 μm), correspond to inter-clod pores, which is formed due to relatively high compaction water content and is also observed in compacted loess by Zhan et al. (2014). As dry density increases, the dominant inter-clod pore diameter decreases from 110 μm to 70 μm, contributing to a higher stiffness in the denser specimen before compression. With increasing stress, the multi-modal pore size distributions are compressed to bi-modal pore

size distributions for both looser and denser specimens, and more pores with a dominant diameter of 0.3 μm exist in the former.

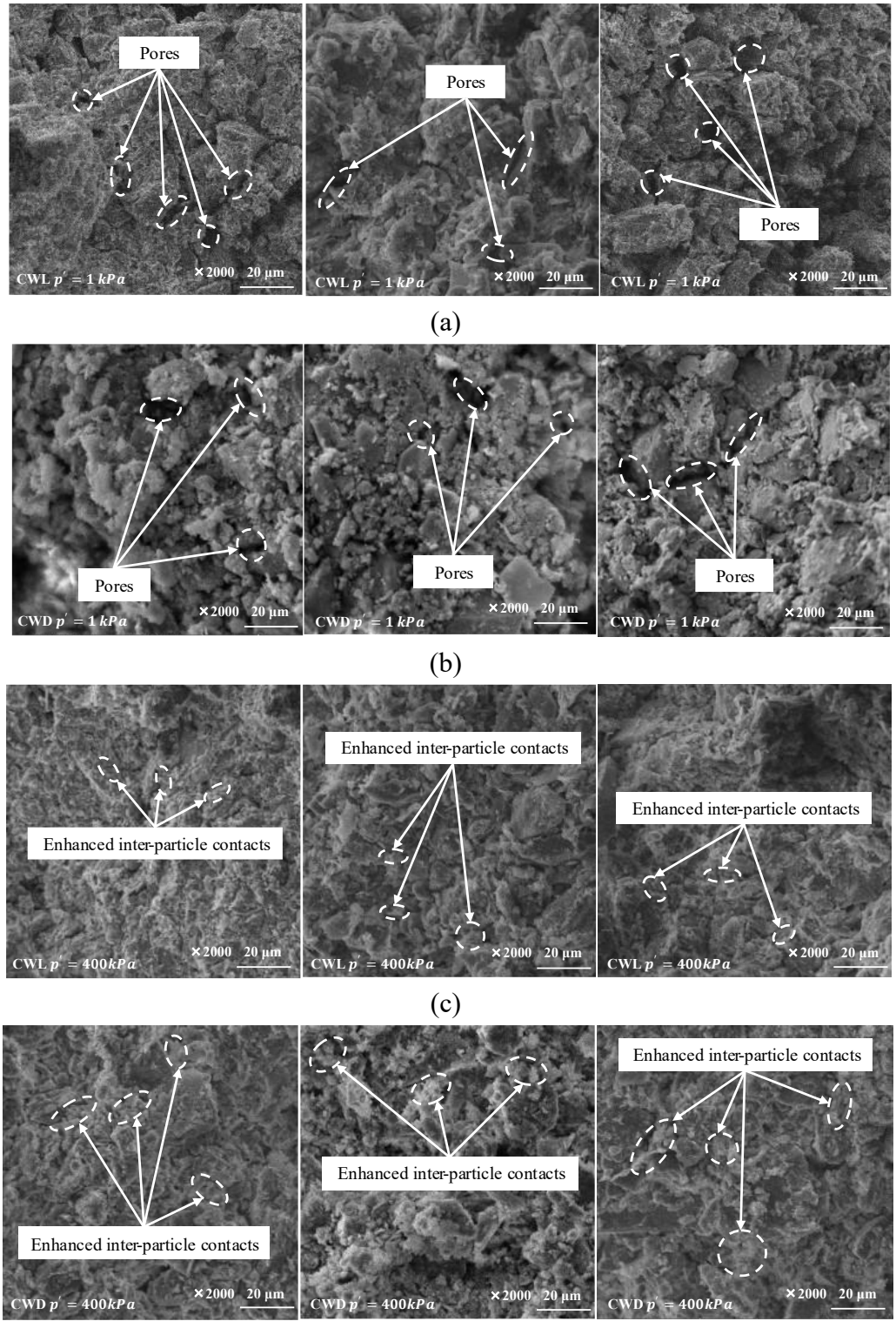

Figure 3-8. SEM results of specimens CWL and CWD: (a) CWL before compression; (b) CWD before compression; (c) CWL after compression; (d) CWD after compression

Based on the SEM results shown in Figure 3-8, it can be concluded that comparable interparticle contacts in looser and denser specimens lead to similar G_{hv} values after compression. By comparing Figure 3-9(a) and (b), it is evident that more pores are compressed in the looser specimen than in the denser one. The more compressed pores in the looser specimen correspond to its larger volumetric strain and the more significant increase in $G_{hv}/f(e)$ compared to the denser specimen.

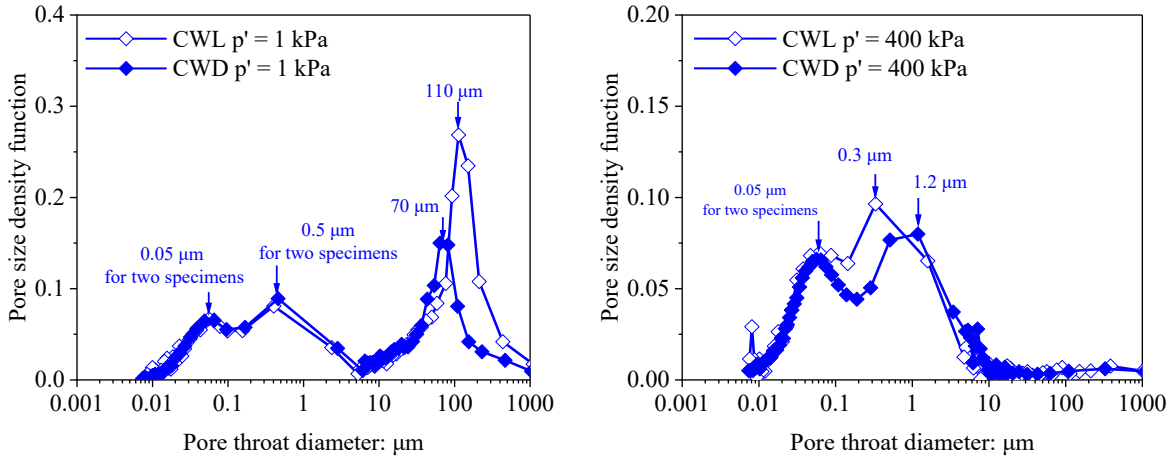

(a) (b)

Figure 3-9. MIP results of specimens with different compaction densities: (a) before compression; (b) after compression

3.3.3 Influence of compaction dry density on stiffness anisotropy

Figure 3-10 shows the variations of stiffness anisotropy with stress for all compacted specimens. At the same compaction water content, stiffness anisotropy is more predominant in the denser specimen than the looser specimen, which is because soil particles/aggregates become more horizontally orientated with increasing compaction effort. As isotropic compression proceeds, the ratio G_{hh}/G_{hv} changes towards unity for all specimens, indicating that the soil fabric becomes isotropically distributed and increasing stress can eliminate the initial anisotropy introduced during specimen preparation. The stress corresponding to a unity value of G_{hh}/G_{hv} for denser specimens is about 100 to 200 kPa, which is approximately five times higher than the yield stress. This stress range is similar to the results of Mitaritonna et al. (2014), who observed that a complete modification of stiffness anisotropy in the reconstituted Lucera clay can be achieved when the applied stress was four times higher than its yield stress.

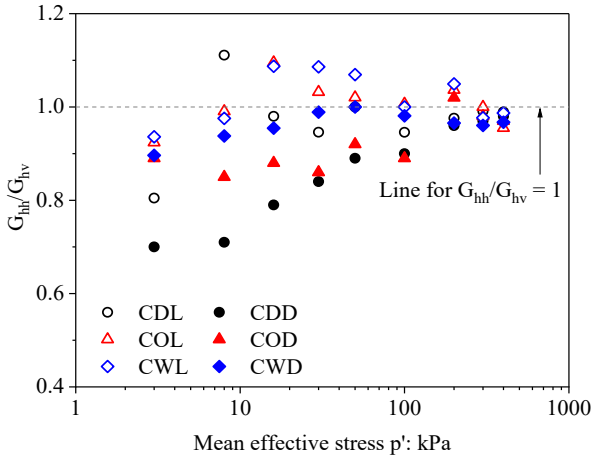

Figure 3-10. Stiffness anisotropies of compacted specimens

3.3.4 Influence of compaction water content on stiffness evolution

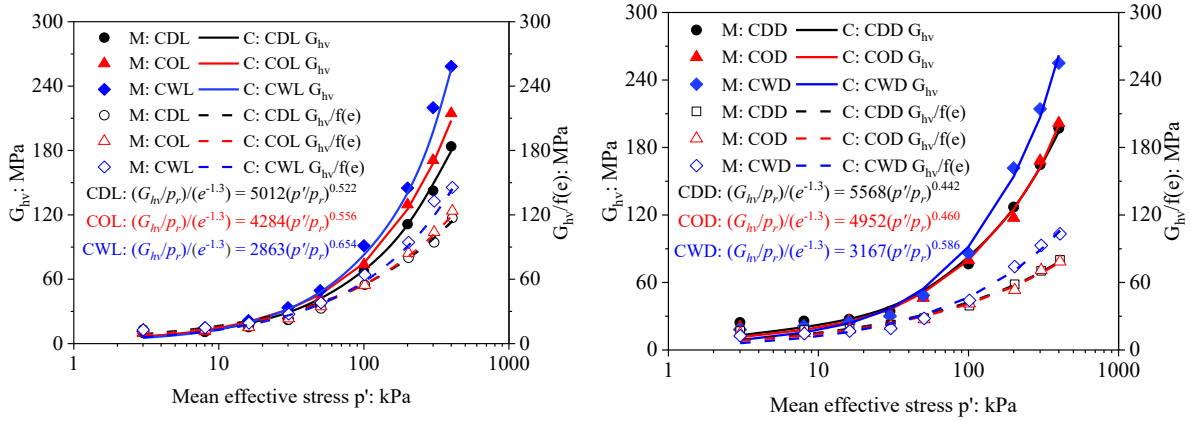

(a) (b)

Figure 3-11. Influence of compaction water content on stiffness and normalised stiffness (M/C: measured/computed): (a) looser specimens; (b) denser specimens

Figure 3-11 shows the influence of compaction water content on stiffness and normalised stiffness for loosely and densely compacted specimens. It can be observed that the effects of compaction water content on G_{hv} and $G_{hv}/f(e)$ follow the same trend; therefore, the following analysis mainly focuses on the normalised stiffness. Before compression, $G_{hv}/f(e)$ decreases with increasing compaction water content. The wet of optimum specimens have about 5% and 25% smaller $G_{hv}/f(e)$ than the dry of optimum specimens in the looser and denser states, respectively. This trend reverses when the stress increases to 400 kPa, where $G_{hv}/f(e)$ increases with increasing compaction water content. At the post-compression state, the wet of optimum specimens exhibit about 25% and 30% larger $G_{hv}/f(e)$ than the dry of optimum specimens in the looser and denser states, respectively.

Figure 3-12 shows the variations of parameters A_{hv} and $(n_h + n_v)/2$ with compaction water content. These values are derived from the results shown in Figure 3-11. For both looser and denser specimens, A_{hv} decreases while $(n_h + n_v)/2$ increases with increasing compaction water content. The reduction in A_{hv} suggests a decline in initial stiffness with higher water contents, whereas the increase in $(n_h + n_v)/2$ implies that stiffness evolves more significantly with stress under wetter compaction conditions, which is consistent with the observation in Figure 3-11. To reveal the mechanisms underlying these observations (i.e., the initial stiffness and stiffness evolution), the effects of compaction water content on soil structure are investigated in Figure 3-13 and Figure 3-14.

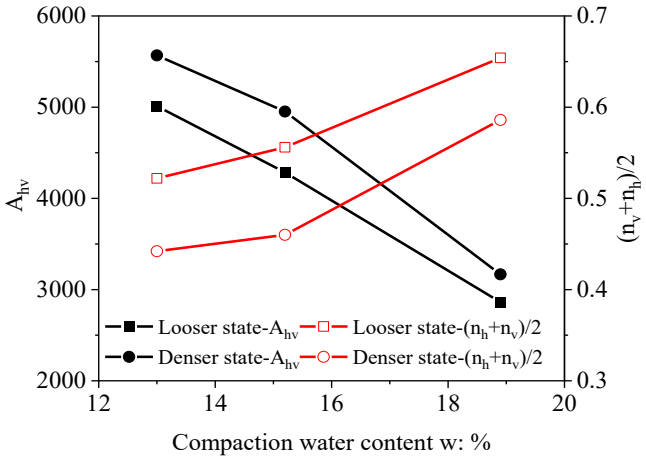

Figure 3-12. Variations of A_{hv} and $(n_h + n_v)/2$ with compaction water content

Figure 3-13 displays the SM (i.e., ×24) and SEM (i.e., ×1000) results for specimens CDD and CWD. The SM images reveal that soil clod size increases with increasing compaction water content. For the wet of optimum specimen, soil clods larger than 1000 μm and inter-clod pores of about several hundred micrometres are observed. The SEM results show that the dry of optimum specimen exhibits an aggregated structure with interaggregate pores approximately 10 μm in size, whereas in the wet of optimum specimen, silt particles are coated with clay particles. These SEM observations are similar with findings reported by Delage et al. (1996), who observed an aggregated structure in the dry of optimum specimen, and a matrix-type structure (silt particles enveloped by clay grains) in the wet of optimum specimen. The SM and SEM results suggest that increasing compaction water content converts the soil fabric from an aggregated structure to one characterised by large soil clods and inter-clod pores.

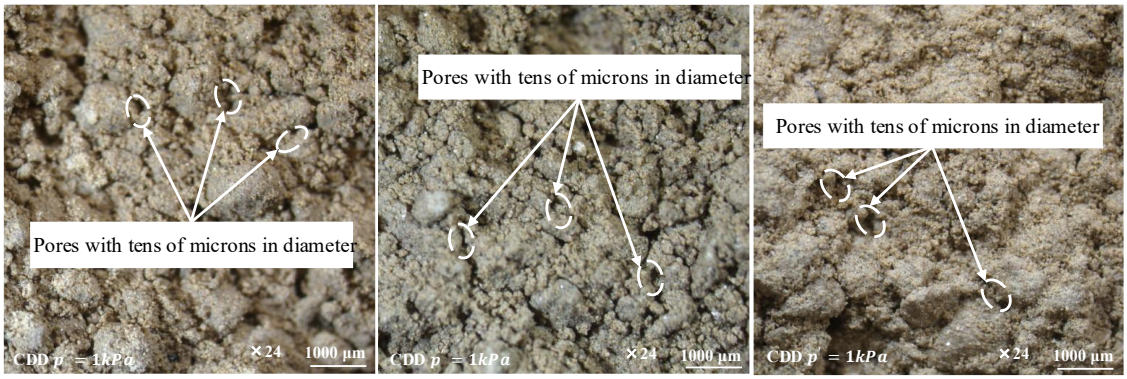

(a)

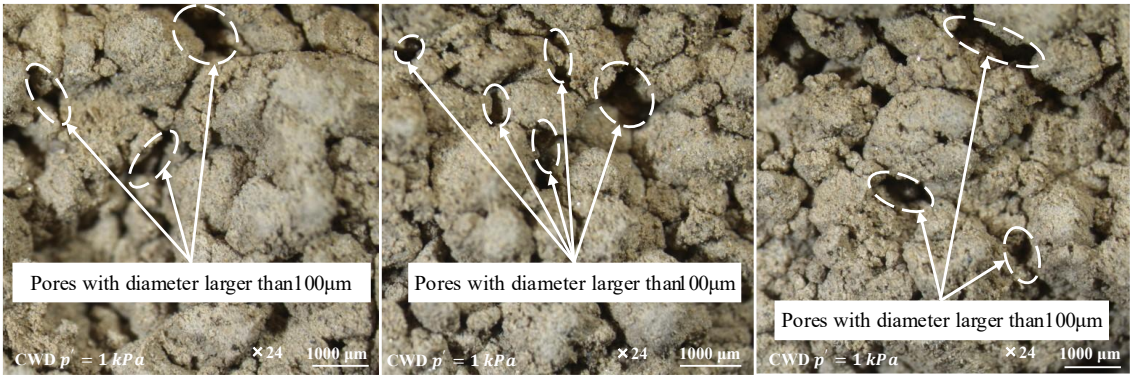

(b)

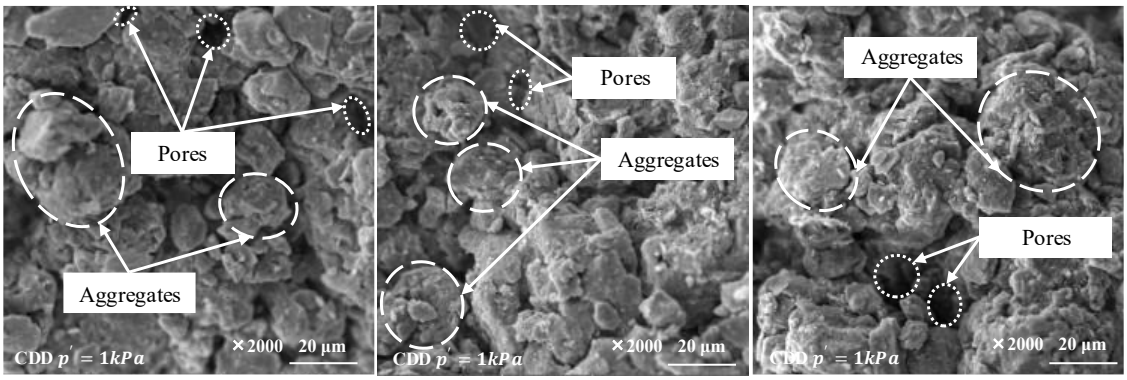

(c)

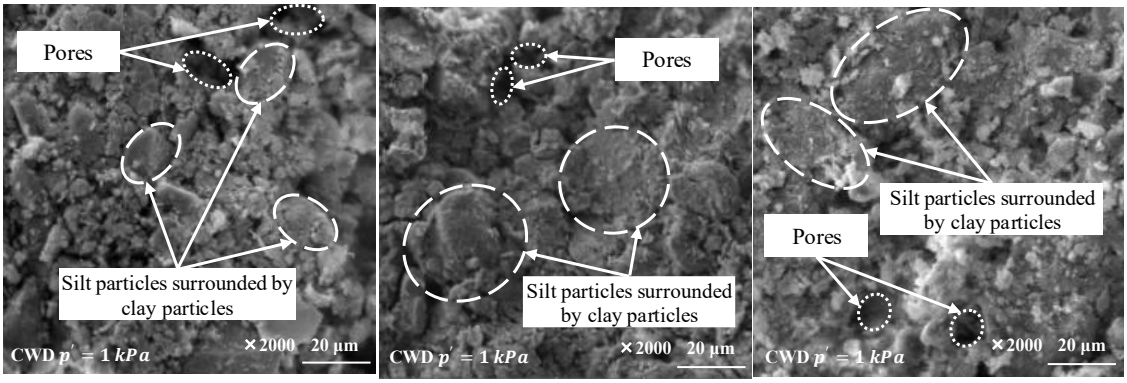

(d)

Figure 3-13. SM and SEM results of CDD and CWD specimens: (a) CDD-SM; (b) CWD-SM; (c) CDD-SEM; (d) CWD-SEM

Figure 3-14(a) exhibits the pore size distributions of specimens CDD and CWD before compression. The dry of optimum specimen exhibits a dominant pore diameter of 12 μm, consistent with the macropores observed in the SEM images. In contrast, the wet of optimum specimen shows a prominent peak at approximately 70 μm, corresponding to the inter-clod pores identified in the SM images. After compression, as shown in Figure 3-14(b), these relatively large pores (i.e., those around 12 μm and 70 μm) are substantially compressed. More importantly, the pore size distribution of the wet of optimum specimen is more markedly altered than that of the dry of optimum specimen, demonstrated by its larger inter-clod pores before compression but fewer pores between 1 to 10 μm after compression.

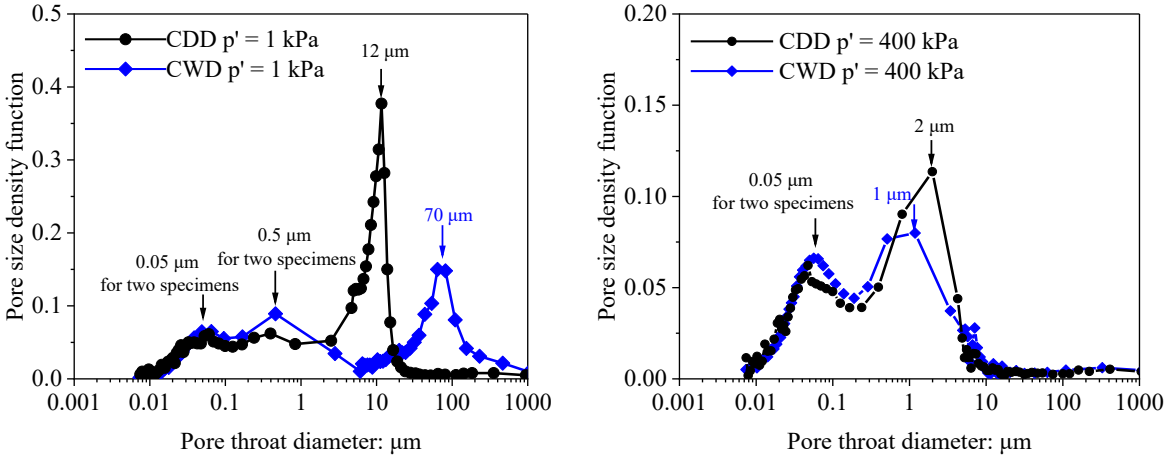

(a) (b)

Figure 3-14. MIP results of specimens CDD and CWD: (a) before compression; (b) after compression

Based on the SM, SEM, and MIP results, the influence of compaction water content on the initial stiffness and its evolution can be explained. One-dimensional compaction induces a structure featured by clods and inter-clod pores for wet of optimum specimens (Figure 3-13). These pores are substantially larger and more compressible than the interaggregate pores in dry of optimum specimens. Therefore, wet of optimum specimens exhibit lower initial stiffness, reflected by smaller $G_{hv}/f(e)$, as shown in Figure 3-7. As stress increases, the more significant alteration in pore size distribution in wet of optimum specimens results in more pronounced stiffness variations (i.e., larger $(n_h + n_v)/2$ in Figure 3-12) and larger post-compression $G_{hv}/f(e)$ (Figure 3-7) than dry of optimum specimens.

3.3.5 Influence of compaction water content on stiffness anisotropy

The variation of stiffness anisotropy G_{hh}/G_{hv} with compaction water content can be identified from Figure 3-10. Prior to compression, specimens compacted at lower water contents exhibit greater stiffness anisotropy. At the denser state, G_{hh}/G_{hv} values are 0.70, 0.89, and 0.91 for specimens compacted at the dry of the optimum, optimum, and wet of the optimum water contents, respectively. With increasing stress, G_{hh}/G_{hv} gradually approaches unity for all specimens. However, a higher stress is required for dry of optimum specimens due to their more pronounced initial anisotropy. These findings indicate that compaction water content affects not only stiffness but also its anisotropic characteristics.

To reveal the mechanism for the influence of compaction water content on stiffness anisotropy, the SEM results of specimens CWD and CDD before compression were used to characterise the directional distributions of soil particles/aggregates. Particles/aggregates observed in the SEM images were manually traced and marked with lines to determine their length and orientation (e.g., Chow et al., 2019). Barton (1974) suggested that at least 400-500 particles should be identified to provide a representative fabric orientation. Accordingly, around 60 images were captured, and approximately 700-800 particles or aggregates were analysed per specimen.

Figure 3-15 presents the particle/aggregate orientation distributions of the dry and wet of optimum specimens before compression. As expected, uniform directional distributions are identified for both specimens in the horizontal plane. In the vertical plane, particles/aggregates predominantly align horizontally, indicating a preferred horizontal orientation. This horizontally orientated particles/aggregates are induced by the higher stress in the vertical direction than in the horizontal direction during one-dimensional compaction. More importantly, more particles tend to lie horizontally for the dry of the optimum specimen in the vertical plane than the wet of the optimum specimen. The more horizontally orientated fabrics in the dry of optimum specimen result in a greater stiffness anisotropy than the wet of the optimum specimen, as shown in Figure 3-10.

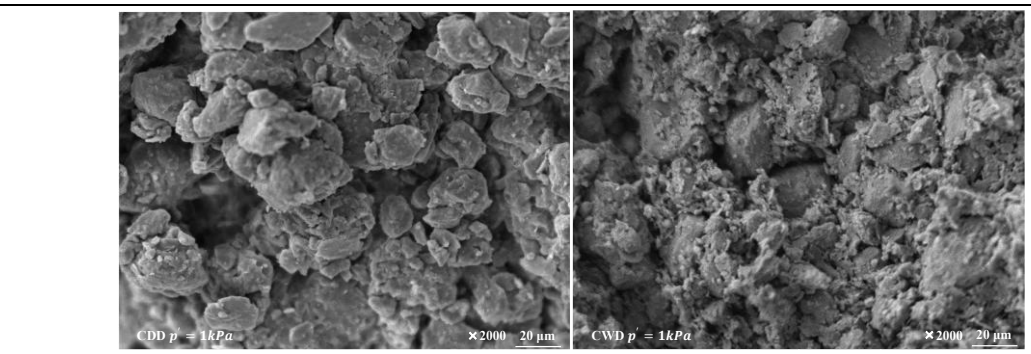

(a)

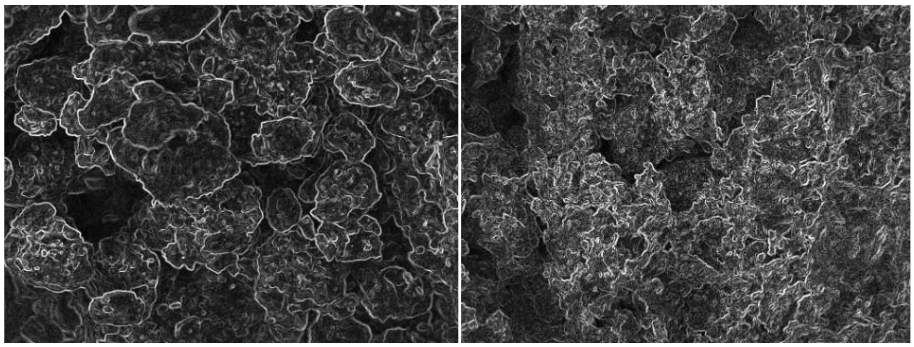

(b)

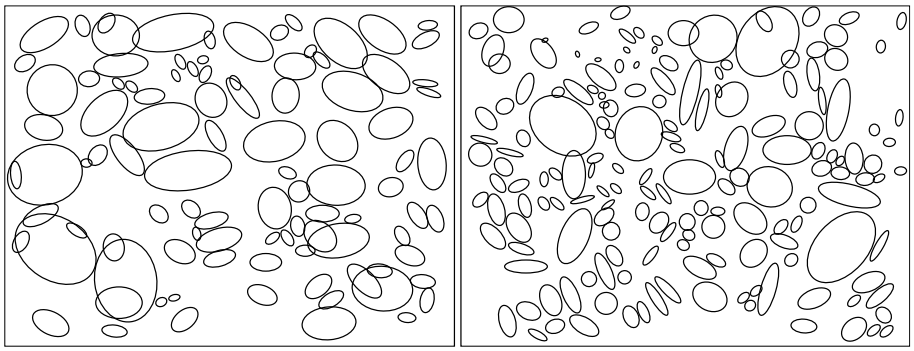

(c)

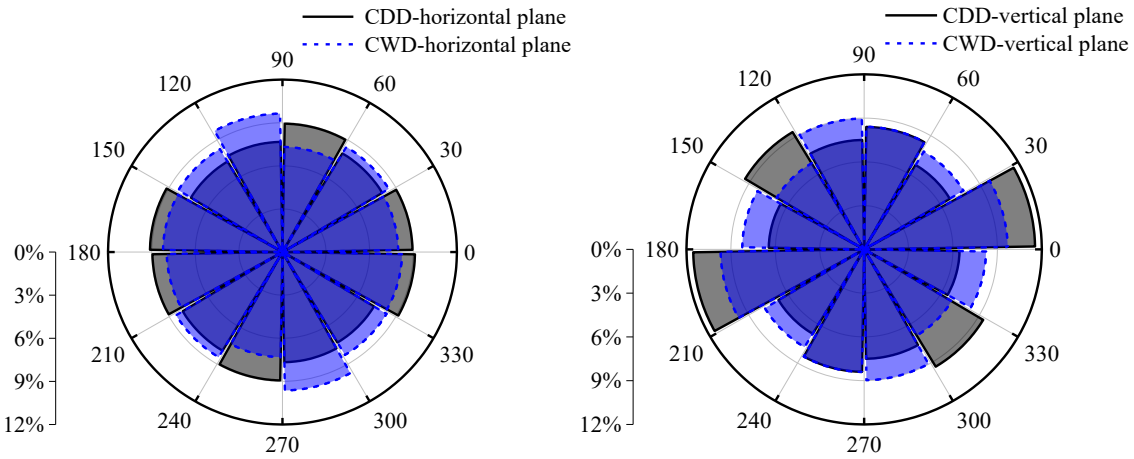

(d)

Figure 3-15. Directional distributions of particles/aggregates for specimens CDD and CWD before compression: (a) SEM images; (b) edge identifications; (c) ellipse fittings; (d) wind rose figures

3.4 Discussion about the structure effects on stiffness evolution

As demonstrated in earlier sections, soil structure plays a crucial role in determining stiffness. Based on the above results, the ratio of normalised stiffness $[G_{hv}/f(e)]_i/[G_{hv}/f(e)]_j$ is calculated, where the subscriptions "i" and "j" refer to the specimens with initially larger and smaller $G_{hv}/f(e)$, respectively. Figure 3-16 illustrates the variations of the normalised stiffness ratio against the normalised stress p'/p'_{yi}, where p'_{yi} is the yield stress of the specimen with an initially larger stiffness (i.e., specimen "i"). Comparisons between intact, compacted, and reconstituted specimens, as well as specimens prepared at different compaction conditions, are incorporated. Before compression, the intact specimen has a larger $G_{hv}/f(e)$ than the compacted and reconstituted specimens, and the $G_{hv}/f(e)$ increases with decreasing compaction water content and increasing dry density. However, these three trends are all reversed with increasing stress, with the value of $[G_{hv}/f(e)]_i/[G_{hv}/f(e)]_j$ being larger and smaller than one before and after compression, respectively. Based on the SM, SEM, and MIP results, the trend reversal is most likely because of structure evolutions, where interparticle contacts are more strengthened (e.g., SEM results in Figure 3-5) and pores are more compressed (e.g., MIP results in Figure 3-6) in initially softer specimens than in initially stiffer specimens.

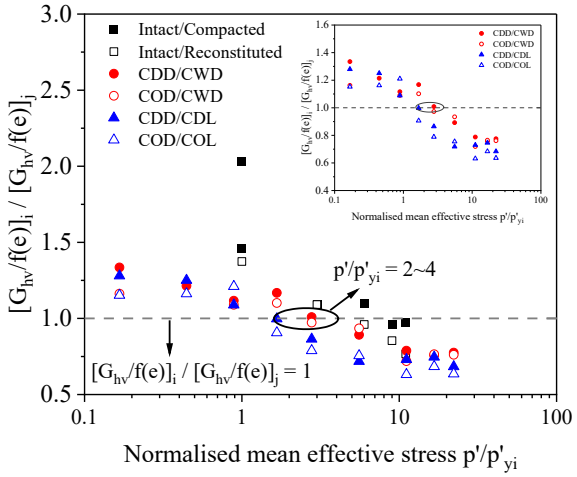

Figure 3-16. Variations of normalised stiffness ratio with normalised mean effective stress

Further inspections of Figure 3-16 show that $[G_{hv}/f(e)]_i/[G_{hv}/f(e)]_j = 1$ is obtained when p'/p'_{yi} falls in the range of 2 to 4. This stress interval aligns with the evolution of

stiffness anisotropy, where stiffness becomes isotropic when the applied stress is approximately three to five times the yield stress, as shown in Figure 3-4(c) and Figure 3-10. The above observations suggest that the soil structure is sufficiently altered at this stress range, leading to substantial changes in both stiffness magnitude and anisotropy.

The comprehensive results demonstrate that the $G_{hv}/f(e)$ of the intact specimen is not always larger than that of the compacted and reconstituted specimens, nor does $G_{hv}/f(e)$ consistently increase with decreasing compaction water content or increasing dry density. As noted in the literature review, inconsistent influence of soil structure on stiffness (i.e., resulting in either a larger or a smaller stiffness value) is observed in previous studies. Based on the above results, one plausible explanation is that prior studies were constrained by limited stress ranges. For instance, Zuo et al. (2024) reported that the $G_{hv}/e^{-1.3}$ of the intact loess was larger than that of the compacted loess. However, the $G_{hv}/e^{-1.3}$ of the compacted loess increased more significantly, resulting in about 100% to 10% smaller $G_{hv}/e^{-1.3}$ than the intact loess as stress increased from 20 to 600 kPa. It is anticipated that the compacted loess may have larger $G_{hv}/e^{-1.3}$ than the intact loess as stress further increases.

Moreover, this study suggests that both A_{hv} and $(n_h + n_v)/2$ in Equation (2-11) vary with structure (see Figure 3-4 and Figure 3-7). The observed variations in A_{hv} and $(n_h + n_v)/2$ indicate that the common assumption in the literature (i.e., only A_{hv} accounts for structure effects while $(n_h + n_v)/2$ is constant and structure-independent) may not be appropriate. One potential method to modify Equation (2-11) with incorporating structure effects is to correlate both A_{hv} and $(n_h + n_v)/2$ with a structure parameter while considering structure evolution with stress. The adoption of structure-dependent parameters is therefore recommended for the prediction of ground movement and the analysis of serviceability limit states in earthen structures.

3.5 Summary and conclusions

This chapter presented the evolutions of anisotropic stiffness and structure of saturated loess during isotropic compression. Both intact loess, reconstituted loess, and compacted loess

with different compaction dry densities and water contents were investigated. The main conclusions are summarised as follows:

Due to its stiffer connector assemblages and oriented particle/aggregate fabric, the intact specimen exhibits approximately twice the $G_{hv}/f(e)$ and more pronounced stiffness anisotropy than the compacted and reconstituted specimens prior to compression. As stress increases, the degradation of connector assemblages in the intact specimen leads to a smaller $G_{hv}/f(e)$ compared to the others, in which interparticle contacts are enhanced under stress. Once the stress exceeds five times the yield stress, all specimens exhibit isotropic stiffness.

Due to the greater compaction effort at a given compaction water content, denser specimens exhibit larger $G_{hv}/f(e)$ and more pronounced stiffness anisotropy prior to compression than looser specimens. The tested loess shows a transitional behaviour, evidenced by the divergence of normal compression lines between looser and denser specimens. With increasing stress, denser specimens attain similar G_{hv} values but maintain lower void ratios compared to looser specimens, leading to smaller $G_{hv}/f(e)$ in the former.

Before compression, $G_{hv}/f(e)$ decreases and stiffness anisotropy diminishes with increasing compaction water content. The reduction in $G_{hv}/f(e)$ is attributed to the stiffer aggregated structure formed at dry of optimum, compared to the clod-dominated structure with inter-clod pores at wet of optimum. The reduced anisotropy is linked to more pronounced particle/aggregate orientation in the aggregated structure. After compression, $G_{hv}/f(e)$ is larger at higher compaction water contents because of greater pore compression.

This study suggests that $G_{hv}/f(e)$ values of initially stiffer specimens become smaller than those of initially softer specimens when the stress reaches 2 to 4 times the yield stress of the former. The trend reversal is likely due to greater strengthening of interparticle contacts and more significant pore compression in the initially softer specimens. These observations provide a plausible explanation for the inconsistent influence of soil structure on stiffness reported in the literature. Additionally, using structure-dependent parameters A_{hv} and $(n_h + n_v)/2$ enhances the reliability of deformation predictions in geotechnical applications.

CHAPTER 4 COUPLED EFFECTS OF SOIL STRUCTURE AND SUCTION ON CYCLIC BEHAVIOUR

This chapter examines the coupled effects of soil structure and suction on the cyclic behaviour of unsaturated loess. The responses of intact and compacted specimens, as well as specimens compacted under different dry densities and water contents, are compared. Particular attention is paid to the accumulation of irreversible strain and resilient modulus, which are important input parameters for pavement designs. The results on structure evolution presented in Chapter 3 are utilised to support the interpretation of the findings.

4.1 Specimen preparation, test apparatus, test program, and test procedures

4.1.1 Specimen preparation

Intact and compacted loess specimens with 76 mm in diameter and 152 mm in height are prepared. The particle size distribution, initial water content (18.9%) and dry density (1.23 g/cm^3) of the compacted specimen are identical to those of the intact specimen, with the primary difference between them being their initial structure. The specimen preparation procedures are detailed in section 3.1.1 and are therefore not reiterated here.

4.1.2 Test apparatus

A suction-controlled triaxial apparatus was utilised, as shown in Figure 4-1. Suction was controlled using the axis-translation technique, where the pore air pressure was applied to the top cap, and the pore water pressure was controlled through the base pedestal equipped with high air entry value (AEV = 200 kPa) ceramic disc. During testing, the air dissolved in the water and passing through the ceramic disc was flushed out and collected at 24-hour intervals. The volume of collected air was used to correct the water content measurements of the specimen.

In addition to a conventional external linear variable differential transformer (LVDT), the apparatus was equipped with internal LVDTs for the measurement of local soil deformation.

These internal LVDTs are expected to provide more accurate strain measurements than the external LVDT because bedding errors and system compliance can be eliminated (Ng and Yung, 2008). During cyclic loading, the specimen deformation was recorded, and the variation in specimen diameter was corrected based on these internal LVDTs.

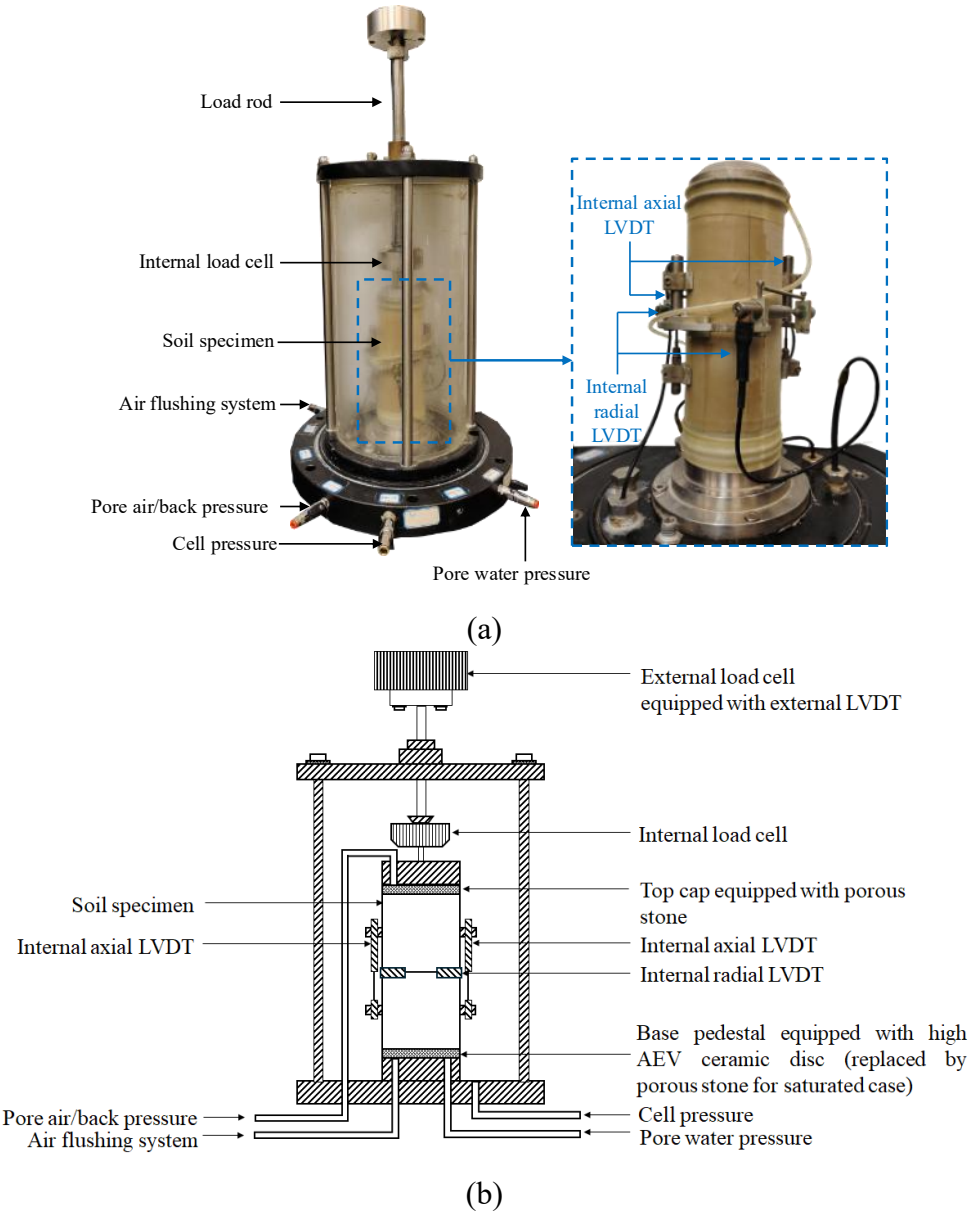

Figure 4-1. Triaxial apparatus for cyclic test: (a) overview; (b) schematic diagram

4.1.3 Test program

Two series of cyclic triaxial tests were conducted. The first series examined the cyclic behaviour of intact and compacted loess specimens prepared with identical initial dry density (1.23 g/cm^3) and water content (18.9%), while the second series focused on compacted

specimens prepared under two dry densities (1.23 g/cm^3 and 1.59 g/cm^3) and two water contents (15.2% and 18.9%).

Table 4-1. Test program for cyclic triaxial tests of intact and compacted specimens

Test ID*	Suction s_0: kPa	Confining pressure p_{c0}: kPa	Degree of saturation before cyclic loading	Void ratio before cyclic loading	Cyclic deviatoric stress q_{cyc}: kPa (cyclic stress ratio $q_{cyc}/2p_{c0}$)
CS0P30	0	30	1.00	0.79	15, 24, 30, 36, 48
IS0P30			1.00	1.15	(0.25, 0.4, 0.5, 0.6, 0.8)
CS0P60		60	1.00	0.74	30, 48, 60, 72, 96
IS0P60			1.00	1.01	(0.25, 0.4, 0.5, 0.6, 0.8)
CS10P30	10	30	0.63	0.98	15, 24, 30, 36, 48
IS10P30			0.73	1.14	(0.25, 0.4, 0.5, 0.6, 0.8)
CS30P30	30	30	0.48	1.07	15, 24, 30, 36, 48
IS30P30			0.52	1.16	(0.25, 0.4, 0.5, 0.6, 0.8)
CS30P60		60	0.53	0.96	30, 48, 60, 72, 96
IS30P60			0.54	1.13	(0.25, 0.4, 0.5, 0.6, 0.8)

*Notation in Test ID: "C" represents a compacted specimen; "I" indicates an intact specimen, "S" is the suction; "P" is the confining pressure; and the numbers after "S" and "P" denote the suction and confining pressure values in kPa, respectively. Zero suction indicates that the specimen is fully saturated under back pressure, with a B value greater than 0.98.

In the first series, the values of suction, confining pressure, degree of saturation, void ratio, and cyclic deviatoric stress, are summarised in Table 4-1. Note that the confining pressure refers to the effective confining pressure (i.e., the difference between total confining pressure and pore water pressure) under saturated conditions, and represents the net confining pressure (i.e., the difference between total confining pressure and pore air pressure) under unsaturated conditions. Three suctions (i.e., 0, 10, and 30 kPa) and two confining pressures (i.e., 30 and 60 kPa) were considered. At a confining pressure of 30 kPa, these suction values correspond to degrees of saturation of 1.00, 0.73, and 0.52 for intact specimens and 1.00, 0.63, and 0.48 for compacted specimens, respectively. Therefore, the relatively wide range of degree of saturation facilitates the investigation of the effects of unsaturation on cyclic behaviour. The selection of these two confining pressures serves two purposes. First, the recommended range of confining pressure for subgrade soils is between 2 and 6 psi (14 to 41 kPa) (AASHTO, 2021). Hence, the confining pressure of 30 kPa is close to the median of this range, while the other is double the

pressure (i.e., 60 kPa). Second, these pressures can highlight the influence of structure degradation on cyclic behaviour under saturated conditions. As shown in Figure 3-3(a), the yield stress of the saturated intact specimen is 35 kPa, which falls within the range of 30 to 60 kPa. It is expected that the soil structure of the saturated intact specimen is well preserved at p_{c0} = 30 kPa, whereas obvious structure degradation occurs at p_{c0} = 60 kPa.

Table 4-2. Test program for cyclic triaxial tests of compacted specimens

Test ID*	Compaction water content w: %	Compaction dry density ρ_d: g/cm^3	Suction before cyclic loading s_0: kPa	Degree of saturation before cyclic loading	Void ratio before cyclic loading
COD-S0	15.2	1.59	0	1.00	0.66
COD-S10			10	0.87	0.67
COD-S30			30	0.65	0.68
CWD-S0	18.9	1.59	0	1.00	0.66
CWD-S10			10	0.86	0.67
CWD-S30			30	0.73	0.67
CWL-S0	18.9	1.23	0	1.00	0.79
CWL-S10			10	0.63	0.98
CWL-S30			30	0.48	1.07

*Notation in Test ID: "C" stands for the compacted specimen; "O" and "W" indicate that the specimens were compacted at the optimum and wet of optimum water contents, respectively; "L" and "D" represent the looser and denser states, respectively; "S" denotes the initial suction before cyclic loading; and the number after "S" is the suction value in kPa. The initial confining pressures of all specimens are 30 kPa.

The test program for the second series is illustrated in Table 4-2. Two compaction dry densities (1.23 g/cm^3 and 1.59 g/cm^3) and two water contents (15.2% and 18.9%) were considered, resulting in the preparation of three series of compacted specimens (CWL, CWD, and COD). These water contents correspond to the optimum and wet of optimum water contents, respectively. The two dry densities represent degrees of compaction of 70% (looser state) and 90% (denser state), respectively. Therefore, the series names refer to specimens compacted at the optimum water content and a relatively dense state (COD), wet of optimum and a relatively dense state (CWD), and wet of optimum and a relatively loose state (CWL), respectively. Note that the degree of compaction for denser specimens is slightly higher than that used in Chapter 3 (i.e., 85%). Within the three series, the differences between COD and

CWD series highlight the effects of compaction water content, while the comparisons between CWD and CWL series reveal the impacts of compaction dry density. Consistent with the first series, three suctions (0, 10, and 30 kPa) were considered. These suctions correspond to degrees of saturation ranging from 0.65 to 1.00 for the COD series, 0.73 to 1.00 for the CWD series, and 0.48 to 1.00 for the CWL series, respectively. The selected suctions are relatively low to reflect a more humid climate in the field (McCartney and Khosravi, 2013), which is particularly critical to the performance of geo-structures. The initial confining pressure was set as 30 kPa.

Each specimen was subjected to one-way multi-stage cyclic loading with a haversine waveform. Five cyclic stress ratio (CSR) levels (0.25, 0.4, 0.5, 0.6, and 0.8) were chosen with reference to existing guidelines and studies (Cai et al., 2018; AASHTO, 2021). The CSR represents the ratio of cyclic deviatoric stress to twice the confining pressure (i.e., $q_{cyc}/2p_{c0}$). The selected CSR range (0.25 to 0.8) is expected to induce significant strain in the intact specimen, thereby revealing the influence of structure degradation on cyclic behaviour. The obtained dataset is valuable for understanding soil behaviour and validating theoretical models. Note that the CSR magnitudes are the same for the specimen under different confining pressures, and thus the cyclic deviatoric stress at p_{c0} of 60 kPa is twice that at p_{c0} of 30 kPa. Each specimen was subjected to 1000 loading cycles at each CSR level, with a total of 5000 cycles applied unless failure was observed. Many criteria have been proposed to define specimen failure during cyclic loading, such as the achievement of zero mean effective stress (Karam et al., 2009), the attainment of a 5% peak vertical strain (Sze and Yang, 2014), and an abrupt increase in both volumetric and vertical strains (Cui et al., 2007). In the present study, specimen failure was concluded when two conditions were satisfied simultaneously: the strain increment per cycle increased with the number of cycles, and the accumulated permanent vertical strain exceeded 10%. A loading frequency of 0.2 Hz was adopted to ensure stable control of vertical stress.

4.1.4 Test procedures

Three stages were involved for each specimen: suction equalisation, isotropic

compression, and cyclic loading. When the specimen was set up in the triaxial cell, its suction was controlled to the target value. The suction equalisation was finished when the daily water content variation was less than 0.04% (Sivakumar, 1993), which typically took about 7 days. Afterwards, the soil specimen was subjected to isotropic compression with a loading rate of 1 kPa per hour (Kaewsong, 2017). When the targeted confining pressure was reached, the pressure was maintained for about 48 hours to ensure the stabilisation of water and volume change (Cui and Delage, 1996). Subsequently, the soil specimen was subjected to cyclic loading. During this stage, the drainage valve for pore air was open. The excess pore air pressure is expected to be negligible due to air's high compressibility and permeability. The influence of air drainage condition is considered negligible for tests exhibiting relatively small volumetric strains (e.g., high suction and low cyclic deviatoric stress) due to minimal variation in pore air pressure. In contrast, for tests with relatively large volumetric strains, compression of the air phase generates higher pore air pressures and suctions, resulting in a more resistant response under air-undrained conditions compared to air-drained conditions. Note that the AASHTO (2021) standard for testing subgrade soil recommends opening the water drainage valve. Given the low permeability of the tested fine-grained loess, especially at unsaturated conditions, water drainage under cyclic loading would be limited even though the drainage valve is open. Consequently, in the current study, the water drainage valve for pore water was closed with the measurement of excess PWP. This is a constant water content condition to achieve a simple drainage condition, which makes the data analysis easier.

4.2 Isotropic compression curves and water retention curves

To facilitate the interpretations of cyclic triaxial test results, the isotropic compression behaviour and soil water retention curves were measured.

4.2.1 Isotropic compression curves under various suctions

Figure 4-2(a) shows the isotropic compression curves of intact and compacted specimens, and the loading collapse curves are presented in Figure 4-2(b). Note that the compacted specimen at s = 30 kPa was compressed only to 60 kPa, as it was subsequently subjected to

cyclic loading (i.e., specimen CS30P60 in Table 4-2). At a given suction, the intact specimen sustains a higher void ratio at a given stress and exhibits a higher isotropic yield stress than the compacted specimen, consistent with findings in the literature (e.g., Burland, 1990; Xu and Coop, 2016; Mu et al., 2023a). This difference is attributed to the stiffer soil skeleton in the intact specimen, as explained in Chapter 3. As suction increases from 0 to 50 kPa, the yield stresses of intact and compacted specimens increase from 35 to 80 kPa and from 1 to 37 kPa, respectively. Moreover, the intact specimen at zero suction exhibits greater post-yielding compressibility ($\lambda(0)$ = 0.15) than the compacted specimen ($\lambda(0)$ = 0.07), but the difference diminishes at a suction of 50 kPa. This difference is likely because the influence of suction on compressibility is more pronounced in the compacted specimen, compensating for the effects of soil structure. Similar findings have been reported in the literature (Mu et al., 2020; Xu et al., 2021a). For example, Xu et al. (2021a) found that the compression index of compacted loess increased from 0.23 to 0.42 as suction increased from 0 to 100 kPa, whereas the compression index of intact loess remained nearly constant under the same suction changes.

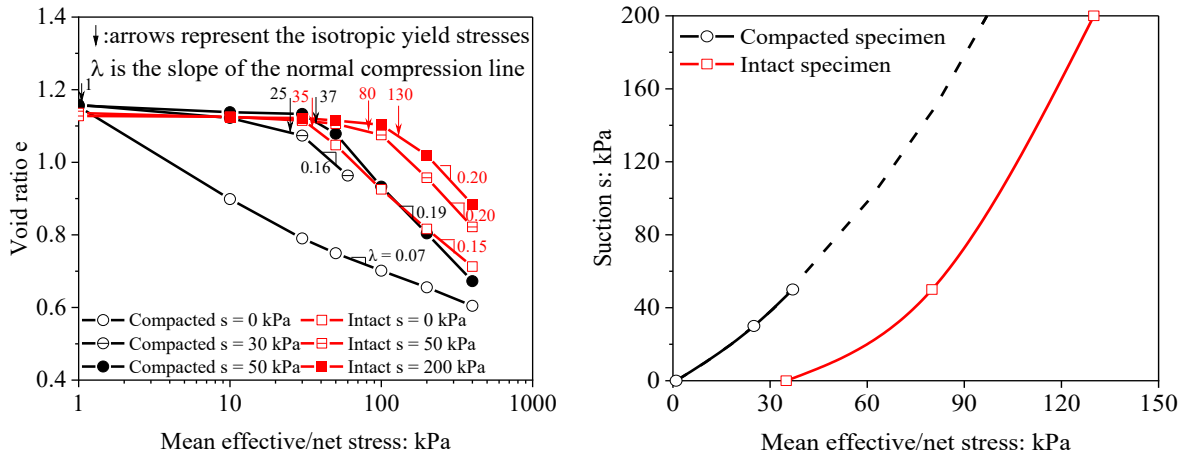

(a) (b)

Figure 4-2. Isotropic compression behaviour of intact and compacted specimens: (a) isotropic compression curves; (b) loading collapse curves

The isotropic compression curves of fully saturated compacted specimens (COD-S0, CWD-S0, and CWL-S0) are presented in Figure 4-3. As expected, the denser specimen CWD-S0 (100 kPa) has a higher isotropic yield stress than the looser specimen CWL-S0 (1 kPa). Moreover, at a given dry density, the specimen compacted at the optimum water content (COD-

S0, 130 kPa) exhibits a higher yield stress than that compacted at the wet of optimum (CWD-S0, 100 kPa). Similar results have been widely observed in the literature, such as those of Xu and Coop (2017) for low-plasticity clay and Oualmakran et al. (2016) for clayey silt. The observed influence of compaction water content on yield stress can be attributed to the distinct soil structures developed during compaction. As shown in Chapter 3, increasing the compaction water content converts the aggregated structure to a structure featured by clods and extra-large inter-cold pores. Due to the existence of inter-clod pores, the specimen compacted at the wet of optimum exhibits a softer soil skeleton than that compacted at the optimum water content, resulting in a lower yield stress in the former.

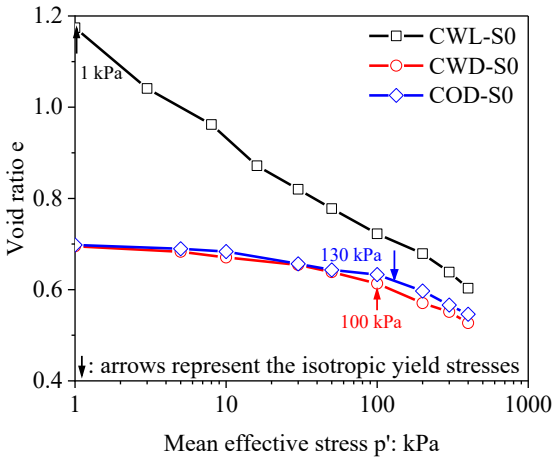

Figure 4-3. Isotropic compression curves of compacted specimens prepared at different compaction conditions

4.2.2 Soil water retention curves

Figure 4-4 presents the soil water retention curves of intact and compacted specimens, both having an initial void ratio of about 1.15. The specimens were wetted to zero suction and then subjected to a drying-wetting cycle under a mean net stress of 3 kPa. Along the drying path, the specimens are expected to follow the main drying curve. However, the wetting process may follow a scanning curve because the applied suction range (0 to 100 kPa) does not reach the residual state. During drying, the intact and compacted specimens have nearly identical air entry suction (i.e., approximately 3 kPa). Afterwards, the degree of saturation of the compacted specimen decreases significantly due to the presence of extra-large inter-clod pores (see Figure 3-9), and the intact specimen shows a higher degree of saturation when the suction is between

3 and 50 kPa. When suction exceeds 50 kPa, the intact specimen exhibits a lower degree of saturation, due to a higher desorption rate associated with its dominant 8 μm pore structure (see Figure 3-6). A similar trend is observed during wetting.

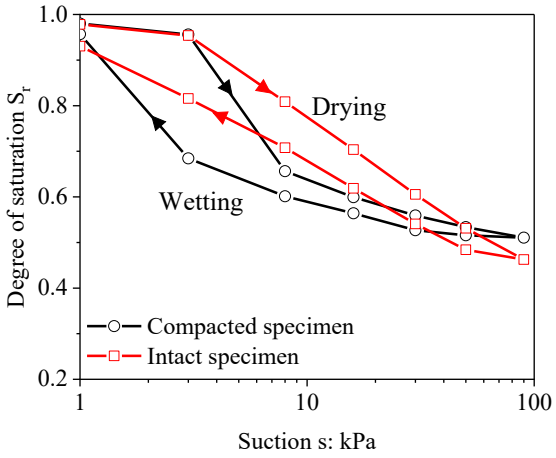

Figure 4-4. Soil water retention curves of intact and compacted specimens

Figure 4-5 presents the measured soil water retention curves for specimens COD (e_0 = 0.68), CWD (e_0 = 0.68), and CWL (e_0 = 1.15) subjected to a wetting-drying cycle under a mean net stress of 3 kPa, starting from their as-compacted states.

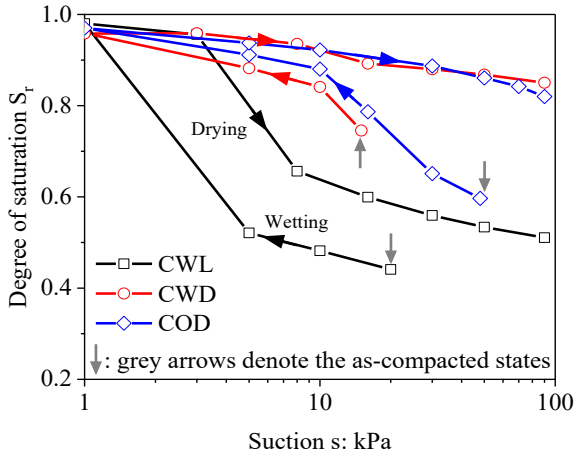

Figure 4-5. Soil water retention curves of compacted specimens prepared at different compaction conditions

At a given suction, the specimen CWD exhibits a lower degree of saturation than the specimen COD during wetting. This observation is consistent with Ng and Peprah-Manu (2023) for compacted silty sand but different from others (Tinjum et al., 1997; Vanapalli et al., 1999; Ng and Pang, 2000a; Birle et al., 2008). This discrepancy arises because in both this study and

that of Ng and Peprah-Manu (2023), the specimen compacted at the wet of optimum exhibits extra-large inter-clod pores, which causes weaker water retention capacity than that compacted at a lower water content. During the drying process, the degree of saturation of these two specimens (CWD and COD) is comparable, possibly because the applied suction (between 0 and 100 kPa) has not reached the main desorption range. Moreover, the degree of saturation for specimen CWD is consistently higher than that of specimen CWL at a given suction, primarily due to the stronger water retention capacity at a lower void ratio (Ng and Pang, 2000b; Gallipoli et al., 2003b; Zhou and Ng, 2014).

4.3 Comparisons of the cyclic behaviour of intact and compacted specimens

4.3.1 Typical cyclic behaviour

Figure 4-6 presents typical cyclic behaviour obtained from specimens CS30P30 and IS30P30. Figure 4-6(a) shows the stress-strain curves for the first cycle under CSRs of 0.25, 0.5, and 0.8. For clarity, the results for CSRs of 0.4 and 0.6 are omitted in the figure. It is evident that the compacted specimen exhibits a larger hysteresis loop than the intact specimen at a given CSR. Figure 4-6(b) shows that for a given CSR, permanent vertical strain accumulates with the number of cycles at a decreasing rate, suggesting that the soil approaches a stable state. Figure 4-6(c) demonstrates that the variation of resilient modulus with the number of cycles is CSR-dependent, with negligible change at low CSRs and pronounced variation at higher CSRs. Furthermore, due to the variation in cyclic deviatoric stress and the nonlinear stress-strain behaviour of soil, the resilient modulus exhibits abrupt changes as CSR varies, as noted by previous studies (e.g., Sivakumar et al., 2013). Figure 4-6(d) illustrates the variation in suction during cyclic loading. For both intact and compacted specimens, suction decreases with the increasing number of cycles and CSR, consistent with findings from previous studies on unsaturated soils (Karam et al., 2009; Sivakumar et al., 2013; Kumar et al., 2022; Azizi et al., 2023). Moreover, the suction reduction in the intact specimen is less than that in the compacted specimen, possibly due to the smaller accumulated strain in the former.

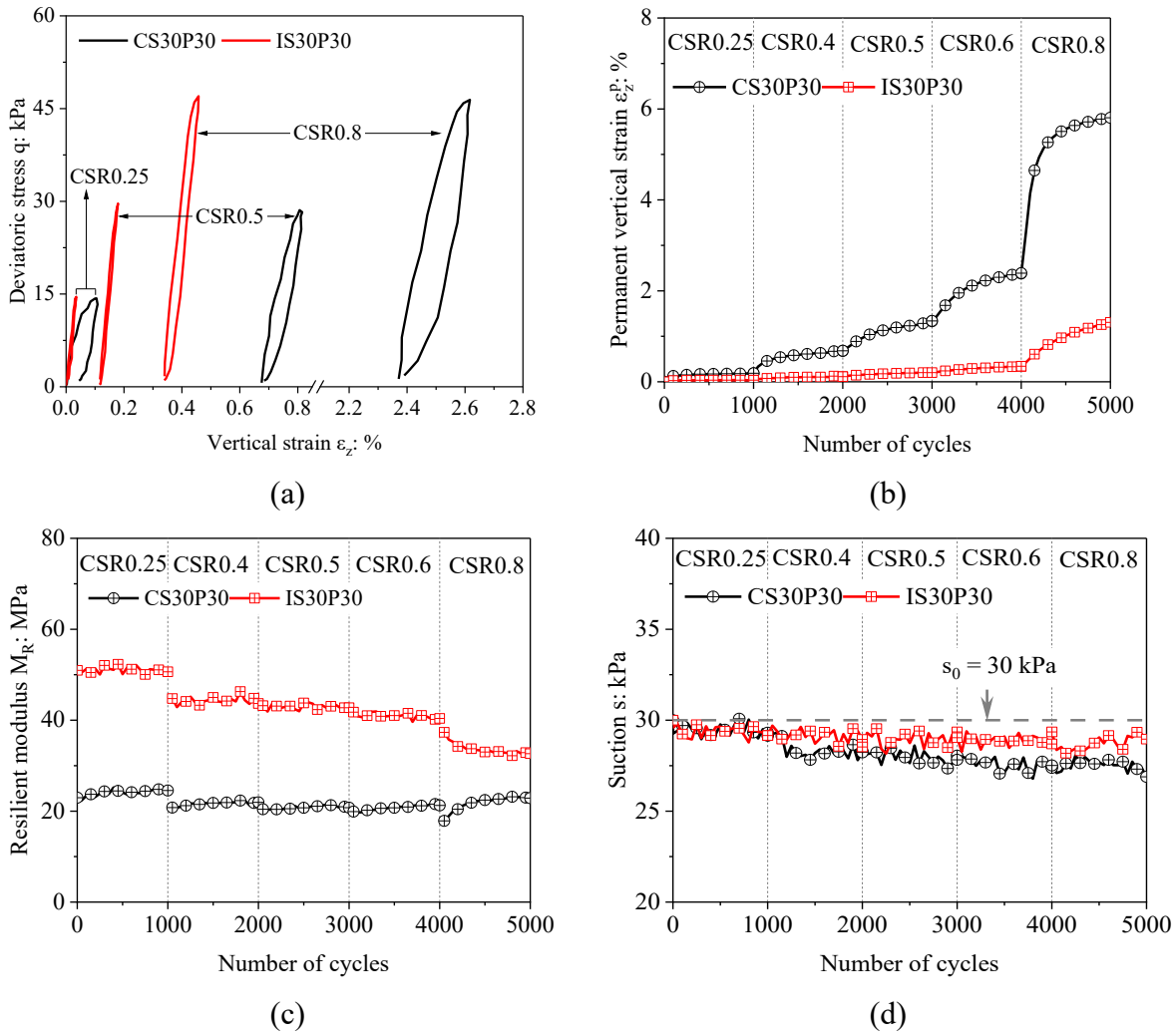

Figure 4-6. Typical cyclic behaviour obtained from specimens CS30P30 and IS30P30: (a) stress-strain curves of the first cycle; (b) permanent vertical strains; (c) resilient moduli; (d) suction variations

4.3.2 Cyclic behaviour of saturated soils under various confining pressures

Figure 4-7 compares the cyclic behaviour of saturated intact and compacted specimens (i.e., IS0P30 and CS0P30) under a CSR of 0.25. The normalised excess PWP, permanent vertical strain, and resilient modulus are shown in Figure 4-7(a), (b), and (c), respectively. It can be observed that excess PWP and permanent vertical strain increase, while resilient modulus decreases with the number of cycles. For the compacted specimen, failure occurs after approximately 70 cycles, at which the permanent vertical strain increases exponentially with the number of cycles. In contrast, the intact specimen is more resistant to cyclic loading in this stress condition, as evidenced by its smaller excess PWP and permanent vertical strain. For instance, in the first cycle, the intact specimen exhibits about 10% smaller excess PWP and 70%

smaller permanent vertical strain than the compacted specimen. Similar results were also reported in previous studies, such as Jana and Stuedlein (2021) for alluvial plastic silt. The differences arise because the intact specimen has a stiffer soil skeleton than the compacted specimen, as observed in the SEM results shown in Figure 3-5. At a confining pressure of 30 kPa, the stiffer soil skeleton is well preserved due to the limited volumetric strain (about 0.8% at 30 kPa, as shown in Figure 4-2). Consequently, the intact specimen shows greater resistance to cyclic loading than the compacted specimen.

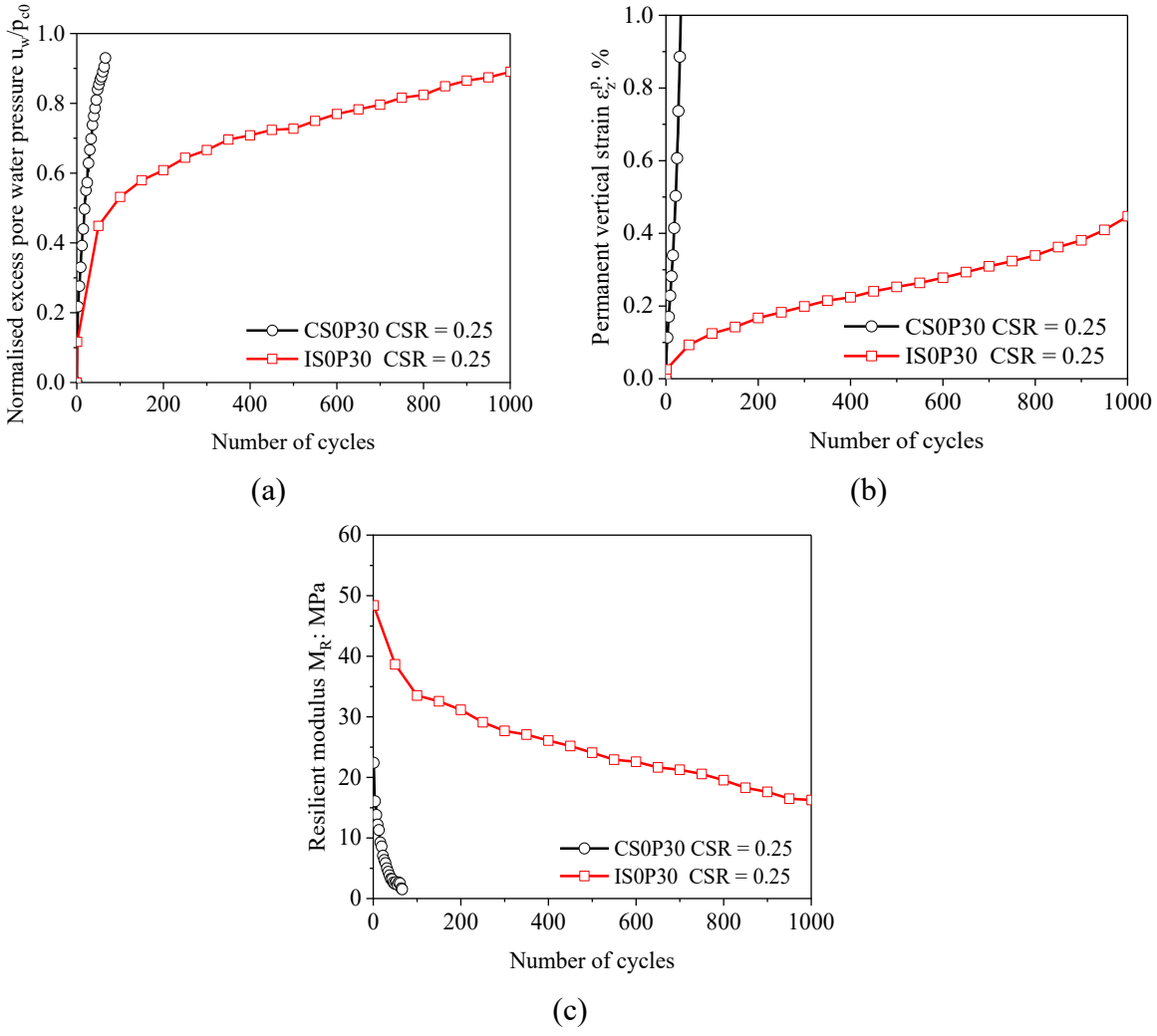

Figure 4-7. Cyclic behaviour of saturated intact and compacted specimens under p_{c0} = 30 kPa: (a) normalised excess PWPs; (b) permanent vertical strains; (c) resilient moduli

Figure 4-8 illustrates the cyclic behaviour of saturated compacted (CS0P60) and intact (IS0P60) specimens under a confining pressure of 60 kPa with a CSR of 0.25. In the first 10 cycles, the intact specimen shows larger excess PWP and permanent vertical strain than the

compacted specimen. Afterwards, opposite results are observed, with smaller excess PWP and permanent vertical strain identified in the intact specimen. For example, the intact specimen shows 110% larger excess PWP and 250% larger permanent vertical strain than the compacted specimen at the first cycle. Conversely, after 40 cycles, the excess PWP and permanent vertical strain of the former are about 5% and 85% smaller than those of the latter, respectively. Similar trends can be identified from Wijewickreme and Sanín (2008) for intact and reconstituted low-plastic Fraser River silt. Their results showed that the intact specimen exhibited a larger excess PWP during the first cycle, whereas in subsequent cycles the reconstituted specimen developed a larger excess PWP than the intact specimen.

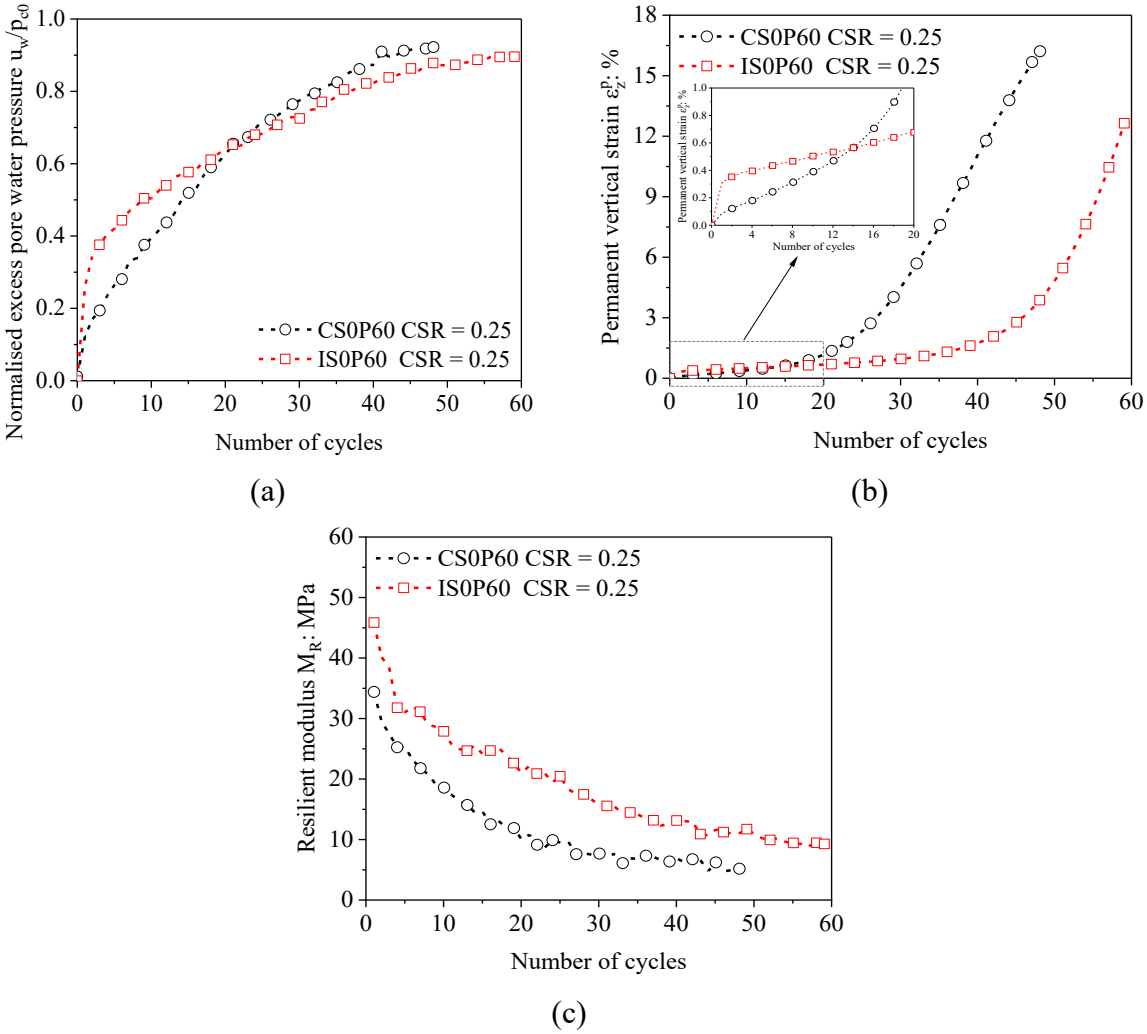

Figure 4-8. Cyclic behaviour of saturated intact and compacted specimens under p_{c0} = 60 kPa: (a) normalised excess PWPs; (b) permanent vertical strains; (c) resilient moduli

The phenomena observed in Figure 4-8(a) and (b) are closely related to the influence of

structure degradation. At a confining pressure of 60 kPa, the intact specimen is in a normally consolidated state, and structure degradation occurs as shown in Figure 3-5. Due to the structure degradation induced additional plastic deformation, the intact specimen is more contractive than the compacted specimen, as evidenced by its higher post-yielding compressibility (see Figure 4-2). This more contractive behaviour in the intact specimen has also been observed in static triaxial shearing studies (e.g., Liu and Carter, 2002; Mu et al., 2023a). Consequently, the more contractive behaviour leads to larger excess PWP and permanent vertical strain in the intact specimen during the first 10 cycles. As loading continues, the compacted specimen is susceptible to failure due to its less stable structure. This observation aligns with the findings in silts by Jana and Stuedlein (2021) and Wijewickreme and Sanín (2008), who reported that fewer cycles were required for the reconstituted specimen to reach failure than the intact specimen. Therefore, the compacted specimen shows larger excess PWP and permanent vertical strain than the intact specimen after approximately 20 cycles. The results indicate that, despite experiencing structure degradation, the intact specimen retains a more stable skeleton than the compacted specimen during cyclic loading.

Figure 4-8(c) presents the variations of resilient modulus with the number of cycles. The resilient modulus decreases for both intact and compacted specimens due to the accumulation of excess PWP. More importantly, the resilient modulus of the intact specimen is consistently larger than that of the compacted specimen at a given cycle, which differs from the structure effects on permanent vertical strain. This is likely because the soil structure affects the reversible and irreversible strains of the intact specimen through different mechanisms. The permanent vertical strain (corresponding to irreversible strain) is mainly affected by structure degradation, which is associated with plastic deformation (Baudet and Stallebrass, 2004; Zhou and Ng, 2018). In contrast, the resilient modulus (related to reversible strain) is dominated by interparticle contacts. Since the intact specimen maintains a more stable soil skeleton during cyclic loading, it consistently shows a larger resilient modulus than the compacted specimen.

Based on the results presented in Figure 4-7 and Figure 4-8, the yield stress of the intact specimen can be considered as a threshold for differentiating the structure effects on cyclic

behaviour. When confining pressure is below this threshold, intact specimens exhibit smaller excess PWP and permanent vertical strain than compacted specimens. Conversely, when confining pressure exceeds the threshold, intact specimens may have larger excess PWP and permanent vertical strain due to significant structure degradation. Moreover, intact specimens exhibits greater resistance to cyclic loading than compacted specimens irrespective of the magnitude of confining pressure, as demonstrated by the greater number of cycles required to reach failure in the former, similar to observations in the literature (e.g., Wijewickreme and Sanín, 2008; Jana and Stuedlein, 2021).

4.3.3 Cyclic behaviour of unsaturated soils under confining pressure of 30 kPa

Figure 4-9 presents the permanent vertical strains of unsaturated intact and compacted specimens under a confining pressure of 30 kPa, obtained from specimens CS10P30, IS10P30, CS30P30, and IS30P30. Figure 4-9(a) shows the variations of permanent vertical strain with the number of cycles. It is evident that an increase in suction leads to a reduction in permanent vertical strain, as the corresponding increases in Bishop's stress and normal force between soil particles stabilise the soil skeleton (Alonso et al., 1990; Gallipoli et al., 2003a). Furthermore, at a given suction and CSR, the intact specimen exhibits a smaller permanent vertical strain than the compacted specimen. This can be attributed to the applied stress being below the yield stress of the intact specimen (see the LC curves in Figure 4-2), whose stiffer initial structure results in a smaller permanent vertical strain.

Figure 4-9(b) illustrates the variations of permanent vertical strain with CSR. The results from the last cycle under different CSRs are presented. It can be observed that the structure effects on permanent vertical strain are suction- and CSR-dependent. At a suction of 10 kPa, the difference in permanent vertical strain between intact and compacted specimens increases with CSR from 0.25 to 0.5 but decreases slightly as CSR rises from 0.5 to 0.6. In contrast, at a suction of 30 kPa, the strain difference continues to increase with CSR. To reveal the suction- and CSR-dependent structure effects, the strain increment per cycle for intact and compacted specimens are calculated and given in Figure 4-10.

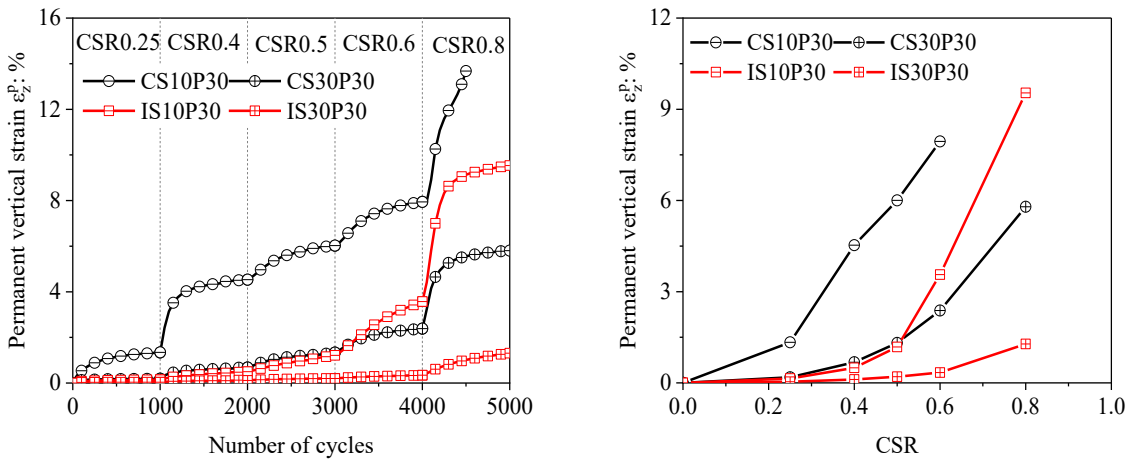

Figure 4-9. Permanent vertical strains of unsaturated intact and compacted specimens under p_{c0} = 30 kPa: (a) variations with the number of cycles; (b) variations with CSR

Figure 4-10(a) shows that under a suction of 10 kPa, the intact specimen has a smaller strain increment per cycle than the compacted specimen at CSRs of 0.25 and 0.4. For CSRs of 0.5 and 0.6, the strain increment in the intact specimen becomes larger after several hundred cycles because of structure degradation induced additional strain. A similar trend is also identified under a suction of 30 kPa in Figure 4-10(b). The intact specimen shows smaller strain increments per cycle for CSRs between 0.25 and 0.6, but at a CSR of 0.8, its strain increment exceeds that of the compacted specimen after several hundred cycles. Additionally, under 10 kPa suction and CSR of 0.8, the intact specimen initially has a smaller strain increment per cycle than the compacted specimen. However, the compacted specimen shows a 'V'-shaped trend in strain increment over cycles (i.e., specimen failure) and eventually shows a larger strain increment than the intact specimen, consistent with the observations in Figure 4-8(b).

According to the results in Figure 4-7, Figure 4-8, and Figure 4-10, the structure effects on permanent vertical strain can be categorised as two types based on the strain increment at the first cycle (i.e., $\Delta\varepsilon_{z,1}^p$). Type I indicates that the intact specimen has a smaller $\Delta\varepsilon_{z,1}^p$ than the compacted specimen (e.g., at a suction of 10 kPa and a CSR of 0.25), while type II refers to a larger $\Delta\varepsilon_{z,1}^p$ in the intact specimen (e.g., at a suction of 10 kPa and a CSR of 0.8). According to the earlier discussion, type I is attributed to the inherently stiffer structure of the intact specimen, while type II is caused by the structure degradation-induced plastic

deformation in the intact specimen. To differentiate these two types, the yield stress of the intact specimen may serve as a threshold, given that significant structure degradation is observed once the intact specimen reaches its yield state. More importantly, the trend in strain increment may change with the number of cycles in both types. In type I, the strain increment of the intact specimen may exceed that of the compacted specimen due to ongoing structure degradation (e.g., at a suction of 10 kPa and a CSR of 0.6). In type II, the strain increment of the intact specimen could become smaller because of failure in the compacted specimen (e.g., at a suction of 10 kPa and a CSR of 0.8).

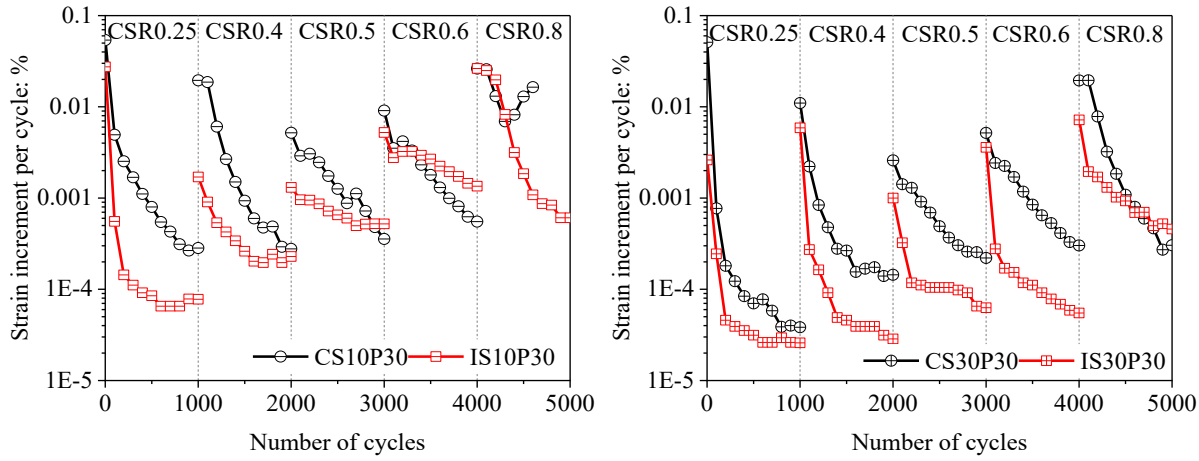

Figure 4-10. Strain increments per cycle of unsaturated intact and compacted specimens under p_{c0} = 30 kPa: (a) s_0 = 10 kPa; (b) s_0 = 30 kPa

Consequently, the CSR- and suction-dependent structure effects observed in Figure 4-9(b) can be explained by the two types of behaviour. At relatively low suction and high CSR, the intact specimen may have a larger strain increment than the compacted specimen due to structure degradation, thereby diminishing their difference in permanent vertical strain as CSR increases (e.g., with CSR from 0.5 to 0.6 at 10 kPa suction). In contrast, at relatively high suction and low CSR, the intact specimen consistently has a smaller strain increment than the compacted specimen, leading to a larger difference in permanent vertical strain with increasing CSR (e.g., with CSR from 0.25 to 0.4 at 30 kPa suction).

Figure 4-11 shows the resilient moduli of unsaturated intact and compacted specimens under a confining pressure of 30 kPa (i.e., CS10P30, IS10P30, CS30P30, and IS30P30). Figure

4-11(a) presents the variations of resilient modulus with the number of cycles. It is evident that the variation of resilient modulus with the number of cycles is different between intact and compacted specimens. For the compacted specimen, the resilient modulus increases slightly with the number of cycles at a given CSR due to soil densification. For example, the resilient modulus of specimen CS10P30 increases from 20.5 MPa to 23.5 MPa after 1000 cycles at a CSR of 0.25. For the intact specimen, the variation of resilient modulus with the number of cycles is influenced by both suction and CSR. Under relatively high suction and low CSR (e.g., s_0 = 30 kPa and CSR = 0.25), the resilient modulus remains nearly constant with the number of cycles, due to limited plastic deformation (see Figure 4-9) and insignificant structure degradation. However, when CSR exceeds 0.5 at 10 kPa suction or CSR reaches 0.8 at 30 kPa suction, a significant reduction in resilient modulus occurs, accompanied by a significant increase in permanent vertical strain, as shown in Figure 4-9. These observations suggest that the reduction in resilient modulus is attributed to plastic strain-related structure degradation.

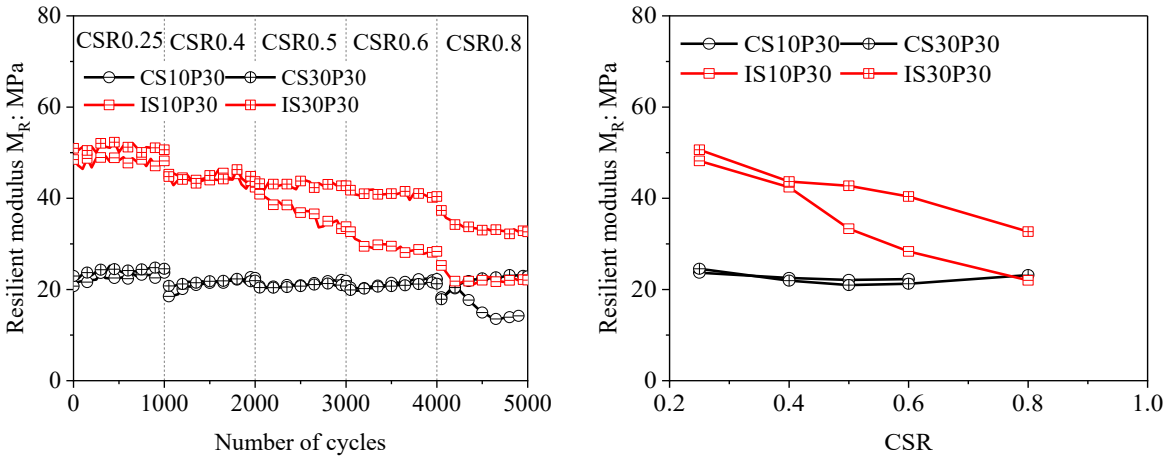

Figure 4-11. Resilient moduli of unsaturated intact and compacted specimens under p_{c0} = 30 kPa: (a) variations with the number of cycles; (b) variations with CSR

Figure 4-11(b) presents the resilient moduli at the last cycle under various CSRs. The variation in resilient modulus with CSR and suction is notably different between intact and compacted specimens. For the compacted specimen, resilient modulus shows minimal variation with CSR and suction, likely because soil densification compensates the effects of increased deviatoric stress and decreased suction. In the intact specimen, however, the resilient

modulus decreases as CSR increases, with more significant reduction at a lower suction because of more significant structure degradation. Therefore, the resilient modulus of the intact specimen is larger than that of the compacted specimen at a given stress state, and the difference diminishes with increasing CSR and decreasing suction. For instance, at a suction of 30 kPa, the intact specimen exhibits twice the resilient modulus of the compacted specimen under a CSR of 0.25. However, when the CSR increases to 0.8, this difference reduces to 40%. A similar pattern was found in the small-strain stiffness of Gault clay (Pennington et al., 1997) and the shear modulus during triaxial shearing of loess (Ng et al., 2017), where the intact specimen had a larger modulus than the compacted specimen, but the difference decreased with structure degradation.

4.3.4 Cyclic behaviour of unsaturated soils under various confining pressures

Figure 4-12 illustrates the permanent vertical strains of unsaturated intact and compacted specimens at a suction of 30 kPa and confining pressures of 30 and 60 kPa (specimens CS30P30, IS30P30, CS30P60, and IS30P60).

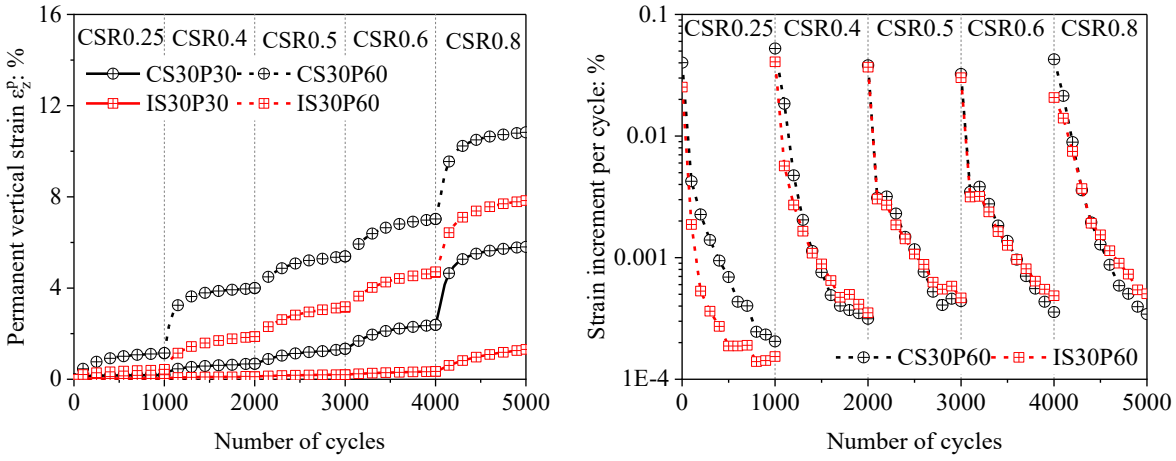

Figure 4-12. Permanent vertical strains of unsaturated intact and compacted specimens under various confining pressures: (a) permanent vertical strains; (b) strain increments per cycle

As shown in Figure 4-12(a), at a given confining pressure, the permanent vertical strain of the intact specimen is consistently smaller than that of the compacted specimen as the CSR increases from 0.25 to 0.8. Figure 4-12(b) presents the strain increments per cycle for

specimens CS30P60 and IS30P60. It can be observed that at a CSR of 0.25, the intact specimen shows a smaller strain increment than the compacted specimen. However, as the CSR exceeds 0.25, the strain increment in the intact specimen is larger than that in the compacted specimen after several hundred cycles. These findings align with the type I behaviour discussed earlier, further supporting the classification of the structure effects on permanent vertical strain.

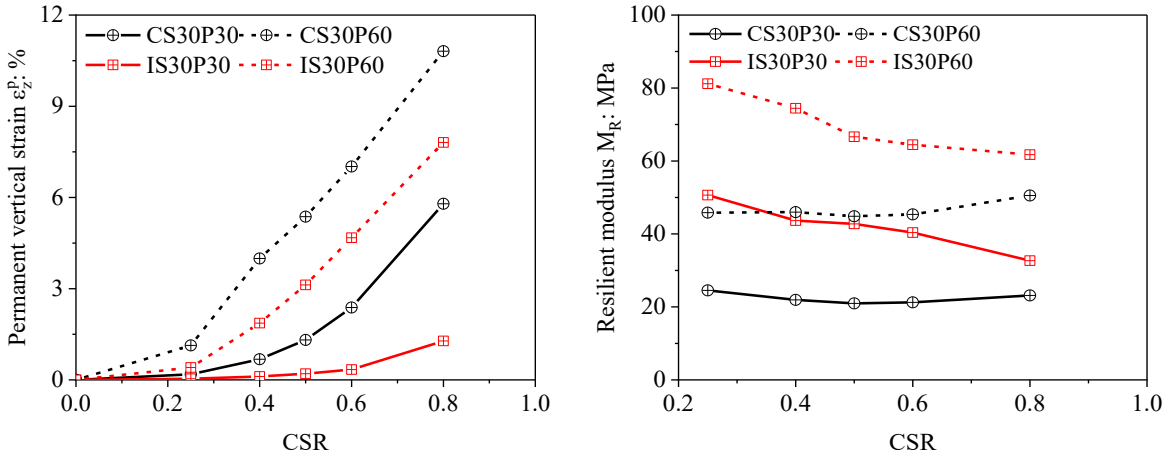

(a) (b)

Figure 4-13. Cyclic behaviour of unsaturated intact and compacted specimens under various confining pressures: (a) permanent vertical strains; (b) resilient moduli

Figure 4-13 presents the variations of permanent vertical strain and resilient modulus with CSR. Figure 4-13(a) indicates that permanent vertical strain increases with increasing confining pressure. This is because the plastic modulus decreases as confining pressure increases at a constant CSR and thus leads to a larger plastic strain. This explanation is supported by the bounding surface theory and previous experimental observations (Dafalias, 1986b; Guo et al., 2013; Cai et al., 2015; Zhou et al., 2015). Figure 4-13(b) demonstrates that resilient modulus increases with increasing confining pressure. The increase is due to stabilised interparticle contacts at higher confining pressures under 30 kPa suction, similar to findings for saturated soils (Guo et al., 2013; Wang et al., 2024). More importantly, Figure 4-13 reveals that as confining pressure increases, the differences between intact and compacted specimens become smaller. For example, at a CSR of 0.8, the intact specimen has about 80% smaller permanent vertical strain and 40% larger resilient modulus than the compacted specimen at 30 kPa confining pressure. These differences reduce to 30% and 20%, respectively, when the

confining pressure increases to 60 kPa. This is due to more evident structure degradation at higher confining pressures, which reduces the difference between intact and compacted specimens.

The results in Figure 4-11 and Figure 4-13 reveal significant differences in the resilient modulus between intact and compacted specimens under a given confining pressure, CSR, and suction. So far, many formulations have been proposed to calculate the resilient modulus under various stress states (Heath et al., 2004; Ng et al., 2013; Han and Vanapalli, 2016; Su et al., 2022). Among them, Ng et al. (2013) proposed the following equation based on unsaturated soil mechanics:

$$M_R = M_0 \left(\frac{p_{c0}}{p_r}\right)^{k_1} \left(1 + \frac{q_{cyc}}{p_r}\right)^{k_2} \left(1 + \frac{s_0}{p_{c0}}\right)^{k_3} \quad (4\text{-}1)$$

When applying Equation (4-1) to the compacted specimen of the present study, M_0, k_1, k_2, and k_3 are 0.19 MPa, 1.41, -0.09, and 0.11, respectively. For the intact specimen, the corresponding values are 0.98 MPa, 1.28, -0.31, and 0.69. The differences in model parameters are closely related to the inherently stiffer structure and its degradation in the intact specimen. The stiffer structure leads to a larger M_0, while its degradation mitigates the hardening effects of confining pressure and enhances the softening effects of cyclic deviatoric stress, yielding smaller k_1 and k_2 values. Moreover, the larger k_3 observed in the intact specimen indicates that its resilient modulus is more sensitive to suction changes. The suction effects differ from the findings of Ng et al. (2017), where compacted loess showed a greater increase in small-strain stiffness than intact loess as suction increased from 0 to 50 kPa. This discrepancy arises because more volumetric contraction occurs in the compacted specimen at a lower suction during cyclic loading, compensating for the suction effects on resilient modulus.

4.4 Cyclic behaviour of specimens compacted at different compaction conditions

4.4.1 Effects of compaction conditions on cyclic behaviour of saturated soils

Figure 4-14 presents the cyclic behaviour of saturated compacted specimens COD-S0, CWD-S0, and CWL-S0, with normalised excess PWP, permanent vertical strain, and resilient

modulus depicted in Figure 4-14(a), (b), and (c), respectively. Given the significant difference in permanent vertical strain between specimen CWL-S0 and the other two specimens, a semi-logarithmic scale is used in Figure 4-14(b) to clearly present the results. As expected, the specimen with a higher dry density exhibits greater resistance to cyclic loading. Under a CSR of 0.25, specimen CWL-S0 fails after approximately 60 cycles, characterised by a normalised excess PWP close to 1, permanent vertical strain larger than 10%, and a substantial reduction in resilient modulus. In contrast, specimen CWD-S0 exhibits plastic shakedown behaviour at a CSR of 0.25, with normalised excess PWP, permanent vertical strain, and resilient modulus remaining nearly constant after several hundred cycles (Werkmeister, 2003).

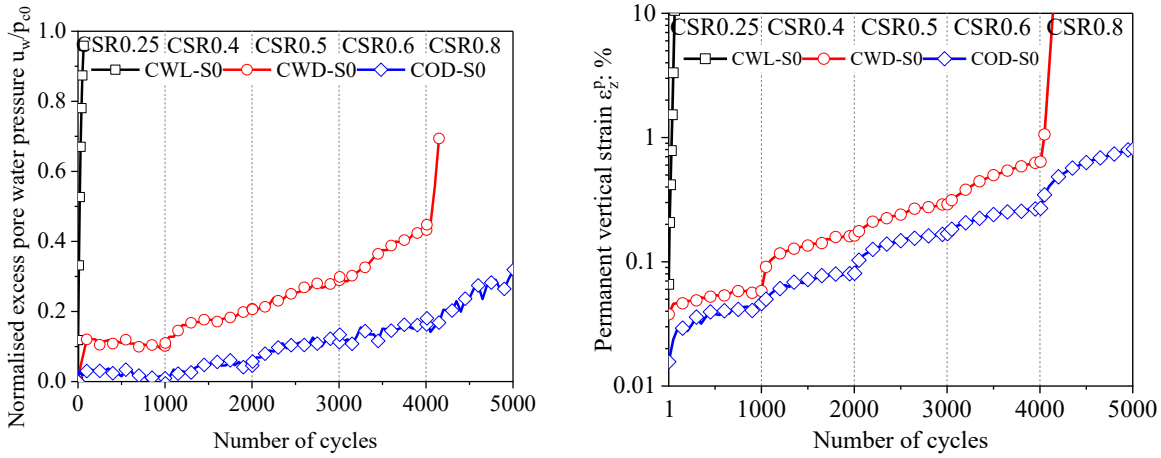

Figure 4-14. Influence of compaction conditions on cyclic behaviour of saturated specimens: (a) normalised excess PWPs; (b) permanent vertical strains; (c) resilient moduli

Additionally, it should be highlighted that the resilient modulus of specimen CWL-S0 at

the first cycle is larger than that of specimen CWD-S0. This is attributed to the approximately 15% volumetric strain experienced by specimen CWL-S0 before cyclic loading, as shown by the isotropic compression curve in Figure 4-3. The substantial volumetric contraction induces densification effects, resulting in a higher initial resilient modulus in specimen CWL-S0 than that of specimen CWD-S0. Similar observations were reported by Wang et al. (2021) and Dai et al. (2025) for low-plasticity clays, where looser specimens may exhibit larger small-strain shear stiffnesses than denser ones when subjected to more substantial volumetric strain and structure evolution.

Under the same dry density, it is evident that the specimen compacted at the optimum water content (COD-S0) exhibits smaller normalised excess PWP and permanent vertical strain and a larger resilient modulus than that compacted at the wet of optimum (CWD-S0). For example, after 1000 cycles at a CSR of 0.25, specimen COD-S0 has approximately 90% smaller normalised excess PWP, 20% smaller permanent vertical strain, and 50% larger resilient modulus than specimen CWD-S0. This observation aligns with Yokohama et al. (2014) for sandy silt, where the specimen compacted at a lower water content is more resistant to cyclic loading. These trends can be attributed to the different structures induced by compaction water content. As illustrated in Figure 3-14, the specimen compacted at the wet of optimum contains extra-large inter-clod pores, which lead to a greater contractive tendency, thus resulting in larger excess PWP and permanent strain and smaller resilient modulus than the specimen compacted at a lower water content.

4.4.2 Effects of compaction dry density and suction on cyclic behaviour

Figure 4-15 shows the variations of permanent vertical strain and resilient modulus with the number of cycles for looser (CWL) and denser (CWD) specimens under suctions of 0, 10, and 30 kPa. Under otherwise identical conditions, the specimen with a lower compaction dry density exhibits a larger permanent vertical strain owing to its softer soil structure. At a given stress state and number of cycles, the permanent vertical strain in the looser specimen can be up to an order of magnitude larger than that in the denser specimen. This excessive deformation

highlights the necessity of achieving the specified dry density during geo-structure construction, as inadequate compaction may lead to severe geohazards such as ground subsidence and slope failure.

Figure 4-15(b) illustrates that the variation in resilient modulus with the number of cycles differs significantly between looser and denser specimens. The resilient moduli of unsaturated looser specimens (CWL-S10 and CWL-S30) slightly increases with the number of cycles at a given suction and CSR because of the contraction-induced densification effects (see Figure 4-15 (a)). In contrast, for denser specimens, the evolution of resilient modulus with the number of cycles is influenced by the applied stress state. At relatively high suction and low CSR (e.g., CWD-S30 with CSR = 0.25), the resilient modulus remains nearly constant with the number of cycles, likely due to limited strains and minimal structure changes. Under lower suctions and higher CSRs (e.g., CWD-S0 with CSR = 0.6), a gradual decrease in resilient modulus is observed, attributed to obvious excess PWP and strain accumulation (see Figure 4-14). The stress state-dependent variations in resilient modulus are consistent with previous observations (e.g., Yang et al., 2008b; Ng et al., 2013; Sivakumar et al., 2013).

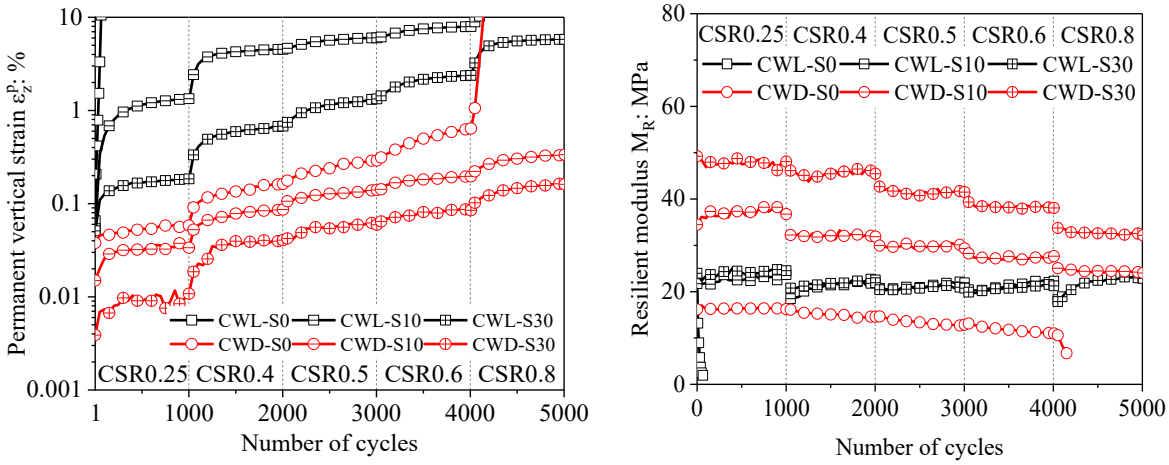

(a) (b)

Figure 4-15. Influence of compaction dry density on cyclic behaviour under various suctions and numbers of cycles: (a) permanent vertical strains; (b) resilient moduli

Figure 4-16 illustrates the variations of permanent vertical strain and resilient modulus with suction and CSR for looser (CWL) and denser (CWD) specimens. The results are extracted from Figure 4-15 at each CSR after 1000 cycles, and no data is obtained when

specimen failure occurs (e.g., CWL-S0). As expected, permanent vertical strain is larger at a higher CSR for all specimens. As CSR increases from 0.25 to 0.8, the permanent vertical strain exhibits up to a tenfold increase, emphasising the necessity of stress regulation to maintain pavement serviceability and prevent excessive deformation. Furthermore, permanent vertical strain decreases significantly with increasing suction. For example, for denser specimens (CWD), permanent vertical strain decreases by approximately 45% as suction increases from 0 to 10 kPa after 1000 cycles under a CSR of 0.25. This is because a higher suction results in an increased mean Bishop's stress and enhances inter-particle contact forces (i.e., suction hardening effects) (Alonso et al., 1990; Gallipoli et al., 2003a), thereby stabilising soil skeleton and reducing strain accumulation during loading.

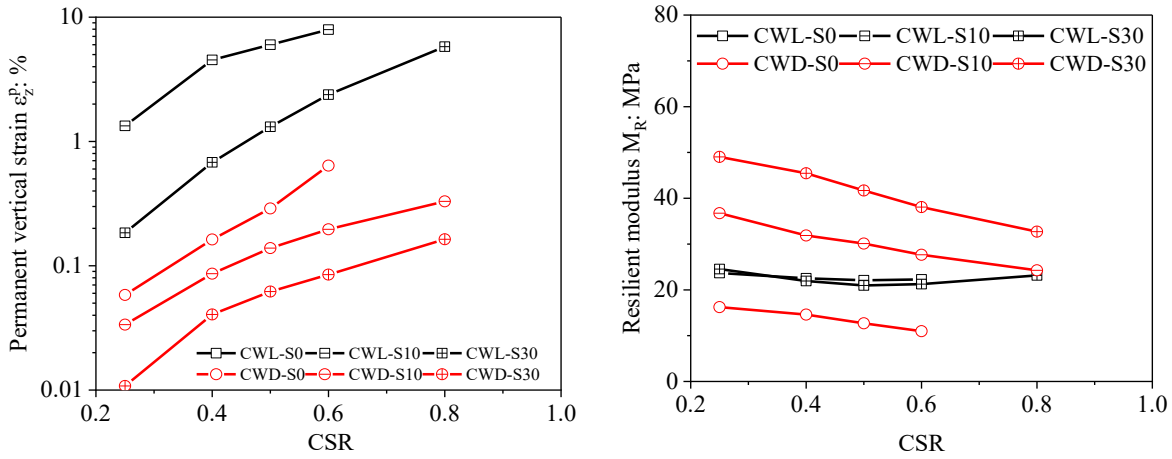

(a) (b)

Figure 4-16. Influence of compaction dry density on cyclic behaviour under various suctions and CSRs: (a) permanent vertical strains; (b) resilient moduli

More importantly, the looser specimen has a larger permanent vertical strain than the denser specimen at a given suction, with the difference diminishing at a higher suction. At a CSR of 0.6, the permanent vertical strain of specimen CWL-S10 is approximately 3900% greater than that of CWD-S10, whereas this difference reduces to 2700% at a suction of 30 kPa. The reduced difference is likely due to the greater stabilising effects of suction on the soil skeleton in looser specimens than denser ones, as evidenced by loading collapse curves of specimens with different initial dry densities (Estabragh et al., 2004; Sun et al., 2007). For example, Estabragh et al. (2004) reported that increasing suction from 0 to 100 kPa resulted in

a 70% increase in isotropic yield stress for loosely compacted low-plasticity clay, whereas the increase was about 40% for densely compacted specimens.

Figure 4-16(b) suggests that the variation of resilient modulus with suction and CSR is significantly affected by compaction dry density. For looser specimens, the resilient modulus remains nearly constant with suction and CSR because of the significant volumetric contraction compensating for the effects of suction and CSR. In contrast, for denser specimens, the resilient modulus increases with suction due to suction hardening effects, and decreases with CSR as a result of the soil's nonlinear stress-strain response. For example, the resilient modulus of denser specimens increases by 200% when suction increases from 0 to 30 kPa at a CSR of 0.25, while it decreases by 35% when CSR increases from 0.25 to 0.8 at a suction of 30 kPa. Consequently, the difference in resilient modulus between looser and denser specimens becomes greater with increasing suction but is reduced with increasing CSR.

4.4.3 Effects of compaction water content and suction on cyclic behaviour

Figure 4-17 presents the variations of permanent vertical strain and resilient modulus with the number of cycles for specimens with different compaction water contents. Figure 4-17(a) shows that permanent vertical strain increases with the number of cycles, with the specimen compacted at the wet of optimum (CWD) exhibiting a larger permanent vertical strain than that compacted at the optimum water content (COD) under identical suction and CSR. The larger permanent vertical strain in the CWD series is attributed to the presence of extra-large inter-clod pores, as supported by the microstructure observations in Figure 3-14. The results indicate that, for a given compaction effort in pavement construction, compacting soil at the optimum water content not only yields a higher dry density (as reflected by the standard compaction curve) but also results in a more stable soil structure (with a smaller accumulated strain) compared to compaction at the wet of optimum.

Figure 4-17(b) compares the resilient moduli of the COD and CWD series as the number of cycles increases. At a given suction and CSR, the COD series consistently exhibits a larger resilient modulus than the CWD series. Similar observations were reported by Mancuso et al.

(2002) for silty sand and Sawangsuriya et al. (2009b) for clayey sand, where the specimen compacted at a lower water content has a larger small-strain shear stiffness at a given suction. Moreover, the variation in resilient modulus with the number of cycles is comparable between the COD and CWD series. At relatively high suction and low CSR (e.g., s_0 = 30 kPa and CSR = 0.25), the variation of resilient modulus with the number of cycles is negligible. In contrast, at lower suctions and higher CSRs (e.g., zero suction and CSR = 0.6), the resilient modulus gradually decreases with the number of cycles.

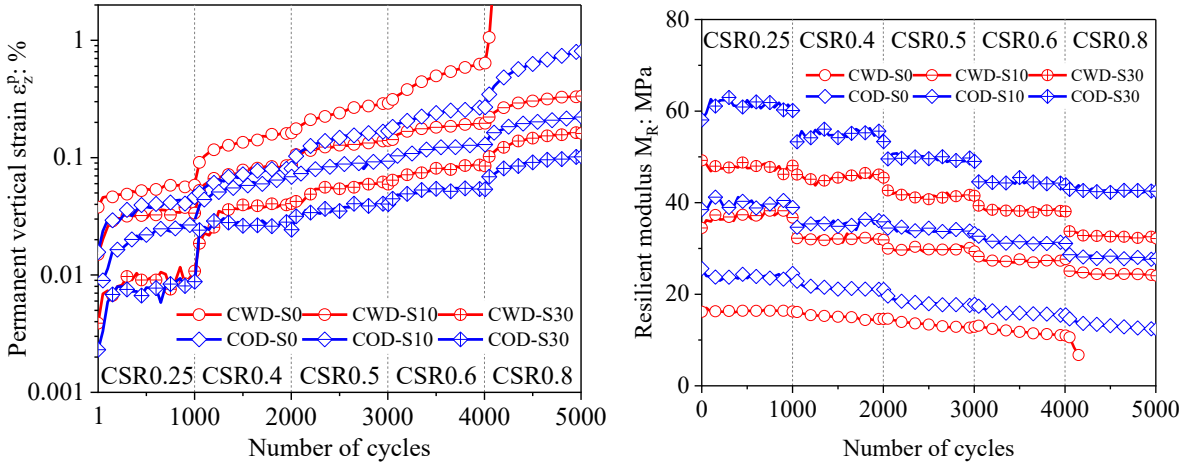

Figure 4-17. Influence of compacted water content on cyclic behaviour under various suctions and numbers of cycles: (a) permanent vertical strains; (b) resilient moduli

Figure 4-18 presents the variations in permanent vertical strain and resilient modulus with CSR for the COD and CWD series under suctions of 0, 10, and 30 kPa. For specimens in both the COD and CWD series, permanent vertical strain increases and resilient modulus decreases consistently with increasing CSR. Moreover, the changes in resilient modulus with CSR are comparable under different suctions. As CSR increases from 0.25 to 0.6, resilient modulus decreases by approximately 30% for all specimens. These observations suggest that the influence of CSR on cyclic behaviour is similar for specimens compacted at different water contents.

More importantly, as the soil state shifts from saturated to unsaturated, the differences in permanent vertical strain and resilient modulus between the COD and CWD series decrease slightly. For example, specimen CWD-S0 exhibits about 30% smaller resilient modulus than

specimen COD-S0 at zero suction, whereas the difference reduces to 10-20% at suctions of 10 and 30 kPa. A similar trend was observed by Mancuso et al. (2002) and Sawangsuriya et al. (2009b), who found that the increase in small-strain shear stiffness with suction was more significant in the specimen compacted at the wet of optimum than that compacted at the optimum water content. This observation is possible because the soil skeleton is more sensitive to suction variation for specimens with higher compaction water contents.

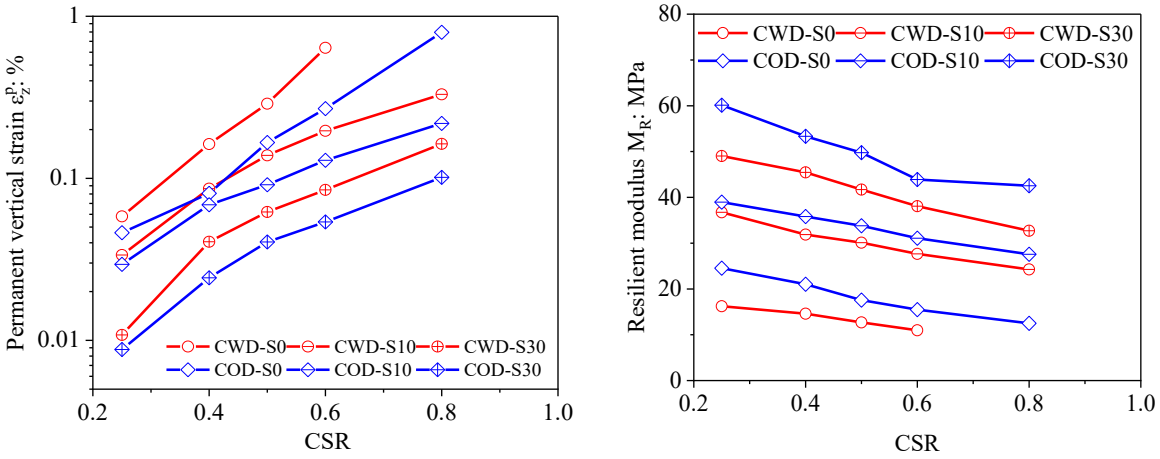

(a) (b)

Figure 4-18. Influence of compaction water content on cyclic behaviour under various suctions and CSRs: (a) permanent vertical strains; (b) resilient moduli

4.4.4 Modelling the effects of compaction conditions on cyclic behaviour

The results from Figure 4-14 to Figure 4-18 highlight the differences in cyclic behaviour between specimens compacted at different dry densities and water contents. However, conducting cyclic tests to assess the influence of compaction conditions on cyclic behaviour under various suctions is time-consuming and impractical for engineering applications. Consequently, semi-empirical equations are employed to analyse the effects of compaction conditions on permanent vertical strain and resilient modulus as follows:

$$M_R = M_0 \left(\frac{p_{c0}}{p_r}\right)^{k_1} \left(1 + \frac{q_{cyc}}{p_{c0}}\right)^{k_2} \left(1 + \frac{s_0}{p_r}\right)^{k_3} \tag{4-2}$$

$$\varepsilon_z^p = \varepsilon_0 \left(\frac{p_{c0}}{p_r}\right)^{z_1'} \left(\frac{q_{cyc}}{p_{c0}}\right)^{z_2'} \left(1 + \frac{s_0}{p_{c0}}\right)^{z_3'} \tag{4-3}$$

where M_0, k_1, k_2, k_3 are parameters for resilient modulus; and ε_0, z_1', z_2', z_3' are model

parameters for calculating permanent vertical strain. Equation (4-2) for resilient modulus was proposed by the authors in a previous study (Dai and Zhou, 2025). Meanwhile, Equation (4-3) for strain calculation adopts a similar form to Equation (4-2) for simplicity. It should be highlighted that the parameters k_1, k_2, k_3 and z_1', z_2', z_3' are assumed to be independent of the compaction condition, and this assumption will be assessed and verified subsequently.

To evaluate the performance of Equations (4-2) and (4-3), the calculated results are compared with the measured data from this study, with the parameters and results presented in Figure 4-19. Moreover, the experimental results from Sivakumar et al. (2013) are used for further validation, as shown in Figure 4-20. Sivakumar et al. (2013) conducted cyclic tests on seven series of speswhite kaolin compacted under different dry densities and water contents in their as-compacted states, and thus seven different groups of ε_0 and M_0 are required. It can be observed that the calculated results match well with the measured data, with most results falling within a 10% error margin. The good match indicates that Equations (4-2) and (4-3) perform well in capturing the influence of compaction conditions on resilient modulus and permanent vertical strain, respectively.

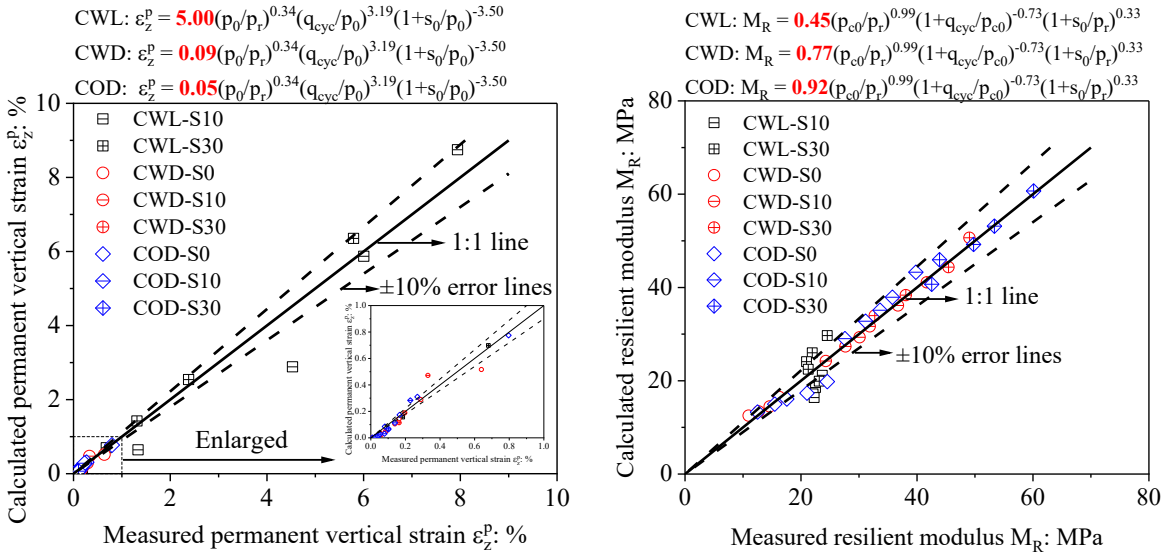

(a) (b)

Figure 4-19. Comparisons between the measured and calculated results for the data from the current study: (a) permanent vertical strains; (b) resilient moduli

The key feature of Equations (4-2) and (4-3) is that only the parameters ε_0 and M_0 vary with compaction conditions, while the significances of confining pressure, CSR, and suction

are assumed to be comparable among specimens compacted at different conditions (i.e., constant k_1, k_2, k_3 and z_1', z_2', z_3'). This simplification is based on the observation that the trends in permanent vertical strain and resilient modulus with respect to suction and CSR are qualitatively similar among specimens (see Figure 4-16 and Figure 4-18), except for minor quantitative differences and a slight deviation in the CWL series. The validation results presented in Figure 4-19 and Figure 4-20 demonstrate that these differences have limited impact on the performance of equations, thereby validating the effectiveness of this simplification. From the perspective of experimental testing, once the parameters M_0, k_1, k_2, k_3 and ε_0, z_1', z_2', z_3' have been calibrated under a specific compaction condition, only one additional test is necessary to calibrate the parameters for a different compaction condition, significantly simplifying the evaluation of compaction condition effects.

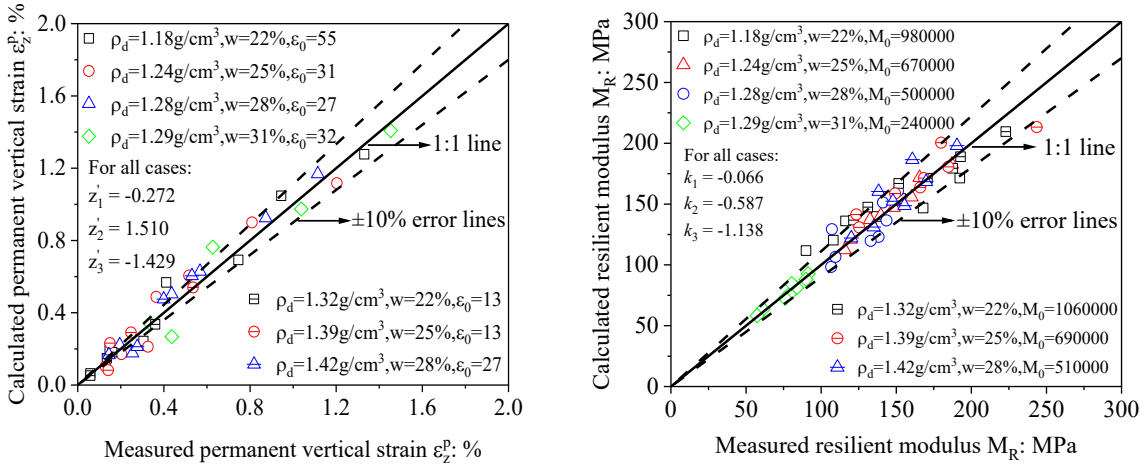

(a) (b)

Figure 4-20. Comparisons between the measured and calculated results for the data from Sivakumar et al. (2013): (a) permanent vertical strains; (b) resilient moduli

4.5 Summary and conclusions

In this chapter, cyclic triaxial tests were conducted on intact and compacted loess specimens, as well as specimens compacted at different compaction conditions. The effects of soil structure, suction, confining pressures, and CSR were investigated. The main conclusions are summarised as follows:

The structure effects on permanent vertical strain can be categorised as two types based on the strain increment at the first cycle (i.e., $\Delta\varepsilon_{z,1}^p$). In type I, the intact specimen exhibits a

smaller $\Delta\varepsilon_{z,1}^{p}$ than the compacted specimen attributed to its inherently stiffer soil structure. In type II, the intact specimen has a larger $\Delta\varepsilon_{z,1}^{p}$ due to structure degradation-induced plastic deformation. For the tested soil, the yield stress of the intact specimen can be used as a threshold confining pressure to distinguish between the two types of behaviour, with type I occurring below and type II above this threshold. More importantly, the trend in strain increment may change with the number of cycles in both types. In type I, the strain increment of the intact specimen may exceed that of the compacted specimen owing to structure degradation. Conversely, in type II, the strain increment of the intact specimen could be smaller due to failure of the compacted specimen. These findings emphasise that when soils in intact and compacted states are both involved, it is not always conservative to adopt parameters from the compacted soil. This is because the strain increment in the compacted soil could be smaller in particular cases, resulting in an underestimation of soil deformation.

The resilient modulus of the intact specimen is consistently larger than that of the compacted specimen across various suctions and stress states. This finding suggests that the soil skeleton of the intact specimen is stiffer during unloading (i.e., with a reduction of vertical stress), with smaller vertical recoverable strains compared to the compacted specimen. The resilient modulus of the intact specimen exhibits less dependence on confining pressure but greater sensitivity to CSR and suction than that of the compacted specimen. This is because the structure degradation in the intact specimen mitigates the hardening effects of confining pressure and amplifies the softening effects of CSR, and volumetric contraction in the compacted specimen compensates for the effects of suction reduction. Consequently, the difference in resilient modulus between intact and compacted specimens diminishes at higher CSRs and confining pressures, and lower suctions.

At a given suction and CSR, the looser specimen has a permanent vertical strain up to an order of magnitude larger than that in the denser specimen, highlighting the necessity of achieving the specified dry density during geo-structure construction. The difference diminishes as suction increases because of the greater stabilising effects of suction on the soil skeleton in looser specimens than denser ones. The resilient modulus of looser specimens

increases slightly with the number of cycles and remains nearly constant with varying suction and CSR because of the significant volumetric contraction compensating for the effects of suction and CSR. In contrast, the resilient modulus of denser specimens decreases with decreasing suction and increasing CSR and is larger than that of looser specimens at a given suction and CSR.

Under otherwise identical conditions, permanent vertical strain is larger and resilient modulus is smaller for the specimen compacted at the wet of optimum than that compacted at the optimum water content. This is because the soil skeleton is softer at a higher compaction water content due to the existence of extra-large inter-clod pores, as supported by microstructural analysis. These observations demonstrate that, for a given compaction effort in pavement construction, compacting soil at the optimum water content not only yields a higher dry density but also results in a more stable soil structure compared to compaction at the wet of optimum. More importantly, these differences slightly decreases when soil becomes unsaturated, possibly because the soil skeleton is more sensitive to suction variation for specimens with higher compaction water contents.

New semi-empirical equations were proposed to unify the influence of compaction conditions on cyclic behaviour. The effects of compaction conditions on permanent vertical strain and resilient modulus are captured by ε_0 and M_0, respectively, while other state-related parameters remain constant. This suggests that the suction and CSR effects on cyclic behaviour can be considered comparable across different compaction conditions in engineering practice. By comparing the calculated results with the measured data from both the present study and a previous study, a good performance of the new equations was observed.

CHAPTER 5 CYCLIC BEHAVIOUR OF UNSATURATED LOESS WITH PRINCIPAL STRESS ROTATION

The influence of soil structure and suction on the cyclic behaviour of unsaturated loess without principal stress rotation was discussed in Chapter 4. Following that, this chapter investigates the role of principal stress rotation in the cyclic behaviour of unsaturated loess under different temperatures and suctions. The adopted stress path effectively represents the soil stress states under repeated traffic loads, and therefore the findings are expected to provide valuable guidance for pavement designs.

5.1 Specimen preparation, test apparatus, test program, and test procedures

5.1.1 Specimen preparation

Hollow cylindrical specimens with an inner diameter of 50 mm, outer diameter of 100 mm, and height of 200 mm were prepared using the static compaction method. The target compaction water content and dry density were 15.2% and 1.59 g/cm^3, corresponding to the optimum water content and 90% degree of compaction, respectively. To prepare the compacted specimens, disturbed soil was oven-dried, crushed using a rubber hammer, and sieved through a 2 mm sieve. The prepared soil was then mixed stepwise with de-aired water. Once the target water content (15.2%) was reached, the mixture was subsequently sieved again through a 2 mm sieve and sealed in plastic bags for 24 hours to ensure moisture equilibrium. It was then statically compacted in ten layers in a specialised split mould for hollow cylinder specimens, with scarification between layers to ensure specimen homogeneity (Ladd, 1978; Kumruzzaman and Yin, 2010). The recorded vertical stress to achieve this density falls in the range of 1160 to 1270 kPa. After compaction, the specimen had an initial suction of approximately 50 kPa based on the null-type axis translation technique (Fredlund and Rahardjo, 1993). Upon saturation, the specimen exhibited a permeability coefficient of approximately 1×10^{-7} m/s and an isotropic yield stress of about 130 kPa.

5.1.2 Test apparatus

As shown in Figure 5-1(a), the dynamic hollow cylinder apparatus includes a temperature- and suction-controlled hollow cylinder cell, a load cell for measuring vertical force and torque, two linear variable differential transformers for recording vertical and torsional deformations, and a loading frame.

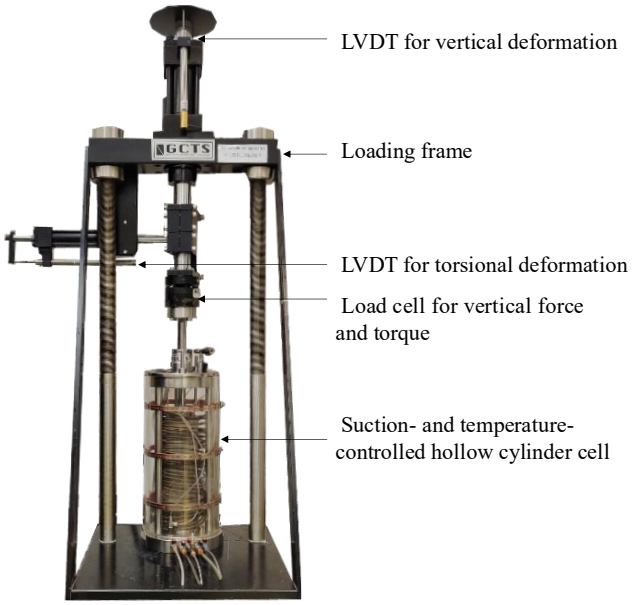

(a)

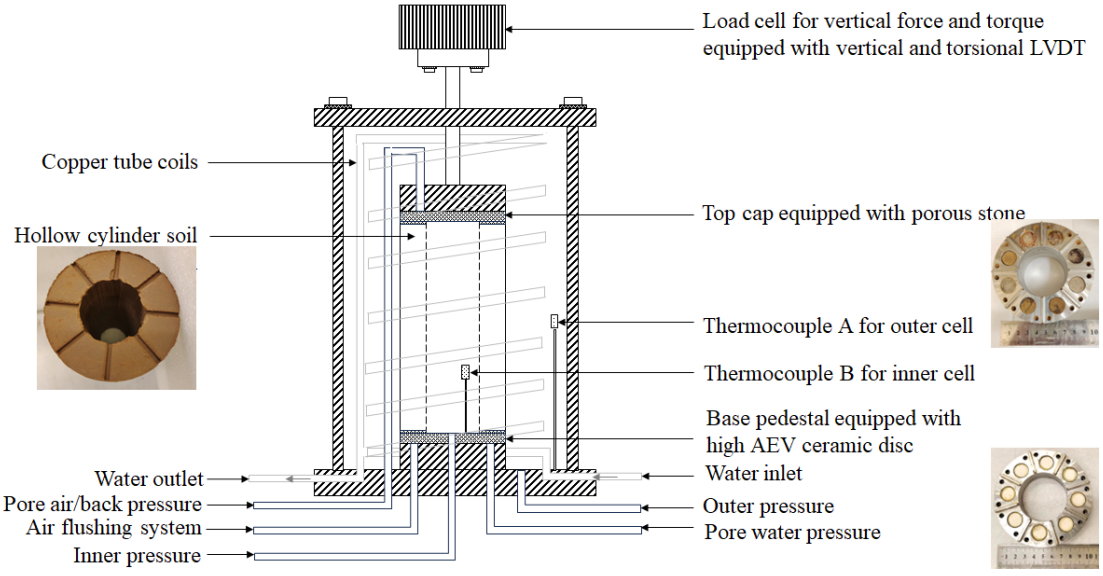

(b)

Figure 5-1. Hollow cylinder apparatus: (a) overview of the whole apparatus; (b) schematic diagram of temperature- and suction-controlled hollow cylinder cell

The hollow cylinder apparatus is able to independently apply dynamic vertical force W_v,

torque T_q, inner cell pressure P_i, and outer cell pressure P_o, with control errors of less than 1N, 0.01N·m, 1 kPa, and 1 kPa, respectively. The vertical stress σ_z, shear stress $\tau_{z\theta}$, radial stress σ_r, and circumferential stress σ_θ can be generated in the specimen and calculated as follows (Hight et al., 1983):

$$\sigma_z = \frac{W_v}{\pi(r_0^2 - r_i^2)} + \frac{P_o r_o^2 - P_i r_i^2}{r_o^2 - r_i^2} \tag{5-1}$$

$$\tau_{z\theta} = \frac{3T_q}{2\pi(r_0^3 - r_i^3)} \tag{5-2}$$

$$\sigma_r = \frac{P_o r_o + P_i r_i}{r_o + r_i} \tag{5-3}$$

$$\sigma_\theta = \frac{P_o r_o - P_i r_i}{r_o - r_i} \tag{5-4}$$

where r_i and r_o are the radii of inner and outer cells, respectively. Based on the stress components defined in Equations (5-1) to (5-4), the three principal stresses, the rotation angle of the major principal stress relative to the vertical direction (denoted as $\bar{\alpha}$), the mean total stress p, and the deviatoric stress q can be calculated as follows (Hight et al., 1983; Yang et al., 2007; Cai et al., 2015):

$$\sigma_1 = \frac{\sigma_z + \sigma_\theta}{2} + \sqrt{\left(\frac{\sigma_z - \sigma_\theta}{2}\right)^2 + \tau_{z\theta}^2} \tag{5-5}$$

$$\sigma_2 = \sigma_r \tag{5-6}$$

$$\sigma_3 = \frac{\sigma_z + \sigma_\theta}{2} - \sqrt{\left(\frac{\sigma_z - \sigma_\theta}{2}\right)^2 + \tau_{z\theta}^2} \tag{5-7}$$

$$\bar{\alpha} = \frac{1}{2}\arctan\frac{2\tau_{z\theta}}{\sigma_z - \sigma_\theta} \tag{5-8}$$

$$p = \frac{\sigma_1 + \sigma_2 + \sigma_3}{3} \tag{5-9}$$

$$q = \sqrt{\frac{1}{2}[(\sigma_1 - \sigma_2)^2 + (\sigma_3 - \sigma_2)^2 + (\sigma_1 - \sigma_3)^2]} \tag{5-10}$$

where σ_1, σ_2, and σ_3 are the major, intermediate, and minor principal stresses, respectively. According to Equations (5-1) to (5-10), the hollow cylinder apparatus allows for independent

control of the magnitudes and orientations of the three principal stresses. This capability enables the simultaneous simulation of deviatoric stress variation and principal stress rotation induced by repeated traffic loads.

As shown in Figure 5-1(b), the axis-translation technique was adopted to control the matric suction in the specimen. Pore air pressure was applied via the top cap equipped with porous stone, while pore water pressure was controlled through the base pedestal using a high air entry value ceramic disc (200 kPa). Different from conventional triaxial apparatus, the porous stone and ceramic disc were subdivided into eight components to facilitate the application of torque. Furthermore, air dissolved in water and passed through the ceramic disc was flushed out and collected with a diffused air volume indicator every 24 hours. The collected air volume was subsequently used to correct changes in the specimen's water content.

A temperature control system was integrated into the hollow cylinder apparatus to facilitate the application of thermal loads. The temperature control system consists of copper tubes, two thermocouples, and an external refrigerated circulator with a working range between 0 and 70 ℃. The soil temperature was controlled by circulating heated/cooled water in spiral copper tubes surrounding the specimen. Two thermocouples (A and B) were installed in the outer and inner cells to monitor the soil temperature and check the temperature uniformity inside the hollow cylinder cell. To minimise the energy loss, the hollow cylinder cell was wrapped with an insulating material during testing.

5.1.3 Test program

Three series of cyclic tests were conducted, as summarised in Table 5-1. Series I examined the cyclic behaviour considering both deviatoric stress variation and principal stress rotation under various temperatures and suctions. Three temperatures (5, 20, and 40℃) and three suctions (0, 10, and 30 kPa) were considered. The selected temperatures were based on field-monitoring data for subgrade soils reported in the literature (McCartney and Khosravi, 2013; Vandoorne et al., 2021). Along the wetting path, at 20 ℃ and a confining pressure of 30 kPa, suctions of 10 and 30 kPa correspond to degrees of saturation of 0.87 and 0.65, respectively,

as indicated by the water retention curve in Figure 4-5. The zero suction condition represents a fully saturated specimen under back pressure, with a B value exceeding 0.98. These suctions and corresponding degrees of saturation are expected to effectively represent a relatively humid climate (McCartney and Khosravi, 2013; Vandoorne et al., 2021), which is crucial to the performance of subgrade soil.

Series II was designed to investigate the cyclic behaviour under various temperatures and suctions without PSR. Note that series I and series II share identical temperature and suction ranges, as well as the magnitude of cyclic deviatoric stress. The only difference is that PSR is incorporated in series I but excluded in series II. Consequently, comparative analysis of these two series allows for the evaluation of PSR effects under various temperatures and suctions.

Series III was conducted to investigate the influence of confining pressure on cyclic behaviour, while maintaining cyclic stress ratios (CSR, $\sigma_z^{cyc}/2p_{c0}$) consistent with those in series I and II. Following AASHTO (2021) guidelines for resilient modulus testing of subgrade soil, two confining pressures were selected: 30 kPa for series I and II, and 60 kPa for series III.

Table 5-1. Test program for cyclic tests with and without PSR

Test ID*	Confining pressure p_{c0}: kPa	Suction s_0: kPa	Temperature T: °C	Cyclic vertical stress σ_z^{cyc}: kPa (CSR = $\sigma_z^{cyc}/2p_{c0}$)	Cyclic shear stress $\tau_{z\theta}^{cyc}$: kPa
S0T5	30	0	5	15, 24, 30, 36, 48 (0.25, 0.4, 0.5, 0.6, 0.8)	3.75, 6, 7.5, 9, 12
S0T20			20		
S0T40			40		
S10T5		10	5		
S10T40			40		
S30T5		30	5		
S30T40			40		
VS0T5	30	0	5	15, 24, 30, 36, 48 (0.25, 0.4, 0.5, 0.6, 0.8)	0, 0, 0, 0, 0
VS0T40			40		
VS10T5		10	5		
VS10T40			40		
PS0T5	60	0	5	30, 48, 60, 72, 96 (0.25, 0.4, 0.5, 0.6, 0.8)	7.5, 12, 15, 18, 24
PS0T40			40		

*Notation in test ID: "S" is the suction; "T" is the temperature; "V" indicates the application of cyclic vertical stress only; "P" denotes a higher confining pressure; and the numbers after "S" and "T" are the values of suction and temperature in kPa and °C, respectively.

For each specimen, multi-stage cyclic loading with five levels of cyclic vertical stress (CSRs = 0.25, 0.4, 0.5, 0.6, and 0.8) was conducted with reference to previous studies and existing guidelines (Cai et al., 2018; AASHTO, 2021). For tests incorporating PSR (series I and III), the ratio of cyclic shear stress ($\tau_{z\theta}^{cyc}$) to cyclic vertical stress (σ_z^{cyc}) was maintained at 0.25, while it was set to zero for tests without PSR (series II). The selected ratio of 0.25 facilitated the identification of PSR effects (Cai et al., 2015) and ensured identical cyclic deviatoric stress across all tests. 1000 cycles were applied under each CSR level, and 5000 cycles were conducted for each specimen. Note that fewer stages were applied when specimen failure occurred. Tests were conducted at a relatively low frequency of 0.2 Hz to ensure stable control of the cyclic vertical and torsional loads. It should be noted that the frequency of traffic loads generally falls within the range of 0.2 Hz to 4 Hz, mainly depending on the vehicle/train speed and wheel spacing (Tang et al., 2008; Xiao et al., 2014; Wu et al., 2022). Within this range, many studies have shown that the subgrade soil is slightly less resistance to cyclic loading as frequency decreases (e.g., Guo et al., 2016; Wang et al., 2019a; Yang et al., 2019). Therefore, a relatively low traffic frequency was selected to represent a more critical condition.

5.1.4 Test procedures

Figure 5-2 presents the stress paths during testing, which included four sequential stages for each specimen: suction equalisation, isotropic compression, thermal equalisation, and cyclic loading. The corresponding thermo-hydro-mechanical paths prior to cyclic loading are shown in Figure 5-2(a). Following installation in the cell, specimens were initially wetted from an initial suction of 50 kPa to the target suction. Suction equalisation was deemed complete when the daily change in water content fell below 0.04% (Sivakumar, 1993), which took about 2-3 weeks for an unsaturated specimen. After suction equalisation, isotropic compression was applied by increasing the confining pressure at a rate of 1 kPa per hour (Kaewsong, 2017). The third stage involved thermal equalisation, during which the specimen was heated or cooled to the target temperature by circulating water through a copper tube. Thermal equalisation was maintained for 24 hours, which was sufficient to achieve a stable and uniform temperature throughout the specimen. Upon reaching thermal equilibrium, the two thermocouples (A and

B), located in the inner and outer cells, recorded nearly identical temperatures, with a difference of less than 0.5 ℃ and a temperature fluctuation below 0.2 ℃. For unsaturated specimens, an additional 3 to 5 days were required to re-establish suction equilibrium following heating or cooling, as the water retention capacity varies with temperature (Romero et al., 2001).

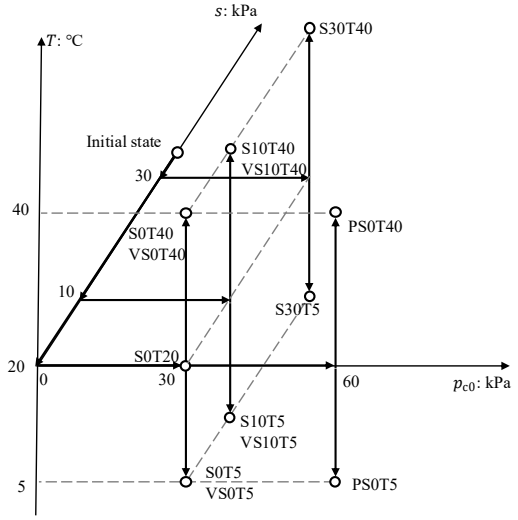

(a)

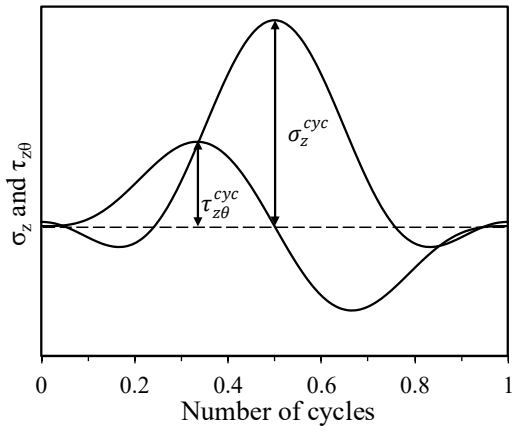

(b)

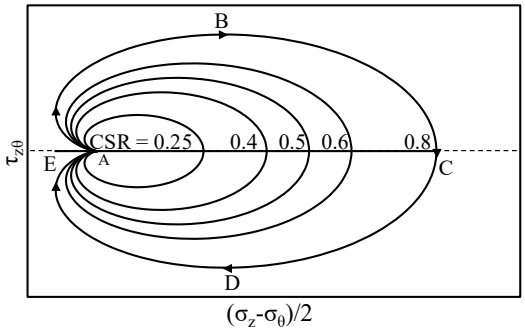

(c)

Figure 5-2. Stress paths: (a) thermo-hydro-mechanical paths before cyclic loading; (b) variations of vertical stress and shear stress during cyclic loading; (c) stress paths in the $\tau_{z\theta} - (\sigma_z - \sigma_\theta)/2$ plane during cyclic loading

As suction and thermal equilibrium were obtained, specimens were subjected to cyclic loading. The variation of vertical stress σ_z and shear stress $\tau_{z\theta}$ in one cycle was given in Figure 5-2(b). The waveforms were defined by the following equations (Cai et al., 2017):

$$\sigma_z = \sigma_z^{cyc}\left[\frac{1}{4}\cos(4\pi Ft) - \frac{1}{2}\cos(2\pi Ft) + \frac{1}{4}\right] \quad (5\text{-}11)$$

$$\tau_{z\theta} = \tau_{z\theta}^{cyc}\left[\frac{4}{3\sqrt{3}}\sin(2\pi Ft) - \frac{2}{3\sqrt{3}}\sin(4\pi Ft)\right] \quad (5\text{-}12)$$

where F is the frequency and t is the time in seconds. Note that the value of $\tau_{z\theta}^{cyc}$ was set as zero in series II, resulting in zero shear stress and the absence of PSR during testing. Noted that the stress and strain distributions in the hollow cylindrical specimen are nonuniform, especially when the inner cell pressure P_i and outer cell pressure P_o are unequal (Hight et al., 1983). Hence, these two pressures were kept identical and constant during cyclic loading.

Figure 5-2(c) shows the applied stress path in the $\tau_{z\theta} - (\sigma_z - \sigma_\theta)/2$ plane, where heart-shaped stress paths were applied. Previous studies have demonstrated that such a heart-shaped stress path can well represent the traffic loads (Cai et al., 2018; Guo et al., 2018; Fedakar et al., 2021). For tests involving PSR (series I and series III), the stress path followed the sequence A→B→C→D→A. In contrast, for tests without PSR (series II), the path followed A→E→C →E→A.

5.2 Cyclic behaviour with principal stress rotation

5.2.1 Typical cyclic behaviour

Figure 5-3 shows the typical cyclic response observed from specimen S0T5. In Figure 5-3(a), the first five cycles at CSRs of 0.25, 0.4, and 0.5, along with the last five cycles before failure, are presented. It is evident that the hysteresis loops of the stress-strain curves enlarge with increasing CSR, and the specimen failed at a CSR of 0.5 after approximately 700 cycles.

Similar to conventional cyclic triaxial tests, permanent vertical strain and resilient modulus are determined based on the stress-strain curve and used to investigate soil deformation quantitatively. As shown in Figure 5-3(b) to (d), excess PWP, permanent vertical

strain, and resilient modulus vary with the number of cycles, with their rates of change dependent on the magnitude of CSR.

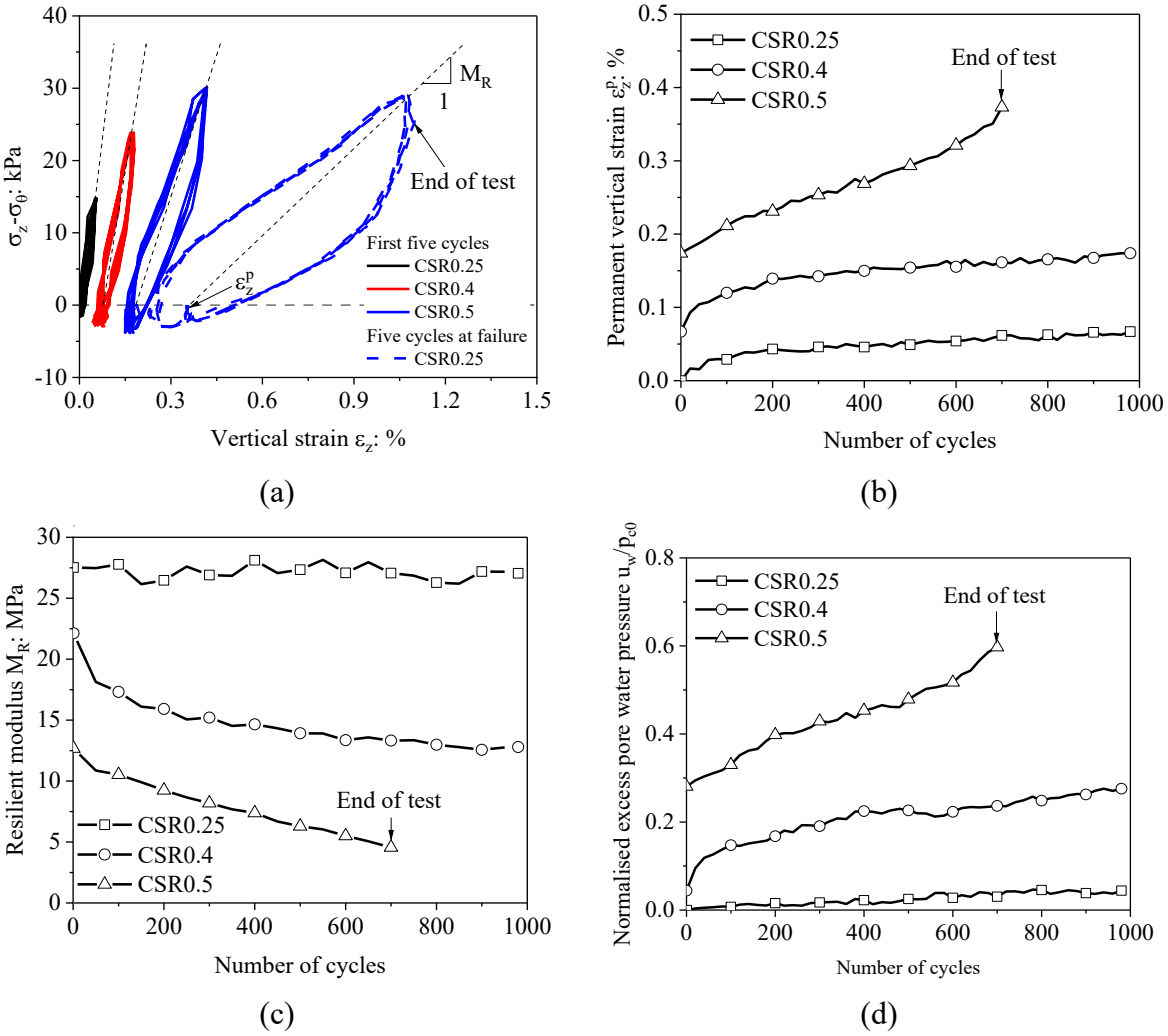

Figure 5-3. Typical cyclic behaviour obtained from specimen S0T5: (a) stress-strain curves; (b) permanent vertical strains; (c) resilient moduli; (d) normalised excess PWPs

At a CSR of 0.25, the permanent vertical strain increases significantly during the initial 500 cycles and subsequently stabilises, indicating a plastic shakedown behaviour (Werkmeister, 2003). The resilient modulus remains nearly constant throughout the loading cycles, despite a reduction in effective confining pressure due to increased excess PWP. The almost constant modulus is likely attributed to the stiffening of the soil skeleton caused by particle rearrangements associated with plastic strain, which offsets the effects of the reduced effective confining pressure. At a CSR of 0.4, both the excess PWP and permanent vertical strain increase with the number of cycles, although the rate of increase diminishes. Concurrently, the

resilient modulus decreases, with the rate of reduction also decreasing gradually. These trends indicate that the specimen is approaching a stable state at a CSR of 0.4. In contrast, at a CSR of 0.5, the excess PWP and permanent vertical strain continue to increase, while the resilient modulus decreases consistently with the number of cycles. The incremental/decremental rates either remain constant or increase with the loading cycle, ultimately leading to specimen failure after several hundred cycles. This behaviour aligns with the incremental collapse mechanism described in shakedown theory (Werkmeister, 2003; Chen et al., 2020). The CSR-dependent response is likely due to the reduction in plastic modulus with increasing cyclic stress (Zhou et al., 2015).

5.2.2 Effects of temperature on cyclic behaviour under various suctions

Figure 5-4 illustrates the effects of temperature on cyclic behaviour under different suctions based on results from test series I. The data from the last ten cycles under different CSRs are presented. Note that the saturated specimens failed at a CSR of 0.5, and thus only results at CSRs of 0.25 and 0.4 are reported for specimens S0T5, S0T20, and S0T40.

Figure 5-4(a) gives the normalised excess PWPs under various temperatures and suctions. It is evident that at suctions of 10 and 30 kPa, the accumulation of excess PWP is negligible, remaining near zero. Under saturated conditions, however, excess PWP increases with temperature. For instance, at a CSR of 0.25, excess PWP increases by approximately 110% as the temperature rises from 5 to 40 ℃. According to the double layer theory (Israelachvili, 2011), an increase in temperature will increase the electric repulsive force between soil particles. The increased repulsive force reduces inter-particle force (Casarella et al., 2021) and results in lower OCRs at elevated temperatures, as widely reported in the literature (Cekerevac and Laloui, 2004; Uchaipichat and Khalili, 2009; Zhou and Ng, 2015). Consequently, a higher temperature leads to a greater tendency for contraction and the generation of a larger excess PWP. Conversely, Cekerevac and Laloui (2010) found that the heated kaolin (a low-plasticity clay) had a smaller excess PWP than the unheated specimen. The difference between these two studies mainly arises from the fact that the specimens were heated under different OCRs. In

the present study, saturated specimens were cooled/heated under an OCR of approximately 4, resulting in largely reversible volumetric strains with limited influence on soil behaviour. In contrast, Cekerevac and Laloui (2010) applied thermal loading under normally consolidated conditions, which induced contractive volumetric strains of about 1%, densifying the soil and thereby reducing the generated excess PWP.

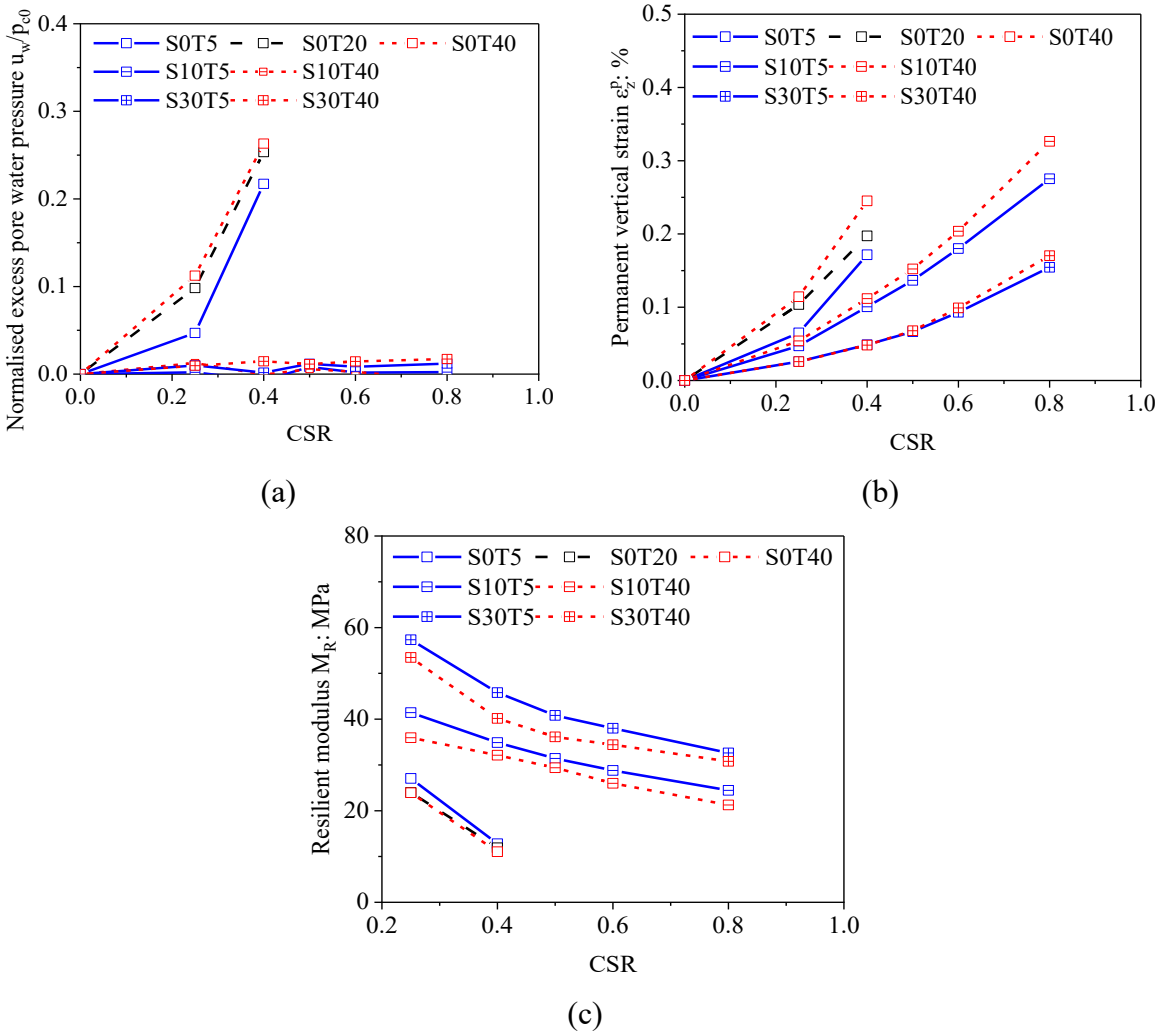

Figure 5-4. Effects of temperature on cyclic behaviour under various suctions: (a) normalised excess PWPs; (b) permanent vertical strains; (c) resilient moduli

Figure 5-4(b) presents the permanent vertical strains under different temperatures and suctions. It can be seen that permanent vertical strain increases with rising temperature. This trend can be attributed to the reduction in preconsolidation pressure with increasing temperature, as reported in previous studies (e.g., kaolin in Cekerevac and Laloui, 2004; silt in Uchaipichat and Khalili, 2009) The decrease in preconsolidation pressure leads to a lower OCR

and therefore a larger permanent vertical strain. More importantly, the effects of temperature become increasingly pronounced at lower suctions and higher CSRs. For instance, as temperature rises from 5 to 40 ℃ at a CSR of 0.25, permanent vertical strain increases by 75%, 15%, and 0% at initial suctions of 0, 10, and 30 kPa, respectively. These suction- and CSR-dependent temperature effects are likely attributed to variations in OCR, which tends to be higher at higher suctions and lower CSRs. As shown by Qian et al. (2019b), permanent strain becomes less sensitive to OCR reduction at higher OCR ranges. Therefore, as temperature increases, the associated reduction in OCR has a limited effect on permanent vertical strain under conditions of higher suction and lower CSR, where OCR remains relatively high (exceeding 6 for specimens with 30 kPa suction and CSR of 0.25). Conversely, for lightly overconsolidated specimens with lower suctions and higher CSRs (e.g., OCR is close to 3 at zero suction and CSR of 0.4), the temperature-induced decrease in OCR leads to a substantial increase in permanent vertical strain.

Figure 5-4(c) shows that resilient modulus decreases with temperature at a given suction and CSR. Moreover, the temperature-induced reduction is more significant under unsaturated conditions than under saturated conditions. Specifically, when the temperature increases from 5 to 40 ℃ at a CSR of 0.25, the resilient modulus decreases by approximately 10% under saturated conditions and 15% under unsaturated conditions. Similar findings were reported by Ng and Zhou (2014) in cyclic triaxial tests without PSR, where the temperature effects on resilient modulus were more pronounced at suctions of 30 and 60 kPa than under saturated conditions. This phenomenon is likely associated with the temperature dependency of surface tension, which decreases with increasing temperature, thereby reducing the capillary-induced normal force between soil particles (Ng and Zhou, 2014). Furthermore, as surface tension decreases, the water retention capacity of soil becomes weaker and the degree of saturation at a given suction decreases (Romero et al., 2001), leading to a reduction in Bishop's stress (Gallipoli et al., 2003a). Consequently, under unsaturated conditions, the combined reductions in capillary-induced normal force and Bishop's stress with increasing temperature result in a more pronounced decrease in resilient modulus compared to saturated conditions.

5.2.3 Effects of suction on cyclic behaviour under different temperatures

Figure 5-5 presents the variations of permanent vertical strain and resilient modulus with suction under various temperatures and CSRs obtained from test series I. It is evident that permanent vertical strain decreases and resilient modulus increases with increasing suction. As suction increases from 0 to 30 kPa, permanent vertical strain decreases by over 50%, while resilient modulus approximately doubles. Similar suction effects on cyclic behaviour have been reported in the literature under room temperature conditions (e.g., low-plasticity clay in Yang et al., 2008b; clayey sand in Azizi et al., 2023), where increasing suction leads to reduced permanent vertical strain and increased resilient modulus. These trends are attributed to the increase in Bishop's stress and the interparticle normal force with increasing suction, which increases the preconsolidation pressure and contributes to the stabilisation of the soil skeleton (Alonso et al., 1990; Wheeler et al., 2003b).

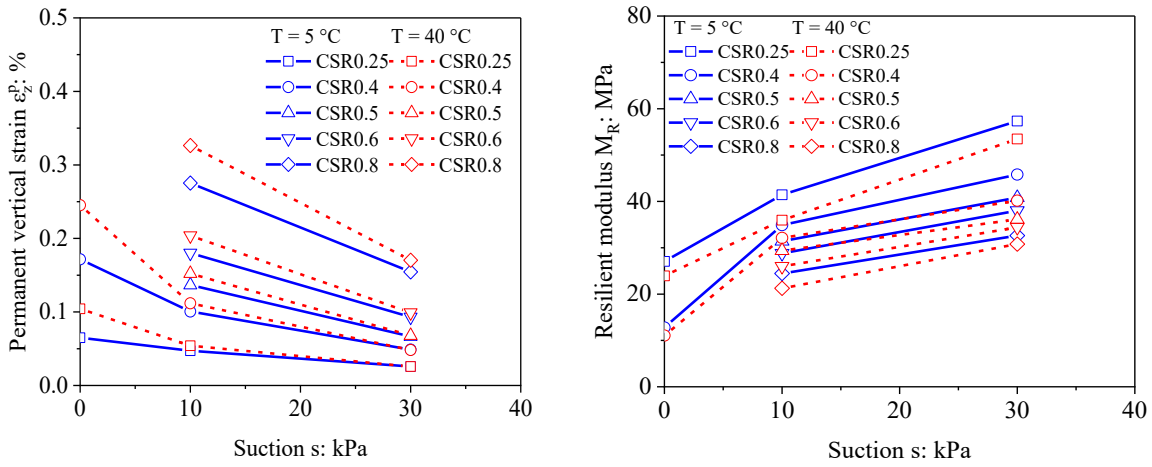

(a) (b)

Figure 5-5. Effects of suction on cyclic behaviour under various temperatures: (a) permanent vertical strains; (b) resilient moduli

Moreover, the reductions in permanent vertical strain and the increases in resilient modulus are more pronounced when suction increases from 0 to 10 kPa, relative to the increment from 10 to 30 kPa. This pattern is primarily attributed to the distribution of water within the soil specimen. At zero suction, the specimen is fully saturated, and its mechanical behaviour is governed by bulk water. As suction increases to 10 and 30 kPa, the soil response progressively transitions to one regulated by meniscus water (Mancuso et al., 2002). In the bulk

water-dominated regime, cyclic loading generates substantial excess PWP (see Figure 5-4(a)), thereby reducing the effective confining pressure and weakening the soil skeleton. In contrast, the presence of water menisci induces additional normal forces between soil particles, thereby stiffening the soil skeleton (Wheeler et al., 2003b). As a result, increasing suction from 0 to 10 kPa transitions the soil behaviour from bulk water-dominated to meniscus water-regulated, leading to a marked reduction in permanent vertical strain and a notable increase in resilient modulus.

5.2.4 Effects of PSR, temperature, and suction on cyclic behaviour

Figure 5-6 illustrates the influence of PSR on the cyclic behaviour of saturated specimens at various temperatures, based on data from series I and II. At a given temperature and CSR, specimens subjected to PSR consistently exhibit larger excess PWP and permanent vertical strain, and smaller resilient modulus than those without PSR. For instance, when PSR is incorporated at a temperature of 5 ℃ and a CSR of 0.25, the excess PWP and permanent vertical strain increase by approximately 75% and 55%, respectively, while the resilient modulus decreases by about 5%. Over the past decade, studies based on saturated tests at room temperature have consistently reported increased permanent vertical strain and reduced resilient modulus due to the incorporation of PSR (Gräbe and Clayton, 2014; Cai et al., 2018; Fedakar et al., 2021). These effects arise because both fixed-direction loading (deviatoric stress variation without PSR) and rotational loading (i.e., PSR) contribute to soil deformation (Li and Dafalias, 2004). The additional deformation induced by PSR leads to greater total deformation under identical cyclic deviatoric stress, thereby rendering the soil overall softer when PSR is applied. This rotational loading mechanism is strongly linked to the stress-induced and inherent anisotropic structure of the soil, with PSR causing additional plastic deformation in anisotropic soils (Li and Dafalias, 2004; Yang et al., 2007; Tian and Yao, 2018; Zhao et al., 2025).

Furthermore, Figure 5-6(b) demonstrates that the additional permanent vertical strain induced by PSR increases with both temperature and CSR. For example, as temperature rises from 5 to 40 ℃ at a CSR of 0.4, the PSR-induced additional permanent vertical strain increases

from 0.10% to 0.17%. This behaviour is primarily due to the reduction in OCR at elevated temperatures and higher CSRs. These findings indicate that the rotational loading mechanism is sensitive to temperature and CSR, which should be incorporated into constitutive models accounting for PSR.

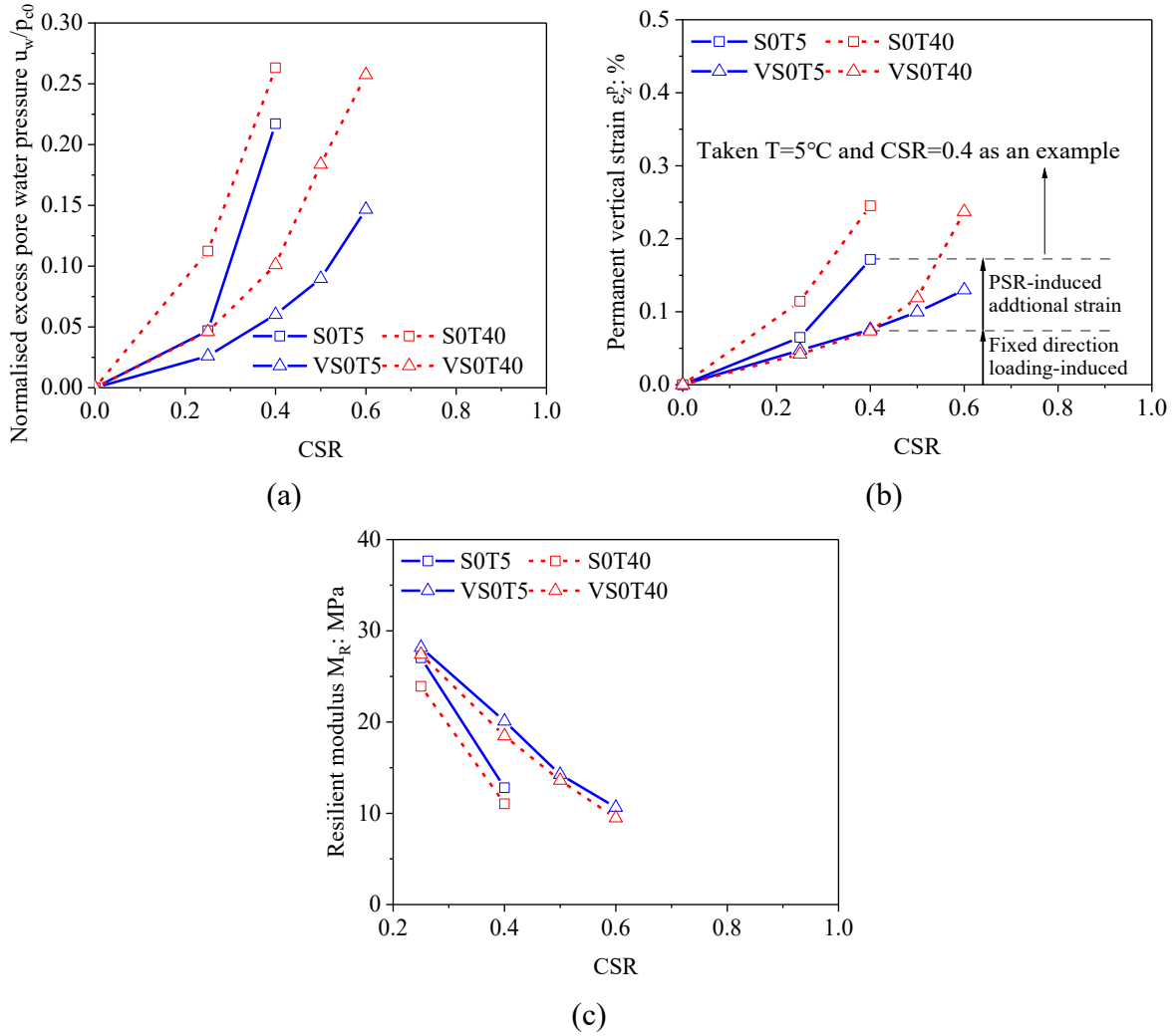

Figure 5-6. Effects of PSR on cyclic behaviour under saturated conditions: (a) normalised excess PWPs; (b) permanent vertical strains; (c) resilient moduli

Figure 5-7 illustrates the effect of PSR on permanent vertical strain and resilient modulus at an initial suction of 10 kPa, obtained from test series I and II. Consistent with the results in Figure 5-6, specimens subjected to PSR exhibit a larger permanent vertical strain and a smaller resilient modulus compared to those without PSR. A comparison between Figure 5-6(b) and Figure 5-7(a) indicates that the PSR-induced additional strain diminishes as suction increases, attributed to the stabilising influence of the water meniscus on the soil skeleton.

More importantly, relative to the strain without PSR, the PSR-induced additional strain becomes increasingly significant at higher temperatures and lower suctions. For instance, at zero suction and a CSR of 0.4, the PSR-induced additional strain reaches 130% and 230% of the strain without PSR at 5 and 40 °C, respectively. When suction increases to 10 kPa, these ratios reduce to 50% and 80%, respectively. The temperature- and suction-dependent PSR effects are attributed to the decrease in OCR with rising temperature and decreasing suction. At lower OCR values, the influence of PSR on permanent vertical strain is more pronounced, as supported by Gräbe (2002).

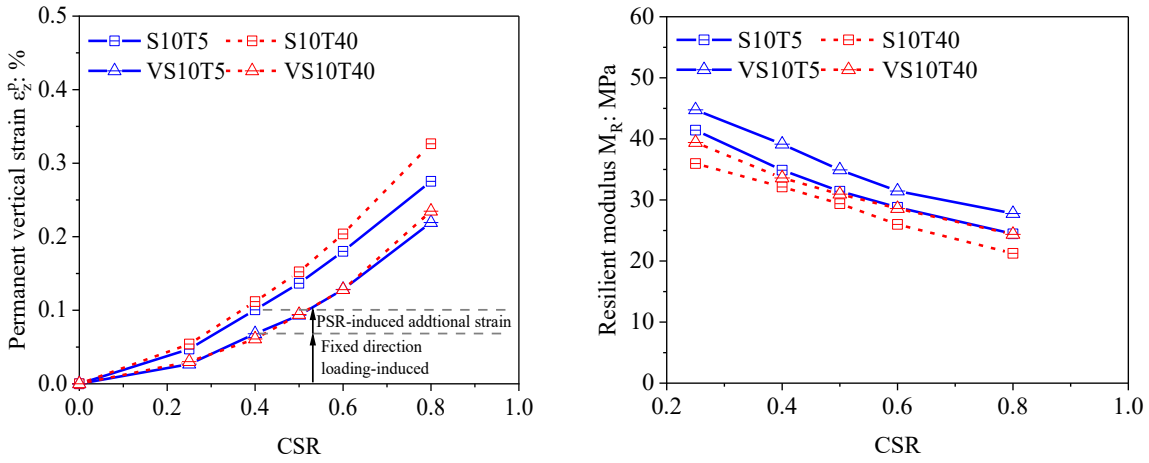

(a) (b)

Figure 5-7. Effects of PSR on cyclic behaviour under unsaturated conditions: (a) permanent vertical strains; (b) resilient moduli

The results presented in Figure 5-6 and Figure 5-7 emphasise the significant influence of PSR on cyclic behaviour across different temperatures and suctions. Generally, permanent deformation is larger and resilient modulus is smaller when PSR is incorporated. Moreover, the impact of PSR intensifies substantially with increasing temperature and decreasing suction. Specifically, under the lowest suction and highest temperature tested in this study (s = 0 kPa and T = 40 °C), PSR induces a 230% increase in permanent vertical strain and a 35% reduction in resilient modulus compared to specimens without PSR at a CSR of 0.4.

5.2.5 Effects of confining pressure and temperature on cyclic behaviour

Figure 5-8 illustrates the influence of confining pressure on cyclic behaviour at temperatures of 5 and 40 °C, based on data from test series I and III. It should be noted that

specimens subjected to an initial confining pressure of 60 kPa failed at a CSR of 0.4, and only results corresponding to a CSR of 0.25 are presented.

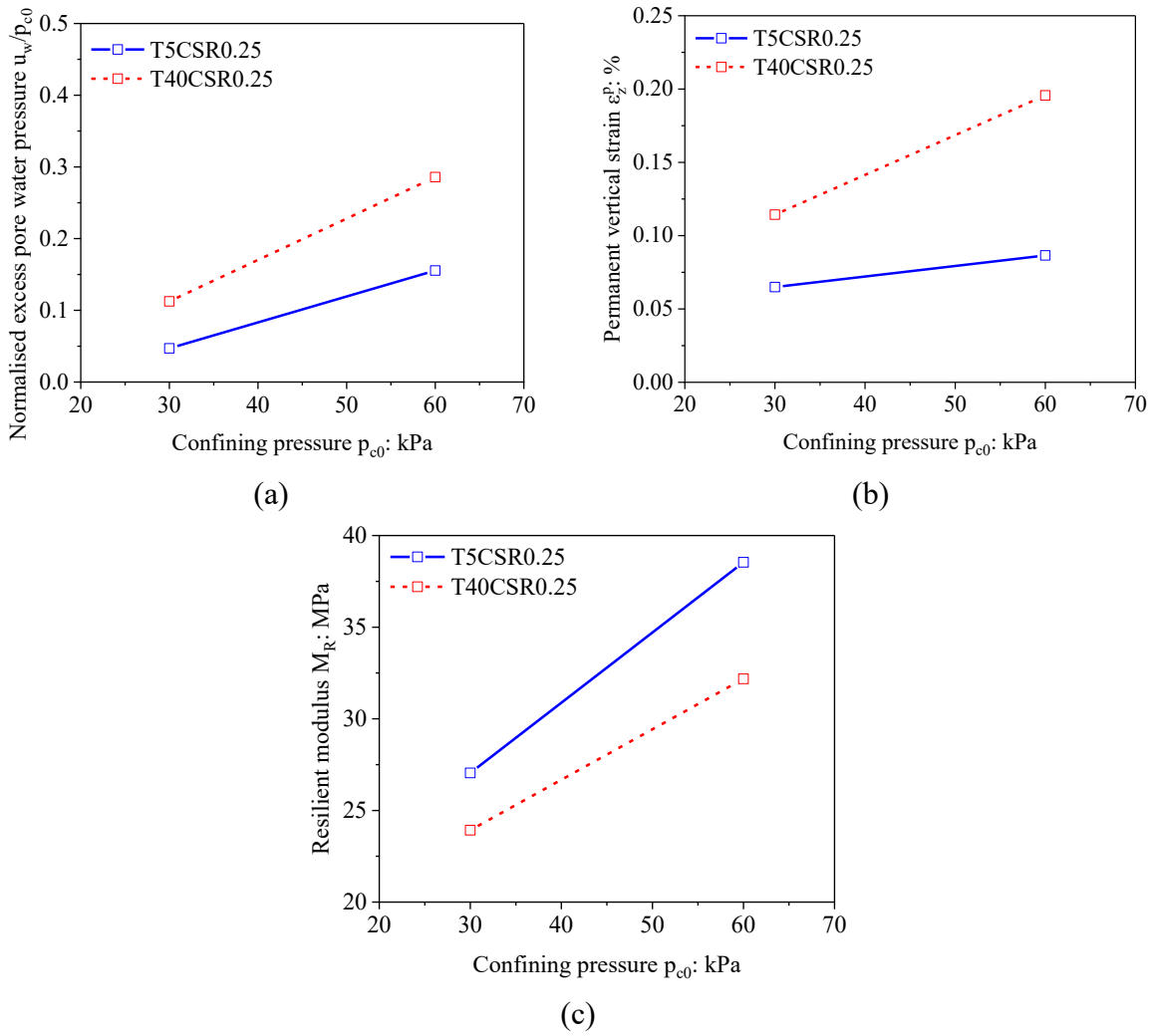

Figure 5-8. Effects of confining pressure on cyclic behaviour: (a) normalised excess PWPs; (b) permanent vertical strains; (c) resilient moduli

It can be observed that normalised excess PWP, permanent vertical strain, and resilient modulus all increase with increasing confining pressure. For instance, when confining pressure increases from 30 to 60 kPa at 5 °C, normalised excess PWP, permanent vertical strain, and resilient modulus increase by approximately 200%, 30%, and 40%, respectively. Consistent trends have been observed by Guo et al. (2013) for a high-plasticity clay and Wang et al. (2024) for a silt. These findings indicate that, under a given CSR, increasing confining pressure leads to increased irreversible deformation during cyclic loading-unloading, while the reversible strain during unloading decreases. The confining pressure appears to influence reversible and

irreversible strains through distinct mechanisms.

Firstly, the influence of confining pressure on irreversible deformation can be attributed to the reduction in the OCR as confining pressure increases under a constant CSR. According to the bounding surface theory (Dafalias, 1986b; Zhou and Ng, 2015), the plastic modulus decreases with decreasing OCR at a given CSR. As a result, the reduced plastic modulus governs the irreversible deformation, leading to increased normalised excess PWP and permanent vertical strain.

Secondly, interparticle contacts are strengthened as confining pressure increases. These enhanced contacts primarily control the resilient modulus under saturated conditions, causing the resilient modulus to increase with rising confining pressure. Note that when confining pressure increases (constant CSR) under unsaturated conditions, resilient modulus may decrease at relatively high suction (e.g., Sivakumar et al., 2013). This is because the Bishop's stress between soil particles remains almost constant as confining pressure increases under relatively high suction, and the interparticle contacts are nearly unaffected. Consequently, the increasing deviatoric stress predominates, leading to a reduction in resilient modulus.

Figure 5-8 also reveals that the influence of temperature on cyclic behaviour is affected by confining pressure. On the one hand, the increments in normalised excess PWP and permanent vertical strain with increasing temperature are more obvious at a higher confining pressure. When temperature rises from 5 to 40 ℃, permanent vertical strain increases by about 75% at a confining pressure of 30 kPa, whereas the increment becomes 125% at a confining pressure of 60 kPa. This trend is attributed to the decrease in OCR with increasing confining pressure, and the temperature effects on plastic deformation are more significant for specimens with a lower OCR, consistent with the results shown in Figure 5-4(b).

On the other hand, the reduction in resilient modulus with increasing temperature is more pronounced at a higher confining pressure. With temperature rises from 5 to 40 ℃, resilient modulus decreases by about 10% and 15% at confining pressures of 30 and 60 kPa, respectively. This finding is most likely because the increment in normalised excess PWP with temperature

is greater at 60 kPa (see Figure 5-8(a)), resulting in a more significant reduction in the effective confining stress and resilient modulus at a higher confining pressure.

Analysis shows that at a constant CSR, the thermal softening effects (manifested by larger normalised excess PWP and permanent strain, and smaller resilient modulus) are more pronounced at higher confining pressures. Therefore, the influence of confining pressure must be carefully considered when integrating thermal effects into pavement design guidelines. Neglecting this factor may lead to nonconservative designs, as elevated confining pressures intensify thermal softening and thus compromise pavement performance.

5.3 Modelling effects of PSR, temperature, and suction on resilient modulus

In most existing pavement design guidelines (e.g., AASHTO, 2020), the resilient modulus is regarded as one of the most critical stiffness parameters for analysing soil deformation under repeated traffic loads. The results of this study, along with findings from the literature (e.g., Gräbe and Clayton, 2014; Ng and Zhou, 2014; Guo et al., 2018; Blackmore et al., 2020), demonstrate that resilient modulus is significantly influenced by PSR, suction, and temperature. Generally, the resilient modulus of subgrade soil decreases with increasing temperature, decreasing suction, and the presence of PSR. However, current design guidelines (e.g., NCHRP, 2004; AASHTO, 2020) only consider the unsaturation effects on resilient modulus in a simplified approach while ignoring the influence of PSR and temperature. The ignorance of PSR and thermal effects may lead to significant underestimation of irreversible deformation in subgrade soils, thereby increasing the risk of pavement distress such as cracking and rutting (Brown, 1996).

It is recommended to conduct temperature- and suction-controlled cyclic torsional shear tests to determine resilient modulus. In the absence of an advanced testing apparatus, this study proposes a novel semi-empirical equation to enable the consideration of the coupled effects of PSR, temperature, and suction on resilient modulus:

$$M_R = M_0 \left(\frac{p_{c0}}{p_r}\right)^{k_1} \left(1 + \sigma_z^{cyc} \sqrt{1 + 4\eta_\tau^2}/p_{c0}\right)^{k_2} \left(1 + \frac{s_0}{p_r}\right)^{k_3} \left(\frac{T+273}{T_r+273}\right)^{k_4} \quad (5\text{-}13)$$

where M_0 denotes the resilient modulus at the reference state, defined by $p_{c0} = p_r$, negligible σ_z^{cyc}, $T = T_r$, and s_0 = 0 kPa; k_1, k_2, k_3, and k_4 are parameters related to the influence of confining pressure, vertical stress and PSR, suction, and temperature, respectively; p_r is a reference pressure, taken as 1 kPa; η_τ represents the ratio of cyclic shear stress to cyclic vertical stress (i.e., $\tau_{z\theta}^{cyc}/\sigma_z^{cyc}$); and T_r is the reference temperature, taken as 20 ℃. The proposed equation demonstrates its uniqueness in modelling the effects of PSR and temperature compared to existing equations for resilient modulus.

In Equation (5-13), the influence of PSR is considered in the stress term $\sigma_z^{cyc}\sqrt{1+4\eta_\tau^2}$, which is the simplified form of $\sqrt{\left(\sigma_z^{cyc}-\sigma_\theta^{cyc}\right)^2+\left(2\tau_{z\theta}^{cyc}\right)^2}$ when the cyclic circumferential stress σ_θ^{cyc} is equal to zero (Guo et al., 2018). The key idea is that the incorporation of PSR can be interpreted as an equivalent increase in cyclic vertical stress, and such an increase becomes more pronounced with a higher shear stress ratio η_τ, consistent with previous experimental observations (Cai et al., 2015; Cai et al., 2018; Guo et al., 2018). One major advantage of this modelling approach is that it incorporates the PSR effects without introducing any new parameters. In the absence of principal stress rotation (i.e., $\eta_\tau = 0$), the stress term $\sigma_z^{cyc}\sqrt{1+4\eta_\tau^2}$ reduces to the cyclic deviatoric stress q^{cyc}, thereby ensuring continuity between test conditions with and without PSR.

To evaluate the performance of Equation (5-13), Figure 5-9 presents a comparison between the measured and computed resilient moduli using the model parameters listed in Table 5-2. Both the data obtained in the current study and those reported in the literature (Ng and Zhou, 2014; Cai et al., 2018; Guo et al., 2018) are included. The effects of temperature and suction in the absence of PSR are validated against the experimental results of Ng and Zhou (2014). Meanwhile, the influence of PSR under room temperature and saturated conditions is assessed using the data from Cai et al. (2018) and Guo et al. (2018). The coupled effects of PSR, temperature, and suction are further examined using the results from the present study. The strong agreement between the computed and measured resilient moduli confirms that (5-13) effectively captures the combined effects of PSR, temperature, and suction.

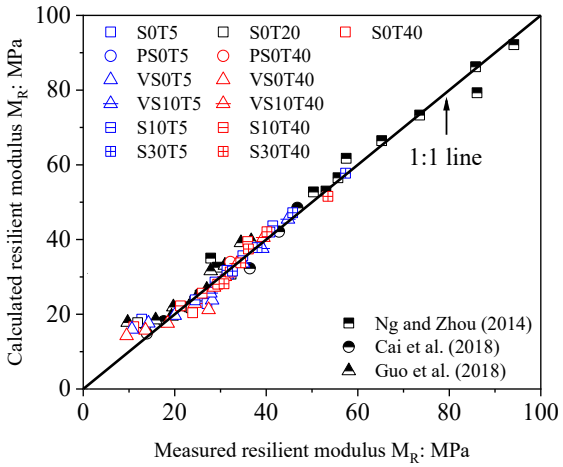

Figure 5-9. Comparisons between the measured and calculated resilient moduli

Table 5-2. Parameters used for calculating resilient modulus

Parameter	Current study	Ng and Zhou (2014)	Guo et al. (2018)	Cai et al. (2018)
M_0: MPa	7.72	1.26	0.96	0.82
k_1	0.44	1.18	0.99	0.97
k_2	-1.04	-1.01	-1.70	-3.81
k_3	0.27	0.24	-*	-
k_4	-0.96	-1.05	-	-

*Notation: the tests of Guo et al. (2018) and Cai et al. (2018) were performed under isothermal and saturated conditions, and the parameters related to temperature and suction (i.e., k_3 and k_4) are unnecessary.

Further inspections of Table 5-2 reveals that the parameter associated with the temperature effects (i.e., k_4) is close to -1 in both this study and the work by Ng and Zhou (2014) , which involved low-plasticity clay and silt, respectively. It suggests that when temperature-controlled tests are not feasible, the thermal effects on resilient modulus can be considered by $[(T+273)/(T_r+273)]^{-1}$ as an approximation, at least for fine-grained soils. Under such circumstances, compared to existing equations for the resilient modulus of subgrade soil (e.g., Ng et al., 2013), Equation (5-13) requires no additional parameters but has new capabilities for incorporating the influence of temperature and PSR.

5.4 Summary and conclusions

In this chapter, temperature- and suction-controlled units were integrated into the existing

dynamic hollow cylinder apparatus. A series of cyclic tests featuring heart-shaped stress paths were performed on compacted loess to investigate the effects of PSR, suction, temperature, and confining pressure. Additionally, a series of cyclic tests without PSR was conducted for comparison. The main conclusions are summarised as follows:

Permanent vertical strain increases and resilient modulus decreases with increasing temperature and decreasing suction, primarily due to reductions in preconsolidation pressure and OCR. The temperature-induced increase in permanent vertical strain is more pronounced at lower suctions because the OCR decreases with decreasing suction, and the significance of thermo-plasticity is more pronounced at lower OCRs. Moreover, the decrease in resilient modulus with rising temperature is more pronounced under unsaturated conditions than in saturated conditions. This results from the temperature-driven reduction in surface tension, which reduces both Bishop's stress and the normal force between soil particles caused by the water meniscus.

Specimens subjected to PSR exhibit larger excess PWP and permanent vertical strain, and smaller resilient modulus than those without PSR. These trends are mainly because rotational loading can induce additional deformation for anisotropic soils. More importantly, the additional strain induced by PSR increases with increasing temperature and decreasing suction, as a result of a less stabilised soil skeleton. In comparison to the strain without PSR, the strain induced by PSR becomes increasingly significant at higher temperatures and lower suctions. At zero suction and a CSR of 0.4, the PSR-induced additional strain is 130% and 230% of the strain without PSR under temperatures of 5 and 40 ℃, respectively. As suction increases to 10 kPa, these two ratios are 50% and 80%, respectively. The coupled effects of PSR, temperature, and suction are likely due to the reduction in OCR with increasing temperature and decreasing suction, wherein the impact of PSR on permanent strain is more pronounced at lower OCRs.

At a given CSR, the normalised excess PWP, permanent vertical strain and resilient modulus all increase as confining pressure increases from 30 to 60 kPa. The increased normalised excess PWP and permanent vertical strain are mainly because the plastic modulus

decreases when OCR decreases while CSR remains constant. The rise in resilient modulus is due to enhanced interparticle contacts at higher confining pressures. Moreover, the influence of temperature on cyclic behaviour becomes more pronounced at 60 kPa, owing to the further reduction in OCR at higher confining pressures.

In light of these new findings, it is essential to incorporate the combined effects of PSR, temperature, and suction on resilient modulus into pavement design practices to ensure safety. To support this consideration, a new and straightforward semi-empirical equation for resilient modulus has been proposed. This equation effectively captures the coupled influences of PSR, temperature, and suction without requiring additional parameters, offering a practical enhancement to current design approaches.

CHAPTER 6 A NEW CONSTITUTIVE MODEL FOR UNSATURATED STRUCTURED AND ANISOTROPIC SOILS

In this chapter, a new constitutive model for unsaturated structured and anisotropic soils under both monotonic and cyclic loading conditions is proposed. Based on experimental results from Chapter 3 to Chapter 5 and in the literature, the structure effects on the loading collapse curve are considered, and the increase in water retention capacity with an increasing degree of anisotropy is incorporated by a new anisotropy- and void ratio-dependent soil water retention equation. The model's performance is validated using experimental data from previous chapters and existing literature.

6.1 Model formulations

6.1.1 Stress and strain variables

The model formulations are presented in the triaxial stress space using the mean Bishop's stress p^* and the deviatoric stress q:

$$\begin{cases} p^* = \frac{\sigma_a + 2\sigma_r}{3} - u_a + sS_r^e \\ q = \sigma_a - \sigma_r \end{cases} \tag{6-1}$$

where σ_a is the axial stress; σ_r is the radial stress; and the effective degree of saturation S_r^e is calculated as $S_r^e = \langle S_r - S_r^r \rangle / (1 - S_r^r)$. It is widely recognised that the inclusion of suction and the effective degree of saturation in Equation (6-1) is not sufficient to capture the behaviour of unsaturated soils. One of the main reasons is that, under unsaturated conditions, water menisci can increase the normal force at inter-particle contacts, resulting in stabilising effects on the soil skeleton (Wheeler et al., 2003b). To model such additional suction effects, the bonding variable ξ, proposed by Gallipoli et al. (2003a) is used as a complementary constitutive variable:

$$\xi = f(s)(1 - S_r^e) \tag{6-2}$$

At the fully saturated state (S_r = 1), p^* reduces to the effective stress formulation of Terzaghi (1943), and ξ becomes zero. Therefore, the stress variables employed ensure continuity between saturated and unsaturated conditions.

6.1.2 Effects of soil structure and unsaturation on the NCL of isotropic soils

Figure 2-9(a) illustrates the typical isotropic compression behaviour of structured and reference (either reconstituted or compacted) soils under both saturated and unsaturated conditions. The normal compression line for the saturated reference soil can be expressed as follows:

$$e = N(0) - \lambda(0) \ln \frac{p^*}{p_r} \tag{6-3}$$

where $N(0)$ and $\lambda(0)$ represent the intercept and slope of the isotropic normal compression line, respectively. Owing to the stabilisation effects of soil structure and unsaturation, the normal compression line under any condition lies above that for the saturated reference soil. As illustrated in Figure 2-9(a), three variables, Δe_1, Δe_2, and Δe_3, are defined at the yield points. These variables represent the additional void ratios attributed to structure effects, unsaturation effects, and the coupled effects of structure and unsaturation, respectively. The calculations of these void ratio increments are provided below.

6.1.2.1 Modelling the structure effects under saturated conditions

A soil specimen with a more resistant structure is characterised by a greater additional void ratio Δe_1 and a higher isotropic yield stress. According to Figure 2-9(a), Δe_1 can be calculated as follows:

$$\Delta e_1 = [\lambda(0) - \kappa] \ln \frac{p_0^s(0)}{p_0^r(0)} \tag{6-4}$$

where $p_0^r(0)$ and $p_0^s(0)$ represent the isotropic yield stresses of isotropic reference and structured soils, respectively. Note that the elastic behaviour of the soil is assumed to be isotropic and independent of soil structure. This simplification reduces the number of model parameters without significantly compromising the model's performance, as the soil response

is typically dominated by plastic strains. Accordingly, the value of κ is considered constant for a given soil.

To describe the structure effects, a structure parameter $R(0)$ is defined for saturated soils as follows:

$$R(0) = \frac{p_0^s(0)}{p_0^r(0)} \tag{6-5}$$

Consequently, Equation (6-4) can be reformulated as:

$$\Delta e_1 = [\lambda(0) - \kappa] \ln R(0) \tag{6-6}$$

6.1.2.2 Modelling reference soils under unsaturated conditions

Soil becomes stiffer with progressive desaturation, accompanied by a greater additional void ratio Δe_2 and a higher isotropic yield stress $p_0^r(\xi)$. As illustrated in Figure 2-9(a), relationship between these two parameters is established through the following equation:

$$\Delta e_2 = [\lambda(0) - \kappa] \ln \frac{p_0^r(\xi)}{p_0^r(0)} \tag{6-7}$$

where $p_0^r(\xi)$ is the isotropic yield stress of the isotropic reference soil at a given ξ. Following the study of Gallipoli et al. (2003a), $p_0^r(\xi)$ is determined using the following equation:

$$p_0^r(\xi) = p_r \exp\left(\frac{aN(0)[\exp(b\xi)-1]+(\lambda(0)-\kappa)\ln\frac{p_0^r(0)}{p_r}}{\lambda(0)[1-a+a\exp(b\xi)]-\kappa}\right) \tag{6-8}$$

where a and b are model parameters. By substituting Equation (6-8) to Equation (6-7), Δe_2 can be expressed as follows:

$$\Delta e_2 = \frac{[\lambda(0)-\kappa]a[\exp(b\xi)-1]}{\lambda(0)[1-a+a\exp(b\xi)]-\kappa}\left[N(0) - \lambda(0)\ln\frac{p_0^r(0)}{p_r}\right] \tag{6-9}$$

6.1.2.3 Modelling the coupled effects of structure and unsaturation

Similarly, the additional void ratio Δe_3, attributed to the coupled effects of soil structure and unsaturation, can be related to the isotropic yield stress of the unsaturated structured soil $p_0^s(\xi)$ as follows:

$$\Delta e_3 = [\lambda(0) - \kappa] \ln \frac{p_0^s(\xi)}{p_0^r(0)} \tag{6-10}$$

Equations (6-4), (6-7), and (6-10) suggest that $\Delta e_3 - \Delta e_1$, expressed as $[\lambda(0) - \kappa] \ln[p_0^s(\xi)/p_0^s(0)]$, represents the sensitivity of isotropic yield stress to moisture conditions in the isotropic structured soil (i.e., the inclination of the normalised LC curve in Figure 2-10(b)). In contrast, Δe_2, given by $[\lambda(0) - \kappa] \ln[p_0^r(\xi)/p_0^r(0)]$, corresponds to the same sensitivity in the isotropic reference soil. The normalised LC curve refers to the yield stress at a given ξ, denoted as $p_0(\xi)$, normalised by its value under saturated conditions, $p_0(0)$. A highly inclined normalised LC curve indicates that the yield stress increases significantly with increasing ξ.

According to experimental results reported in the literature, the inclination of the normalised loading collapse curve for structured soils may be smaller than (case-I), greater than (case-II), or equal to (case-III) that of reference soils, as illustrated in Figure 2-10 (Koliji et al., 2009; Arroyo et al., 2013; Mu et al., 2020; Zhang et al., 2020; Mu et al., 2022). Case I is typically observed in soils with strong cementation bonding (Arroyo et al., 2013; Zhang et al., 2020), where the stabilising effects of structure are relatively insensitive to changes in moisture conditions. Accordingly, the value of $\Delta e_3 - \Delta e_1$ is smaller than Δe_2. An example in case-I is cemented soils, where the increase in yield stress with increasing ξ is less pronounced than in uncemented soils, resulting in a less inclined normalised LC curve. Case-II exists in some intact soils dominated by fabric effects, such as intact loess, where clay particles tend to accumulate at inter-particle contacts and stiffen the soil skeleton (Koliji et al., 2009; Mu et al., 2022). The stabilisation effects of these clay particles are significantly enhanced with increasing ξ, producing a highly inclined normalised LC curve. As a result, the difference $\Delta e_3 - \Delta e_1$ exceeds Δe_2. Case-III is identified in structured soils where cementation and fabric effects contribute comparably (Mu et al., 2020). In such cases, the structure effects on the normalised LC curve become negligible, and $\Delta e_3 - \Delta e_1$ equals Δe_2. The above discussion can be summarised by the following equation:

$$\begin{cases} Case-I: \Delta e_3 - \Delta e_1 < \Delta e_2 \\ Case-II: \Delta e_3 - \Delta e_1 > \Delta e_2 \\ Case-III: \Delta e_3 - \Delta e_1 = \Delta e_2 \end{cases} \quad (6\text{-}11)$$

The three cases described in this equation correspond to different types of soil structure, each associated with a particular trend in the normalised LC curves. To properly predict the behaviour of various structured soils, it is essential to develop a unified modelling approach capable of representing all three cases. Moreover, Δe_3 should always be greater than or equal to both Δe_1 and Δe_2, a condition consistently supported by extensive experimental evidence in the literature (Pereira et al., 2014; Haeri, 2016; Zhou and Ng, 2018; Rotisciani et al., 2021). Otherwise, the isotropic yield stress of the structured soil in unsaturation conditions would be lower than that in saturated conditions, and the NCL at a given ξ of the structured soil would lie beneath that of the reference soil, which are not supported by any data in the literature.

Given the above considerations, the following equation is proposed for Δe_3:

$$\Delta e_3 = \Delta e_1 + \Delta e_2 + c \times \frac{\Delta e_1 \Delta e_2}{\Delta e_1 + \Delta e_2} \quad (6\text{-}12)$$

where c is a model parameter that governs the sensitivity of the isotropic yield stress to changes in moisture conditions. Case-I, II, and III are predicted when $c < 0$, $c > 0$, and $c = 0$, respectively. To satisfy the established constraints (i.e., $\Delta e_3 > \Delta e_1$ and $\Delta e_3 > \Delta e_2$), c should be larger than -1. The value of c changes during structure degradation, as elaborated later.

Based on Equations (6-3) to (6-12), the NCL of the unsaturated structured soil under isotropic conditions is described as follows:

$$e = N(0)[1 - a + a\exp(b\xi)] - \left[\lambda(0)[1 - a + a\exp(b\xi)]\right]\ln\frac{p^*}{p_r} + [\lambda(0)[1 - a + a\exp(b\xi)] - \kappa]\ln R(\xi) \quad (6\text{-}13)$$

where $R(\xi)$ is a structure parameter under unsaturated conditions, defined as the ratio $p_0^s(\xi)/p_0^r(\xi)$. When the soil becomes saturated, it yields $R(0)$. By substituting Equations (6-6),

(6-9), and (6-10) into Equation (6-12), the structure parameter $R(\xi)$ can be determined as follows:

$$R(\xi) = R(0)^{1+c/\left[1+\ln R(0)/\ln\frac{p_0^r(\xi)}{p_0^r(0)}\right]} \tag{6-14}$$

Equation (6-14) indicates that when the value of c is negative (case-I), positive (case-II), or zero (case-III), the value of $R(\xi)$ is correspondingly smaller than, greater than, or equal to $R(0)$, respectively.

6.1.3 Elasto-plasticity

6.1.3.1 Elasticity

The total incremental volumetric strain ($d\varepsilon_v$) and deviatoric strain ($d\varepsilon_q$), which are work-conjugate to the mean stress and deviatoric stress, respectively, are decomposed into elastic and plastic components:

$$d\varepsilon_v = d\varepsilon_v^e + d\varepsilon_v^p \tag{6-15}$$

$$d\varepsilon_q = d\varepsilon_q^e + d\varepsilon_q^p \tag{6-16}$$

where the superscripts 'e' and 'p' denote the elastic and plastic components of strain, respectively. The elastic strain is calculated as follows:

$$\begin{cases} d\varepsilon_v^e = \frac{dp^*}{K} \\ d\varepsilon_q^e = \frac{dq}{3G} \end{cases} \tag{6-17}$$

where K and G are the elastic bulk modulus and shear modulus, respectively, and are calculated as follows:

$$\begin{cases} K = \frac{(1+e)p^*}{\kappa} \\ G = \frac{3(1-2\mu)}{2(1+\mu)}K \end{cases} \tag{6-18}$$

6.1.3.2 Bounding surface and mapping rule

Figure 6-1 illustrates the bounding surface of an anisotropic and structured soil. Unlike the yield surface in the classical elasto-plasticity framework, plastic deformation can occur even when loading remains within the bounding surface. The figure also includes the bounding surface of a reference soil that shares the same void ratio and degree of anisotropy as the structured soil. This reference surface serves as a basis for modelling the behaviour of the structured material. Additionally, a loading surface is depicted to define the mapping rule that governs plastic strain rates during loading and unloading within the bounding surface. The mathematical formulations and physical interpretations of these three surfaces are elaborated in the subsequent sections.

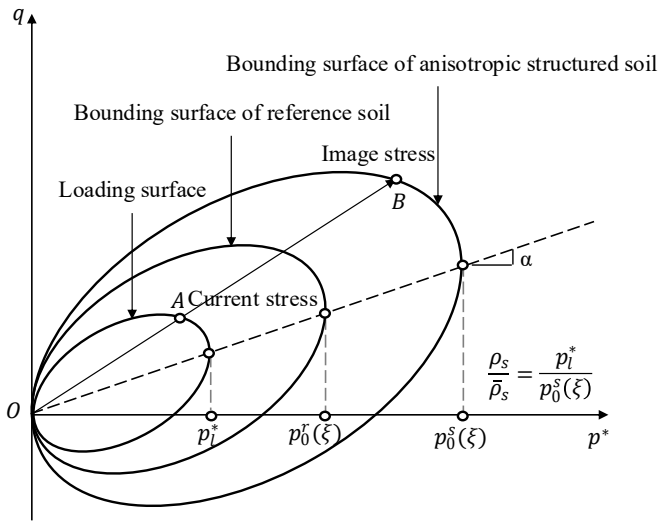

Figure 6-1. Bounding surface and loading surface in the $q - p^*$ plane

Many models for anisotropic soils have been proposed in the literature (e.g., Cui and Delage, 1996; Wheeler et al., 2003a; Dafalias et al., 2006; Dafalias and Taiebat, 2013; Vecchia and Romero, 2013; Al-Sharrad and Gallipoli, 2016; Liao and Yang, 2021a; Liao and Yang, 2021b), although most do not account for the effects of soil structure. In these models, a rotated ellipse is commonly adopted to represent the yield surface or bounding surface (e.g., Dafalias et al., 2002; Wheeler et al., 2003a; Dafalias et al., 2006; Dafalias and Taiebat, 2013,2014; Sitarenios and Kavvadas, 2020). Experimental and theoretical studies have shown that a rotated ellipse is also suitable for anisotropic and structured soils (Belokas and Kavvadas, 2010; Jiang

and Ling, 2010; Liu et al., 2013). Therefore, following the approach adopted for reference soils (Dafalias et al., 2002), the bounding surface of anisotropic and structured soils is modelled using Equation (6-19) and illustrated in Figure 6-1:

$$f = (q - \alpha p^*)^2 - (N^2 - \alpha^2)p^*(p_0^s(\xi) - p^*) = 0 \quad (6\text{-}19)$$

where $p_0^s(\xi)$ defines the size of the bounding surface for the anisotropic structured soil at a given ξ; and α defines the rotation angle of the bounding surface, with α = 0 for isotropic conditions. Its value evolves with plastic strain, as will be discussed later. Experimental results indicate that the inclination of the bounding surface remains consistent under different suctions (Cui and Delage, 1996; Al-Sharrad, 2013; Al-Sharrad et al., 2017). Accordingly, it is assumed that α is independent of suction.

The term $N^2 - \alpha^2$ is the aspect ratio of the bounding surface, where N takes the triaxial compression value N_c when the stress ratio $\eta > \alpha$, and the triaxial extension value N_e when $\eta < \alpha$, with the stress ratio defined as $\eta = q/p^*$. In some constitutive models, the parameter N is set equal to the slope of the critical state line (i.e., $N = M$) (Anandarajah and Dafalias, 1986; Wheeler et al., 2003a). However, some studies have shown that using different values for N and M can enhance the model's ability to capture soil yielding behaviour (Newson and Davies, 1996; Jiang and Ling, 2010; Dafalias and Taiebat, 2013; Al-Sharrad et al., 2017).

In this study, the radial mapping rule is adopted due to its simplicity and effectiveness across a wide range of stress paths (Dafalias, 1986b; Russell and Khalili, 2004; Russell and Khalili, 2006; Zhou and Ng, 2015). The radial mapping rule defines a loading surface that shares the same inclination as the bounding surface of the structured soil but differs in size, as illustrated in Figure 6-1. Accordingly, the loading surface is formulated as follows:

$$f_l = (q - \alpha p^*)^2 - (N^2 - \alpha^2)p^*(p_l^* - p^*) = 0 \quad (6\text{-}20)$$

where p_l^* denotes the size of the loading surface. When the stress state lies within the current bounding surface, points O, A, and B represent the projection centre, the current stress state, and the image stress state, respectively. Based on their relative positions, two Euclidean

distances are defined: ρ_s, the distance between the projection centre and the current stress state $|OA|$, and $\bar{\rho}_s$, the distance between the projection centre and the image stress state $|OB|$. The ratio of these two distances is defined as follows:

$$\frac{\rho_s}{\bar{\rho}_s} = \frac{|OA|}{|OB|} = \frac{p_i^*}{p_0^s(\xi)} \tag{6-21}$$

The ratio $\rho_s/\bar{\rho}_s$ reflects the effects of the stress history and plays a crucial role in the calculation of plastic strains, as discussed later. Note that the adoption of the radial mapping rule is primarily aimed at capturing the gradual yielding behaviour of overconsolidated soils.

6.1.3.3 Flow rule

Based on the principle of plastic work dissipation, Dafalias (1986a) proposed an expression for the plastic potential surface in saturated soils. Following the same methodology, the plastic potential surface in the proposed model is formulated as follows:

$$g = (q - \alpha p^*)^2 - (M^2 - \alpha^2)p^*(p_\alpha^* - p^*) = 0 \tag{6-22}$$

where p_α^* denotes the size of the plastic potential surface. M takes the value M_c when the stress ratio η is higher than α, and M_e when η is lower than α. Based on the plastic potential surface, the increments of plastic volumetric and deviatoric strains are expressed as follows:

$$\begin{cases} d\varepsilon_v^p = \langle L \rangle \frac{\partial g}{\partial p^*} = \langle L \rangle p^*(M^2 - \eta^2) \\ d\varepsilon_q^p = \langle L \rangle \frac{\partial g}{\partial q} = \langle L \rangle 2p^*(\eta - \alpha) \end{cases} \tag{6-23}$$

where the plastic multiplier L is determined using the consistency condition of the bounding surface. The symbol $\langle \ \ \rangle$ is the Macaulay bracket, which distinguishes between plastic loading and elastic unloading: when $L > 0$, plastic loading occurs and $\langle L \rangle = L$; when $L < 0$, elastic unloading occurs and $\langle L \rangle = 0$. When the stress state lies on the bounding surface, the flow rule is computed using Equation (6-22) as follows:

$$\frac{d\varepsilon_v^p}{d\varepsilon_q^p} = \frac{M^2 - \eta^2}{2(\eta - \alpha)} \tag{6-24}$$

When the stress state lies within the bounding surface, Equation (6-22) is modified by incorporating Equation (6-21) and is expressed as follows (Zhou and Ng, 2015):

$$\frac{d\varepsilon_v^p}{d\varepsilon_q^p} = \frac{(M\rho_s/\bar{\rho}_s)^2 - \eta^2}{2(\eta - \alpha)} \tag{6-25}$$

Equation (6-25) indicates that as the ratio $\rho_s/\bar{\rho}_s$ increases with decreasing overconsolidation ratio, the soil exhibits more contractive behaviour. This prediction aligns with experimental observations, which show that soil response transitions from dilative to contractive as OCR decreases (e.g., Zhou and Ng, 2015). Furthermore, when the stress state lies on the bounding surface under normally consolidated conditions, the ratio $\rho_s/\bar{\rho}_s$ becomes to 1 and Equation (6-24) is recovered.

6.1.3.4 Hardening law

To describe the evolution of the size ($p_0^s(\xi)$) and the inclination (α) of the bounding surface, an isotropic hardening law and a rotational hardening law are required, respectively. On the one hand, the change in the size of the bounding surface is related to the plastic volumetric strain increment $d\varepsilon_v^p$, the bonding variable increment $d\xi$, and the structure degradation $dR(\xi)$, and is expressed as follows:

$$dp_0^s(\xi) = \frac{\partial p_0^s(\xi)}{\partial p_0^r(\xi)}\frac{\partial p_0^r(\xi)}{\partial p_0^r(0)}\frac{\partial p_0^r(0)}{\partial \varepsilon_v^p} d\varepsilon_v^p + \frac{\partial p_0^s(\xi)}{\partial p_0^r(\xi)}\frac{\partial p_0^r(\xi)}{\partial \xi} d\xi + \frac{\partial p_0^s(\xi)}{\partial R(\xi)} dR(\xi) \tag{6-26}$$

The first term on the right-hand side of this equation represents volumetric hardening, a mechanism widely adopted in constitutive models. The second term yields $d\xi = (\partial\xi/\partial S_r)dS_r + (\partial\xi/\partial \mathrm{s})ds$ where each partial derivative will be defined later. The third term accounts for structure degradation, which is calculated based on (6-14) as follows:

$$dR(\xi) = \left(\frac{\partial R(\xi)}{\partial p_0^r(0)}\frac{\partial p_0^r(0)}{\partial \varepsilon_v^p} + \frac{\partial R(\xi)}{\partial p_0^r(\xi)}\frac{\partial p_0^r(\xi)}{\partial p_0^r(0)}\frac{\partial p_0^r(0)}{\partial \varepsilon_v^p}\right) d\varepsilon_v^p + \frac{\partial R(\xi)}{\partial p_0^r(\xi)}\frac{\partial p_0^r(\xi)}{\partial \xi} d\xi + \frac{\partial R(\xi)}{\partial R(0)} dR(0) + \frac{\partial R(\xi)}{\partial c} dc \tag{6-27}$$

where $dR(0)$ and dc represent structure degradation under saturated and unsaturated conditions, respectively. Under saturated conditions, the structure degradation $dR(0)$ is closely related to the increments of plastic volumetric and deviatoric strains (Baudet and Stallebrass, 2004; Zhou and Ng, 2018). Under unsaturated conditions, the normalised LC curve

of structured soil shifts towards that of the reference soil as the structure degrades, indicating that the parameter c tends towards zero. Therefore, $dR(0)$ and dc are calculated using the following equations:

$$\begin{cases} \frac{dR(0)}{R(0)-1} = -\beta_1 \sqrt{\left(d\varepsilon_v^p\right)^2 + \left(d\varepsilon_q^p\right)^2} \\ \frac{dc}{c} = \beta_2 \frac{dR(0)}{R(0)-1} \end{cases} \tag{6-28}$$

where β_1 and β_2 are model parameters that control structure degradation under saturated and unsaturated conditions, respectively.

On the other hand, following the approach proposed by Dafalias and Taiebat (2013), the following rotational hardening law is adopted:

$$d\alpha = p_r \langle L \rangle x \frac{p^*}{p_0^s(\xi)} [\alpha_b(\eta) - \alpha] \tag{6-29}$$

where x is a model parameter that controls the evolution rate of α; and $\alpha_b(\eta)$ is the bounding value of α when the soil is subjected to loading under a fixed stress ratio η. This bounding value is calculated using the following equation:

$$\alpha_b(\eta) = \pm \frac{M}{z_1} \left[1 - \exp\left(-z_2 \left|\frac{\eta}{M}\right|\right)\right] \tag{6-30}$$

where the sign "±" takes a positive value when $\eta \geq 0$ and a negative value when $\eta < 0$; and z_1 and z_2 are model parameters that define the bounding value $\alpha_b(\eta)$. Equation (6-30) implies that the inclination of the bounding surface remains non-zero at the critical state ($\eta = M$). Since there is no consistent conclusion regarding soil fabric is isotropic or anisotropic at the critical state, the present study adopts the assumption of an anisotropic fabric.

6.1.3.5 Condition of consistency

The consistency condition for the bounding surface is expressed as follows:

$$df = \frac{\partial f}{\partial p^*} dp^* + \frac{\partial f}{\partial q} dq + \frac{\partial f}{\partial \alpha} d\alpha + \frac{\partial f}{\partial p_0^s(\xi)} dp_0^s(\xi) = 0 \tag{6-31}$$

Based on Equations (6-24) to (6-30), this condition can be reformulated as:

$$df = \frac{\partial f}{\partial p^*}dp^* + \frac{\partial f}{\partial q}dq + \frac{\partial f}{\partial \alpha}d\alpha + \frac{\partial f}{\partial p_0^s(\xi)}\frac{\partial p_0^s(\xi)}{\partial \xi}d\xi + \frac{\partial f}{\partial p_0^s(\xi)}\frac{\partial p_0^s(\xi)}{\partial \varepsilon_v^p}p^*(M^2-\eta^2)\langle L\rangle + \frac{\partial f}{\partial p_0^s(\xi)}\frac{\partial p_0^s(\xi)}{\partial R(0)}\Big[-\beta_1[R(0)-$$

$$1]p^*\sqrt{(M^2-\eta^2)^2+4(\eta-\alpha)^2}\Big]\langle L\rangle + \frac{\partial f}{\partial p_0^s(\xi)}\frac{\partial p_0^s(\xi)}{\partial c}\Big[-c\beta_1\beta_2 p^*\sqrt{(M^2-\eta^2)^2+4(\eta-\alpha)^2}\Big]\langle L\rangle = 0 \quad (6\text{-}32)$$

When the stress state lies on the bounding surface, the plastic multiplier is directly calculated using Equation (6-32). However, when the stress state is located within the bounding surface, Equation (6-32) should be modified to account for the influence of the overconsolidation ratio by the distance between the loading surface and the bounding surface, $\bar{\rho}_s/\rho_s$. Previous studies have shown that as OCR increases, the plastic modulus increases and the resulting plastic strain decreases (e.g., Zhou and Ng, 2015). Following the methodology of Zhou and Ng (2015), Equation (6-32) is modified as follows:

$$df = \frac{\partial f}{\partial p^*}dp^* + \frac{\partial f}{\partial q}dq + \frac{\partial f}{\partial \alpha}d\alpha + \frac{\partial f}{\partial p_0^s(\xi)}\frac{\partial p_0^s(\xi)}{\partial \xi}d\xi + \frac{\partial f}{\partial p_0^s(\xi)}\frac{\partial p_0^s(\xi)}{\partial \varepsilon_v^p}p^*((M\bar{\rho}_s/\rho_s)^2-\eta^2)\langle L\rangle + \frac{\partial f}{\partial p_0^s(\xi)}\frac{\partial p_0^s(\xi)}{\partial R(0)}\Big[-\beta_1[R(0)-$$

$$1]p^*\sqrt{((M\bar{\rho}_s/\rho_s)^2-\eta^2)^2+4(\eta-\alpha)^2}\Big]\langle L\rangle + \frac{\partial f}{\partial p_0^s(\xi)}\frac{\partial p_0^s(\xi)}{\partial c}\Big[-c\beta_1\beta_2 p^*\sqrt{((M\bar{\rho}_s/\rho_s)^2-\eta^2)^2+4(\eta-\alpha)^2}\Big]\langle L\rangle = 0 \quad (6\text{-}33)$$

Note that the ratio $\bar{\rho}_s/\rho_s$ incorporated in Equation (6-33) is the inverse of the ratio $\rho_s/\bar{\rho}_s$ used in Equation (6-25). This inversion arises from the distinct purposes of the two expressions. The inclusion of $\rho_s/\bar{\rho}_s$ in Equation (6-25) is intended to induce more dilative behaviour as the OCR increases, which is consistent with experimental findings (Pestana et al., 2002). In contrast, the use of $\bar{\rho}_s/\rho_s$ in Equation (6-33) results in a smaller plastic multiplier $\langle L\rangle$, and consequently, smaller plastic strain increments with increasing OCR (Zhou and Ng, 2015).

Equation (6-33) also incorporates the effects of anisotropy and structure through the third term and the last two terms on the right-hand side, respectively. The third term becomes zero when anisotropy effects are not considered, while the last two terms vanish for reference soils (with $R(0) = 1$ and $c = 0$). As a result, the model ensures continuity between anisotropic and isotropic conditions, as well as between structured and reference soil states.

6.1.4 Soil water retention curve considering anisotropy effects

As illustrated in section 2.3.2, anisotropic soils exhibit a stronger water retention capacity

than isotropic soils at a given void ratio (Tse, 2007; Sivakumar et al., 2010; Al-Sharrad, 2013; Habasimbi and Nishimura, 2018). Based on experimental results reported in the literature, Zhou and Chen (2021) proposed a water retention model that accounts for the influence of anisotropy, without incorporating density effects. In this study, a modified model is proposed, extending the framework of Zhou and Chen (2021) to include both void ratio and anisotropy dependencies, as illustrated in Figure 6-2:

$$\begin{cases} S_r = \left[1 + \left(\frac{se^{m_1}}{m_2^d}\frac{1}{h}\right)^{m_3}\right]^{-\frac{1}{m_1 m_3}} \\ S_r = \left[1 + \left(\frac{se^{m_1}}{m_2^w}\frac{1}{h}\right)^{m_3}\right]^{-\frac{1}{m_1 m_3}} \end{cases} \tag{6-34}$$

where m_1, m_2^d/m_2^w, and m_3 are model parameters related to the SWRC of isotropic soils, with m_2^d and m_2^w corresponded to the main drying and wetting curves, respectively; and the variable h accounts for the effects of anisotropy on the water retention curve. For anisotropic soils, h is larger than 1, ensuring a stronger water retention capacity compared to isotropic soils. When the soil fabric becomes isotropic, h = 1, and the model reduces to the water retention model for isotropic soils. Equation (6-34) assumes that the anisotropy effects on the main drying/wetting curves are comparable and can be represented by a single parameter h.

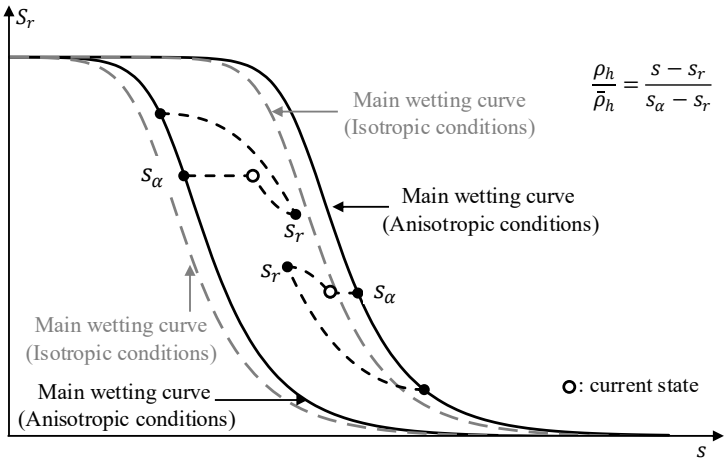

Figure 6-2. Soil water retention curves for isotropic and anisotropic soils

Given that both parameters α and h are closely associated with soil anisotropy, a potential correlation between them is explored using the results of Al-Sharrad (2013). Under both isotropic and anisotropic conditions, Al-Sharrad (2013) provided data on water retention

curves and bounding surfaces, from which the values of h and α can be determined, respectively. For water retention behaviour, the data for isotropic soils are used to calibrate the parameters m_1, m_2^w, and m_3, with the results shown in Figure 6-3(a). Notably, at a given suction, Al-Sharrad (2013) measured the degree of saturation under various void ratios (ranging from 0.9 to 1.3). To evaluate the model performance in a direct and clear manner, the comparison is conducted in the plane of calculated versus measured degree of saturation, rather than in the $S_r - s$ plane. Furthermore, since the results reported by Al-Sharrad (2013) are limited to wetting processes, the parameter m_2^d is not required. Subsequently, the water retention data for anisotropic soils are used to determine the value of h corresponding to a given α, using the following equation:

$$h = \frac{s e^{m_1}}{m_2^w \left(s_r^{-m_1 m_3} - 1\right)^{\frac{1}{m_3}}} \tag{6-35}$$

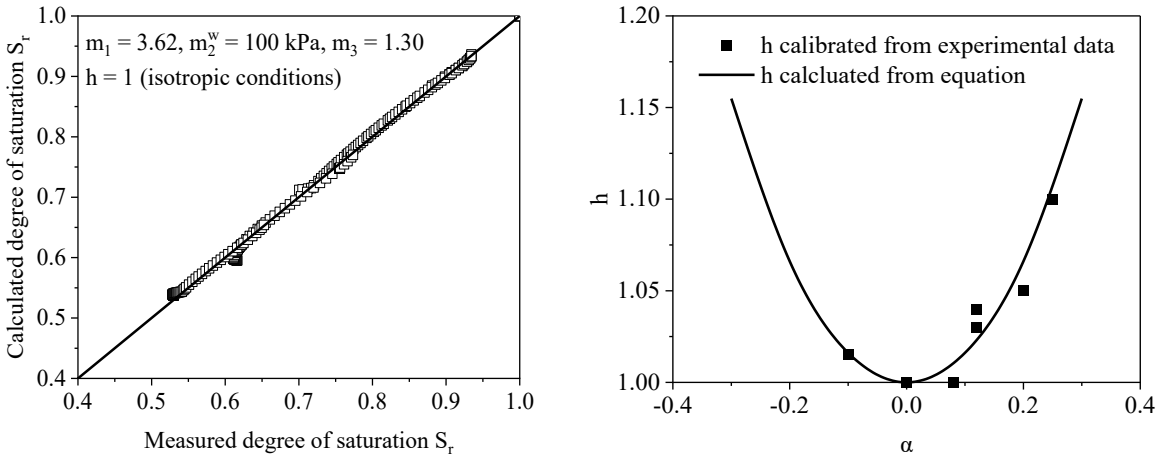

Figure 6-3. Model derivation for the SWRC: (a) isotropic conditions; (b) anisotropic conditions

The calculated values of h are represented by the discrete points in Figure 6-3(b), where the corresponding values of α are obtained by fitting the bounding surface using Equation (6-19). The results indicate that h increases exponentially with increasing α. Based on these experimental findings, the following relationship between α and h is proposed:

$$h = \exp(\omega \alpha^2) \tag{6-36}$$

where ω is a model parameter that accounts for the effects of anisotropy on the water retention

curve. The squared term of α ensures that specimens with either positive or negative α exhibit the same water retention capacity. Equation (6-36) implies that h = 1 when $\alpha = 0$ (i.e., isotropic case), thereby ensuring continuity between isotropic and anisotropic conditions.

The equations presented above model the main drying and wetting curves but are not capable of simulating scanning curves. To address this limitation, the change in the unsaturation state along a more general hydraulic path is evaluated using the concept of bounding surface plasticity theory, as illustrated in Figure 6-2 (Zhou et al., 2015). The bounding surface that describes the evolution of the unsaturation state is defined in the $S_r - s$ plane as follows:

$$f_h = s - s_\alpha = 0 \tag{6-37}$$

where s_α is the image suction on the main drying or wetting curve, as shown in Figure 6-2. Based on Equation (6-34), s_α is expressed as follows:

$$s_\alpha = \frac{hm_2}{e^{m_1}}\left(S_r^{-m_1 m_2} - 1\right)^{\frac{1}{m_3}} \tag{6-38}$$

The mapping rule for the water retention curve is illustrated in Figure 6-2. The suction s_r, corresponding to the point of the last suction reversal (i.e., the transition from drying to wetting or vice versa), serves as the projection centre. Similar to Equation (6-21), two Euclidean distances are identified, and their ratio is expressed as follows:

$$\frac{\rho_h}{\overline{\rho}_h} = \frac{s - s_r}{s_\alpha - s_r} \tag{6-39}$$

The consistency condition for the bounding surface in the $S_r - s$ plane implies:

$$df_h = \frac{\partial f_h}{\partial s}ds + \frac{\partial f_h}{\partial s_\alpha}\frac{\partial s_\alpha}{\partial S_r}dS_r + \frac{\partial f_h}{\partial s_\alpha}\frac{\partial s_\alpha}{\partial e}\left(\frac{\partial e}{\partial \varepsilon_v^e}\frac{\partial \varepsilon_v^e}{\partial p^*}dp^* + \frac{\partial e}{\partial \varepsilon_v^p}d\varepsilon_v^p\right) + \frac{\partial f_h}{\partial s_\alpha}\frac{\partial s_\alpha}{\partial h}\frac{\partial h}{\partial \alpha}d\alpha = 0 \tag{6-40}$$

When the current suction lies on the main drying or wetting curve, the change in the degree of saturation is directly computed using Equation (6-40). However, when the current suction deviates from the main drying or wetting curve, Equation (6-40) should be modified to account for the distance between the current suction and the corresponding main curve:

$$df_h = \frac{\partial f_h}{\partial s}ds + \frac{\partial f_h}{\partial s_\alpha}\frac{\partial s_\alpha}{\partial S_r}\left(\frac{\overline{\rho}_h}{\rho_h}\right)dS_r + \frac{\partial f_h}{\partial s_\alpha}\frac{\partial s_\alpha}{\partial e}\left(\frac{\partial e}{\partial \varepsilon_v^e}\frac{\partial \varepsilon_v^e}{\partial p^*}dp^* + \frac{\partial e}{\partial \varepsilon_v^p}d\varepsilon_v^p\right) + \frac{\partial f_h}{\partial s_\alpha}\frac{\partial s_\alpha}{\partial h}\frac{\partial h}{\partial \alpha}d\alpha = 0 \quad (6\text{-}41)$$

Similar to the ratio $\overline{\rho}_s/\rho_s$ in Equation (6-33), the term $\overline{\rho}_h/\rho_h$ is introduced to simulate the decreasing desorption/adsorption rate as suction deviates further from the main drying or wetting curve. When the unsaturation state lies on the main drying or wetting curve, the ratio $\overline{\rho}_h/\rho_h$ equals 1, and Equation (6-41) reduces to Equation (6-40).

In addition, it should be noted that the structure effects on the water retention curve are considered by adopting different values for the parameters m_1, m_2^w/m_2^d, and m_3. This simplification arises due to the limited availability of experimental data concerning the influence of structure degradation on water retention behaviour. Further experimental and theoretical investigations are planned to address this gap.

6.1.5 Differential terms in the consistency conditions

The differential terms in Equation (6-33) are presented as follows:

$$\frac{\partial f}{\partial p^*} = p^*(N^2 - \eta^2) \quad (6\text{-}42)$$

$$\frac{\partial f}{\partial q} = 2p^*(\eta - \alpha) \quad (6\text{-}43)$$

$$\frac{\partial f}{\partial p_0^s(\xi)} = -(N^2 - \alpha^2)p^* \quad (6\text{-}44)$$

$$\frac{\partial f}{\partial \alpha} = \frac{2(N^2 - \alpha\eta)(\alpha - \eta)}{N^2 - \alpha^2}p^{*2} \quad (6\text{-}45)$$

$$\frac{\partial p_0^s(\xi)}{\partial \xi} = \frac{\partial p_0^s(\xi)}{\partial p_0^r(\xi)}\frac{\partial p_0^r(\xi)}{\partial \xi} + \frac{\partial p_0^s(\xi)}{\partial R(\xi)}\frac{\partial R(\xi)}{\partial p_0^r(\xi)}\frac{\partial p_0^r(\xi)}{\partial \xi} \quad (6\text{-}46)$$

$$\frac{\partial p_0^s(\xi)}{\partial \varepsilon_v^p} = \frac{\partial p_0^s(\xi)}{\partial p_0^r(\xi)}\frac{\partial p_0^r(\xi)}{\partial p_0^r(0)}\frac{\partial p_0^r(0)}{\partial \varepsilon_v^p} + \frac{\partial p_0^s(\xi)}{\partial R(\xi)}\left(\frac{\partial R(\xi)}{\partial p_0^r(0)}\frac{\partial p_0^r(0)}{\partial \varepsilon_v^p} + \frac{\partial R(\xi)}{\partial p_0^r(\xi)}\frac{\partial p_0^r(\xi)}{\partial p_0^r(0)}\frac{\partial p_0^r(0)}{\partial \varepsilon_v^p}\right) \quad (6\text{-}47)$$

$$\frac{\partial p_0^s(\xi)}{\partial R(0)} = \frac{\partial p_0^s(\xi)}{\partial R(\xi)}\frac{\partial R(\xi)}{\partial R(0)} \quad (6\text{-}48)$$

$$\frac{\partial p_0^s(\xi)}{\partial c} = \frac{\partial p_0^s(\xi)}{\partial R(\xi)}\frac{\partial R(\xi)}{\partial c} \quad (6\text{-}49)$$

$$\frac{\partial p_0^s(\xi)}{\partial p_0^r(\xi)} = R(\xi) \quad (6\text{-}50)$$

$$\frac{\partial p_0^s(\xi)}{\partial R(\xi)} = p_0^r(\xi) \tag{6-51}$$

$$\frac{\partial R(\xi)}{\partial p_0^r(0)} = -\frac{cR(\xi)[\ln R(0)]^2}{(1+F_2)^2 F_1^2 p_0^r(0)} \tag{6-52}$$

$$\frac{\partial R(\xi)}{\partial p_0^r(\xi)} = \frac{cR(\xi)[\ln R(0)]^2}{(1+F_2)^2 F_1^2 p_0^r(\xi)} \tag{6-53}$$

$$\frac{\partial R(\xi)}{\partial R(0)} = \frac{R(\xi)}{R(0)}\left(1+\frac{c}{1+F_2}\right) - \frac{cR(\xi)\ln R(0)}{(1+F_2)^2 R(0) F_1} \tag{6-54}$$

$$\frac{\partial R(\xi)}{\partial c} = \frac{R(\xi)\ln R(0)}{1+F_2} \tag{6-55}$$

$$F_1 = \ln\frac{p_0^r(\xi)}{p_0^r(0)} \tag{6-56}$$

$$F_2 = \frac{\ln R(0)}{F_1} \tag{6-57}$$

$$\frac{\partial p_0^r(\xi)}{\partial \xi} = \frac{[N(0)-\lambda(0)\ln p_0^r(\xi)]p_0^r(\xi)ab\exp(b\xi)}{\lambda(0)[1-a+a\exp(b\xi)]-\kappa} \tag{6-58}$$

$$\frac{\partial \xi}{\partial s} = (1-S_r^e)\frac{\partial f(s)}{\partial s} \tag{6-59}$$

$$\frac{\partial \xi}{\partial S_r} = -f(s) \tag{6-60}$$

$$\frac{\partial p_0^r(\xi)}{\partial p_0^r(0)} = \frac{\lambda(0)-\kappa}{\lambda(0)[1-a+a\exp(b\xi)]-\kappa}\frac{p_0^r(\xi)}{p_0^r(0)} \tag{6-61}$$

$$\frac{\partial p_0^r(0)}{\partial \varepsilon_v^p} = \frac{(1+e)p_0^r(0)}{\lambda(0)-\kappa} \tag{6-62}$$

The differential terms in Equation (6-41) are presented as follows:

$$\frac{\partial f_h}{\partial s} = 1 \tag{6-63}$$

$$\frac{\partial f_h}{\partial s_\alpha} = -1 \tag{6-64}$$

$$\frac{\partial s_\alpha}{\partial S_r} = \frac{m_1 s_\alpha}{S_r\left(S_r^{m_1 m_3}-1\right)} \tag{6-65}$$

$$\frac{\partial s_\alpha}{\partial e} = -\frac{m_1 s_\alpha}{e} \tag{6-66}$$

$$\frac{\partial e}{\partial \varepsilon_v^e} = -(1+e) \tag{6-67}$$

$$\frac{\partial \varepsilon_v^e}{\partial p^*} = \frac{\kappa}{(1+e)p^*} \tag{6-68}$$

$$\frac{\partial e}{\partial \varepsilon_v^p} = -(1+e) \tag{6-69}$$

$$\frac{\partial h}{\partial \alpha} = 2\omega\alpha \exp(\omega\alpha^2) \tag{6-70}$$

6.2 Calibration of model parameters

The model parameters are categorised into four groups: (i) $N(0)$, $\lambda(0)$, κ, M_c, M_e, N_c, N_e, and μ, which describe the reference soil behaviour under saturated conditions; (ii) a, b, m_1, m_2^d, m_2^w, and m_3, which account for unsaturation effects; (iii) x, z_1, z_2, and ω, which incorporate anisotropy effects; and (iv) $R(0)$, c, β_1, and β_2, which represent structure effects. The model parameters and their corresponding physical meanings are summarised in Table 6-1.

To calibrate the required parameters for reference soils under saturated conditions, $N(0)$, $\lambda(0)$, and κ can be readily obtained from the isotropic compression curve of saturated isotropic soils. M_c and M_e are obtained from the slopes of the critical state lines in the $q - p^*$ plane under triaxial compression and extension, respectively. N_c and N_e can be determined from the bounding surface using Equation (6-19) (Al-Sharrad, 2013). The Poisson's ratio μ can be calculated from the initial slope of the volumetric strain versus deviatoric strain curve during triaxial shearing.

Under unsaturated conditions, a and b can be calibrated from the size of the bounding surface under different ξ values based on Equation (6-8). Following the procedure of Gallipoli et al. (2003b), m_1, m_2^d, m_2^w, and m_3 can be calibrated using the water retention curve under isotropic conditions, as described by Equation (6-34).

The parameters related to structured effects can be calibrated as follows: $R(0)$ can be readily determined from the relative size of the structured and reference bounding surfaces under saturated conditions, based on Equation (6-5). The parameter c can be calibrated from

the LC curve of structured soils using Equation (6-14). Finally, β_1 and β_2 can be obtained from the compression curve of structured soils, based on Equation (6-28).

Table 6-1. Model parameters and corresponding physical meanings

Model parameter	Physical meaning
Elasticity	
κ	slope of the unloading or reloading line in the $e - \ln p^*$ plane
μ	Poisson's ratio
Elasto-plasticity	
$N(0),\ \lambda(0)$	intercept and slope of the isotropic compression line under isotropic and saturated conditions, respectively
$M_c,\ M_e$	slopes of the critical state lines in the $q - p^*$ plane under triaxial compression and extension, respectively
$N_c,\ N_e$	parameters used to define the bounding surfaces under triaxial compression and extension, respectively
$a,\ b$	parameters used to define the size of the bounding surface under unsaturated conditions
x	parameter used to control the evolution rate of anisotropy
$z_1,\ z_2$	parameters used to calculate $\alpha_b(\eta)$
$R(0)$	structure parameter under saturated conditions
c	parameter used to calculate $R(\xi)$
$\beta_1,\ \beta_2$	parameters used to control structure degradation
Water retention behaviour	
$m_1,\ m_2^d/m_2^w,\ m_3$	parameters used to define the SWRC of isotropic soils
ω	parameter used to incorporate the anisotropy effects on the SWRC

For the parameters related to anisotropy effects, z_1 and z_2 can be determined from the inclination of the bounding surface under different stress ratios, based on Equation (6-30) (Dafalias and Taiebat, 2013). For example, the bounding value of α at K_0 consolidation, $\alpha_b(\eta_{K_0})$, can be used, where η_{K_0} is the stress ratio at K_0 consolidation. The value of $\alpha_b(\eta_{K_0})$ is calculated as follows (Wheeler et al., 2003a):

$$\alpha_b(\eta_{K_0}) = \frac{\eta_{K_0}^2 + 3\eta_{K_0} - M^2}{3} \tag{6-71}$$

Moreover, x can be calibrated by best fitting the experimental data using Equation (6-29), such as undrained shearing results from K_0 consolidated specimens (Dafalias et al., 2006). The parameter ω can be determined from the water retention curve of anisotropic soils using Equations (6-34) and (6-36).

6.3 Model validation

Figure 6-4 presents typical model responses for simulating triaxial compression tests on an unsaturated and structured soil, both with and without considering anisotropy effects. The specimen is sheared under constant suction with a constant incremental ratio, dq/dp_n of 3. For the simulation incorporating anisotropy effects, the initial value of α is set to 0.25, and α evolves with plastic deformation. In contrast, the simulation without anisotropy effects maintains $\alpha = 0$ under all conditions. In both simulations, the initial conditions are as follows: mean net stress of 50 kPa, deviatoric stress of 0 kPa, void ratio of 1.0, suction of 50 kPa, degree of saturation of 0.80, and structure parameter $R(0)$ of 5. All other model parameters are consistent with those of Kaewsong (2017) in Table 6-2. Based on Equation (6-1), the initial value of the mean Bishop's stress is 90 kPa. The initial stress state prior to shearing is indicated by Point A in Figure 6-4(a) and (b).

Figure 6-4(a) illustrates the stress path and the evolution of the bounding surface in the $q - p^*$ plane with anisotropy effects incorporated. As the axial strain increases from 0% to 20%, the bounding surface expands, evidenced by an increase in $p_0^s(\xi)$ from 200 to 385 kPa, and rotates, as indicated by a change in α from 0.25 to 0.34. These changes are consistent with the isotropic and rotational hardening laws described in (6-26) and (6-29), respectively. Additionally, the structure parameter $R(0)$ decreases from 5.0 to 3.1, reflecting the degradation of soil structure due to plastic deformation, in accordance with Equations (6-27) and (6-28). Figure 6-4(b) illustrates the evolution of the bounding surface without considering anisotropy effects. In this case, the bounding surface expands, with $p_0^s(\xi)$ from 200 to 425 kPa, but no rotation occurs, as the anisotropy parameter α remains zero. Structure degradation due to plastic deformation is observed, with the structure parameter $R(0)$ decreasing from 5.0 to 3.0. Notably, the bounding surface undergoes a greater degree of expansion (as indicated by $p_0^s(\xi)$) and more significant structure degradation (as reflected in $R(0)$) compared to the case with anisotropy effects.

Figure 6-4(c) compares the stress-strain and volumetric strain curves of specimens

subjected to shearing, with and without the consideration of anisotropy effects. The specimen without anisotropy demonstrates a more compliant mechanical response, evidenced by a lower deviatoric stress and a higher volumetric strain at the same axial strain level. This behaviour is attributed to the initial stress state of the isotropic specimen being closer to the bounding surface when sheared under a constant incremental ratio $dq/dp_n = 3$, as depicted in Figure 6-4(a) and (b). As a result, the isotropic specimen reaches the bounding surface at a lower stress level, which leads to a smaller plastic modulus and consequently greater plastic deformation. The increased plastic strain contributes to a more pronounced expansion of the bounding surface and a more significant degradation of the material structure.

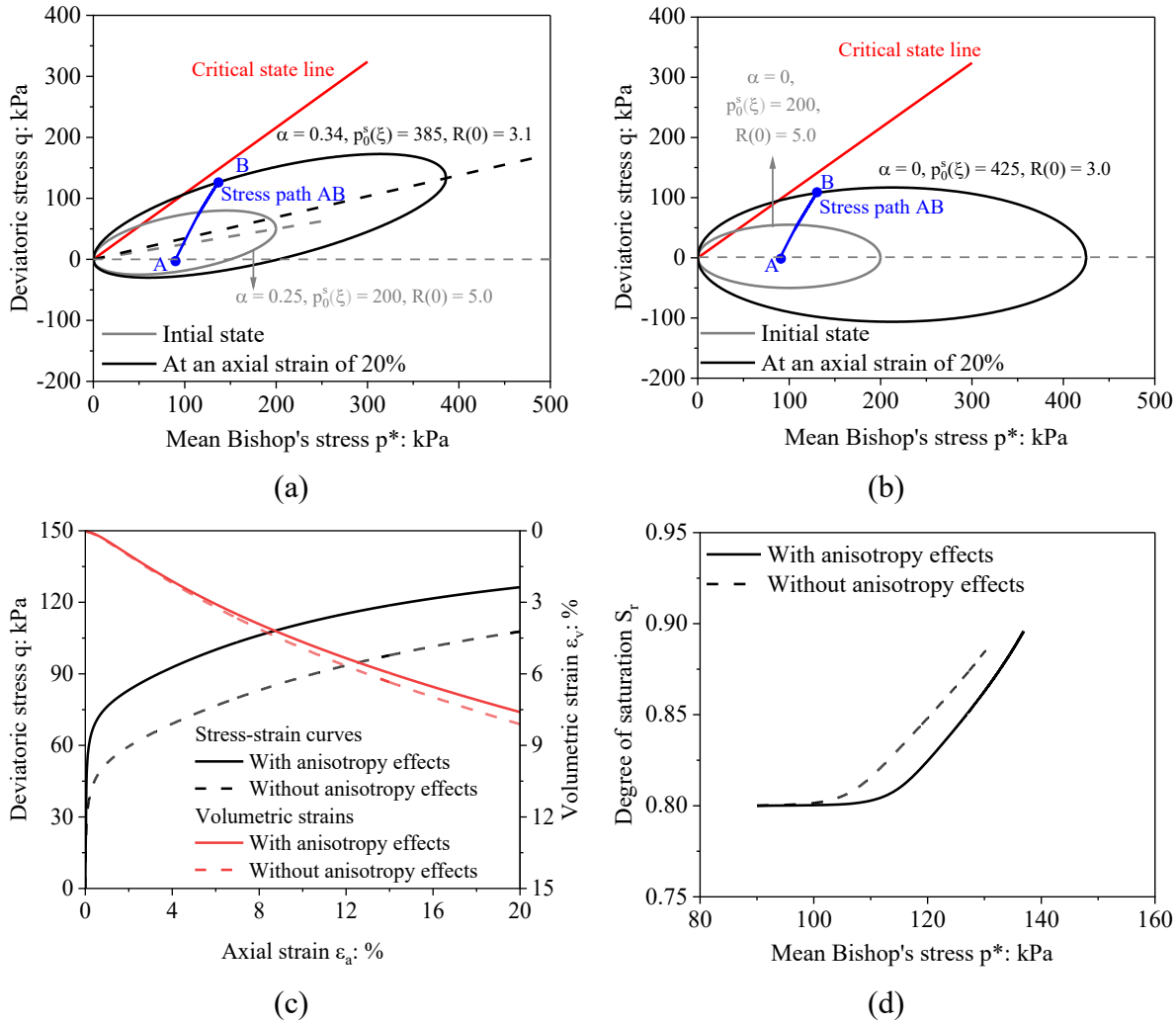

Figure 6-4. Example illustrating the effects of anisotropy on the shearing behaviour of an unsaturated and structured soil: (a) evolution of bounding surface considering anisotropy effects; (b) evolution of bounding surface without anisotropy effects; (c) stress-strain curves and volumetric strains; (d) variations in degree of saturation

Table 6-2. Summary of model parameter values

Model parameter	Lower Cromer Till (LCT) (Gens, 1982)	Speswhite kaolin (Al-Sharrad, 2013)	Taihu clay (Liu et al., 2013)	Loess (Kaewsong, 2017)	This study
Elasticity					
κ	0.009	0.04	0.019	0.005	0.005
μ	0.15	0.20	0.30	0.10	0.20
Elasto-plasticity					
$N(0)$	0.787	1.891	1.172	1.421	1.200
$\lambda(0)$	0.066	0.168	0.074	0.121	0.100
M_c	1.180	0.800	1.420	1.080	1.400
M_e	0.864	0.800	1.420	1.080	1.200
N_c	0.785	0.810	1.420	0.550	1.400
N_e	0.600	0.980	1.420	0.550	1.200
a	-*	5.848	-	0.085	2.050
b	-	0.105	-	2.135	0.280
x	25000	1700	15000	1000	12000
z_1	1.58	1.70	1.60	1.66	1.60
z_2	1.58	1.70	1.60	1.66	1.60
$R(0)$	-	-	19.1	2.62	11.8
c	-	-	-	-0.50	-1.00
β_1	-	-	8.0	3.0	7.0
β_2	-	-	-	3.0	0.1
Water retention behaviour (parameters in the bracket are for intact specimens)					
m_1	-	3.62	-	4.78 (2.20)	5.50 (3.20)
m_2^d	-	-	-	8.50 (45.0)	3.50 (10.00)
m_2^w	-	100.00	-	2.30 (15.0)	1.00 (8.00)
m_3	-	1.30	-	1.53 (2.50)	2.50 (2.50)
ω	-	2.38	-	1.50	1.20

*Notation: parameters denoted as '-' are unnecessary.

Figure 6-4(d) gives the variations of degree of saturation as a function of mean Bishop's stress during the shearing process. For the specimen incorporating anisotropy effects, the degree of saturation exhibits minimal variation when the mean Bishop's stress is below 110 kPa. This limited change is due to the stress state remaining well within the bounding surface, as shown in Figure 6-4(a), resulting in negligible volumetric strain and saturation change. Notably, when the mean Bishop's stress exceeds 115 kPa, the specimen with anisotropy effects demonstrates a more pronounced increase in saturation compared to its isotropic counterpart. The higher increase rate is primarily due to the rotation of the bounding surface induced by

shearing, which intensifies anisotropic behaviour and increases the specimen's water retention capacity, as described by Equations (6-34) and (6-36).

In conclusion, the omission of inherent anisotropy in the analysis of unsaturated and structured soils results in markedly different yielding behaviour and structure degradation patterns, as evidenced in Figure 6-4(a) and (b). Additionally, the findings presented in Figure 6-4(c) and (d) indicate that the mechanical responses, specifically the stress-strain relationship, volumetric deformation, and variation in degree of saturation, are highly sensitive to the presence of anisotropy and its progressive development during shearing.

To examine the performance of the proposed model, a comprehensive five-stage validation framework is implemented. This framework evaluates the model's performance under five representative conditions: (i) anisotropic reconstituted soils under saturated conditions, to capture the effects of anisotropy; (ii) anisotropic reconstituted soils under unsaturated conditions, incorporating both anisotropy and suction effects; (iii) anisotropic intact soils under saturated conditions, addressing the combined influence of anisotropy and soil structure; (iv) anisotropic intact soils under unsaturated conditions, encompassing the full interaction among unsaturation, anisotropy, and structure; and (v) anisotropic intact soils subjected to cyclic loading, accounting for the combined effects of structure, anisotropy, unsaturation, and loading cycles. For numerical implementation, an explicit sub-stepping algorithm is employed, which utilises the Euler integration scheme to solve for stress increments based on prescribed strain increments (Potts and Zdravkovic, 1999). A relatively high accuracy is obtained by adopting small-strain increments.

6.3.1 Simulating anisotropic reconstituted soils under saturated conditions

Gens (1982) examined the mechanical behaviour of saturated and reconstituted Lower Cromer Till (LCT) through a series of drained and undrained triaxial compression and extension tests. The tests were conducted on specimens with a range of overconsolidation ratios to capture the influence of stress history. Various consolidation methods, including isotropic consolidation, K_0 consolidation, and constant K_c (i.e., σ_1/σ_3) consolidation, were adopted

for preparing specimens with different degrees of initial anisotropy. The model parameters calibrated for this study are summarised in Table 6-2. Given that the specimens are both saturated and reconstituted, parameters associated with unsaturation and structure effects are excluded from the analysis.

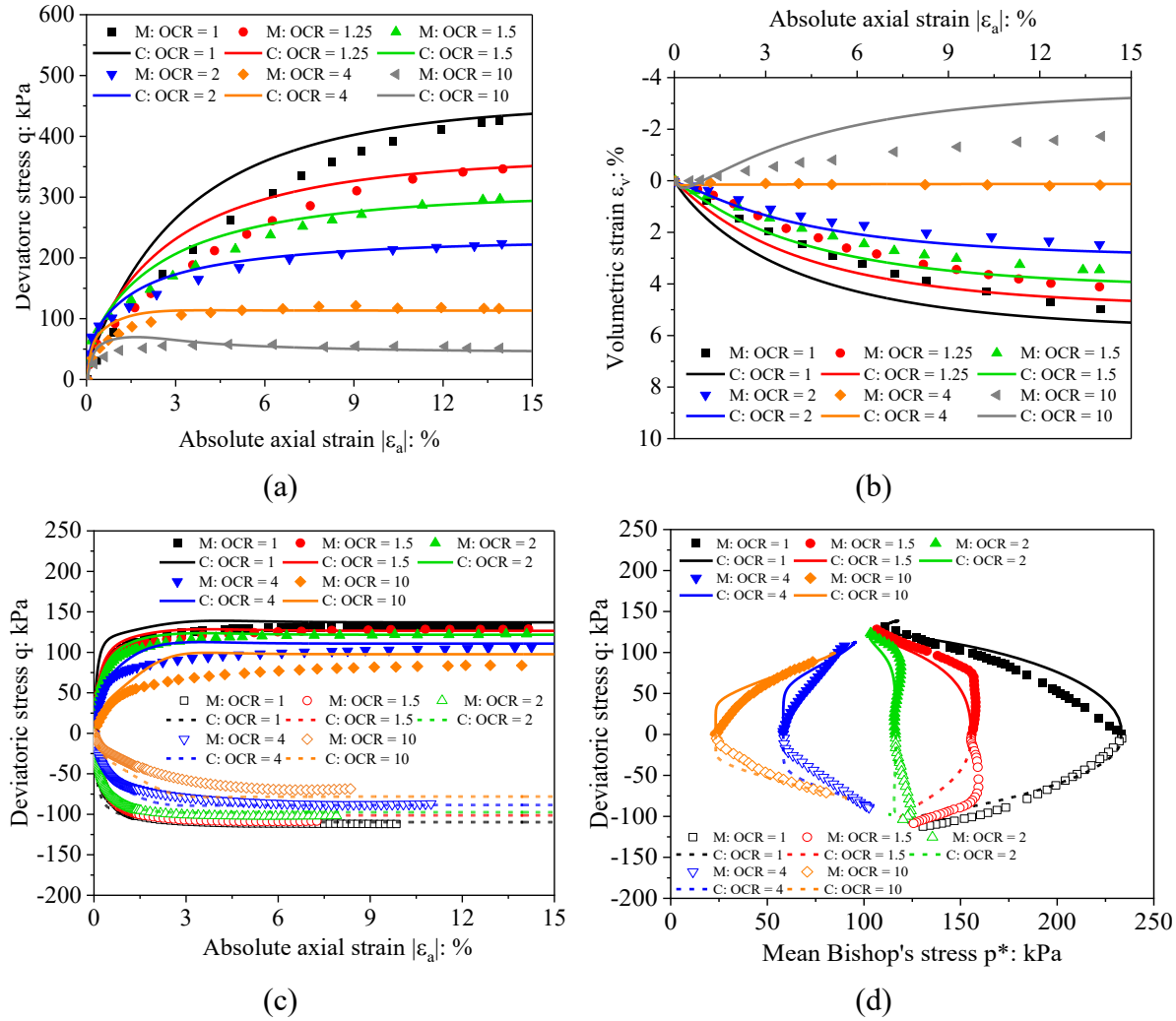

Figure 6-5. Comparisons between the measured (M) and computed (C) results for the isotropically consolidated LCT specimens: (a) stress-strain curves under drained compression; (b) volumetric strains under drained compression; (c) stress-strain curves under undrained compression and extension; (d) stress paths under undrained compression and extension

Figure 6-5 presents a comparison between measured (denoted as "M") and computed (refer to "C") results for the isotropically consolidated LCT specimens. Figure 6-5(a) and (b) illustrate the results under drained conditions for specimens with various OCRs. Figure 6-5(a) shows that the stress-strain curves are well captured when axial strain is larger than 5%,

whereas the deviatoric stress is slightly overestimated at axial strain smaller than 5%. The minor differences in the lower strain range are probably because the hardening law in Equation (6-26) results in an overestimated plastic modulus. It is observed from Figure 6-5(b) that soil behaviour translates from contraction to dilation with increasing OCR, which is well captured by the proposed model. Under undrained conditions, Figure 6-5(c) and (d) show that the model can well simulate the stress-strain behaviour (Figure 6-5(c)) and the stress paths (Figure 6-5(d)) under various OCRs, demonstrating the effectiveness of the radial mapping rule in Equation (6-21) and considering the influence of OCR on plastic modulus and dilatancy.

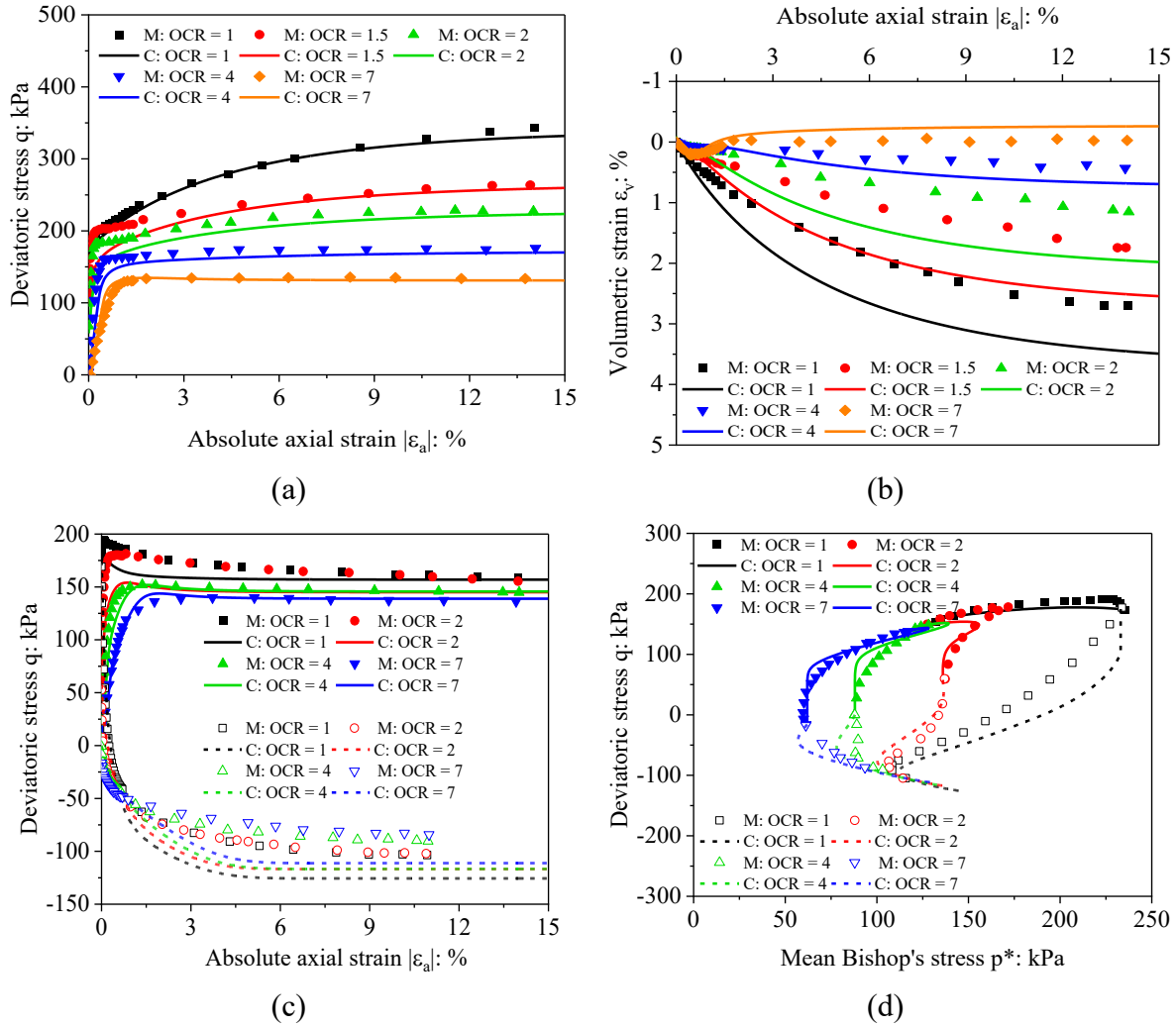

Figure 6-6. Comparisons between the measured (M) and computed (C) results for the K_0 consolidated LCT specimens: (a) stress-strain curves under drained compression; (b) volumetric strains under drained compression; (c) stress-strain curves under undrained compression and extension; (d) stress paths under undrained compression and extension

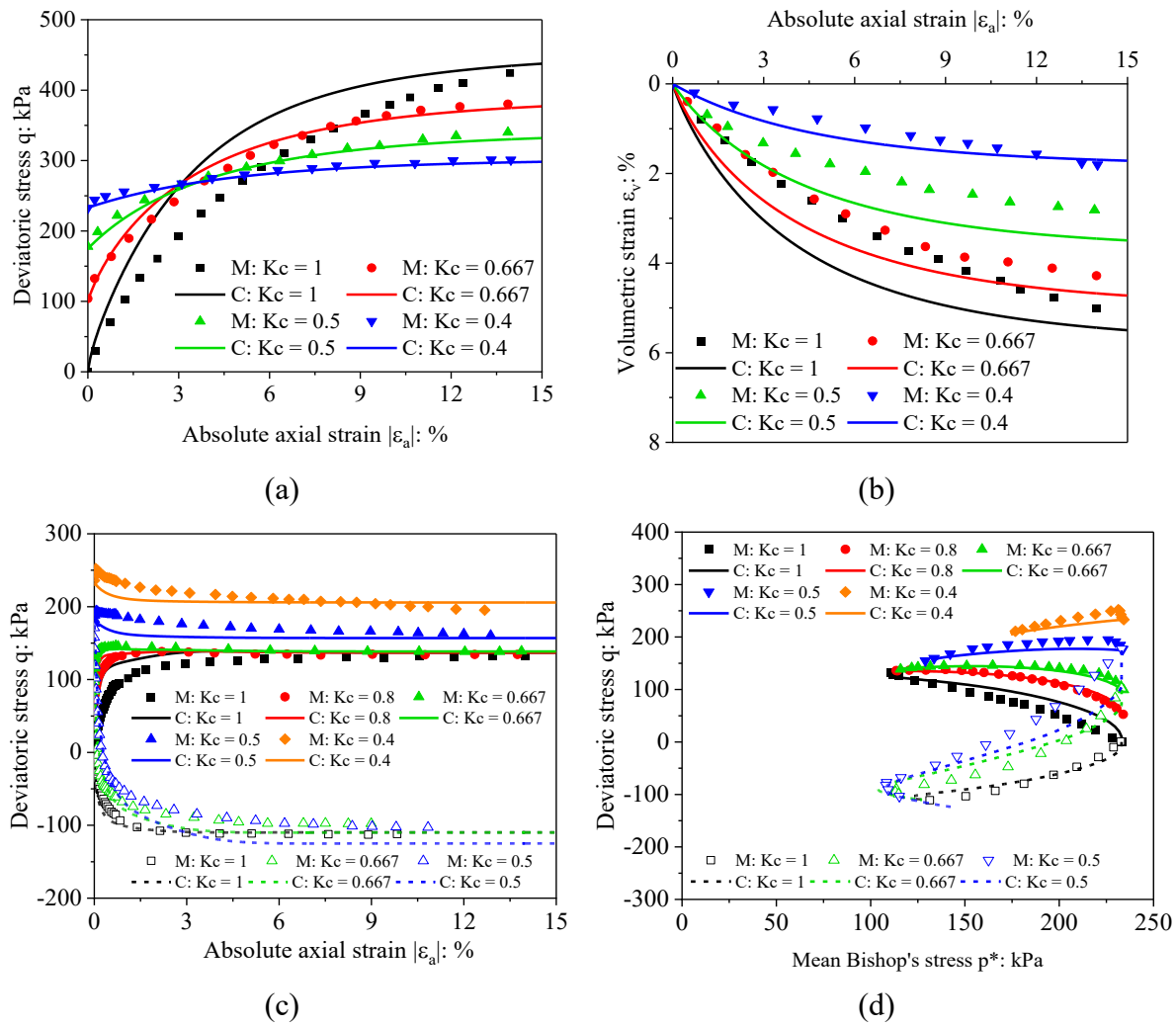

Figure 6-7. Comparisons between the measured (M) and computed (C) results for the K_c consolidated LCT specimens: (a) stress-strain curves under drained compression; (b) volumetric strains under drained compression; (c) stress-strain curves under undrained compression and extension; (d) stress paths under undrained compression and extension

Figure 6-6 presents the measured and computed results for the K_0 consolidated LCT specimens. Figure 6-6(a) shows that the measured and calculated stress-strain curves are well-matched under drained triaxial compression. As illustrated in Figure 6-6(b), the model well captures the transition from contractive behaviour to dilative behaviour with increasing OCR, consistent with trends observed in the isotropically consolidated specimens. Figure 6-6(c) and (d) depict the model's performance under undrained conditions. While the stress-strain responses and stress paths are generally well reproduced, a slight overestimation of deviatoric stress is noted at the critical state during triaxial extension. This discrepancy arises because, upon reaching the critical state line in the $q - p^*$ plane, the bounding surface continues to

rotate to ensure that the anisotropy variable α attains its bounding value $\alpha_b(M)$, as defined in Equation (6-29). This mechanism causes the stress state to evolve along the critical state line, leading to a modest overprediction of stress (Dafalias and Taiebat, 2013).

Figure 6-7 compares the measured and computed responses of the K_c consolidated LCT specimens. All specimens are normally consolidated but exhibit different initial anisotropic fabrics due to varying consolidation stress ratios. The results demonstrate that the model well predicts the stress-strain behaviour, volumetric deformation, and effective stress paths under both drained and undrained conditions across specimens with different degrees of anisotropy. These findings confirm the model's strong capability in capturing anisotropic soil behaviour under saturated conditions.

6.3.2 Simulating anisotropic reconstituted soils under unsaturated conditions

Al-Sharrad (2013) investigated the mechanical response of compacted speswhite kaolin subjected to different degrees of anisotropy and suctions. Specimens were consolidated to a mean net stress of 250 kPa under two net stress ratios: q/p_n = 0 for isotropic specimens (denoted as I) and q/p_n = 1.2 for anisotropic specimens (refer to A). Due to the differing stress ratios during consolidation, isotropic specimens (with e_0 = 1.32 ± 0.01, S_{r_0} = 0.49 ± 0.005, and α_0 = 0) exhibited higher void ratios, lower degrees of saturation, and lower degrees of anisotropy than anisotropic specimens (with e_0=1.17 ± 0.01, S_{r_0}=0.55 ± 0.005, α_0 = 0.2). Following consolidation, all specimens were unloaded to approximately p_n = 10 kPa and q = 0 kPa, then wetted to target suctions of 0, 100, and 300 kPa. Shearing was subsequently performed under constant suction conditions at various incremental stress ratios, with dq/dp_n = 3, 2, 1, -1, and -1.5. The model parameters are summarised in Table 6-2, and the analysis primarily focuses on unsaturated conditions, as the model's capacity to capture anisotropy in saturated soils has already been verified.

Figure 6-8 compares the measured and calculated initial LC curves for both isotropic and anisotropic specimens prior to shearing. Note that the measured LC curves are derived from stress-strain responses obtained during constant suction shearing. As the stress state approaches

the bounding surface, the plastic modulus decreases, influencing the slope of the stress-strain curve. Thus, in line with classical elasto-plasticity theory (e.g., Cui and Delage, 1996), these stress-strain relations can be effectively employed to identify the bounding surface. The results indicate that the anisotropic specimen exhibit a larger bounding surface size than the isotropic specimen across various values of ξ, primarily due to its lower initial void ratio. Furthermore, the LC curves computed using Equation (6-8) align well with the experimental data, confirming the equation's capability to capture the yield behaviour of both isotropic and anisotropic soils.

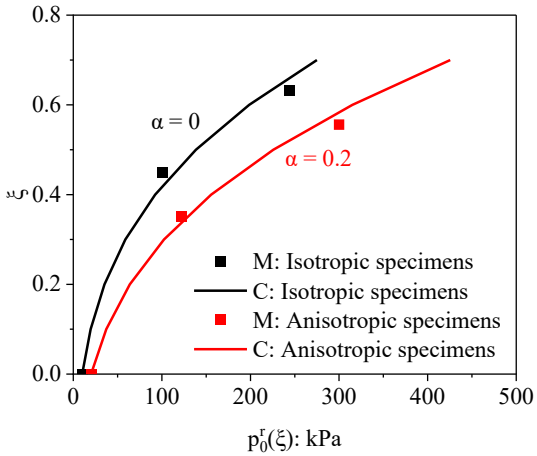

Figure 6-8. LC curves of isotropically and anisotropically consolidated speswhite kaolin

Figure 6-9 presents shearing results under a suction of 100 kPa. Figure 6-9(a), (c), and (e) correspond to triaxial compression, while Figure 6-9(b), (d), and (f) give the results of triaxial extension. The stress-strain curves, volumetric deformation, and changes of degrees of saturation are presented. Symbols "I" and "A" denote isotropically and anisotropically consolidated specimens, respectively; the number following indicates suction value in kPa, and the bracketed value represents the incremental stress ratio dq/dp_n. Figure 6-9(a) to (d) illustrates that, under otherwise identical conditions, the anisotropically consolidated specimen exhibits a higher initial deviatoric stress and a smaller volumetric strain than the isotropically consolidated specimen, due to the lower initial void ratio in the former.

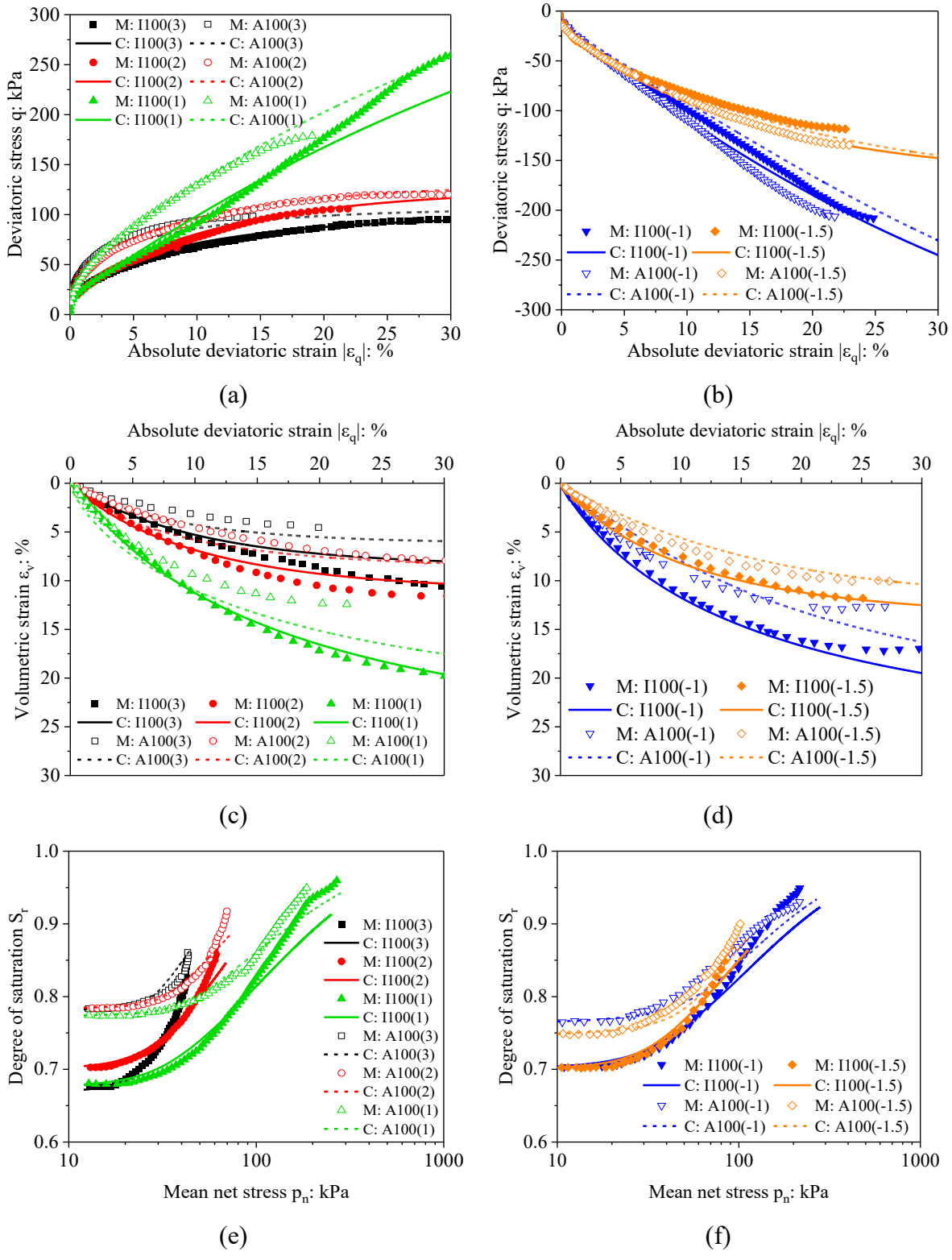

Figure 6-9. Constant suction compression and extension of speswhite kaolin under s = 100 kPa: (a-b) stress-strain curves; (c-d) volumetric strains; (e-f) variations of degree of saturation

More importantly, Figure 6-9(e) and (f) indicate that the anisotropically consolidated specimen has a higher initial degree of saturation than the isotropically consolidated specimens,

attributed to the lower void ratio and more pronounced anisotropic fabrics in the former. As deviatoric strain increases, the void ratio difference between the two specimen types decreases, and the degree of anisotropy for both evolves toward the bounding value $\alpha_b(M)$, as described in Equations (6-29) and (6-30). For instance, specimens I100(1) and A100(1) initially have void ratios of 1.37 and 1.22 and degrees of anisotropy of 0 and 0.2, respectively, under a net mean stress of 10 kPa. When the net mean stress increases to 200 kPa, the differences in void ratio and anisotropy fall below 5%, leading to comparable degrees of saturation. These trends are well captured by the model, thereby validating the effectiveness of (6-34) and (6-36) in calculating the variations in S_r under different consolidation conditions.

Figure 6-10 presents the constant suction shearing results at a suction of 300 kPa. Align with the observations at 100 kPa, the anisotropically consolidated specimen displays a higher initial deviatoric stress and a smaller volumetric strain compared to the isotropically consolidated specimen. Additionally, the anisotropically consolidated specimen exhibits a higher initial degree of saturation. This difference gradually decreases as strain increases due to diminished differences in both void ratio and degree of anisotropy. Furthermore, due to suction-induced stiffening, specimens sheared at 300 kPa exhibit a higher deviatoric stress and a smaller volumetric strain at a given deviatoric strain compared to those sheared at 100 kPa. These trends are generally well captured by the proposed model. However, a slight discrepancy is observed between the measured and calculated deviatoric stresses. This deviation is likely due to the limitations of the radial mapping rule when applied to soils with high OCRs, particularly in cases where the initial OCR exceeds 10 in specimens with a suction of 300 kPa. Given that the objective of this study is to develop an effective yet simple model capable of reproducing the primary trends identified in laboratory tests, no further modifications to the mapping rule are introduced. Overall, the model demonstrates satisfactory performance in capturing the effects of anisotropy on the behaviour of unsaturated soils.

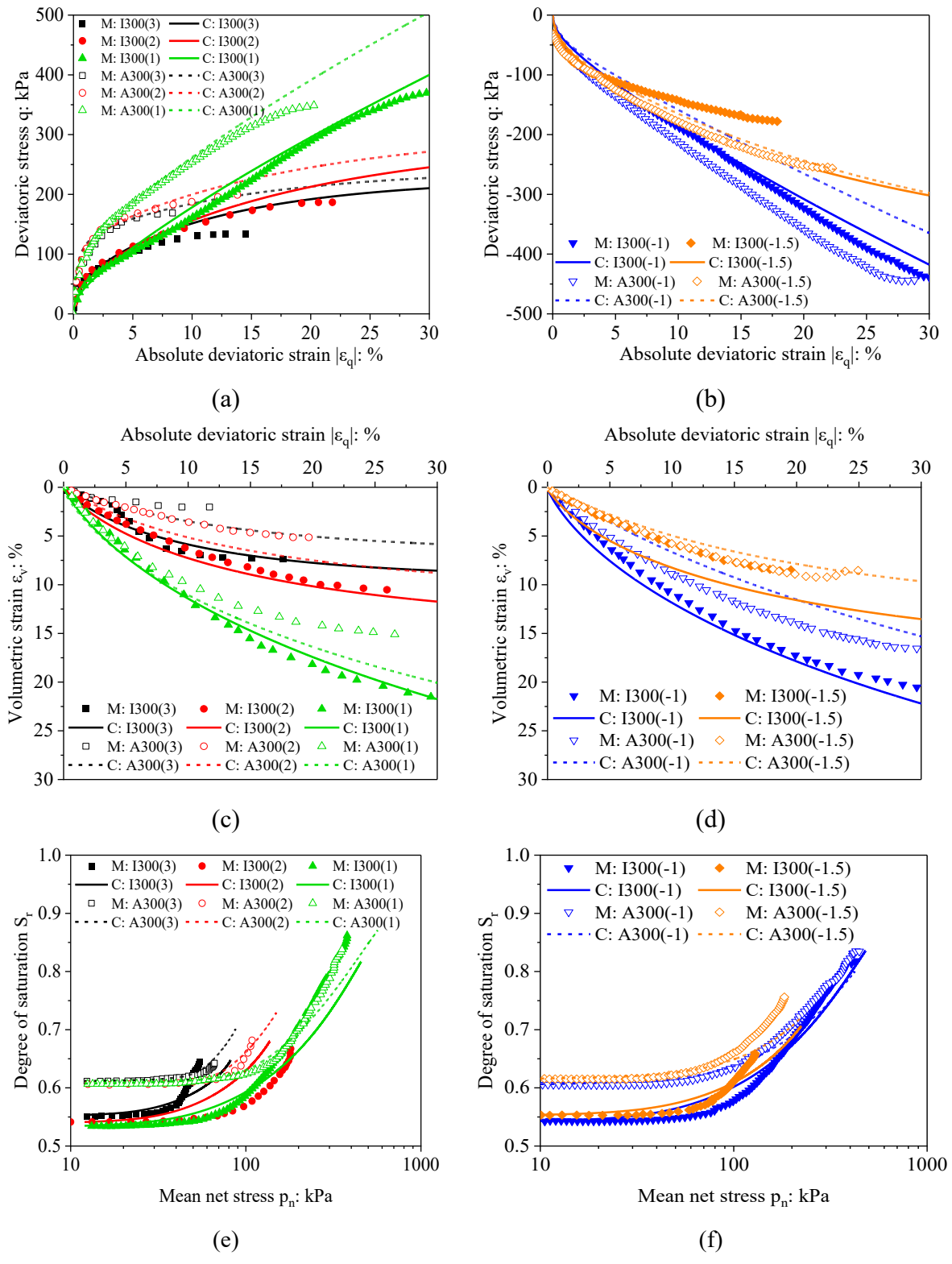

Figure 6-10. Constant suction compression and extension of speswhite kaolin under s = 300 kPa: (a-b) stress-strain curves; (c-d) volumetric strains; (e-f) variations of degree of saturation

6.3.3 Simulating anisotropic intact soils under saturated conditions

Liu et al. (2013) conducted a series of triaxial compression and extension tests on saturated,

intact Taihu clay. Both intact and reconstituted specimens were initially consolidated to an in-situ stress state of approximately p^* = 30 kPa and q = 30 kPa. Subsequent shearing was carried out at constant incremental stress ratios dq/dp^* of 2.5, 1, 0, and -1.5, as well as at constant p^*, as illustrated in Figure 6-11. The reconstituted soil was used as the reference material for model calibration, and the associated parameters are listed in Table 6-2.

Figure 6-11 presents both the computed and measured bounding surfaces for intact Taihu clay. Overall, the bounding surface defined by (6-19) effectively captures the yield behaviour of the intact clay, with the exception of two extension test results. These discrepancies could potentially be addressed by employing alternative bounding surface formulations, such as that presented by Zhou and Ng (2015). Nevertheless, to preserve the simplicity and practicality of the proposed model, no additional modifications have been made.

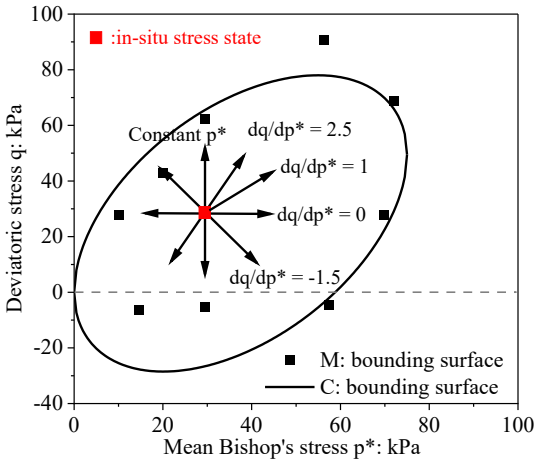

Figure 6-11. Bounding surface of intact Taihu clay

Figure 6-12 presents the one-dimensional compression results for both intact and reconstituted Taihu clay. The intact specimen demonstrates a higher yield stress and retains a higher void ratio compared to the reconstituted specimen, primarily due to structure stiffening effects. As consolidation progresses, structure degradation in the intact specimen leads to increased compressibility, resulting in a gradual convergence of the compression curves of both specimen types. The influence of soil structure is accurately captured by Equations (6-14) and (6-28), as reflected by the close agreement between the measured and computed results.

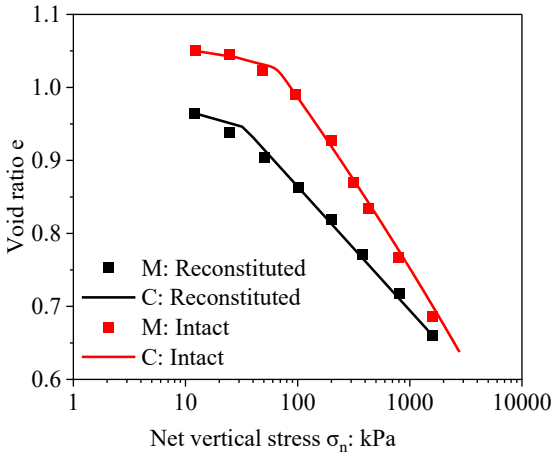

Figure 6-12. One-dimensional compression curves of intact and reconstituted Taihu clay

Figure 6-13 presents the triaxial compression test results for both intact and reconstituted Taihu clay. Note that Liu et al. (2013) only reported the results under a constant incremental stress ratio dq/dp^* of 1. As shown in Figure 6-13(a), the intact specimen exhibits a higher deviatoric stress than the reconstituted specimen at a given deviatoric strain. Figure 6-13(b) further indicates that the intact specimen undergoes a smaller volumetric strain. This difference arises because the initial stress state of the intact specimen lies well within the bounding surface, whereas the reconstituted specimen begins on the bounding surface. As a result, the intact specimen has a significantly higher initial shear modulus, leading to reduced volumetric deformation.

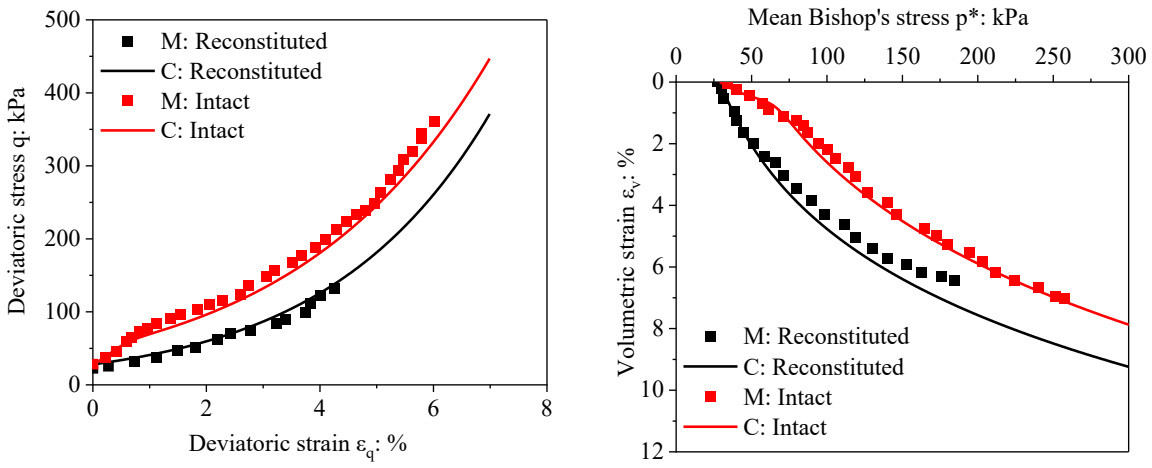

(a) (b)

Figure 6-13. Constant incremental stress ratio loading of intact and reconstituted Taihu clay: (a) stress-strain curves; (b) volumetric strains

The close agreement between the measured and calculated results in Figure 6-11, Figure

6-12, and Figure 6-13 confirms the model's ability to effectively reproduce the behaviour of saturated structured soils.

6.3.4 Simulating anisotropic intact soils under unsaturated conditions

Ng et al. (2017) examined the shear behaviour of intact and compacted loess under both saturated and unsaturated conditions. In their study, specimens were initially compressed to a mean net stress of 50 kPa and then wetted to various levels of suction. Shearing was subsequently carried out under constant suction and constant mean net stress. The compacted loess was designated as the reference soil for model calibration. To determine the model parameters, isotropic compression curves and soil water retention data obtained under different mean net stresses by Kaewsong (2017) and Cheng (2017) were employed. The model parameters calibrated from these experimental data are listed in Table 6-2.

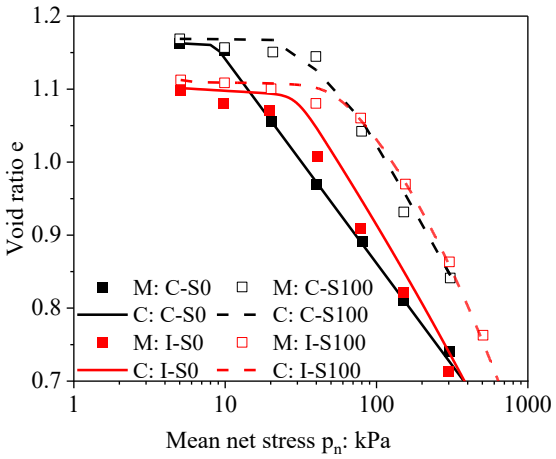

Figure 6-14. Isotropic compression curves of intact and compacted loess under different suctions

Figure 6-14 presents the isotropic compression curves for compacted and intact loess under suctions of 0 and 100 kPa. In the figure, the symbols "I" and "C" denote the intact and compacted specimens, respectively, while "S" refers to the suction, with the subsequent number indicating the suction value in kPa. It is evident that intact specimens exhibit higher yield stresses than compacted specimens under both saturated and unsaturated conditions. Consistent with the observations in Figure 6-12, the compression curves of intact specimens gradually converge toward those of compacted specimens due to structure degradation, a phenomenon

captured by Equation (6-28). Overall, Figure 6-14 demonstrates that the proposed model effectively simulates the isotropic compression behaviour of intact soils across different saturation conditions.

Figure 6-15 presents the triaxial test results for intact and compacted specimens under suctions of 0 and 50 kPa. Under saturated conditions, the stress-strain responses of intact and compacted specimens are similar. This similarity is attributed to significant structure degradation in the intact specimen prior to shearing, where the structure parameter $R(0)$ decreases from 3.4 to 1.5 due to compression (p_n = 50 kPa) and wetting (see Figure 6-14). Under unsaturated conditions, the intact specimen exhibits a higher deviatoric stress than the compacted specimen, although this difference diminishes with increasing strain. The initially stiffer response of the intact specimen is attributed to structure stiffening effects (Ng et al., 2017). As plastic deformation progresses, structure degradation leads to the convergence of deviatoric stress between the intact and compacted specimens. Moreover, the computed stress-strain curves show good agreement with experimental data, indicating the model's robust performance in capturing anisotropic and structured soil behaviour under both saturated and unsaturated conditions.

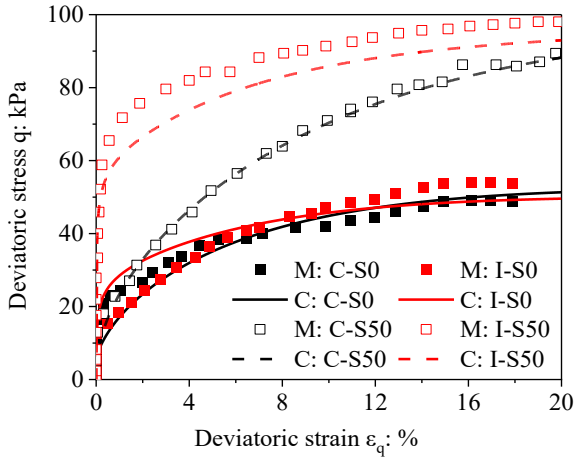

Figure 6-15. Stress-strain curves of intact and compacted loess under different suctions

6.3.5 Simulating anisotropic intact loess subjected to cyclic loading

In this section, the results from Chapter 3 to Chapter 5 are utilised for model validation. The compacted loess specimen is adopted as the reference state. Model parameters are listed

in Table 6-2. First, the model was employed to calculate the isotropic compression curves of both compacted and intact specimens under different suctions (i.e., the results shown in Figure 4-2). A comparison between the measured and calculated LC is presented in Figure 6-16. The results clearly show that isotropic yield stress increases with decreasing saturation, and that the intact specimen consistently exhibits a higher yield stress than the compacted specimen at a given unsaturation state. These trends are well reproduced by the proposed model.

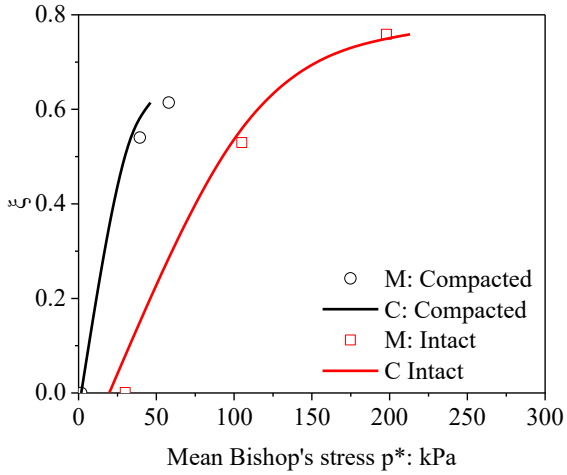

Figure 6-16. Loading collapse curves for compacted and intact specimens

Figure 6-17 compares the measured and calculated isotropic compression curves. At a given suction and stress state, the intact specimen maintains a higher void ratio than the compacted specimen. This difference in void ratio diminishes with increasing stress, owing to the structure degradation-induced greater compressibility of the intact specimen.

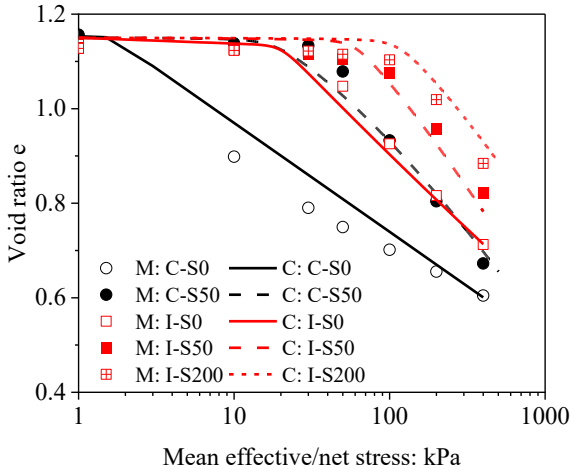

Figure 6-17. Isotropic compression curves for compacted and intact specimens under various suctions

Furthermore, the cyclic behaviour of compacted and intact specimens under different suctions was calculated using the proposed model. A comparison between the measured and calculated stress-strain responses over the first five loading cycles is shown in Figure 6-18.

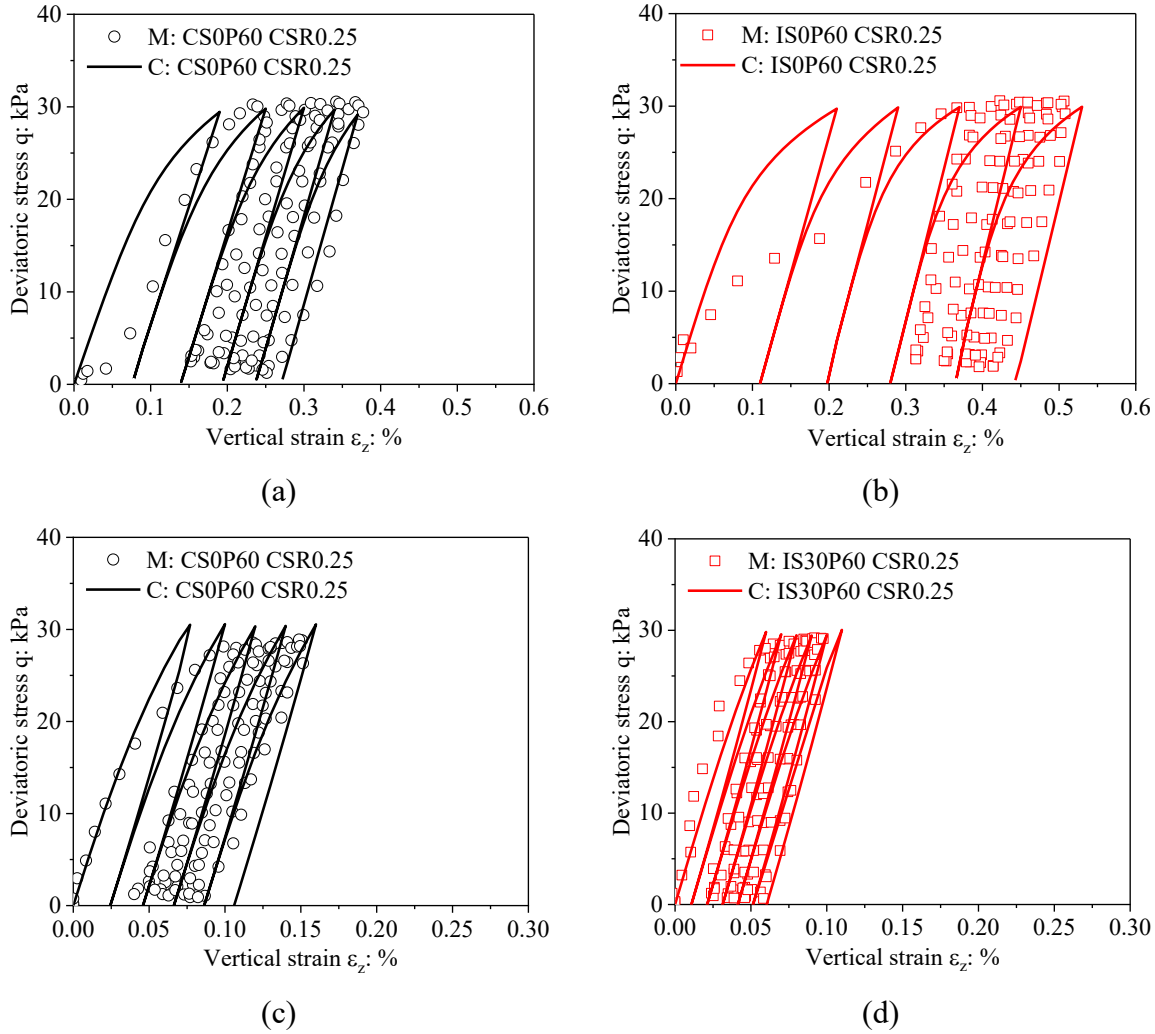

Figure 6-18. Stress-strain curves of the first five cycles under a confining pressure of 60 kPa and a CSR of 0.25: (a) saturated compacted specimen; (b) saturated intact specimen; (c) compacted specimen with s_0 = 30 kPa; (c) intact specimen with s_0 = 30 kPa

For a given number of cycles, the saturated intact specimen develops more permanent vertical strain than the saturated compacted specimen. This is because the applied confining pressure (60 kPa) exceeds the isotropic yield stress of the intact specimen (35 kPa), resulting in significant structure degradation and additional permanent strain in the saturated intact specimen. In contrast, under unsaturated conditions, the intact specimen accumulates less permanent vertical strain than the compacted specimen, owing to its stiffer soil skeleton and negligible structure degradation under such stress states. More importantly, the calculated

results show good agreement with the measured data, demonstrating the effectiveness of the proposed model.

6.4 Summary and conclusions

In this chapter, a new bounding surface model was proposed to describe the hydro-mechanical behaviour of anisotropic and structured soils under both saturated and unsaturated conditions. To the best of the authors' knowledge, this is the first model that incorporates anisotropic effects into both the mechanical and hydraulic responses of structured soils in unsaturated conditions.

The proposed model incorporates the effects of anisotropy and structure on the mechanical behaviour of soils, such as the LC curve. Experimental results indicate that the inclination of the normalised LC curve for structured soils may be smaller than, larger than, or equal to that of reference soils. These variations are integrated within a unified framework. Moreover, the model successfully captures the LC curve under both isotropic and anisotropic conditions.

Furthermore, experimental data reveal that the anisotropic specimen exhibits a higher degree of saturation than the isotropic specimen under identical suction and void ratio conditions. To capture this behaviour, a new water retention model was developed, which accounts for the enhanced water retention capacity associated with increasing anisotropy. In addition, a new equation was proposed to relate the inclination of the bounding surface (α) to the parameter representing anisotropy effects on the soil water retention curve (h). Therefore, the anisotropy effects on the mechanical behaviour and SWRC are well-linked.

Through a carefully designed validation strategy, it was demonstrated that the model effectively captures the behaviour of anisotropic structured soils under both saturated and unsaturated conditions.

CHAPTER 7 LOESS IMPROVEMENT WITH LIME AND GROUND GRANULATED BLAST FURNACE SLAG

Due to its aeolian depositional origin, loess usually exhibits a metastable and highly porous structure that is susceptible to collapse under hydromechanical loads (Muñoz-Castelblanco et al., 2012; Xu and Coop, 2016; Mu et al., 2023b). Field investigations have shown that the high collapse potential of loess poses significant risks to the safety of earthen structures (Delage et al., 2005; Ma et al., 2017; Sadeghi et al., 2019; Peng et al., 2020). For instance, loess collapse has caused numerous sinkholes near the TGV high-speed railway in northern France (Delage et al., 2005) and the national Chabahar-Zahedan railway in Iran (Sadeghi et al., 2019). Loess collapse has also resulted in excessive ground movements along the canals in the western United States (Gibbs and Bara, 1962) and northeastern Iran (Tabarsa et al., 2018). Therefore, loess is commonly stabilised with cement or lime during geo-structure construction to reduce its collapse potential. However, given the energy-intensive and environmentally unsustainable properties of these commonly used binders, industrial by-products such as ground granulated blast furnace slag (GGBS) are being considered as partial substitutes in loess improvement. This chapter investigates the collapse susceptibility of lime- and GGBS-modified loess. The effects of binder (total mass amount of lime and GGBS) content, GGBS-to-binder ratio and dry density on collapse index are presented. The mechanisms underlying loess modification by lime and GGBS are studied by TGA, SEM, and MIP tests.

7.1 Basic properties of binders

Quicklime and GGBS are utilised as binder materials, with their particle size distributions presented in Figure 7-1. The particle size distribution of GGBS is comparable to that of the tested loess, whereas lime has a smaller median diameter than both loess and GGBS.

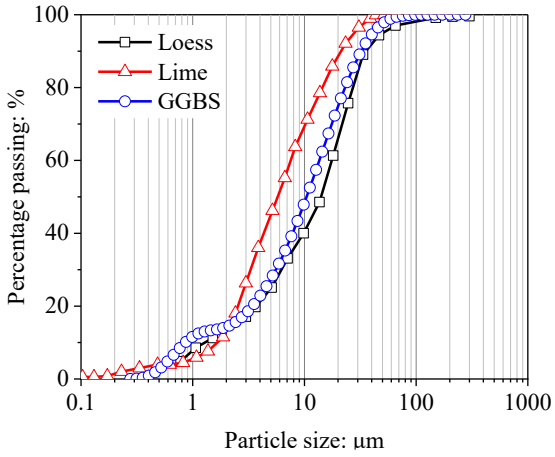

Figure 7-1. Particle size distributions of the tested loess, lime, and GGBS

The chemical compositions of lime and GGBS are detailed in Table 7-1. The primary component of lime is CaO (96.8%), while the major constituents of GGBS include CaO (43.9%), SiO_2 (29.4%), Al_2O_3 (15.2%), and MgO (8.0%).

Table 7-1. Relative weights (%) of chemical compositions in quicklime and GGBS

Composition	SiO_2	Al_2O_3	CaO	Fe_2O_3	MgO	K_2O	P_2O_5	SO_3	TiO_2
Quicklime	1.4	0.6	96.8	0.1	0.7	0.1	0.1	0.2	0.0
GGBS	29.4	15.2	43.9	0.4	8.0	0.3	0.1	2.1	0.6

7.2 Specimen preparation, test program, and test procedures

7.2.1 Specimen preparation

To align with the field construction process, the specimen preparation involved the following procedures: (i) preparation of soil powder; (ii) mixing the soil powder with lime and GGBS; (iii) compaction of the mixture; and (iv) allowing time for hydration (Yi et al., 2016; Haeri et al., 2019).

To prepare the soil powder, disturbed soil collected from the field was oven-dried, crushed with a rubber hammer, and passed through a 2 mm sieve. De-aired water was then sprayed onto the soil, followed by thorough mixing to achieve a target water content of 10%. The soil powder was subsequently sieved again using a 2 mm sieve and stored in sealed plastic bags for 24 hours to allow for moisture equalisation. Depending on the binder content and GGBS-to-binder ratio, predetermined amounts of lime and GGBS were then mixed with the soil powder. Additional

water was sprayed during mixing to maintain the soil-binder mixture at a water content of 10%.

The homogenised soil-binder mixture was compacted into an oedometer ring (70 mm in diameter and 20 mm in height) in two layers using a displacement-controlled compression machine at a loading rate of 1 mm/min. Upon reaching the target dry density (1.23 or 1.50 g/cm^3), the specimens were wrapped in plastic film and sealed in plastic bags for hydration. One-dimensional compression tests were performed after a 14-day curing period. This duration was deemed sufficient according to Haeri et al. (2019), who reported that changes in the collapse potential of lime-stabilised loess became insignificant beyond this period.

Samples for microstructure investigation and hydration product analysis were prepared following the methodology described by Yi et al. (2016). Small cubes (about 10^{-6} m^3 in volume) were extracted from the cured specimens, immersed in acetone to terminate hydration reactions, and subsequently freeze-dried by vacuum-pumping. The dried cubes were used for SEM and MIP tests, while ground sample powder, sieved through a 150 μm sieve, was utilised for TGA.

7.2.2 Test program

Table 7-2 outlines the experimental program for one-dimensional compression tests conducted on specimens with varying binder contents, GGBS-to-binder ratios, and dry densities. The binder content is defined as the mass ratio of lime and GGBS to dry soil, quantifying the total binder present in the soil matrix. Meanwhile, the GGBS-to-binder ratio denotes the mass ratio of GGBS to the total binder, indicating the proportion of lime substituted by GGBS.

Specimens were prepared with two dry densities (1.23 and 1.50 g/cm^3), corresponding to degrees of compaction of 70% and 85%, respectively. The lower dry density is identical to that of in-situ loess, while the higher density is close to the target degree of compaction specified in the Chinese standard for loess compaction (JTG/T D31-05, 2017). An initial water content of 10% was selected to represent a relatively dry condition. The binder contents and GGBS-to-binder ratios were selected based on previous research on lime- and GGBS-stabilised loess (Haeri et al., 2019; Guo et al., 2022). Haeri et al. (2019) showed that the collapse of loess

became negligible after adding 3% lime to untreated loess. Moreover, Guo et al. (2022) observed a continuous increase in unconfined compressive strength as the GGBS-to-binder ratio increased from 0% to 50% at a fixed binder content. Consequently, four binder contents (0%, 1%, 2%, and 3%) and three GGBS-to-binder ratios (0%, 25%, and 50%) were selected to examine the trends in collapse susceptibility variations with binder and GGBS contents. The consideration of these dry densities, binder contents, and GGBS-to-binder ratios resulted in a total of 20 one-dimensional compression tests.

Table 7-2. Test program of one-dimensional compression tests

Test ID*	Binder content: %	GGBS-to-binder ratio: %	Initial dry density: g/cm^3
B0R0-L	0	0	1.23
B0R0-D			1.50
B1R0-L	1	0	1.23
B1R0-D			1.50
B1R25-L		25	1.23
B1R25-D			1.50
B1R50-L		50	1.23
B1R50-D			1.50
B2R0-L	2	0	1.23
B2R0-D			1.50
B2R25-L		25	1.23
B2R25-D			1.50
B2R50-L		50	1.23
B2R50-D			1.50
B3R0-L	3	0	1.23
B3R0-D			1.50
B3R25-L		25	1.23
B3R25-D			1.50
B3R50-L		50	1.23
B3R50-D			1.50

*Notation: “B” is the binder content, defined as the mass ratio of binder (lime and GGBS) to dry soil; “R” is the GGBS-to-binder ratio, representing the proportion of GGBS in the total binder; and “L” and “D” represent looser and denser states, respectively.

To examine the influence of lime and GGBS on microstructure and hydration products, SEM, MIP, and TGA were performed on specimens B0R0-D, B3R0-D, and B3R50-D prior to consolidation. The SEM, MIP, and TGA were conducted using VEGA3 TESCAN, PoreMaster

33, and Thermo Plus EVO2, respectively. In interpreting the MIP results, a contact angle of 140° was assumed, and pore diameter was determined following the approach outlined by Romero and Simms (2008). For each specimen used in TGA, two parallel tests were conducted to ensure repeatability.

7.2.3 Test procedures

One-dimensional compression tests with wetting at a vertical stress of 200 kPa were conducted. After the curing period, the specimen was placed in the loading apparatus, and a seating stress of 5 kPa was applied for 5 minutes. The specimen was then subjected to a series of vertical stress levels (12, 25, 50, 100, and 200 kPa) under a constant water content, with each stress level maintained for 1 hour to minimise moisture evaporations (ASTM, 2003).

Upon completion of loading at 200 kPa, the specimen was inundated with de-aired water, with the water flowing from the bottom to the top of the specimen to prevent air entrapment. Deformation after wetting was recorded at intervals of approximately 0.1, 0.25, 0.5, 1, 1.5, 2, 4, 12, and 30 minutes, and at 1, 2, 4, 8, and 24 hours. The wetting stage lasted for 24 hours, after which the specimen was further consolidated to 2000 kPa and unloaded to 5 kPa.

To quantify soil collapse, the experimental method outlined in ASTM (2003) is widely used in engineering practices. The collapse potential is measured through one-dimensional compression tests with wetting at different vertical stresses. Accordingly, a collapse index (I_e) is defined as follows:

$$I_e = \frac{\Delta e}{1+e_0} \times 100\% \tag{7-1}$$

where Δe represents the wetting-induced void ratio change at a vertical stress of 200 kPa; and e_0 is the initial void ratio of the specimen. Depending on the magnitude of the collapse index, the degree of collapse is categorised as: non-collapse (I_e = 0.0%), slight collapse (0.1% < I_e < 2.0%), moderate collapse (2.1% < I_e < 6.0%), moderately severe collapse (6.1% < I_e < 10.0%), and severe collapse (I_e > 10.0%).

Similarly, the collapse susceptibility of loess in the Chinese standard is also evaluated

using oedometer tests (JTG/T D31-05, 2017). Different from ASTM (2003), the vertical stress at which collapse is assessed is not fixed at 200 kPa but varies depending on the burial depth of the soil. Based on the wetting-induced volumetric strain, the degree of collapse is classified as: non-collapse (< 1.5%), slight collapse (1.5% - 3.0%), moderate collapse (3.0% - 7.0%), and severe collapse (> 7.0%).

7.3 Effects of binder content on the hydro-mechanical behaviour of loess

7.3.1 One-dimensional compression curves and wetting-induced collapse

Figure 7-2 presents the test results with binder contents of 0%, 1%, 2%, and 3%, and a zero GGBS-to-binder ratio. At a specified binder content, the looser specimen has a higher void ratio than the denser specimen before wetting. Upon wetting under a vertical stress of 200 kPa, a significant volumetric reduction in the looser specimen is observed, whereas the denser specimen exhibits insignificant deformation. This is attributed to the yield stress of the saturated denser specimen exceeding 200 kPa, as evidenced by the post-wetting compression curve. According to the concept of loading collapse curve proposed by Alonso et al. (1990), wetting-induced collapse is insignificant when the yield stress of the saturated specimen is higher than the applied stress. After wetting and loading to 2000 kPa, the void ratios of looser and denser specimens tend to converge, indicating that a unified compression curve is reached.

Moreover, the wetting-induced deformation over time for loosely and densely compacted specimens is presented in Figure 7-2(a). The results indicate that, at a given time, the denser specimen (B0R0-D) exhibits a smaller volumetric strain compared to the looser specimen (B0R0-L). Furthermore, volumetric contraction is initiated within 6 seconds after wetting in the looser specimen, whereas in the denser specimen, this process takes approximately 90 seconds. This delayed response in the denser specimen is consistently observed across different binder contents and GGBS-to-binder ratios, which is mainly due to its lower permeability at a higher dry density (Xu et al., 2021b; Li et al., 2023). Specifically, the measured permeabilities of the saturated looser and denser specimens are approximately 4.8×10^{-7} m/s and 2.5×10^{-7} m/s, respectively.

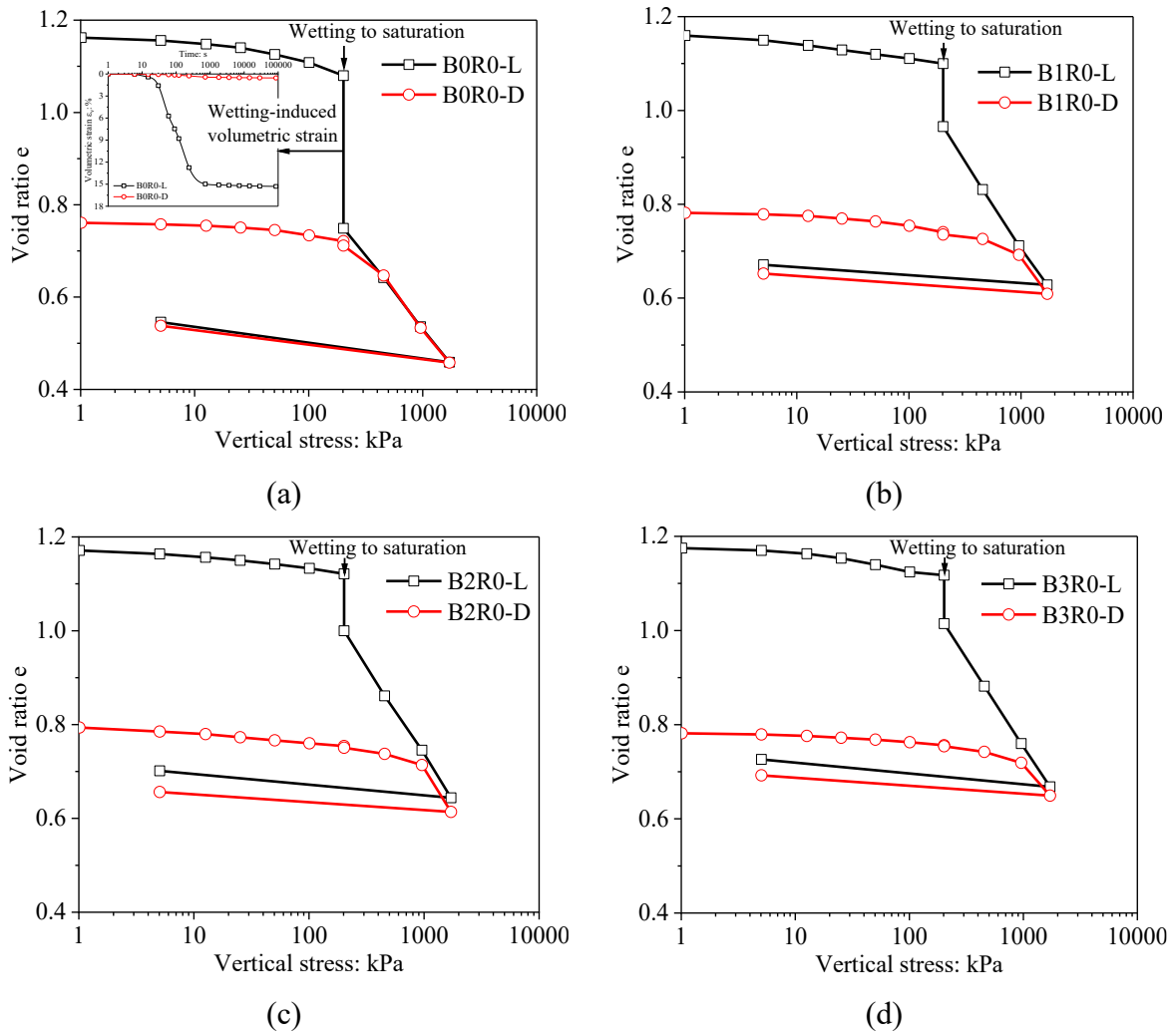

Figure 7-2. Influence of dry density on compression curve for specimens with different binder contents: (a) 0%; (b) 1%; (c) 2%; (d) 3%

Figure 7-3 illustrates the influence of binder content on the compression curve for specimens with GGBS-to-binder ratios of 0%, 25%, and 50%. At a given initial dry density and GGBS-to-binder ratio, the compression curves prior to wetting are nearly identical across different binder contents. During the wetting stage, specimens with higher binder contents experience less pronounced collapse, suggesting an enhanced and more stable soil structure. Specifically, in the looser specimen with a zero GGBS-to-binder ratio, the wetting-induced volumetric compression is reduced from 15.3% to 4.7% as the binder content increases from 0% to 3%. After wetting, the compression curve exhibits an upward shift with increasing binder content. This behaviour is likely because more hydration products are generated at higher binder contents (Guo et al., 2024), which allows the soil skeleton to sustain a higher void ratio under a given stress state, similar to the observations in cemented soils (e.g., Arroyo et al.,

2013).

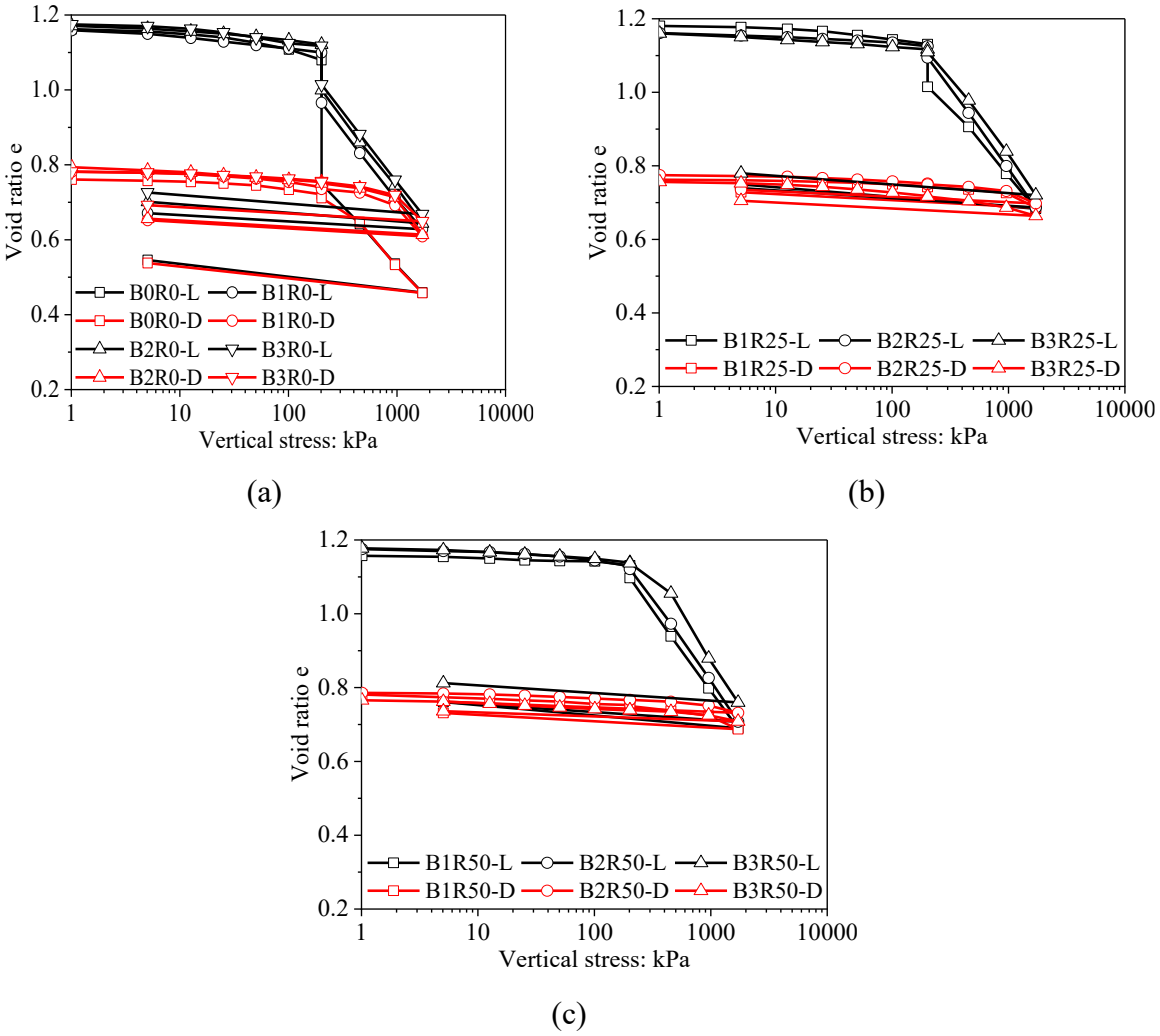

Figure 7-3. Influence of binder content on compression curve for specimens with different GGBS-to-binder ratios: (a) 0%; (b) 25%; (c) 50%

Based on the volumetric deformation measured after 24 hours of wetting, the collapse index is calculated for each specimen using Equation (7-1). Figure 7-4 illustrates the variations in collapse index with binder content for specimens with different dry densities and GGBS-to-binder ratios. Note that no collapse occurs for the two denser specimens, B2R50-D and B3R50-D, and thus their results are excluded from the figure. It is evident that, for a given condition, the collapse index decreases linearly as binder content increases from 0% to 3% on a semilogarithmic scale. More importantly, the reduction is more significant at lower dry densities and higher GGBS-to-binder ratios. For example, when binder content of looser specimens increases from 0% to 3%, the collapse index decreases from 15.3% to 4.7% at zero

GGBS content, while it decreases to 0.06% at a GGBS-to-binder ratio of 50%. This observation suggests that, within the considered range of binder contents and GGBS-to-binder ratios, the partial replacement of lime with GGBS improves the binder's ability to mitigate wetting-induced collapse. This improvement is closely associated with the varying quantities of hydration products formed when lime is partially substituted by GGBS, as explained in the subsequent sections.

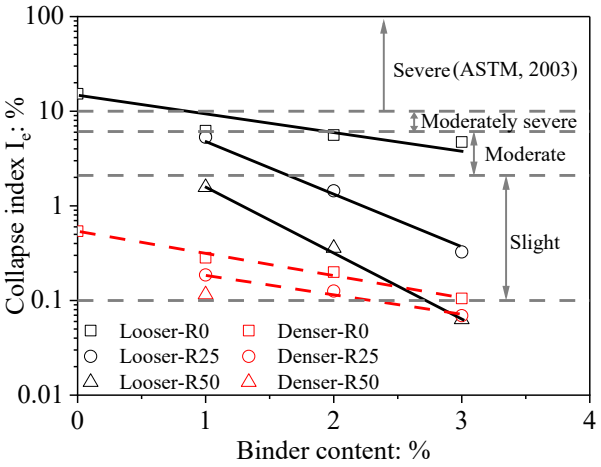

Figure 7-4. Influence of binder content on the wetting collapse

Figure 7-5 exhibits the impacts of the GGBS-to-binder ratio on compression curve for specimens with binder contents of 1%, 2%, and 3%. Under the same initial dry density and binder content, wetting-induced volumetric strain decreases significantly with increasing GGBS-to-binder ratio. For example, wetting-induced volumetric contraction decreases from 6.2% to 1.5% as the GGBS-to-binder ratio increases from 0% to 50% for the looser specimen at a binder content of 1%. This observation highlights the effectiveness of GGBS as a partial replacement for lime in reducing the collapse susceptibility of loess. Additionally, the compression curve is shifted upward as GGBS-to-binder ratio increases, likely because of the greater amount of hydration products.

Figure 7-6 gives the variations of collapse index with GGBS-to-binder ratio under different dry densities and binder contents. Under a given condition, the collapse index decreases linearly as the GGBS-to-binder ratio increases from 0% to 50% on a semilogarithmic scale. Furthermore, the reduction in collapse index with increasing GGBS-to-binder ratio is

more significant at higher binder contents due to the formation of more hydration products (Yi et al., 2016; Guo et al., 2024).

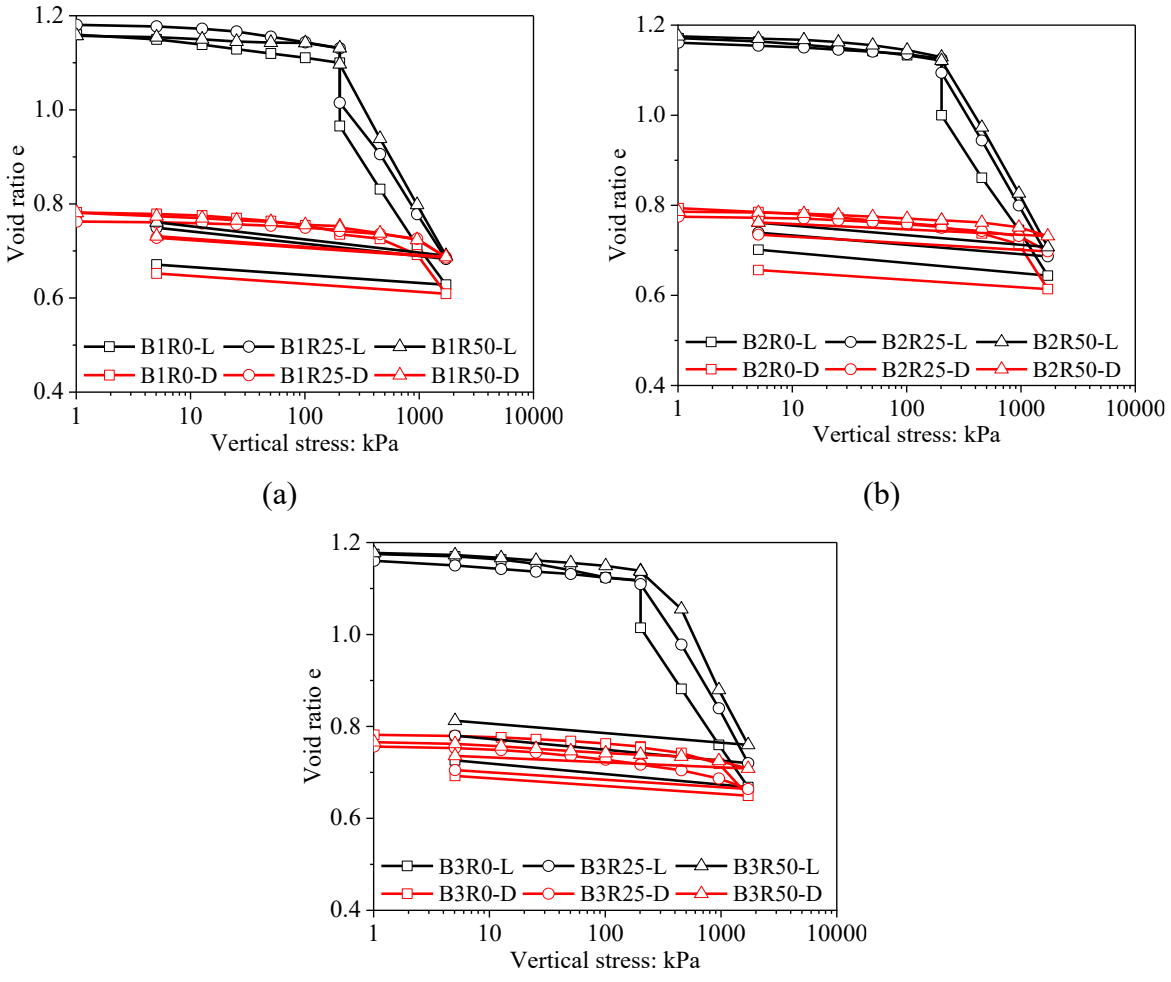

Figure 7-5. Influence of GGBS-to-binder ratio on compression curve for specimens with different binder contents: (a) 1%; (b) 2%; (c) 3%

To evaluate the degree of specimen collapse, the collapse index classification suggested by ASTM (2003) is employed. The collapse classification boundaries are outlined in Figure 7-4 and Figure 7-6.It can be observed that the untreated looser specimen (B0R0-L) exhibits severe collapse, rendering it unacceptable for engineering applications in loess regions. When treated with lime, the looser loess shows moderately severe collapse at 1% lime content (B1R0-L) and moderate collapse at 2% and 3% lime contents (B2R0-L and B3R0-L). According to construction guidelines for loess regions (JTG/T D31-05, 2017), loess with a collapse index exceeding 4% requires additional treatment or compaction. This suggests that adding 3% lime

to a looser specimen (I_e = 4.7%) is insufficient for construction. When 50% of the lime is replaced with GGBS, looser specimens exhibit slight collapse at binder contents of 1% and 2% (B1R50-L and B2R50-L), and the collapse index is below the lower limit for slight collapse at a binder content of 3% (B3R50-L). These observations indicate that the partial replacement of lime with GGBS can effectively reduce the collapse of looser loess, thereby satisfying engineering requirements. Furthermore, denser specimens with different lime contents and a zero GGBS-to-binder ratio exhibit slight collapse. When the GGBS-to-binder ratio increases to 50% at lime contents of 2% and 3% (B2R50-D and B3R50-D), the denser specimens are classified as non-collapse loess, which is preferable during geo-structure constructions.

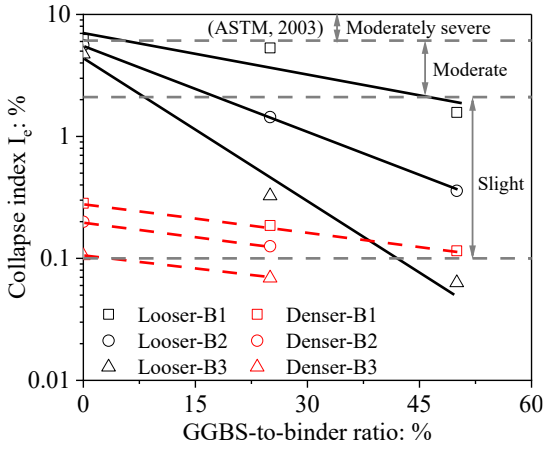

Figure 7-6. Influence of binder composition on the wetting collapse

Based on the results presented in Figure 7-2 to Figure 7-6, it can be concluded that an increase in binder content and GGBS-to-binder ratio leads to a reduction in wetting-induced volumetric strain and an upward shift in the normal compression curve. On a semilogarithmic scale, the collapse index decreases linearly as the binder content increases from 0% to 3% or as the GGBS-to-binder ratio rises from 0% to 50%. More importantly, a more pronounced reduction is observed at higher GGBS-to-binder ratios, suggesting that partially replacing lime with GGBS effectively mitigates the collapse susceptibility of loess.

7.3.2 Compression and swelling indices of saturated specimens

Figure 7-7 compares the compression and swelling indices for specimens with varying initial dry densities, binder contents, and GGBS-to-binder ratios. Note that the compression

indices of denser specimens are not presented, as most have not reached the normally consolidated state, as indicated in Figure 7-3. However, it is expected that looser and denser specimens have similar compression indices, given the convergence of their compression curves observed in Figure 7-2.

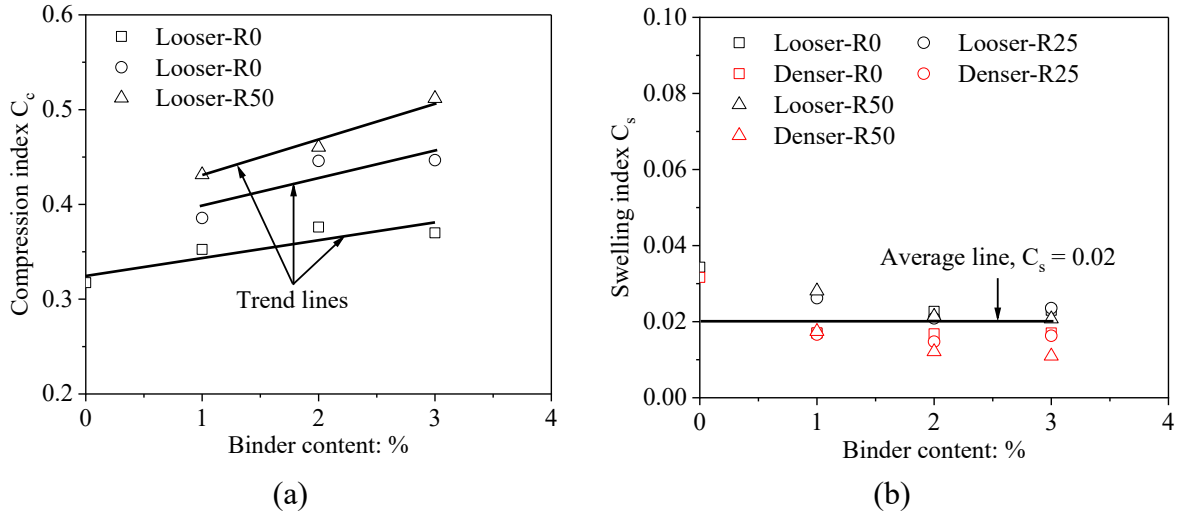

(a) (b)

Figure 7-7. Variations of compression and swelling indices with dry density, binder content, and GGBS-to-binder ratio: (a) compression indices; (b) swelling indices

Figure 7-7(a) demonstrates that the compression index increases with increasing binder content and GGBS-to-binder ratio. This trend is likely due to the formation of additional bonds, whose breakage induces larger plastic deformation and consequently leads to increased post-yield compressibility (Yan and Li, 2011; Dai et al., 2024). A similar trend has been observed in comparisons between the cemented and uncemented silty sand (Arroyo et al., 2013), as well as between intact and reconstituted loess (Xu and Coop, 2016). Figure 7-7(b) illustrates that the swelling index decreases slightly with increasing dry density and binder content, while its variation with respect to GGBS-to-binder content is insignificant. For simplicity, a mean value of 0.02 may be adopted as a reference swelling index under various states.

7.4 Investigation of soil stabilisation mechanisms

To investigate the influence of lime and GGBS on microstructures and hydration products, SEM, MIP, and TGA were conducted on specimens B0R0-D, B3R0-D, and B3R50-D. The results are presented from Figure 7-8 to Figure 7-10.

7.4.1 Influence of lime and GGBS on soil microstructure

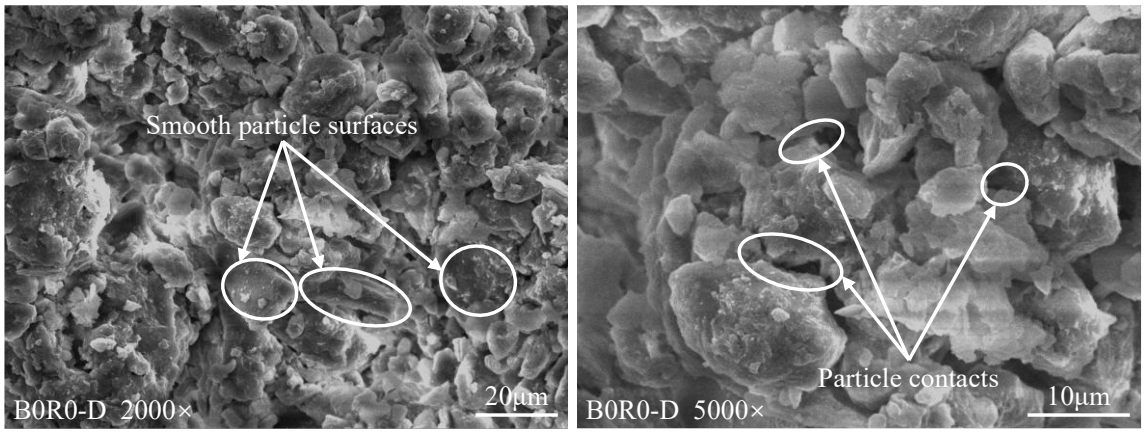

(a)

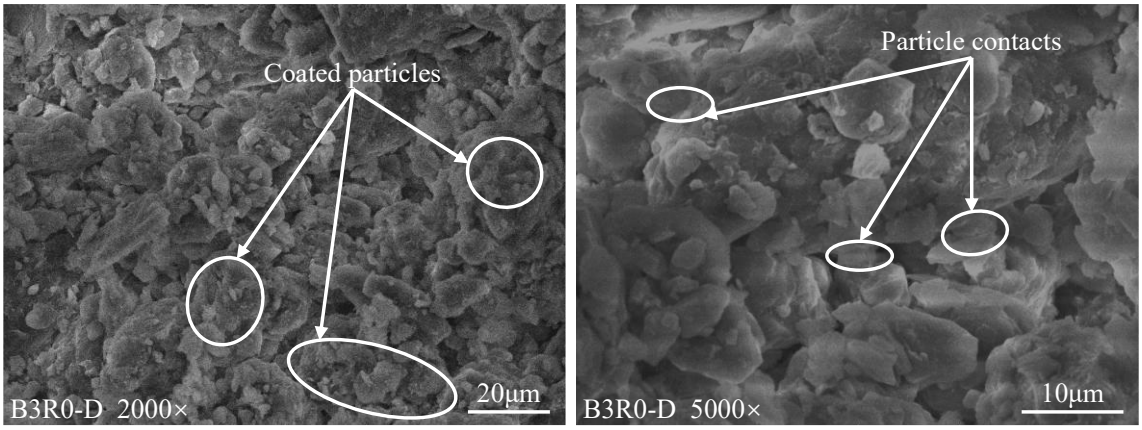

(b)

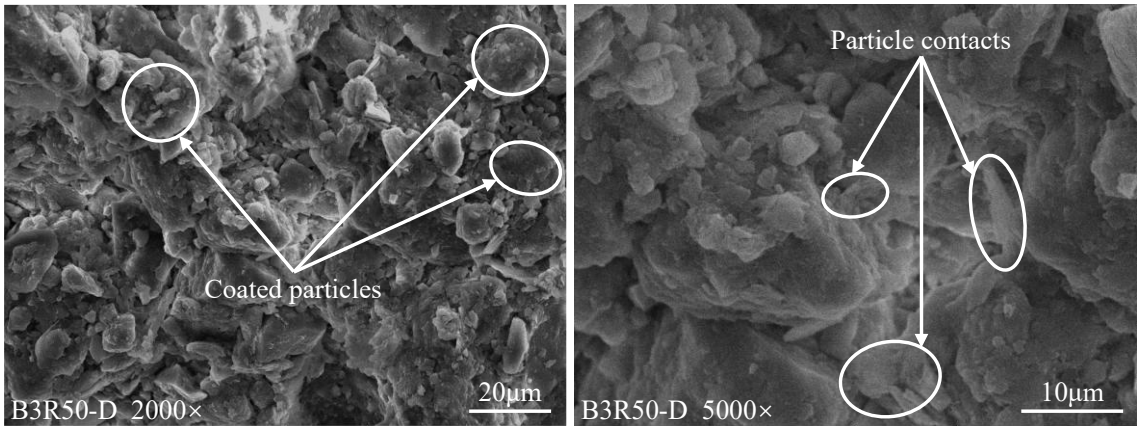

(c)

Figure 7-8. SEM results for specimens with different binder contents and GGBS-to-binder ratios: (a) B0R0-D; (b) B3R0-D; (c) B3R50-D

Figure 7-8 presents the SEM images of specimens B0R0-D, B3R0-D, and B3R50-D,

captured at magnifications of 2000× and 5000×. The results at 2000× magnification show that soil particles in untreated loess exhibit relatively smooth and distinct surfaces, whereas those in lime- and GGBS-treated loess are coated with soil grains or hydration products. More importantly, SEM images at 5000× magnification reveal the existence of visible pores between particles in specimen B0R0-D, whereas connection assemblages are identified between silt particles in specimens B3R0-D and B3R50-D.

Figure 7-9 shows the pore size distribution curves obtained from MIP tests. Following the methodology of Ng et al. (2016), a delimiting pore size of 0.2 μm, corresponding to the valley between two dominant peaks in the pore size distribution curve, is used to distinguish micropores from macropores. All specimens exhibit bimodal distributions, with one peak in the micropore range (< 0.2 μm) and another in the macropore range (> 0.2 μm). Moreover, the dominant macropore size slightly decreases with lime and GGBS treatments. Specifically, the dominant diameters for specimens B0R0-D, B3R0-D, and B3R50-D are 6.6 μm, 4.0 μm, and 5.7 μm, respectively.

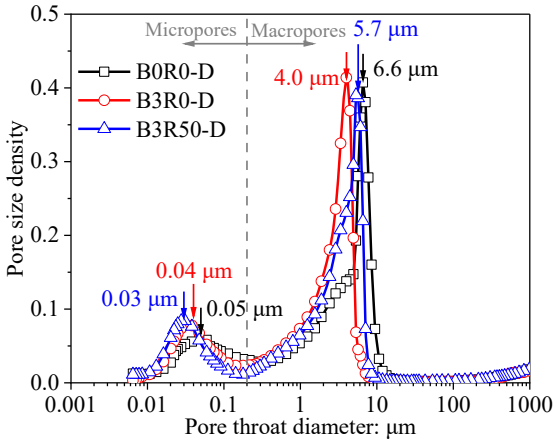

Figure 7-9. MIP results for specimens with different binder contents and GGBS-to-binder ratios

7.4.2 Hydration products of lime- and GGBS-treated loess

Figure 7-10(a) gives the thermogravimetry (TG) curves for the tested specimens. It is evident that the total weight loss increases with higher lime and GGBS contents, indicating the presence of additional hydration or mineralogical components. Specifically, the weight losses

for specimens B0R0-D, B3R0-D, and B3R50-D are 9.9%, 11.0%, and 11.2%, respectively. To examine the component differences, the differential thermogravimetry (DTG) curves are derived from the TG curves and presented in Figure 7-10(b). It can be observed that the major differences occur in three temperature ranges: (i) 50 to 600 °C, (ii) 400 to 500 °C, and (iii) 600 to 800 °C, which are associated with the thermal decomposition of calcium silicate hydrate (CSH), calcium hydroxide ($Ca(OH)_2$), and calcium carbonate ($CaCO_3$), respectively (Scrivener et al., 2016; Zhao et al., 2024). These three compounds represent the dominant hydration products formed in lime-stabilised and lime-GGBS-stabilised soils (James et al., 2008; Oti et al., 2009; Yi et al., 2016; Guo et al., 2024). It is therefore appropriate to examine the differences in these hydration products among the tested specimens based on the DTG curves.

Compared to untreated loess (B0R0-D), the addition of 3% lime (B3R0-D) primarily increases the contents of $Ca(OH)_2$ and $CaCO_3$. These compounds may form cementation bonds between soil particles and fill inter-particle pores, as evidenced by the SEM and MIP results in Figure 7-8 and Figure 7-9, leading to a stiffer soil skeleton and reducing collapse index in lime-treated loess. More importantly, a comparison between specimens B3R0-D and B3R50-D reveals that partial replacement of lime with GGBS reduces the $Ca(OH)_2$ content while promoting the formation of additional CSH compounds.

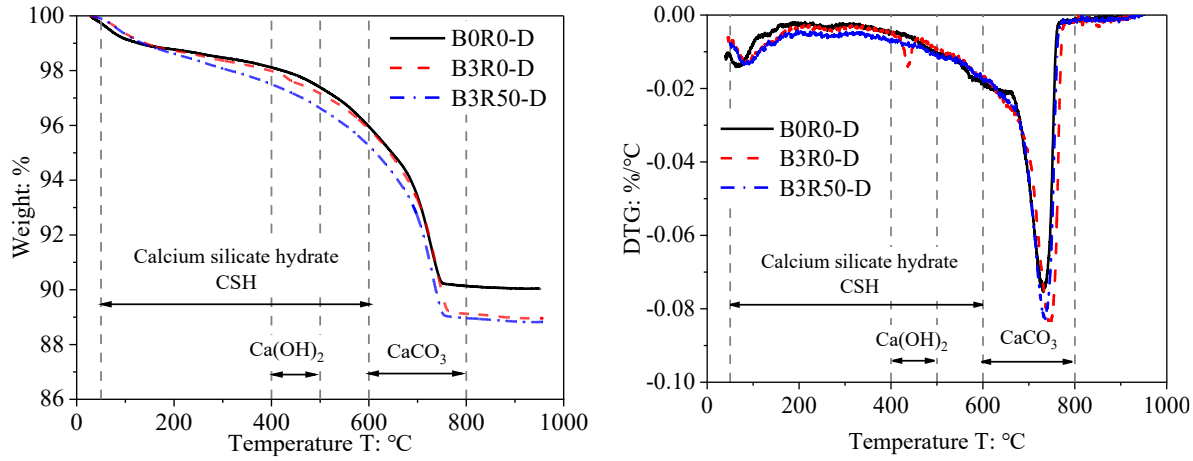

Figure 7-10. Thermogravimetry analysis for specimens with different binder contents and GGBS-to-binder ratios: (a) thermogravimetry curves; (b) differential thermogravimetry curves

7.4.3 Influence of microstructure and hydration products on macro-behaviour

The findings from Figure 7-8 and Figure 7-9 indicate that lime and GGBS modify the loess microstructure by coating soil particles, filling interparticle voids, and reducing the dominant macropore size, thereby enhancing soil structure and mitigating collapse susceptibility. Specifically, the dominant diameters for specimens B0R0-D, B3R0-D, and B3R50-D are 6.6 μm, 4.0 μm, and 5.7 μm, respectively. These observations align with Guo et al. (2024), who attributed the lime-induced loess improvement to the effects of cementation and pore-filling.

Figure 7-10 suggests that more CSH compounds are formed when lime is partially replaced by GGBS. As highlighted in previous studies (Yi et al., 2016; Zhao et al., 2024), CSH compound plays a significant role in the strength development of stabilised soils. Consequently, its presence likely contributes to the further reduction in collapse index observed when lime is partially replaced with GGBS, consistent with the trends observed in Figure 7-4 and Figure 7-6.

It should be noted that the specimen treated with lime only (i.e., B3R0-D, 4.0 μm) exhibits a smaller dominant macropore diameter than the specimen treated with both lime and GGBS (i.e., B3R50-D, 5.7 μm). This observation appears inconsistent with the finding that partial replacement of lime with GGBS is more effective in reducing wetting-induced collapse. A possible explanation is that the difference in pore size distribution is relatively minor, whereas the hydration products differ significantly, with the latter exerting a greater influence on the macroscopic behaviour.

7.5 Summary and conclusions

This chapter investigated the compression curves, collapse indices, microstructures, and hydration products of compacted loess with different dry densities, binder contents, and GGBS-to-binder ratios. The major conclusions are summarised as follows:

As dry density increases, wetting-induced volumetric strain decreases significantly, while the normal compression curves remain nearly identical between looser and denser specimens.

An increase in binder content and GGBS-to-binder ratio leads to a reduction in wetting-induced volumetric strain, an upward shift in the normal compression curve, and an increase in the compression index. These observations are because higher binder and GGBS contents create more cementation bonds, allowing the soil to maintain a higher void ratio at a given stress. Meanwhile, bond breakage under loading induces more plastic deformation, resulting in a higher compression index.

On a semilogarithmic scale, the collapse index decreases linearly with an increase in binder content from 0% to 3% or as the GGBS-to-binder ratio rises from 0% to 50%. More importantly, the effects of binder content on the collapse index are more pronounced at higher GGBS-to-binder ratios. For example, the untreated looser specimen presents a collapse index of 15.3%, a value categorised as severe collapse based on the ASTM (2003) standard. When the binder content increases to 3%, the collapse index decreases to 4.7% (indicating moderate collapse) at zero GGBS-to-binder ratio. Moreover, substituting 50% of the lime with GGBS further reduces the collapse index to 0.06%, which falls below the lower limit for slight collapse (i.e., 0.1%). These observations indicate that the partial replacement of lime with GGBS can effectively reduce the collapse susceptibility of loess and satisfy engineering requirements.

SEM and MIP results reveal that lime and GGBS modify the loess microstructure by coating soil particles, filling interparticle voids, and reducing the dominant macropore size. Specifically, the dominant diameters for specimens B0R0-D, B3R0-D, and B3R50-D are 6.6 μm, 4.0 μm, and 5.7 μm, respectively. Moreover, TG and DTG curves demonstrate that the addition of lime and GGBS leads to the formation of hydration products, with a higher content observed when lime is partially replaced by GGBS. The addition of lime primarily increases the contents of $Ca(OH)_2$ and $CaCO_3$, while partial replacement of lime with GGBS consumes the $Ca(OH)_2$ content and promotes the formation of additional CSH compounds. The presence of CSH likely contributes to the further reduction in collapse index observed when lime is partially replaced with GGBS.

CHAPTER 8 CONCLUSIONS AND FURTHER WORK

This chapter summarises the key findings of the thesis and offers recommendations for future research. Although loess was used as the test material, the experimental and theoretical outcomes are expected to provide valuable insights into the behaviour of other structured soils.

8.1 Major conclusions

8.1.1 Influence of soil structure and its evolution on soil behaviour under hydro-mechanical loads

8.1.1.1 Evolution of soil structure and anisotropic stiffness during isotropic compression

Due to its stiffer connector assemblages and oriented particle/aggregate fabric, the intact specimen exhibits approximately twice the $G_{hv}/f(e)$ and more pronounced stiffness anisotropy than the compacted and reconstituted specimens prior to compression. As stress increases, the degradation of connector assemblages in the intact specimen leads to a smaller $G_{hv}/f(e)$ compared to the others, in which interparticle contacts are enhanced under stress. Once the stress exceeds five times the yield stress, all specimens exhibit isotropic stiffness.

Due to the greater compaction effort at a given compaction water content, denser specimens exhibit larger $G_{hv}/f(e)$ and more pronounced stiffness anisotropy prior to compression than looser specimens. The tested loess shows a transitional behaviour, evidenced by the divergence of normal compression lines between looser and denser specimens. With increasing stress, denser specimens attain similar G_{hv} values but maintain lower void ratios compared to looser specimens, leading to smaller $G_{hv}/f(e)$ in the former.

Before compression, $G_{hv}/f(e)$ decreases and stiffness anisotropy diminishes with increasing compaction water content. The reduction in $G_{hv}/f(e)$ is attributed to the stiffer aggregated structure formed at dry of optimum, compared to the clod-dominated structure with inter-clod pores at wet of optimum. The reduced anisotropy is linked to more pronounced particle/aggregate orientation in the aggregated structure. After compression, $G_{hv}/f(e)$ is

larger at higher compaction water contents because of greater pore compression.

It can be concluded that $G_{hv}/f(e)$ values of initially stiffer specimens become smaller than those of initially softer specimens when the stress reaches 2 to 4 times the yield stress of the former. The trend reversal is likely due to greater strengthening of interparticle contacts and more significant pore compression in the initially softer specimens. These observations provide a plausible explanation for the inconsistent influence of soil structure on stiffness reported in the literature. Additionally, using structure-dependent parameters A_{hv} and $(n_h + n_v)/2$ enhances the reliability of deformation predictions in geotechnical applications.

8.1.1.2 Influence of soil structure on the cyclic behaviour of unsaturated specimens

It is newly found that the structure effects on permanent vertical strain can be categorised as two types based on the strain increment at the first cycle (i.e., $\Delta\varepsilon_{z,1}^{p}$). In type I, the intact specimen exhibits a smaller $\Delta\varepsilon_{z,1}^{p}$ than the compacted specimen attributed to its inherently stiffer soil structure. In type II, the intact specimen has a larger $\Delta\varepsilon_{z,1}^{p}$ due to structure degradation-induced plastic deformation. For the tested soil, the yield stress of the intact specimen can be used as a threshold confining pressure to distinguish between the two types of behaviour, with type I occurring below and type II above this threshold. More importantly, the trend in strain increment may change with the number of cycles in both types. In type I, the strain increment of the intact specimen may exceed that of the compacted specimen owing to structure degradation. Conversely, in type II, the strain increment of the intact specimen could be smaller due to failure of the compacted specimen. These findings emphasise that when soils in intact and compacted states are both involved, it is not always conservative to adopt parameters from the compacted soil. This is because the strain increment in the compacted soil could be smaller in particular cases, resulting in an underestimation of soil deformation.

The resilient modulus of the intact specimen is consistently larger than that of the compacted specimen across various suctions and stress states. This finding suggests that the soil skeleton of the intact specimen is stiffer during unloading (i.e., with a reduction of vertical stress), with smaller vertical recoverable strains compared to the compacted specimen. The

resilient modulus of the intact specimen exhibits less dependence on confining pressure but greater sensitivity to CSR and suction than that of the compacted specimen. This is because the structure degradation in the intact specimen mitigates the hardening effects of confining pressure and amplifies the softening effects of CSR, and volumetric contraction in the compacted specimen compensates for the effects of suction reduction. Consequently, the difference in resilient modulus between intact and compacted specimens diminishes at higher CSRs and confining pressures, and lower suctions.

At a given suction and CSR, the looser specimen has a permanent vertical strain up to an order of magnitude larger than that in the denser specimen, highlighting the necessity of achieving the specified dry density during geo-structure construction. The difference diminishes as suction increases because of the greater stabilising effects of suction on the soil skeleton in looser specimens than denser ones. The resilient modulus of looser specimens increases slightly with the number of cycles and remains nearly constant with varying suction and CSR because of the significant volumetric contraction compensating for the effects of suction and CSR. In contrast, the resilient modulus of denser specimens decreases with decreasing suction and increasing CSR and is larger than that of looser specimens at a given suction and CSR.

Under otherwise identical conditions, permanent vertical strain is larger and resilient modulus is smaller for the specimen compacted at the wet of optimum than that compacted at the optimum water content. This is because the soil skeleton is softer at a higher compaction water content due to the existence of extra-large inter-clod pores, as supported by microstructural analysis. These observations demonstrate that, for a given compaction effort in pavement construction, compacting soil at the optimum water content not only yields a higher dry density but also results in a more stable soil structure compared to compaction at the wet of optimum. More importantly, these differences slightly decreases when soil becomes unsaturated, possibly because the soil skeleton is more sensitive to suction variation for specimens with higher compaction water contents.

New semi-empirical equations were proposed to unify the influence of compaction conditions on cyclic behaviour. The effects of compaction conditions on permanent vertical strain and resilient modulus are captured by ε_0 and M_0, respectively, while other state-related parameters remain constant. This suggests that the suction and CSR effects on cyclic behaviour can be considered comparable across different compaction conditions in engineering practice. By comparing the calculated results with the measured data from both the present study and a previous study, a good performance of the new equations was observed.

8.1.1.3 Cyclic behaviour with principal stress rotation

Under otherwise identical conditions, the specimen subjected to PSR exhibits larger excess PWP and permanent vertical strain, and smaller resilient modulus than that without PSR. These trends are mainly because rotational loading can induce additional deformation for anisotropic soils. More importantly, the additional strain induced by PSR increases with increasing temperature and decreasing suction, as a result of a less stabilised soil skeleton. In comparison to the strain without PSR, the strain induced by PSR becomes increasingly significant at higher temperatures and lower suctions. At zero suction and a CSR of 0.4, the PSR-induced additional strain is 130% and 230% of the strain without PSR under temperatures of 5 and 40 ℃, respectively. As suction increases to 10 kPa, these two ratios are 50% and 80%, respectively. The coupled effects of PSR, temperature, and suction are likely due to the reduction in OCR with increasing temperature and decreasing suction, wherein the impact of PSR on permanent strain is more pronounced at lower OCRs.

At a given CSR, the normalised excess PWP, permanent vertical strain and resilient modulus all increase as confining pressure increases from 30 to 60 kPa. The increased normalised excess PWP and permanent vertical strain are mainly because the plastic modulus decreases when OCR decreases, while CSR remains constant. The rise in resilient modulus is due to enhanced interparticle contacts at higher confining pressures. Moreover, the influence of temperature on cyclic behaviour becomes more pronounced at 60 kPa, owing to the further reduction in OCR at higher confining pressures.

In light of these new findings, it is essential to incorporate the combined effects of PSR, temperature, and suction on resilient modulus into pavement design practices to ensure safety. To support this consideration, a new and straightforward semi-empirical equation for resilient modulus has been proposed. This equation effectively captures the coupled influences of PSR, temperature, and suction without requiring additional parameters, offering a practical enhancement to current design approaches.

8.1.2 Constitutive modelling

A new bounding surface model was proposed to describe the hydro-mechanical behaviour of unsaturated anisotropic and structured soils under both monotonic and cyclic loading conditions. The proposed model incorporates the effects of anisotropy and structure on the mechanical behaviour of soils, such as the LC curve. Experimental results indicate that the inclination of the normalised LC curve for structured soils may be smaller than, larger than, or equal to that of reference soils. These variations are integrated within a unified framework. Moreover, the model successfully captures the LC curve of both isotropic and anisotropic soils.

Furthermore, experimental data reveal that the anisotropic specimen exhibits a higher degree of saturation than the isotropic specimen under identical suction and void ratio conditions. To capture this behaviour, a new water retention model was developed, which accounts for the enhanced water retention capacity associated with increasing anisotropy. In addition, a new equation was proposed to relate the inclination of the bounding surface (α) to the parameter representing anisotropy effects on the soil water retention curve (h). Therefore, the anisotropy effects on the mechanical behaviour and SWRC are well-linked.

Through a carefully designed validation strategy, it was demonstrated that the model effectively captures the behaviour of unsaturated anisotropic and structured soils under both monotonic and cyclic loading conditions.

8.1.3 Loess improvement

An increase in binder content and GGBS-to-binder ratio leads to a reduction in wetting-

induced volumetric strain, an upward shift in the normal compression curve, and an increase in the compression index. These observations are because higher binder and GGBS contents create more cementation bonds, allowing the soil to maintain a higher void ratio at a given stress. Meanwhile, bond breakage under loading induces more plastic deformation, resulting in a higher compression index.

On a semilogarithmic scale, the collapse index decreases linearly with an increase in binder content from 0% to 3% or as the GGBS-to-binder ratio rises from 0% to 50%. More importantly, the effects of binder content on the collapse index are more pronounced at higher GGBS-to-binder ratios. For example, the untreated looser specimen presents a collapse index of 15.3%, a value categorised as severe collapse based on the ASTM (2003) standard. When the binder content increases to 3%, the collapse index decreases to 4.7% (indicating moderate collapse) at zero GGBS-to-binder ratio. Moreover, substituting 50% of the lime with GGBS further reduces the collapse index to 0.06%, which falls below the lower limit for slight collapse (i.e., 0.1%). These observations indicate that the partial replacement of lime with GGBS can effectively reduce the collapse susceptibility of loess and satisfy engineering requirements.

SEM and MIP results reveal that lime and GGBS modify the loess microstructure by coating soil particles, filling interparticle voids, and reducing the dominant macropore size. Moreover, TG and DTG curves demonstrate that the addition of lime and GGBS leads to the formation of hydration products, with a higher content observed when lime is partially replaced by GGBS. The addition of lime primarily increases the contents of $Ca(OH)_2$ and $CaCO_3$, while partial replacement of lime with GGBS consumes the $Ca(OH)_2$ content and promotes the formation of additional CSH compounds. The presence of CSH likely contributes to the further reduction in collapse index observed when lime is partially replaced with GGBS.

8.2 Recommended further work

8.2.1 Suggestions for experimental testing

The test results of this study indicate that small-strain shear stiffness anisotropy is strongly influenced by soil structure. Intact loess typically exhibits greater stiffness anisotropy than

compacted specimens under identical initial void ratio and water content. Furthermore, anisotropy becomes more pronounced in specimens compacted at higher dry densities and lower water contents. Nevertheless, this investigation is limited to fully saturated conditions. Previous research has demonstrated that stiffness anisotropy is also influenced by suction, although the underlying mechanisms remain unclear. Further research is required to study the coupled effects of soil structure and suction on the stiffness anisotropy of unsaturated soils.

The present study on the influence of soil structure on the cyclic behaviour of unsaturated soils does not account for the effects of hydraulic hysteresis. However, soils in the field are often exposed to drying-wetting cycles resulting from daily and seasonal fluctuations in water content. Future research could incorporate specimens with varying microstructures and hydraulic histories to better reflect in-situ conditions.

This study demonstrates that permanent vertical strain increases when principal stress rotation is considered, with the effect being more pronounced at lower suctions and higher temperatures. To the author's knowledge, the combined influence of soil structure and principal stress rotation on the cyclic behaviour of unsaturated soils has not yet been explored. In future research, new apparatus will be developed to prepare intact hollow cylindrical specimens, allowing for a comparison of the responses of intact and compacted specimens subjected to cyclic loading both with and without principal stress rotation.

Furthermore, soil suction is normally treated as a scalar parameter that influences soil behaviour by modifying the mean effective stress applied to the specimen. However, several studies have indicated that suction can intensify soil anisotropy, leading to more pronounced stiffness anisotropy at higher suctions. These findings suggest that, although suction is commonly regarded as a scalar, it may exert tensorial effects. Further experimental investigations are therefore warranted to clarify the anisotropic impacts of soil suction. For instance, measuring the small-strain stiffness along different shear planes during drying and wetting can provide valuable insights. Alternatively, evaluating the shear strength under different principal stress orientations and suctions also offers a viable approach.

8.2.2 Suggestions for constitutive modelling

In Chapter 5, the coupled influence of principal stress rotation and suction on the accumulation of permanent vertical strain and the variation of resilient modulus is recognised. However, existing models that consider the effects of PSR on cyclic behaviour have primarily focused on saturated soils. The less pronounced effects of PSR on strain accumulation under higher suction conditions have not been incorporated. Therefore, a new constitutive model is needed to capture the coupled effects of PSR and suction on the cyclic behaviour of unsaturated soils.

The newly developed model in Chapter 6 is developed in the triaxial stress space and can be extended to the multiaxial stress space, thereby enabling its integration into numerical analyses. Consequently, the performance of the proposed model can be further validated through engineering cases.

REFERENCES

AASHTO. (2020). Mechanistic-empirical pavement design guide: a manual of practice. American Association of State Highway and Transportation Officials.

AASHTO. (2021). Standard method of test for determining the resilient modulus of soils and aggregate materials. AASHTO T307-99 (2021), American Association of State Highway and Transportation Officials.

Aitchison, G. D. (1960). Relationships of moisture stress and effective stress functions in unsaturated soils. In *Proceedings of Pore Pressure and Suction in Soils*, pp. 47-52.

Aitchison, G. D. (ed) (1965) *Moisture equilibria and moisture changes in soils beneath covered areas*, A symposium in print. Butterworths, Sydney, Australia.

Akbari Garakani, A., Haeri, S. M., Desai, C. S., Hosein Seyed Ghafouri, S. M., Sadollahzadeh, B. and Hashemi Senejani, H. (2019). Testing and constitutive modeling of lime-stabilized collapsible loess. II: modeling and validations. *International Journal of Geomechanics* **19(4)**:04019007.

Al-Sharrad, M. A. (2013). Evolving anisotropy in unsaturated soils: experimental investigation and constitutive modelling. *PhD Thesis, University of Glasgow.*

Al-Sharrad, M. A. and Gallipoli, D. (2014). An elasto-plastic model for unsaturated soils with evolving anisotropy. In *Proceedings of 6th International Conference on Unsaturated Soils*, pp. 433-439.

Al-Sharrad, M. A. and Gallipoli, D. (2016). Incorporating anisotropy in the Barcelona basic model. In *Proceedings of E3S Web of Conferences* **vol. 9**, pp. 17003.

Al-Sharrad, M. A., Gallipoli, D. and Wheeler, S. J. (2017). Experimental investigation of evolving anisotropy in unsaturated soils. *Géotechnique* **67(12)**:1033-1049.

Alonso, E. E. and Gens, A. (1994). Keynote lecture: on the mechanical behaviour of arid soils. In *Proceedings of Engineering Characteristics of Arid Soils*, pp. 173-205.

Alonso, E. E., Gens, A. and Josa, A. (1990). A constitutive model for partially saturated soils. *Géotechnique* **40(3)**:405-430.

Alonso, E. E., Pereira, J. M., Vaunat, J. and Olivella, S. (2010). A microstructurally based effective stress for unsaturated soils. *Géotechnique* **60(12)**:913-925.

Alonso, E. E., Pinyol, N. M. and Gens, A. (2013). Compacted soil behaviour: initial state, structure and constitutive modelling. *Géotechnique* **63(6)**:463-478.

Amini, D., Maghoul, P., Holländer, H. and Bilodeau, J. P. (2024). A critical state-based thermo-elasto-viscoplastic constitutive model for thermal creep deformation of frozen soils. *Acta Geotechnica* **19(5)**:2955-2973.

Amorosi, A., Rollo, F. and Dafalias, Y. F. (2021). Relating elastic and plastic fabric anisotropy of clays. *Géotechnique* **71(7)**:583-593.

Anagnostopoulos, A. G., Kalteziotis, N., Tsiambaos, G. K. and Kavvadas, M. (1991). Geotechnical properties of the Corinth Canal marls. *Geotechnical and Geological Engineering* **9**:1-26.

Anandarajah, A. M. Y. F. and Dafalias, Y. F. (1986). Bounding surface plasticity. III: application to anisotropic cohesive soils. *Journal of Engineering Mechanics* **112(12)**:1292-1318.

Arroyo, M., Amaral, M. F., Romero, E. and Viana da Fonseca, A. (2013). Isotropic yielding of unsaturated cemented silty sand. *Canadian Geotechnical Journal* **50(8)**:807-819.

ASTM. (2003). Standard test method for measurement of collapse potential of soils. D5333-03, American Society for Testing and Materials.

ASTM. (2017). Standard test methods for liquid limit, plastic limit, and plasticity index of soils. D4318-17e1, American Society for Testing and Materials.

ASTM. (2021a). Standard test method for particle-size distribution (gradation) of fine-grained soils using the sedimentation (hydrometer) analysis. D7928-21e1, American Society for Testing and Materials.

ASTM. (2021b). Standard test methods for laboratory compaction characteristics of soil using standard effort. D698-12(2021), American Society for Testing and Materials.

ASTM. (2025). Standard practice for classification of soils for engineering purposes (Unified Soil Classification System). D2487-17(2025), American Society for Testing and Materials.

Atkinson, J. H. (2000). Non-linear soil stiffness in routine design. *Géotechnique* **50(5)**:487-508.

Azizi, A., Kumar, A. and Toll, D. G. (2023). Coupling cyclic and water retention response of a clayey sand subjected to traffic and environmental cycles. *Géotechnique* **73(5)**:401-417.

Ba, M., Nokkaew, K., Fall, M. and Tinjum, J. M. (2013). Effect of matric suction on resilient modulus of compacted aggregate base courses. *Geotechnical and Geological Engineering* **31**:1497-1510.

Baker, R. and Frydman, S. (2009). Unsaturated soil mechanics: critical review of physical foundations. *Engineering Geology* **106(1-2)**:26-39.

Banerjee, P. K. and Yousif, N. B. (1986). A plasticity model for the mechanical behaviour of anisotropically consolidated clay. *International Journal for Numerical and Analytical Methods in Geomechanics* **10(5)**:521-541.

Barton, C. M. (1974). Micromorphological soil-investigation work of Dr. Lafeber. In *Proceedings of Soil Micromorphology*, pp. 1-19.

Baudet, B. and Stallebrass, S. (2004). A constitutive model for structured clays. *Géotechnique* **54(4)**:269-278.

Bellotti, R., Jamiolkowski, M., Presti, D. C. F. L. and O'neill, D. A. (1996). Anisotropy of small strain stiffness in Ticino sand. *Géotechnique* **46(1)**:115-131.

Belokas, G. and Kavvadas, M. (2010). An anisotropic model for structured soils: Part I: Theory. *Computers and Geotechnics* **37(6)**:737-747.

Biglari, M., Ashayeri, I., Gallipoli, D. and Moradpour, S. (2021). A unified small-strain shear stiffness model for saturated and unsaturated soils. *Computers and Geotechnics* **136**:104241.

Biglari, M., d'Onofrio, A., Mancuso, C., Jafari, M. K., Shafiee, A. and Ashayeri, I. (2012). Small-strain stiffness of Zenoz kaolin in unsaturated conditions. *Canadian Geotechnical Journal* **49(3)**:311-322.

Biglari, M., Mancuso, C., d'Onofrio, A., Jafari, M. K. and Shafiee, A. (2011). Modelling the initial shear stiffness of unsaturated soils as a function of the coupled effects of the void

ratio and the degree of saturation. *Computers and Geotechnics* **38(5)**:709-720.

Birle, E., Heyer, D. and Vogt, N. (2008). Influence of the initial water content and dry density on the soil-water retention curve and the shrinkage behavior of a compacted clay. *Acta Geotechnica* **3**:191-200.

Bishop, A. W. (1959). The principle of effective stress. *Teknisk Ukeblad* **39**:859-863.

Blackmore, L., Clayton, C. R. I., Powrie, W., Priest, J. A. and Otter, L. (2020). Saturation and its effect on the resilient modulus of a pavement formation material. *Géotechnique* **70(4)**:292-302.

Brown, S. F. (1996). Soil mechanics in pavement engineering. *Géotechnique* **46(3)**:383-426.

Bruno, A. W., Gallipoli, D., Rouainia, M. and Lloret Cabot, M. (2020). A bounding surface mechanical model for unsaturated cemented soils under isotropic stresses. *Computers and Geotechnics* **125**:103673.

Burland, J. B. (1990). On the compressibility and shear strength of natural clays. *Géotechnique* **40(3)**:329-378.

Cai, G. H., Zhou, Y. F., Li, J. S., Han, L. J. and Poon, C. S. (2022). Deep insight into mechanical behavior and microstructure mechanism of quicklime-activated ground granulated blast-furnace slag pastes. *Cement and Concrete Composites* **134**:104767.

Cai, W. L. and Zhu, C. (2024). Constitutive model for thermo–hydro–mechanical behaviors of saturated partially frozen cohesionless soils: a theoretical pore-scale study. *Journal of Geotechnical and Geoenvironmental Engineering* **150(4)**:04024007.

Cai, Y. Q., Guo, L., Jardine, R. J., Yang, Z. X. and Wang, J. (2017). Stress-strain response of soft clay to traffic loading. *Géotechnique* **67(5)**:446-451.

Cai, Y. Q., Sun, Q., Guo, L., Juang, C. H. and Wang, J. (2015). Permanent deformation characteristics of saturated sand under cyclic loading. *Canadian Geotechnical Journal* **52(6)**:795-807.

Cai, Y. Q., Wu, T. Y., Guo, L. and Wang, J. (2018). Stiffness degradation and plastic strain accumulation of clay under cyclic load with principal stress rotation and deviatoric stress variation. *Journal of Geotechnical and Geoenvironmental Engineering* **144(5)**:04018021.

Callisto, L. and Calabresi, G. (1998). Mechanical behaviour of a natural soft clay. *Géotechnique* **48(4)**:495-513.

Casarella, A., Pedrotti, M., Tarantino, A. and Di Donna, A. (2021). A critical review of the effect of temperature on clay inter-particle forces and its effect on macroscopic thermal behaviour of clay. In *Proceedings of 16th International Conference of the International Association for Computer Methods and Advances in Geomechanics*. Springer, pp. 608-615.

Cascante, G. and Santamarina, J. (1996). Interparticle contact behavior and wave propagation. *Journal of Geotechnical Engineering* **122(10)**:831-839.

Castro, J. and Sivasithamparam, N. (2017). A constitutive model for soft clays incorporating elastic and plastic cross-anisotropy. *Materials* **10(6)**:584.

Cekerevac, C. and Laloui, L. (2004). Experimental study of thermal effects on the mechanical behaviour of a clay. *International Journal for Numerical and Analytical Methods in*

Geomechanics **28(3)**:209-228.

Cekerevac, C. and Laloui, L. (2010). Experimental analysis of the cyclic behaviour of kaolin at high temperature. *Géotechnique* **60(8)**:651-655.

Chamberlain, E., Groves, C. and Perham, R. (1972). The mechanical behaviour of frozen earth materials under high pressure triaxial test conditions. *Géotechnique* **22(3)**:469-483.

Chamberlain, E. J. and Hoekstra, P. (1970). The isothermal compressibility of frozen soil and ice to 30 kilobars at -10 C. Corps of Engineers, US Army Cold Regions Research and Engineering Laboratory.

Chan, F. W. K. and Brown, S. F. (1994). Significance of principal stress rotation in pavements. In *Proceedings of International Conference on Soil Mechanics and Foundation Engineering*, pp. 1823-1826.

Chen, J. Y., Alonso, E. E., Gu, C., Cao, Z. G. and Cai, Y. Q. (2018). Long term cyclic behavior of unsaturated granular soils. *Transportation Geotechnics* **17**:48-55.

Chen, W. B., Feng, W. Q., Yin, J. H., Chen, J. M., Borana, L. and Chen, R. P. (2020). New model for predicting permanent strain of granular materials in embankment subjected to low cyclic loadings. *Journal of Geotechnical and Geoenvironmental Engineering* **146(9)**:04020084.

Chen, Y. N. and Yang, Z. X. (2020). A bounding surface model for anisotropically overconsolidated clay incorporating thermodynamics admissible rotational hardening rule. *International Journal for Numerical and Analytical Methods in Geomechanics* **44(5)**:668-690.

Cheng, Q. (2017). Volumetric behaviour of intact and recompacted collapsible loess under thermo-hydro-mechanical loading. *PhD Thesis, Hong Kong University of Science and Technology.*

Cheng, Q., Ng, C. W. W., Zhou, C. and Tang, C. S. (2019). A new water retention model that considers pore non-uniformity and evolution of pore size distribution. *Bulletin of Engineering Geology and the Environment* **78(7)**:5055-5065.

Chiu, C. F. and Ng, C. W. W. (2003). A state-dependent elasto-plastic model for saturated and unsaturated soils. *Géotechnique* **53(9)**:809-829.

Cho, G. C. and Santamarina, J. C. (2001). Unsaturated particulate materials-particle-level studies. *Journal of Geotechnical and Geoenvironmental Engineering* **127(1)**:84-96.

Choo, J., Jung, Y. H. and Chung, C. K. (2011). Effect of directional stress history on anisotropy of initial stiffness of cohesive soils measured by bender element tests. *Soils and Foundations* **51(4)**:737-747.

Chow, J. K., Li, Z. F. and Wang, Y. H. (2019). Comprehensive microstructural characterizations of 1-D consolidated kaolinite samples with fabric tensors and pore elongation factors. *Engineering Geology* **248**:22-33.

Christopher, B. R., Schwartz, C. and Boudreau, R. (2006). *Geotechnical aspects of pavements*. FHWA NHI-05-037, National Highway Institute. Federal Highway Administration.

Clayton, C. R. I. (2011). Stiffness at small strain: research and practice. *Géotechnique* **61(1)**:5-37.

Coleman, J. D. (1962). Stress strain relations for partly saturated soil. *Correspondence to*

Géotechnique **12(4)**:348-350.

Cui, Y. J. and Delage, P. (1996). Yielding and plastic behaviour of an unsaturated compacted silt. *Géotechnique* **46(2)**:291-311.

Cui, Y. J., Tang, A. M., Marcial, D., Terpereau, J. M., Marchadier, G. and Boulay, X. (2007). Use of a differential pressure transducer for the monitoring of soil volume change in cyclic triaxial test on unsaturated soils. *Geotechnical Testing Journal* **30(3)**:227-233.

D'Onza, F., Gallipoli, D. and Wheeler, S. J. (2010). Effect of anisotropy on the prediction of unsaturated soil response under triaxial and oedometric conditions. In *Proceedings of 5th International Conference on Unsaturated Soils* **vol. 2**, pp. 787-794.

Dafalias, Y. F. (1986a). An anisotropic critical state soil plasticity model. *Mechanics Research Communications* **13(6)**:341-347.

Dafalias, Y. F. (1986b). Bounding surface plasticity. I: mathematical foundation and hypoplasticity. *Journal of Engineering Mechanics* **112(9)**:966-987.

Dafalias, Y. F., Manzari, M. T. and Akaishi, M. (2002). A simple anisotropic clay plasticity model. *Mechanics Research Communications* **29(4)**:241-245.

Dafalias, Y. F., Manzari, M. T. and Papadimitriou, A. G. (2006). SANICLAY: simple anisotropic clay plasticity model. *International Journal for Numerical and Analytical Methods in Geomechanics* **30(12)**:1231-1257.

Dafalias, Y. F. and Taiebat, M. (2013). Anatomy of rotational hardening in clay plasticity. *Géotechnique* **63(16)**:1406-1418.

Dafalias, Y. F. and Taiebat, M. (2014). Rotational hardening with and without anisotropic fabric at critical state. *Géotechnique* **64(6)**:507-511.

Dai, B. L. and Zhou, C. (2025). Coupled effects of principal stress rotation, temperature, and suction on the cyclic behaviour of unsaturated loess. *Canadian Geotechnical Journal* **62**:1-16.

Dai, B. L., Zhou, C., Mu, Q. Y. and Peng, J. B. (2025). Evolution of structure and anisotropic shear stiffness of compacted loess during compression. *Canadian Geotechnical Journal* **62**:1-13.

Dai, B. L., Zhou, C., Tang, A. M. and Guayacán-Carrillo, L. M. (2024). A bounding surface model for anisotropic and structured soils under saturated and unsaturated conditions. *Computers and Geotechnics* **173**:106533.

Delage, P., Audiguier, M., Cui, Y. J. and Howat, M. D. (1996). Microstructure of a compacted silt. *Canadian Geotechnical Journal* **33(1)**:150-158.

Delage, P., Cui, Y. J. and Antoine, P. (2005). Geotechnical problems related with loess deposits in Northern France. In *Proceedings of International Conference on Problematic Soils*, pp. 517-540.

Dong, Y., Lu, N. and McCartney, J. S. (2016). Unified model for small-strain shear modulus of variably saturated soil. *Journal of Geotechnical and Geoenvironmental Engineering* **142(9)**:04016039.

Duong, T. V., Tang, A. M., Cui, Y. J., Trinh, V. N., Dupla, J. C., Calon, N., Canou, J. and Robinet, A. (2013). Effects of fines and water contents on the mechanical behavior of interlayer soil in ancient railway sub-structure. *Soils and Foundations* **53(6)**:868-878.

Estabragh, A. R., Javadi, A. A. and Boot, J. C. (2004). Effect of compaction pressure on consolidation behaviour of unsaturated silty soil. *Canadian Geotechnical Journal* **41(3)**:540-550.

Fearon, R. E. and Coop, M. R. (2000). Reconstitution: what makes an appropriate reference material? *Géotechnique* **50(4)**:471-477.

Fedakar, H. I., Cetin, B. and Rutherford, C. J. (2021). Deformation characteristics of medium-dense sand-clay mixtures under a principal stress rotation. *Transportation Geotechnics* **30**:100616.

Fisher, R. A. (1926). On the capillary forces in an ideal soil; correction of formulae given by WB Haines. *The Journal of Agricultural Science* **16(3)**:492-505.

Fredlund, D. G. and Morgenstern, N. R. (1977). Stress state variables for unsaturated soils. *Journal of the Geotechnical Engineering Division* **103(5)**:447-466.

Fredlund, D. G. and Rahardjo, H. (1993). Soil mechanics for unsaturated soils. New York, USA, John Wiley and Sons, Inc.

Fredlund, D. G. and Xing, A. Q. (1994). Equations for the soil-water characteristic curve. *Canadian Geotechnical Journal* **31(4)**:521-532.

Futai, M. M. and Almeida, M. S. S. (2005). An experimental investigation of the mechanical behaviour of an unsaturated gneiss residual soil. *Géotechnique* **55(3)**:201-213.

Gagnon, R. E. and Gammon, P. H. (1995). Triaxial experiments on iceberg and glacier ice. *Journal of Glaciology* **41(139)**:528-540.

Gallipoli, D. (2012). A hysteretic soil-water retention model accounting for cyclic variations of suction and void ratio. *Géotechnique* **62(7)**:605-616.

Gallipoli, D. and Bruno, A. W. (2017). A bounding surface compression model with a unified virgin line for saturated and unsaturated soils. *Géotechnique* **67(8)**:703-712.

Gallipoli, D., Bruno, A. W., D'onza, F. and Mancuso, C. (2015). A bounding surface hysteretic water retention model for deformable soils. *Géotechnique* **65(10)**:793-804.

Gallipoli, D., Gens, A., Sharma, R. and Vaunat, J. (2003a). An elasto-plastic model for unsaturated soil incorporating the effects of suction and degree of saturation on mechanical behaviour. *Géotechnique* **53(1)**:123-135.

Gallipoli, D., Wheeler, S. J. and Karstunen, M. (2003b). Modelling the variation of degree of saturation in a deformable unsaturated soil. *Géotechnique* **53(1)**:105-112.

Gan, J. K. M. and Fredlund, D. G. (1996). Shear strength characteristics of two saprolitic soils. *Canadian Geotechnical Journal* **33(4)**:595-609.

Gao, Y. Y., Qian, H., Li, X. Y., Chen, J. and Jia, H. (2018). Effects of lime treatment on the hydraulic conductivity and microstructure of loess. *Environmental Earth Sciences* **77**:1-15.

Gao, Z. W. and Zhao, J. D. (2015). Constitutive modeling of anisotropic sand behavior in monotonic and cyclic loading. *Journal of Engineering Mechanics* **141(8)**:04015017.

Gasparre, A., Nishimura, S., Coop, M. R. and Jardine, R. J. (2007). The influence of structure on the behaviour of London Clay. *Géotechnique* **57(1)**:19-31.

Ge, M. M., Han, X. N., Yang, R. and Zhu, C. H. (2024). Small-strain stiffness of compacted loess upon wetting, drying and loading: experiments and model interpretation.

Transportation Geotechnics **48**:101341.

Gens, A. (1982). Stress-strain and strength characteristics of a low plasticity clay. *PhD Thesis, University of London.*

Gens, A. (2010). Soil-environment interactions in geotechnical engineering. *Géotechnique* **60(1)**:3-74.

Gens, A. and Alonso, E. E. (1992). A framework for the behaviour of unsaturated expansive clays. *Canadian Geotechnical Journal* **29(6)**:1013-1032.

Ghayoomi, M., McCartney, J. S. and Ko, H. Y. (2013). Empirical methodology to estimate seismically induced settlement of partially saturated sand. *Journal of Geotechnical and Geoenvironmental Engineering* **139(3)**:367-376.

Ghionna, V. N. and Porcino, D. (2006). Liquefaction resistance of undisturbed and reconstituted samples of a natural coarse sand from undrained cyclic triaxial tests. *Journal of Geotechnical and Geoenvironmental Engineering* **132(2)**:194-202.

Ghoreishian Amiri, S. A., Grimstad, G., Kadivar, M. and Nordal, S. (2016). Constitutive model for rate-independent behavior of saturated frozen soils. *Canadian Geotechnical Journal* **53(10)**:1646-1657.

Gibbs, H. J. and Bara, J. P. (1962). *Predicting surface subsidence from basic soil tests*. Vol. 658. US Department of the Interior, Bureau of Reclamation, Division of the Interior, Bureau of Reclamation, Division of Engineering Laboratories.

Gibbs, H. J. and Holland, W. Y. (1960). *Petrographic and engineering properties of loess*. No 28. Technical Information Branch, Denver Federal Center.

Gräbe, P. J. (2002). Resilient and permanent deformation of railway foundations under principal stress rotation. *PhD Thesis, University of Southampton.*

Gräbe, P. J. and Clayton, C. R. I. (2009). Effects of principal stress rotation on permanent deformation in rail track foundations. *Journal of Geotechnical and Geoenvironmental Engineering* **135(4)**:555-565.

Gräbe, P. J. and Clayton, C. R. I. (2014). Effects of principal stress rotation on resilient behavior in rail track foundations. *Journal of Geotechnical and Geoenvironmental Engineering* **140(2)**:04013010.

Graham, J. and Houlsby, G. T. (1983). Anisotropic elasticity of a natural clay. *Géotechnique* **33(2)**:165-180.

Guo, J., Jia, L., Wei, Z. Q., Yao, K. and Wu, R. J. (2024). Mechanical properties and engineering applications of low-dosage cement/lime-stabilized loess improved with nano-MgO and nan-SiO2. *Transportation Geotechnics* **49**:101450.

Guo, J., Jia, L., Wei, Z. Q. and Zhang, L. (2022). Evaluation on the mechanical performance of lime-ground granulated blast-furnace slag stabilized loess. *Arabian Journal of Geosciences* **15(15)**:1361.

Guo, L., Cai, Y. Q., Jardine, R. J., Yang, Z. X. and Wang, J. (2018). Undrained behaviour of intact soft clay under cyclic paths that match vehicle loading conditions. *Canadian Geotechnical Journal* **55(1)**:90-106.

Guo, L., Chen, J. M., Wang, J., Cai, Y. Q. and Deng, P. (2016). Influences of stress magnitude and loading frequency on cyclic behavior of K0-consolidated marine clay involving

principal stress rotation. *Soil Dynamics and Earthquake Engineering* **84**:94-107.

Guo, L., Wang, J., Cai, Y. Q., Liu, H. L., Gao, Y. F. and Sun, H. L. (2013). Undrained deformation behavior of saturated soft clay under long-term cyclic loading. *Soil Dynamics and Earthquake Engineering* **50**:28-37.

Habasimbi, P. and Nishimura, T. (2018). Comparison of soil-water characteristic curves in one-dimensional and isotropic stress conditions. *Soil Systems* **2(3)**:43.

Haeri, S. M. (2016). Hydro-mechanical behavior of collapsible soils in unsaturated soil mechanics context. *Japanese Geotechnical Society Special Publication* **2(1)**:25-40.

Haeri, S. M., Akbari Garakani, A., Roohparvar, H. R., Desai, C. S., Seyed Ghafouri, S. M. H. and Salemi Kouchesfahani, K. (2019). Testing and constitutive modeling of lime-stabilized collapsible loess. I: experimental investigations. *International Journal of Geomechanics* **19(4)**:04019006.

Haeri, S. M., Khosravi, A., Garakani, A. A. and Ghazizadeh, S. (2017). Effect of soil structure and disturbance on hydromechanical behavior of collapsible loessial soils. *International Journal of Geomechanics* **17(1)**:04016021.

Han, Z. and Vanapalli, S. K. (2015). Model for predicting resilient modulus of unsaturated subgrade soil using soil-water characteristic curve. *Canadian Geotechnical Journal* **52(10)**:1605-1619.

Han, Z. and Vanapalli, S. K. (2016). Relationship between resilient modulus and suction for compacted subgrade soils. *Engineering Geology* **211**:85-97.

Hardin, B. O. (1978). The nature of stress-strain behavior for soils. In *Proceedings of ASCE Geotechnical Engineering Division Specialty Conference on Earthquake Engineering and Soil Dynamics* **vol. 1**, pp. 3-39.

Hardin, B. O. and Blandford, G. E. (1989). Elasticity of particulate materials. *Journal of Geotechnical Engineering* **115(6)**:788-805.

Hardin, B. O. and Richart, F. E., Jr. (1963). Elastic wave velocities in granular soils. *Journal of the Soil Mechanics and Foundations Division* **89(1)**:33-65.

Hasan, A. M. and Wheeler, S. J. (2014). Influence of compaction procedure on elastic anisotropy. In *Proceedings of 5th International Conference on Unsaturated Soils* **vol. 1**, pp. 285-289.

Heath, A. C., Pestana, J. M., Harvey, J. T. and Bejerano, M. O. (2004). Normalizing behavior of unsaturated granular pavement materials. *Journal of Geotechnical and Geoenvironmental Engineering* **130(9)**:896-904.

Heitor, A., Indraratna, B. and Rujikiatkamjorn, C. (2013). Laboratory study of small-strain behavior of a compacted silty sand. *Canadian Geotechnical Journal* **50(2)**:179-188.

Heitor, A., Indraratna, B. and Rujikiatkamjorn, C. (2015a). Effect of suction history on the small strain response of a dynamically compacted soil. In *Proceedings of 12th Australia New Zealand Conference on Geomechanics*, pp. 1-8.

Heitor, A., Indraratna, B. and Rujikiatkamjorn, C. (2015b). The role of compaction energy on the small strain properties of a compacted silty sand subjected to drying-wetting cycles. *Géotechnique* **65(9)**:717-727.

Higgins, D. (2007). Briefing: GGBS and sustainability. In *Proceedings of Institution of Civil*

Engineers-Construction Materials **vol. 160**, pp. 99-101.

Hight, D. W., Gens, A. and Symes, M. J. (1983). The development of a new hollow cylinder apparatus for investigating the effects of principal stress rotation in soils. *Géotechnique* **33(4)**:355-383.

Houlsby, G. T. (1997). The work input to an unsaturated granular material. *Géotechnique* **47(1)**:193-196.

Houlsby, G. T. and Wroth, C. P. (1991). The variation of shear modulus of a clay with pressure and overconsolidation ratio. *Soils and Foundations* **31(3)**:138-143.

Hoyos, L. R., Suescún-Florez, E. A. and Puppala, A. J. (2015). Stiffness of intermediate unsaturated soil from simultaneous suction-controlled resonant column and bender element testing. *Engineering Geology* **188**:10-28.

Hoyos, L. R., Suescun, E. A. and Puppala, A. J. (2011). Small-strain stiffness of unsaturated soils using a suction-controlled resonant column device with bender elements. In *Proceedings of Geo-Frontiers 2011: Advances in Geotechnical Engineering*, pp. 4313-4322.

Hu, R., Chen, Y. F., Liu, H. H. and Zhou, C. B. (2013). A water retention curve and unsaturated hydraulic conductivity model for deformable soils: consideration of the change in pore-size distribution. *Géotechnique* **63(16)**:1389-1405.

Huang, S. G. (2019). Dynamic response research and cumulative settlement control analysis of embankment-cut transition section of heavy haul railway in loess region (In Chinese). *PhD Thesis, Beijing Jiaotong University.*

Hueckel, T. and Tutumluer, E. (1994). Modeling of elastic anisotropy due to one-dimensional plastic consolidation of clays. *Computers and Geotechnics* **16(4)**:311-349.

Israelachvili, J. N. (2011). Intermolecular and surface forces. Academic press.

Iwasaki, T. and Tatsuoka, F. (1977). Effects of grain size and grading on dynamic shear moduli of sands. *Soils and Foundations* **17(3)**:19-35.

James, R., Kamruzzaman, A. H. M., Haque, A. and Wilkinson, A. (2008). Behaviour of lime-slag-treated clay. *Proceedings of the Institution of Civil Engineers-Ground Improvement* **161(4)**:207-216.

Jamiolkowski, M., Lancellotta, R. and Lo Presti, D. C. F. (1995). Remarks on the stiffness at small strains of six Italian clays. In *Proceedings of Pre-failure Deformation of Geomaterials* **vol. 2**, pp. 12-14.

Jana, A. and Stuedlein, A. W. (2021). Monotonic, cyclic, and postcyclic responses of an alluvial plastic silt deposit. *Journal of Geotechnical and Geoenvironmental Engineering* **147(3)**:04020174.

Jefferson, I., Evstatiev, D. and Karastanev, D. (2008). The treatment of collapsible loess soils using cement materials. In *Proceedings of GeoCongress 2008: Geosustainability and Geohazard Mitigation*, pp. 662-669.

Jennings, J. E. B. and Burland, J. B. (1962). Limitations to the use of effective stresses in partly saturated soils. *Géotechnique* **12(2)**:125-144.

Jia, L., Zhang, L., Guo, J., Yao, K., Lim, S. M., Li, B. and Xu, H. (2019). Evaluation on strength properties of lime-slag stabilized loess as pavement base material. *Sustainability*

11(15):4099.

Jiang, J. H. and Ling, H. I. (2010). A framework of an anisotropic elastoplastic model for clays. *Mechanics Research Communications* **37(4)**:394-398.

Jiang, M. J., Hu, H. J., Peng, J. B. and Leroueil, S. (2011). Experimental study of two saturated natural soils and their saturated remoulded soils under three consolidated undrained stress paths. *Frontiers of Architecture and Civil Engineering in China* **5**:225-238.

Jimenez, A. and Russell, A. R. (2023). Estimations of water retention curves for fine-grained soils and tailings using their fractal particle size distributions. In *Proceedings of E3S Web of Conferences*. EDP Sciences **vol. 382**, pp. 16002.

Jones, S. J. (1982). The confined compressive strength of polycrystalline ice. *Journal of Glaciology* **28(98)**:171-178.

Josa, A., Balmaceda, A., Gens, A. and Alonso, E. E. (1992). An elastoplastic model for partially saturated soils exhibiting a maximum of collapse. In *Proceedings of 3rd International Conference on Computational Plasticity* **vol. 1**, pp. 815-826.

Jovičić, V. and Coop, M. P. (1998). The measurement of stiffness anisotropy in clays with bender element tests in the triaxial apparatus. *Geotechnical Testing Journal* **21(1)**:3-10.

JTG/T3610. (2019). Technical specifications for construction of highway subgrades (In Chinese). Ministry of Transport, China.

JTG/T D31-05. (2017). Technical specifications for design and construction of highway subgrade in loess region (In Chinese). Ministry of Transport, China.

Kaewsong, R. (2017). Anisotropic small-strain stiffness of unsaturated compacted and intact collapsible loess. *PhD Thesis, Hong Kong University of Science and Technology.*

Kamon, M. and Nontananandh, S. (1991). Combining industrial wastes with lime for soil stabilization. *Journal of Geotechnical Engineering* **117(1)**:1-17.

Karam, J. P., Cui, Y. J., Tang, A. M., Terpereau, J. M. and Marchadier, G. (2009). Experimental study on the cyclic resistance of a natural loess from Northern France. *Soils and Foundations* **49(3)**:421-429.

Karube, D. and Kato, S. (1994). An ideal unsaturated soil and the Bishop's soil. In *Proceedings of 13th International Conference on Soil Mechanics and Foundation Engineering* **vol. 1**, pp. 43-46.

Kavvadas, M. and Amorosi, A. (2000). A constitutive model for structured soils. *Géotechnique* **50(3)**:263-273.

Khalili, N., Geiser, F. and Blight, G. E. (2004). Effective stress in unsaturated soils: review with new evidence. *International Journal of Geomechanics* **4(2)**:115-126.

Khalili, N., Habte, M. A. and Zargarbashi, S. (2008). A fully coupled flow deformation model for cyclic analysis of unsaturated soils including hydraulic and mechanical hystereses. *Computers and Geotechnics* **35(6)**:872-889.

Khalili, N. and Khabbaz, M. H. (1998). A unique relationship for χ for the determination of the shear strength of unsaturated soils. *Géotechnique* **48(5)**:681-687.

Khalili, N., Romero, E. and Marinho, F. A. M. (2022). State of the art report. Advances in unsaturated soil mechanics: constitutive modelling, experimental investigation, and field instrumentation. In *Proceedings of 20th International Conference on Soil*

Mechanics and Geotechnical Engineering, pp. 297-348.

Khalili, N. and Zargarbashi, S. (2010). Influence of hydraulic hysteresis on effective stress in unsaturated soils. *Géotechnique* **60(9)**:729-734.

Khosravi, A. (2011). Small strain shear modulus of unsaturated, compacted soils during hydraulic hysteresis. *PhD Thesis, University of Colorado at Boulder.*

Khosravi, A., Ghayoomi, M., McCartney, J. and Ko, H. Y. (2010). Impact of effective stress on the dynamic shear modulus of unsaturated sand. In *Proceedings of GeoFlorida 2010: Advances in Analysis, Modeling and Design*, pp. 410-419.

Khosravi, A. and McCartney, J. S. (2012). Impact of hydraulic hysteresis on the small-strain shear modulus of low plasticity soils. *Journal of Geotechnical and Geoenvironmental Engineering* **138(11)**:1326-1333.

Khoury, N., Brooks, R., Boeni, S. Y. and Yada, D. (2013). Variation of resilient modulus, strength, and modulus of elasticity of stabilized soils with postcompaction moisture contents. *Journal of Materials in Civil Engineering* **25(2)**:160-166.

Khoury, N. N. and Zaman, M. M. (2004). Correlation between resilient modulus, moisture variation, and soil suction for subgrade soils. *Transportation Research Record* **1874(1)**:99-107.

Kokusho, T., Yoshida, Y. and Esashi, Y. (1982). Dynamic properties of soft clay for wide strain range. *Soils and Foundations* **22(4)**:1-18.

Koliji, A., Laloui, L. and Vulliet, L. (2009). Behaviour of unsaturated aggregated soil in oedometric condition. *Soils and Foundations* **49(3)**:369-380.

Koliji, A., Laloui, L. and Vulliet, L. (2010a). Constitutive modeling of unsaturated aggregated soils. *International Journal for Numerical and Analytical Methods in Geomechanics* **34(17)**:1846-1876.

Koliji, A., Vulliet, L. and Laloui, L. (2010b). Structural characterization of unsaturated aggregated soil. *Canadian Geotechnical Journal* **47(3)**:297-311.

Krahn, J. and Fredlund, D. G. (1972). On total, matric and osmotic suction. *Soil Science* **114(5)**:339-348.

Kumar, A., Azizi, A. and Toll, D. G. (2022). Application of suction monitoring for cyclic triaxial testing of compacted soils. *Journal of Geotechnical and Geoenvironmental Engineering* **148(4)**:04022009.

Kumruzzaman, M. and Yin, J. H. (2010). Influences of principal stress direction and intermediate principal stress on the stress-strain-strength behaviour of completely decomposed granite. *Canadian Geotechnical Journal* **47(2)**:164-179.

Ladanyi, B. and Morel, J. F. (1990). Effect of internal confinement on compression strength of frozen sand. *Canadian Geotechnical Journal* **27(1)**:8-18.

Ladd, R. S. (1978). Preparing test specimens using undercompaction. *Geotechnical Testing Journal* **1(1)**:16-23.

Lai, Y. M., Jin, L. and Chang, X. X. (2009). Yield criterion and elasto-plastic damage constitutive model for frozen sandy soil. *International Journal of Plasticity* **25(6)**:1177-1205.

Lai, Y. M., Liao, M. K. and Hu, K. (2016). A constitutive model of frozen saline sandy soil

based on energy dissipation theory. *International Journal of Plasticity* **78**:84-113.

Lai, Y. M., Xu, X. T., Dong, Y. H. and Li, S. Y. (2013). Present situation and prospect of mechanical research on frozen soils in China. *Cold Regions Science and Technology* **87**:6-18.

Laloui, L., Geiser, F. and Vulliet, L. (2001). Constitutive modelling of unsaturated soils. *Revue Française de Génie Civil* **5(6)**:797-807.

Landon, M. M. and DeGroot, D. J. (2006). Measurement of small strain shear modulus anisotropy on unconfined clay samples using bender elements. In *Proceedings of GeoCongress 2006: Geotechnical Engineering in the Information Technology Age*, pp. 1-6.

Lashkari, A. (2010). A SANISAND model with anisotropic elasticity. *Soil Dynamics and Earthquake Engineering* **30(12)**:1462-1477.

Lee, E. (2004). The compression behaviour of transitional soils. *Master's thesis, Imperial College London, London, UK.*

Lee, J. S. and Santamarina, J. C. (2005). Bender elements: performance and signal interpretation. *Journal of Geotechnical and Geoenvironmental Engineering* **131(9)**:1063-1070.

Li, K. Q. and Yin, Z. Y. (2025). State of the art of coupled thermo-hydro-mechanical-chemical modelling for frozen soils. *Archives of Computational Methods in Engineering* **32**:1039-1096.

Li, K. Q., Yin, Z. Y., Qi, J. L. and Liu, Y. (2024). State-of-the-art constitutive modelling of frozen soils. *Archives of Computational Methods in Engineering* **31(7)**:3801-3842.

Li, P., Pan, Z. H., Xiao, T. and Wang, J. D. (2023). Effects of molding water content and compaction degree on the microstructure and permeability of compacted loess. *Acta Geotechnica* **18(2)**:921-936.

Li, Q., Ng, C. W. W. and Liu, G. B. (2012). Determination of small-strain stiffness of Shanghai clay on prismatic soil specimen. *Canadian Geotechnical Journal* **49(8)**:986-993.

Li, X. S. and Dafalias, Y. F. (2000). Dilatancy for cohesionless soils. *Géotechnique* **50(4)**:449-460.

Li, X. S. and Dafalias, Y. F. (2004). A constitutive framework for anisotropic sand including non-proportional loading. *Géotechnique* **54(1)**:41-55.

Li, X. S. and Dafalias, Y. F. (2012). Anisotropic critical state theory: role of fabric. *Journal of Engineering Mechanics* **138(3)**:263-275.

Li, Y. R., Shi, W. H., Aydin, A., Beroya-Eitner, M. A. and Gao, G. H. (2020). Loess genesis and worldwide distribution. *Earth-Science Reviews* **201**:102947.

Liang, R. Y., Rabab'ah, S. and Khasawneh, M. (2008). Predicting moisture-dependent resilient modulus of cohesive soils using soil suction concept. *Journal of Transportation Engineering* **134(1)**:34-40.

Liao, D. and Yang, Z. X. (2021a). Hypoplastic modeling of anisotropic sand behavior accounting for fabric evolution under monotonic and cyclic loading. *Acta Geotechnica* **16**:2003-2029.

Liao, D. and Yang, Z. X. (2021b). Non-coaxial hypoplastic model for sand with evolving fabric

anisotropy including non-proportional loading. *International Journal for Numerical and Analytical Methods in Geomechanics* **45(16)**:2433-2463.

Liu, M. D. and Carter, J. P. (1999). Virgin compression of structured soils. *Géotechnique* **49(1)**:43-57.

Liu, M. D. and Carter, J. P. (2000). Modelling the destructuring of soils during virgin compression. *Géotechnique* **50(4)**:479-483.

Liu, M. D. and Carter, J. P. (2002). A structured Cam Clay model. *Canadian Geotechnical Journal* **39(6)**:1313-1332.

Liu, W. Z., Shi, M. L., Miao, L. C., Xu, L. R. and Zhang, D. W. (2013). Constitutive modeling of the destructuration and anisotropy of natural soft clay. *Computers and Geotechnics* **51**:24-41.

Liu, X., Zhang, N. and Lan, H. X. (2019a). Effects of sand and water contents on the small-strain shear modulus of loess. *Engineering Geology* **260**:105202.

Liu, X. Y., Liu, E. L., Zhang, D., Zhang, G. and Song, B. T. (2019b). Study on strength criterion for frozen soil. *Cold Regions Science and Technology* **161**:1-20.

Liu, X. Y., Liu, E. L., Zhang, D., Zhang, G., Yin, X. and Song, B. T. (2019c). Study on effect of coarse-grained content on the mechanical properties of frozen mixed soils. *Cold Regions Science and Technology* **158**:237-251.

Liu, X. Y., Zhang, X. W., Kong, L. W., Wang, G. and Yin, S. (2023). Inherent and stress-induced stiffness anisotropy of natural granite residual soil. *Acta Geotechnica* **18(11)**:5681-5699.

Liu, Z., Liu, F. Y., Ma, F. L., Wang, M., Bai, X. H., Zheng, Y. L., Yin, H. and Zhang, G. P. (2016). Collapsibility, composition, and microstructure of loess in China. *Canadian Geotechnical Journal* **53(4)**:673-686.

Lloret, A., Villar, M. V., Sanchez, M., Gens, A., Pintado, X. and Alonso, E. E. (2003). Mechanical behaviour of heavily compacted bentonite under high suction changes. *Géotechnique* **53(1)**:27-40.

Lo Presti, D. C. F., Jamiolkowski, M., Pallara, O., Cavallaro, A. and Pedroni, S. (1997). Shear modulus and damping of soils. *Géotechnique* **47(3)**:603-617.

Loret, B. and Khalili, N. (2002). An effective stress elastic-plastic model for unsaturated porous media. *Mechanics of Materials* **34(2)**:97-116.

Love, A. E. H. (1927). A treatise on the mathematical theory of elasticity. Cambridge University Press.

Lu, N. (2008). Is matric suction a stress variable? *Journal of Geotechnical and Geoenvironmental Engineering* **134(7)**:899-905.

Lu, N., Godt, J. W. and Wu, D. T. (2010). A closed-form equation for effective stress in unsaturated soil. *Water Resources Research* **46(5)**.

Lu, Y., Fu, W. B. and Xue, D. X. (2020). Deformation characteristics of soft marine soil tested under cyclic loading with low frequency. *Advances in Civil Engineering* **2020(1)**:8875315.

Ma, F. L., Yang, J. and Bai, X. H. (2017). Water sensitivity and microstructure of compacted loess. *Transportation Geotechnics* **11**:41-56.

Ma, L., Qi, J. L., Yu, F. and Yao, X. L. (2016). Experimental study on variability in mechanical

properties of a frozen sand as determined in triaxial compression tests. *Acta Geotechnica* **11**:61-70.

Ma, W., Wu, Z. W., Zhang, L. X. and Chang, X. X. (1999). Analyses of process on the strength decrease in frozen soils under high confining pressures. *Cold Regions Science and Technology* **29(1)**:1-7.

Macari, E. J. and Hoyos, L., Jr. (1996). Effect of degree of weathering on dynamic properties of residual soils. *Journal of Geotechnical Engineering* **122(12)**:988-997.

Mancuso, C., Vassallo, R. and d'Onofrio, A. (2002). Small strain behavior of a silty sand in controlled-suction resonant column torsional shear tests. *Canadian Geotechnical Journal* **39(1)**:22-31.

Marcuson, W. F., III and Wahls, H. E. (1972). Time effects on dynamic shear modulus of clays. *Journal of the Soil Mechanics and Foundations Division* **98(12)**:1359-1373.

Martins, F. B., Bressani, L. A., Coop, M. R. and Bica, A. V. D. (2001). Some aspects of the compressibility behaviour of a clayey sand. *Canadian Geotechnical Journal* **38(6)**:1177-1186.

Mašín, D. (2010). Predicting the dependency of a degree of saturation on void ratio and suction using effective stress principle for unsaturated soils. *International Journal for Numerical and Analytical Methods in Geomechanics* **34(1)**:73-90.

McCartney, J. S. and Khosravi, A. (2013). Field-monitoring system for suction and temperature profiles under pavements. *Journal of Performance of Constructed Facilities* **27(6)**:818-825.

Mendoza, C. E. and Colmenares, J. E. (2006). Influence of the suction on the stiffness at very small strains. In *Proceedings of 4th International Conference on Unsaturated Soils*, pp. 529-540.

Mendoza, C. E., Colmenares, J. E. and Merchan, V. E. (2005). Stiffness of an unsaturated compacted clayey soil at very small strains. In *Proceedings of Advanced Experimental Unsaturated Soil Mechanics EXPERUS 2005*, pp. 199-204.

Metelková, Z., Boháč, J., Přikryl, R. and Sedlářová, I. (2012). Maturation of loess treated with variable lime admixture: pore space textural evolution and related phase changes. *Applied Clay Science* **61**:37-43.

Mitaritonna, G., Amorosi, A. and Cotecchia, F. (2014). Experimental investigation of the evolution of elastic stiffness anisotropy in a clayey soil. *Géotechnique* **64(6)**:463-475.

Mitchell, J. K. and Soga, K. (2005). Fundamentals of soil behavior. John Wiley and Sons New York.

Moghaddasi, H., Shahbodagh, B. and Khalili, N. (2021). A bounding surface plasticity model for unsaturated structured soils. *Computers and Geotechnics* **138**:104313.

Mu, Q. Y., Dai, B. L. and Zhou, C. (2023a). A constitutive model for structured soils under saturated and unsaturated conditions. *International Journal for Numerical and Analytical Methods in Geomechanics* **47(14)**:2562-2586.

Mu, Q. Y., Dai, B. L., Zhou, C., Meng, L. L., Zheng, J. G., Zhang, J. W., Yu, Y. T. and Liu, Z. H. (2023b). A new and simple method for predicting the collapse susceptibility of intact loess. *Computers and Geotechnics* **158**:105408.

Mu, Q. Y., Dong, H., Liao, H. J., Zhou, C., Li, S. B. and Zhang, J. W. (2022). Effects of in situ wetting-drying cycles on the mechanical behaviour of an intact loess. *Canadian Geotechnical Journal* **59(7)**:1281-1284.

Mu, Q. Y., Zhou, C. and Ng, C. W. W. (2020). Compression and wetting induced volumetric behavior of loess: macro-and micro-investigations. *Transportation Geotechnics* **23**:100345.

Muñoz-Castelblanco, J. A., Pereira, J. M., Delage, P. and Cui, Y. J. (2012). The water retention properties of a natural unsaturated loess from northern France. *Géotechnique* **62(2)**:95-106.

Murrell, S. A. F., Sammonds, P. R. and Rist, M. A. (1991). Strength and failure modes of pure ice and multi-year sea ice under triaxial loading. In *Proceedings of Ice-Structure Interaction: IUTAM/IAHR Symposium St. John's, Newfoundland Canada 1989*. Springer, pp. 339-361.

NCHRP. (2004). *Guide for mechanistic-empirical design of new and rehabilitated pavement structures*. National Cooperative Highway Research Program, ARA, Inc., ERES Division.

Newson, T. A. and Davies, M. C. R. (1996). A rotational hardening constitutive model for anisotropically consolidated clay. *Soils and Foundations* **36(3)**:13-20.

Ng, C. W. and Pang, Y. W. (2000a). Experimental investigations of the soil-water characteristics of a volcanic soil. *Canadian Geotechnical Journal* **37(6)**:1252-1264.

Ng, C. W. W., Baghbanrezvan, S., Kadlicek, T. and Zhou, C. (2020). A state-dependent constitutive model for methane hydrate-bearing sediments inside the stability region. *Géotechnique* **70(12)**:1094-1108.

Ng, C. W. W., Kaewsong, R., Zhou, C. and Alonso, E. E. (2017). Small strain shear moduli of unsaturated natural and compacted loess. *Géotechnique* **67(7)**:646-651.

Ng, C. W. W., Mu, Q. Y. and Zhou, C. (2019). Effects of specimen preparation method on the volume change of clay under cyclic thermal loads. *Géotechnique* **69(2)**:146-150.

Ng, C. W. W. and Pang, Y. W. (2000b). Influence of stress state on soil-water characteristics and slope stability. *Journal of Geotechnical and Geoenvironmental Engineering* **126(2)**:157-166.

Ng, C. W. W. and Peprah-Manu, D. (2023). Pore structure effects on the water retention behaviour of a compacted silty sand soil subjected to drying-wetting cycles. *Engineering Geology* **313**:106963.

Ng, C. W. W., Sadeghi, H., Hossen, S. K. B., Chiu, C. F., Alonso, E. E. and Baghbanrezvan, S. (2016). Water retention and volumetric characteristics of intact and re-compacted loess. *Canadian Geotechnical Journal* **53(8)**:1258-1269.

Ng, C. W. W. and Xu, J. (2012). Effects of current suction ratio and recent suction history on small-strain behaviour of an unsaturated soil. *Canadian Geotechnical Journal* **49(2)**:226-243.

Ng, C. W. W., Xu, J. and Yung, S. Y. (2009). Effects of wetting-drying and stress ratio on anisotropic stiffness of an unsaturated soil at very small strains. *Canadian Geotechnical Journal* **46(9)**:1062-1076.

Ng, C. W. W. and Yung, S. Y. (2008). Determination of the anisotropic shear stiffness of an unsaturated decomposed soil. *Géotechnique* **58(1)**:23-35.

Ng, C. W. W. and Zhou, C. (2014). Cyclic behaviour of an unsaturated silt at various suctions and temperatures. *Géotechnique* **64(9)**:709-720.

Ng, C. W. W., Zhou, C. and Ni, J. J. (2024). Advanced unsaturated soil mechanics: theory and applications. CRC Press.

Ng, C. W. W., Zhou, C., Yuan, Q. and Xu, J. (2013). Resilient modulus of unsaturated subgrade soil: experimental and theoretical investigations. *Canadian Geotechnical Journal* **50(2)**:223-232.

Nishimura, S., Gens, A., Olivella, S. and Jardine, R. J. (2009). THM-coupled finite element analysis of frozen soil: formulation and application. *Géotechnique* **59(3)**:159-171.

Nishimura, S., Kawasaki, H. and Sato, I. (2022). On limit strength of frozen clay undergoing triaxial tension. *Géotechnique* **74(12)**:1241-1253.

Nishimura, S. and Wang, J. Y. (2019). A simple framework for describing strength of saturated frozen soils as multi-phase coupled system. *Géotechnique* **69(8)**:659-671.

Nuth, M. and Laloui, L. (2008a). Advances in modelling hysteretic water retention curve in deformable soils. *Computers and Geotechnics* **35(6)**:835-844.

Nuth, M. and Laloui, L. (2008b). Effective stress concept in unsaturated soils: clarification and validation of a unified framework. *International Journal for Numerical and Analytical Methods in Geomechanics* **32(7)**:771-801.

Obuzor, G. N., Kinuthia, J. M. and Robinson, R. B. (2011). Enhancing the durability of flooded low-capacity soils by utilizing lime-activated ground granulated blastfurnace slag (GGBS). *Engineering Geology* **123(3)**:179-186.

Oh, W. T. and Vanapalli, S. K. (2014). Semi-empirical model for estimating the small-strain shear modulus of unsaturated non-plastic sandy soils. *Geotechnical and Geological Engineering* **32**:259-271.

Osinubi, K. J. (2006). Influence of compactive efforts on lime-slag treated tropical black clay. *Journal of Materials in Civil Engineering* **18(2)**:175-181.

Oti, J. E., Kinuthia, J. M. and Bai, J. (2009). Compressive strength and microstructural analysis of unfired clay masonry bricks. *Engineering Geology* **109(3-4)**:230-240.

Oualmakran, M., Mercatoris, B. C. N. and François, B. (2016). Pore-size distribution of a compacted silty soil after compaction, saturation, and loading. *Canadian Geotechnical Journal* **53(12)**:1902-1909.

Ouria, A. (2017). Disturbed state concept-based constitutive model for structured soils. *International Journal of Geomechanics* **17(7)**:04017008.

Oztoprak, S. and Bolton, M. D. (2013). Stiffness of sands through a laboratory test database. *Géotechnique* **63(1)**:54-70.

Parameswaran, V. R. and Jones, S. J. (1981). Triaxial testing of frozen sand. *Journal of Glaciology* **27(95)**:147-155.

Parhizkar, A., Nazarpour, A. and Khayat, N. (2024). Investigation of geotechnical and microstructure characteristics of gypsum soil using ground granulated blast-furnace slag (GGBS), fly ash, and lime. *Construction and Building Materials* **418**:135358.

Pedrotti, M. and Tarantino, A. (2019). A conceptual constitutive model unifying slurried (saturated), compacted (unsaturated) and dry states. *Géotechnique* **69(3)**:217-233.

Pei, X. J., Zhang, F. Y., Wu, W. J. and Liang, S. Y. (2015). Physicochemical and index properties of loess stabilized with lime and fly ash piles. *Applied Clay Science* **114**:77-84.

Peng, J. B., Sun, X. H., Lu, Q. Z., Meng, L. C., He, H. Q., Qiao, J. W. and Wang, F. Y. (2020). Characteristics and mechanisms for origin of earth fissures in Fenwei basin, China. *Engineering Geology* **266**:105445.

Pennington, D. S., Nash, D. F. T. and Lings, M. L. (1997). Anisotropy of G0 shear stiffness in Gault Clay. *Géotechnique* **47(3)**:391-398.

Pereira, J. M., Rouainia, M. and Manzanal, D. (2014). Combined effects of structure and partial saturation in natural soils. *Journal of Geo-Engineering Sciences* **2(1-2)**:3-16.

Pestana, J. M., Whittle, A. J. and Gens, A. (2002). Evaluation of a constitutive model for clays and sands: part II-clay behaviour. *International Journal for Numerical and Analytical Methods in Geomechanics* **26(11)**:1123-1146.

Philip, J. R. (1977). Unitary approach to capillary condensation and adsorption. *The Journal of Chemical Physics* **66(11)**:5069-5075.

Potts, D. M. and Zdravkovic, L. (1999). Finite element analysis in geotechnical engineering: theory Thomas Telford.

Pye, K. (1995). The nature, origin and accumulation of loess. *Quaternary Science Reviews* **14(7-8)**:653-667.

Qi, J. L. and Ma, W. (2007). A new criterion for strength of frozen sand under quick triaxial compression considering effect of confining pressure. *Acta Geotechnica* **2**:221-226.

Qian, J. G., Du, Z. B., Lu, X. L., Gu, X. Q. and Huang, M. S. (2019a). Effects of principal stress rotation on stress-strain behaviors of saturated clay under traffic-load-induced stress path. *Soils and Foundations* **59(1)**:41-55.

Qian, J. G., Li, S. Y., Zhang, J. L., Jiang, J. H. and Wang, Q. Y. (2019b). Effects of OCR on monotonic and cyclic behavior of reconstituted Shanghai silty clay. *Soil Dynamics and Earthquake Engineering* **118**:111-119.

Qian, J. G., Wang, Y. G., Yin, Z. Y. and Huang, M. S. (2016). Experimental identification of plastic shakedown behavior of saturated clay subjected to traffic loading with principal stress rotation. *Engineering Geology* **214**:29-42.

Rampello, S., Viggiani, G. M. B. and Amorosi, A. (1997). Small-strain stiffness of reconstituted clay compressed along constant triaxial effective stress ratio paths. *Géotechnique* **47(3)**:475-489.

Rist, M. A. and Murrell, S. A. F. (1994). Ice triaxial deformation and fracture. *Journal of Glaciology* **40(135)**:305-318.

Roesler, S. K. (1979). Anisotropic shear modulus due to stress anisotropy. *Journal of the Geotechnical Engineering Division* **105(7)**:871-880.

Romero, E., Gens, A. and Lloret, A. (2001). Temperature effects on the hydraulic behaviour of an unsaturated clay. In *Unsaturated Soil Concepts and Their Application in Geotechnical Practice.* Springer Science, Business Media Dordrecht, pp. 311-332.

Romero, E. and Jommi, C. (2008). An insight into the role of hydraulic history on the volume

changes of anisotropic clayey soils. *Water Resources Research* **44(5)**.

Romero, E. and Simms, P. H. (2008). Microstructure investigation in unsaturated soils: a review with special attention to contribution of mercury intrusion porosimetry and environmental scanning electron microscopy. *Geotechnical and Geological Engineering* **26(6)**:705-727.

Romero, E. and Vaunat, J. (2000). Retention curves of deformable clays. *Experimental evidence and theoretical approaches in unsaturated soils* **91**:106.

Rotisciani, G. M., Desideri, A. and Amorosi, A. (2021). Unsaturated structured soils: constitutive modelling and stability analyses. *Acta Geotechnica* **16(11)**:3355-3380.

Rouainia, M. and Muir Wood, D. (2000). A kinematic hardening constitutive model for natural clays with loss of structure. *Géotechnique* **50(2)**:153-164.

Russell, A. R. (2011). A compression line for soils with evolving particle and pore size distributions due to particle crushing. *Géotechnique Letters* **1(1)**:5-9.

Russell, A. R. (2014). How water retention in fractal soils depends on particle and pore sizes, shapes, volumes and surface areas. *Géotechnique* **64(5)**:379-390.

Russell, A. R. and Buzzi, O. (2012). A fractal basis for soil-water characteristics curves with hydraulic hysteresis. *Géotechnique* **62(3)**:269-274.

Russell, A. R. and Khalili, N. (2004). A bounding surface plasticity model for sands exhibiting particle crushing. *Canadian Geotechnical Journal* **41(6)**:1179-1192.

Russell, A. R. and Khalili, N. (2006). A unified bounding surface plasticity model for unsaturated soils. *International Journal for Numerical and Analytical Methods in Geomechanics* **30(3)**:181-212.

Sadeghi, H., Kiani, M., Sadeghi, M. and Jafarzadeh, F. (2019). Geotechnical characterization and collapsibility of a natural dispersive loess. *Engineering Geology* **250**:89-100.

Santucci de Magistris, F. and Tatsuoka, F. (2004). Effects of moulding water content on the stress-strain behaviour of a compacted silty sand. *Soils and Foundations* **44(2)**:85-101.

Sariosseiri, F. and Muhunthan, B. (2009). Effect of cement treatment on geotechnical properties of some Washington State soils. *Engineering Geology* **104(1-2)**:119-125.

Sawangsuriya, A. (2006). Stiffness-suction-moisture relationship for compacted soils. *PhD Thesis, The University of Wisconsin-Madison.*

Sawangsuriya, A., Edil, T. B. and Benson, C. H. (2009a). Effect of suction on resilient modulus of compacted fine-grained subgrade soils. *Transportation Research Record* **2101(1)**:82-87.

Sawangsuriya, A., Edil, T. B. and Bosscher, P. J. (2009b). Modulus-suction-moisture relationship for compacted soils in postcompaction state. *Journal of Geotechnical and Geoenvironmental Engineering* **135(10)**:1390-1403.

Sayles, F. H. (1974). Triaxial constant strain rate tests and triaxial creep tests on frozen Ottawa sand. Corps of Engineers, US Army Cold Regions Research and Engineering Laboratory.

Scrivener, K., Snellings, R. and Lothenbach, B. (2016). A practical guide to microstructural analysis of cementitious materials. CRC press, Boca Raton, FL, USA.

Senetakis, K., Anastasiadis, A. and Pitilakis, K. (2012). Small strain shear modulus and

damping ratio of quartz and volcanic sands. *Geotechnical Testing Journal* **35(6)**:964-980.

Senetakis, K., Anastasiadis, A. and Pitilakis, K. (2013). Normalized shear modulus reduction and damping ratio curves of quartz sand and rhyolitic crushed rock. *Soils and Foundations* **53(6)**:879-893.

Sheng, D. C., Fredlund, D. G. and Gens, A. (2008). A new modelling approach for unsaturated soils using independent stress variables. *Canadian Geotechnical Journal* **45(4)**:511-534.

Shibuya, S., Hwang, S. C. and Mitachi, T. (1997). Elastic shear modulus of soft clays from shear wave velocity measurement. *Géotechnique* **47(3)**:593-601.

Simpson, B., Atkinson, J. H. and Jovicic, V. (1996). The influence of anisotropy on calculations of ground settlements above tunnels. In *Proceedings of Geotechnical Aspects of Underground Construction in Soft Ground*, pp. 591-594.

Sitarenios, P. and Kavvadas, M. (2020). A plasticity constitutive model for unsaturated, anisotropic, nonexpansive soils. *International Journal for Numerical and Analytical Methods in Geomechanics* **44(4)**:435-454.

Sivakumar, V. (1993). A critical state framework for unsaturated soil. *PhD Thesis, University of Sheffield.*

Sivakumar, V., Kodikara, J., O'hagan, R., Hughes, D., Cairns, P. and McKinley, J. D. (2013). Effects of confining pressure and water content on performance of unsaturated compacted clay under repeated loading. *Géotechnique* **63(8)**:628-640.

Sivakumar, V., Sivakumar, R., Murray, E. J., Mackinnon, P. and Boyd, J. (2010). Mechanical behaviour of unsaturated kaolin (with isotropic and anisotropic stress history). Part 1: wetting and compression behaviour. *Géotechnique* **60(8)**:581-594.

Sivakumar, V. and Wheeler, S. J. (2000). Influence of compaction procedure on the mechanical behaviour of an unsaturated compacted clay. Part 1: wetting and isotropic compression. *Géotechnique* **50(4)**:359-368.

Song, B. H., Tsinaris, A., Anastasiadis, A., Pitilakis, K. and Chen, W. W. (2017). Small-strain stiffness and damping of Lanzhou loess. *Soil Dynamics and Earthquake Engineering* **95**:96-105.

Stokoe, K., II, Hwang, S. K., Lee, J. N. K. and Andrus, R. D. (1995). Effects of various parameters on the stiffness and damping of soils at small to medium strains. In *Proceedings of Pre-failure Deformation of Geomaterials* **vol. 2**, pp. 785-816.

Stropeit, K., Wheeler, S. and Cui, Y. J. (2008). An anisotropic elasto-plastic model for unsaturated soils.

Stuedlein, A. W., Dadashiserej, A., Jana, A. and Evans, T. M. (2023). Liquefaction susceptibility and cyclic response of intact nonplastic and plastic silts. *Journal of Geotechnical and Geoenvironmental Engineering* **149(1)**:04022125.

Su, Y. and Cui, Y. J. (2022). Modelling the suction-dependent plastic shakedown limit of unsaturated fine/coarse soil mixture with consideration of soil-water retention curve. *Transportation Geotechnics* **32**:100698.

Su, Y., Cui, Y. J., Dupla, J. C. and Canou, J. (2022). Modeling the suction- and deviator stress-dependent resilient modulus of unsaturated fine/coarse soil mixture by considering soil-

water retention curve. *Acta Geotechnica* **17**:3747-3763.

Sun, D. A., Sheng, D. C. and Xu, Y. F. (2007). Collapse behaviour of unsaturated compacted soil with different initial densities. *Canadian Geotechnical Journal* **44(6)**:673-686.

Sun, K. and Zhou, A. N. (2021). A multisurface elastoplastic model for frozen soil. *Acta Geotechnica* **16(11)**:3401-3424.

Sun, Z. Z., Zhang, S. J., Wang, Y. P., Bai, R. Q. and Li, S. Y. (2022). Mechanical behavior and microstructural evolution of frozen soils under the combination of confining pressure and water content. *Engineering Geology* **308**:106819.

Sze, H. Y. and Yang, J. (2014). Failure modes of sand in undrained cyclic loading: impact of sample preparation. *Journal of Geotechnical and Geoenvironmental Engineering* **140(1)**:152-169.

Tabarsa, A., Latifi, N., Meehan, C. L. and Manahiloh, K. N. (2018). Laboratory investigation and field evaluation of loess improvement using nanoclay-A sustainable material for construction. *Construction and Building Materials* **158**:454-463.

Takkabutr, P. (2006). Experimental investigations on small-strain stiffness properties of partially saturated soils via resonant column and bender element testing. *PhD Thesis, The University of Texas at Arlington.*

Tang, Y., Yang, P., Li, L. and Zhou, Z. L. (2024). Experimental study on strength characteristics and constitutive behavior of frozen chloride silty clay. *Cold Regions Science and Technology* **219**:104126.

Tang, Y. Q., Cui, Z. D., Zhang, X. and Zhao, S. K. (2008). Dynamic response and pore pressure model of the saturated soft clay around the tunnel under vibration loading of Shanghai subway. *Engineering Geology* **98(3-4)**:126-132.

Tarantino, A. (2009). A water retention model for deformable soils. *Géotechnique* **59(9)**:751-762.

Tarantino, A. and De Col, E. (2008). Compaction behaviour of clay. *Géotechnique* **58(3)**:199-213.

Tarantino, A. and Tombolato, S. (2005). Coupling of hydraulic and mechanical behaviour in unsaturated compacted clay. *Géotechnique* **55(4)**:307-317.

Terzaghi, K. (1943). Theoretical soil mechanics. John Wiley and Sons, New York, NY.

Thakur, V. and Degago, S. A. (2012). Quickness of sensitive clays. *Géotechnique Letters* **2(3)**:87-95.

Tian, Y. and Yao, Y. P. (2018). Constitutive modeling of principal stress rotation by considering inherent and induced anisotropy of soils. *Acta Geotechnica* **13**:1299-1311.

Tinjum, J. M., Benson, C. H. and Blotz, L. R. (1997). Soil-water characteristic curves for compacted clays. *Journal of Geotechnical and Geoenvironmental Engineering* **123(11)**:1060-1069.

Todisco, M. C., Coop, M. R. and Pereira, J. M. (2018). Fabric characterisation in transitional soils. *Granular Matter* **20(2)**:1-12.

Tse, M. K. (2007). Influence of stress states on soil-water characteristics, conjunctive surface-subsurface flow modelling and stability analysis. *Master's thesis, Hong Kong University of Science and Technology.*

Tuller, M., Or, D. and Dudley, L. M. (1999). Adsorption and capillary condensation in porous media: liquid retention and interfacial configurations in angular pores. *Water Resources Research* **35(7)**:1949-1964.

Uchaipichat, A. and Khalili, N. (2009). Experimental investigation of thermo-hydro-mechanical behaviour of an unsaturated silt. *Géotechnique* **59(4)**:339-353.

Vahedifard, F., Thota, S. K., Cao, T. D., Samarakoon, R. A. and McCartney, J. S. (2020). Temperature-dependent model for small-strain shear modulus of unsaturated soils. *Journal of Geotechnical and Geoenvironmental Engineering* **146(12)**:04020136.

Van Genuchten, M. T. (1980). A closed-form equation for predicting the hydraulic conductivity of unsaturated soils. *Soil Science Society of America Journal* **44(5)**:892-898.

Vanapalli, S. K., Fredlund, D. G. and Pufahl, D. E. (1999). The influence of soil structure and stress history on the soil-water characteristics of a compacted till. *Géotechnique* **49(2)**:143-159.

Vanapalli, S. K., Fredlund, D. G., Pufahl, D. E. and Clifton, A. W. (1996). Model for the prediction of shear strength with respect to soil suction. *Canadian Geotechnical Journal* **33(3)**:379-392.

Vandoorne, R., Gräbe, P. J. and Heymann, G. (2021). Soil suction and temperature measurements in a heavy haul railway formation. *Transportation Geotechnics* **31**:100675.

Vassallo, R., Mancuso, C. and Vinale, F. (2007). Effects of net stress and suction history on the small strain stiffness of a compacted clayey silt. *Canadian Geotechnical Journal* **44(4)**:447-462.

Vecchia, G. D. and Romero, E. (2013). A fully coupled elastic-plastic hydromechanical model for compacted soils accounting for clay activity. *International Journal for Numerical and Analytical Methods in Geomechanics* **37(5)**:503-535.

Viggiani, G. and Atkinson, J. H. (1995). Stiffness of fine-grained soil at very small strains. *Géotechnique* **45(2)**:249-265.

Wang, F. T., Li, D. Q., Du, W. Q., Zarei, C. and Liu, Y. (2021). Bender element measurement for small-strain shear modulus of compacted loess. *International Journal of Geomechanics* **21(5)**:04021063.

Wang, J., Zhou, Z., Hu, X. Q., Guo, L. and Cai, Y. Q. (2019a). Effects of principal stress rotation and cyclic confining pressure on behavior of soft clay with different frequencies. *Soil Dynamics and Earthquake Engineering* **118**:75-85.

Wang, J. H., Moran, K. and Baxter, C. D. P. (2006). Correlation between cyclic resistance ratios of intact and reconstituted offshore saturated sands and silts with the same shear wave velocity. *Journal of Geotechnical and Geoenvironmental Engineering* **132(12)**:1574-1580.

Wang, J. T., Kong, L. W., Yan, J. B. and Zhou, Z. H. (2022). Comparative investigation on small-strain stiffness characteristics of undisturbed and compacted highly weathered granites at various densities. *Geofluids* **2022**:3935815.

Wang, J. Y. (2017). Laboratory study on mechanical properties of frozen clay through state concept. *PhD Thesis, Hokkaido University.*

Wang, J. Y., Nishimura, S., Okajima, S. and Joshi, B. R. (2019b). Small-strain deformation characteristics of frozen clay from static testing. *Géotechnique* **69(9)**:816-827.

Wang, R., Dafalias, Y. F., Fu, P. C. and Zhang, J. M. (2020). Fabric evolution and dilatancy within anisotropic critical state theory guided and validated by DEM. *International Journal of Solids and Structures* **188**:210-222.

Wang, Y. K., Jiang, R., Gao, Y. F. and Shao, J. G. (2024). Resilient strain and stiffness degradation of Yellow River silt under cyclic loads. *Proceedings of the Institution of Civil Engineers-Geotechnical Engineering* **177(2)**:169-178.

Watabe, Y., Leroueil, S. and Le Bihan, J. P. (2000). Influence of compaction conditions on pore-size distribution and saturated hydraulic conductivity of a glacial till. *Canadian Geotechnical Journal* **37(6)**:1184-1194.

Werkmeister, S. (2003). Permanent deformation behaviour of unbound granular materials in pavement constructions. *PhD Thesis, Technische Universität Dresden.*

Wheeler, S. J. and Karube, D. (1996). Constitutive modelling. In *Proceedings of 1st International Conference on Unsaturated Soils* **vol. 3**, pp. 1323-1356.

Wheeler, S. J., Näätänen, A., Karstunen, M. and Lojander, M. (2003a). An anisotropic elastoplastic model for soft clays. *Canadian Geotechnical Journal* **40(2)**:403-418.

Wheeler, S. J., Sharma, R. S. and Buisson, M. S. R. (2003b). Coupling of hydraulic hysteresis and stress-strain behaviour in unsaturated soils. *Géotechnique* **53(1)**:41-54.

Wheeler, S. J. and Sivakumar, V. (1995). An elasto-plastic critical state framework for unsaturated soil. *Géotechnique* **45(1)**:35-53.

Wheeler, S. J. and Sivakumar, V. (2000). Influence of compaction procedure on the mechanical behaviour of an unsaturated compacted clay. Part 2: shearing and constitutive modelling. *Géotechnique* **50(4)**:369-376.

Whittle, A. J. and Kavvadas, M. J. (1994). Formulation of MIT-E3 constitutive model for overconsolidated clays. *Journal of Geotechnical Engineering* **120(1)**:173-198.

Wijewickreme, D. and Sanín, M. V. (2008). Cyclic shear response of undisturbed and reconstituted low-plastic Fraser River silt. In *Proceedings of Geotechnical Earthquake Engineering and Soil Dynamics IV*, pp. 1-10.

Wijewickreme, D., Soysa, A. and Verma, P. (2019). Response of natural fine-grained soils for seismic design practice: a collection of research findings from British Columbia, Canada. *Soil Dynamics and Earthquake Engineering* **124**:280-296.

Wild, S., Kinuthia, J. M., Jones, G. I. and Higgins, D. D. (1998). Effects of partial substitution of lime with ground granulated blast furnace slag (GGBS) on the strength properties of lime-stabilised sulphate-bearing clay soils. *Engineering Geology* **51(1)**:37-53.

Wong, K. S., Mašín, D. and Ng, C. W. W. (2014). Modelling of shear stiffness of unsaturated fine grained soils at very small strains. *Computers and Geotechnics* **56**:28-39.

Wu, G., Li, G. Y., Bing, H., Chen, D., Cao, Y. P., Tang, L. Y. and Jia, H. L. (2023). Effects of confining pressure and temperature on strength and deformation behavior of frozen saline silty clay. *Research in Cold and Arid Regions* **15(1)**:1-10.

Wu, T. Y., Jin, H. X., Guo, L., Sun, H. L., Tong, J. H., Jiang, Y. C. and Wei, P. F. (2022). Predicting method on settlement of soft subgrade soil caused by traffic loading

involving principal stress rotation and loading frequency. *Soil Dynamics and Earthquake Engineering* **152**:107023.

Xiao, J. H., Juang, C. H., Wei, K. and Xu, S. Q. (2014). Effects of principal stress rotation on the cumulative deformation of normally consolidated soft clay under subway traffic loading. *Journal of Geotechnical and Geoenvironmental Engineering* **140(4)**:04013046.

Xiao, T., Li, P., Pan, Z. H. and Wang, J. D. (2022). Effect of compaction condition on the water retention capacity, microstructure and its evolution during drying of compacted loess. *Geoenvironmental Disasters* **9(1)**:27.

Xu, G. (2014). Hypoplastic constitutive models for frozen soil. *PhD Thesis, University of Natural Resources and Life Sciences.*

Xu, H., Zhao, F. T., Hu, Y., Gao, F. and Zheng, Y. W. (2024). Cumulative deformation behavior of coarse-grained red mudstone soil under cyclic loading. *International Journal of Geomechanics* **24(11)**:04024245.

Xu, L. and Coop, M. R. (2016). Influence of structure on the behavior of a saturated clayey loess. *Canadian Geotechnical Journal* **53(6)**:1026-1037.

Xu, L. and Coop, M. R. (2017). The mechanics of a saturated silty loess with a transitional mode. *Géotechnique* **67(7)**:581-596.

Xu, L., Lan, T. G. and Mu, Q. Y. (2021a). Effects of structure on the compression behavior of unsaturated loess. *International Journal of Geomechanics* **21(4)**:06021007.

Xu, P. P., Zhang, Q. Y., Qian, H., Qu, W. G. and Li, M. N. (2021b). Microstructure and permeability evolution of remolded loess with different dry densities under saturated seepage. *Engineering Geology* **282**:105875.

Xu, X. T., Lai, Y. M., Dong, Y. H. and Qi, J. L. (2011). Laboratory investigation on strength and deformation characteristics of ice-saturated frozen sandy soil. *Cold Regions Science and Technology* **69(1)**:98-104.

Xu, X. T., Li, Q. L., Lai, Y., Pang, W. T. and Zhang, R. P. (2019). Effect of moisture content on mechanical and damage behavior of frozen loess under triaxial condition along with different confining pressures. *Cold Regions Science and Technology* **157**:110-118.

Xu, Y. F. (2004). Fractal approach to unsaturated shear strength. *Journal of Geotechnical and Geoenvironmental Engineering* **130(3)**:264-273.

Yan, W. M. and Li, X. S. (2011). A model for natural soil with bonds. *Géotechnique* **61(2)**:95-106.

Yang, C., Carter, J. P. and Sheng, D. C. (2014a). Description of compression behaviour of structured soils and its application. *Canadian Geotechnical Journal* **51(8)**:921-933.

Yang, C., Cui, Y. J., Pereira, J. M. and Huang, M. S. (2008a). A constitutive model for unsaturated cemented soils under cyclic loading. *Computers and Geotechnics* **35(6)**:853-859.

Yang, H., Khoshghalb, A. and Russell, A. R. (2014b). Fractal-based estimation of hydraulic conductivity from soil–water characteristic curves considering hysteresis. *Géotechnique Letters* **4(1)**:1-10.

Yang, Q., Tang, Y. Q., Yuan, B. and Zhou, J. (2019). Cyclic stress-strain behaviour of soft clay under traffic loading through hollow cylinder apparatus: effect of loading frequency.

Road Materials and Pavement Design **20(5)**:1026-1058.

Yang, S. R., Lin, H. D., Kung, J. H. S. and Huang, W. H. (2008b). Suction-controlled laboratory test on resilient modulus of unsaturated compacted subgrade soils. *Journal of Geotechnical and Geoenvironmental Engineering* **134(9)**:1375-1384.

Yang, Y. G., Lai, Y. M., Dong, Y. H. and Li, S. Y. (2010). The strength criterion and elastoplastic constitutive model of frozen soil under high confining pressures. *Cold Regions Science and Technology* **60(2)**:154-160.

Yang, Z. X., Li, X. S. and Yang, J. (2007). Undrained anisotropy and rotational shear in granular soil. *Géotechnique* **57(4)**:371-384.

Yates, K. and Russell, A. R. (2023). The unsaturated characteristics of natural loess in slopes, New Zealand. *Géotechnique* **73(10)**:871-884.

Yates, K. and Russell, A. R. (2024). Field measurements and modelling of climate-driven hydraulic flux, water content, and suction in a loess slope. *Canadian Geotechnical Journal* **62**:1-19.

Yi, Y. L., Li, C., Liu, S. Y. and Al-Tabbaa, A. (2014a). Resistance of MgO-GGBS and CS-GGBS stabilised marine soft clays to sodium sulfate attack. *Géotechnique* **64(8)**:673-679.

Yi, Y. L., Liska, M. and Al-Tabbaa, A. (2014b). Properties of two model soils stabilized with different blends and contents of GGBS, MgO, lime, and PC. *Journal of Materials in Civil Engineering* **26(2)**:267-274.

Yi, Y. L., Liska, M., Jin, F. and Al-Tabbaa, A. (2016). Mechanism of reactive magnesia-ground granulated blastfurnace slag (GGBS) soil stabilization. *Canadian Geotechnical Journal* **53(5)**:773-782.

Yokohama, S., Miura, S. and Matsumura, S. (2014). Change in the hydromechanical characteristics of embankment material due to compaction state conditions. *Soils and Foundations* **54(4)**:731-747.

Yu, F., Guo, P. J. and Na, S. (2022). A framework for constructing elasto‐plastic constitutive models for frozen and unfrozen soils. *International Journal for Numerical and Analytical Methods in Geomechanics* **46(2)**:436-466.

Yu, H. S. (1998). CASM: A unified state parameter model for clay and sand. *International Journal for Numerical and Analytical Methods in Geomechanics* **22(8)**:621-653.

Yu, Y. and Yang, Z. X. (2023). Bounding surface rotational hardening model for overconsolidated clay accounting for evolving fabric anisotropy. *International Journal for Numerical and Analytical Methods in Geomechanics* **47(3)**:370-391.

Zhan, T. L. T., Yang, Y. B., Chen, R., Ng, C. W. W. and Chen, Y. M. (2014). Influence of clod size and water content on gas permeability of a compacted loess. *Canadian Geotechnical Journal* **51(12)**:1468-1474.

Zhang, C. L., Jiang, G. L., Su, L. J. and Zhou, G. D. (2017a). Effect of cement on the stabilization of loess. *Journal of Mountain Science* **14(11)**:2325-2336.

Zhang, D. F., Wang, J. D., Chen, C. L. and Wang, S. H. (2020). The compression and collapse behaviour of intact loess in suction-monitored triaxial apparatus. *Acta Geotechnica* **15**:529-548.

Zhang, F. Y., Pei, X. J. and Yan, X. D. (2018a). Physicochemical and mechanical properties of lime-treated loess. *Geotechnical and Geological Engineering* **36**:685-696.

Zhang, J. H., Peng, J. H., Zheng, J. L., Dai, L. L. and Yao, Y. S. (2019a). Prediction of resilient modulus of compacted cohesive soils in South China. *International Journal of Geomechanics* **19(7)**:04019068.

Zhang, J. H., Zhang, A. S., Li, J. and Fan, H. S. (2024). Enhanced understanding on permanent deformation behaviour of subgrade compacted clay under long-term cyclic loading. *Soil Dynamics and Earthquake Engineering* **187**:108972.

Zhang, M., Guo, H., El-Korchi, T., Zhang, G. P. and Tao, M. J. (2013). Experimental feasibility study of geopolymer as the next-generation soil stabilizer. *Construction and Building Materials* **47**:1468-1478.

Zhang, S. J., Du, H. M. and Harbor, J. (2017b). The Effect of Confining Pressure and Water Content on Compressive Strength and Deformation of Ice‐rich Silty Sand. *Permafrost and Periglacial Processes* **28(1)**:298-305.

Zhang, S. J., Lai, Y. M., Sun, Z. Z. and Gao, Z. H. (2007). Volumetric strain and strength behavior of frozen soils under confinement. *Cold Regions Science and Technology* **47(3)**:263-270.

Zhang, T. W., Cui, Y. J., Lamas-Lopez, F., Calon, N. and Costa D'Aguiar, S. (2018b). Compacted soil behaviour through changes of density, suction, and stiffness of soils with remoulding water content. *Canadian Geotechnical Journal* **55(2)**:182-190.

Zhang, W. Y., Guo, A. B. and Lin, C. (2019b). Effects of cyclic freeze and thaw on engineering properties of compacted loess and lime-stabilized loess. *Journal of Materials in Civil Engineering* **31(9)**:04019205.

Zhang, Y. and Michalowski, R. L. (2015). Thermal-hydro-mechanical analysis of frost heave and thaw settlement. *Journal of Geotechnical and Geoenvironmental Engineering* **141(7)**:04015027.

Zhao, F. T., Qiu, Z. J., Zheng, Y. W. and Wu, Q. X. (2025). Development of pore water pressure in anisotropically consolidated sand under cyclic torsional loading. *Acta Geotechnica* **20(4)**:1703-1721.

Zhao, R. D., Chen, W. B., Zhou, C., Song, D. B., Zhang, R. J. and Yin, J. H. (2024). Mechanical characterization of stabilized dredged marine deposits with high water content using industrial wastes and vacuum preloading. *Acta Geotechnica*:1-14.

Zhao, X. D., Zhou, G. Q. and Chen, G. Z. (2013). Triaxial compression strength for artificial frozen clay with thermal gradient. *Journal of Central South University* **20(1)**:218-225.

Zheng, Y. W., Hatami, K. and Miller, G. A. (2017). Numerical simulation of wetting-induced settlement of embankments. *Journal of Performance of Constructed Facilities* **31(3)**:D4017001.

Zhou, A. N., Sheng, D. C., Sloan, S. W. and Gens, A. (2012). Interpretation of unsaturated soil behaviour in the stress-saturation space, I: volume change and water retention behaviour. *Computers and Geotechnics* **43**:178-187.

Zhou, C. (2014). Experimental study and constitutive modelling of cyclic behaviour at small strains of unsaturated silt at various temperatures. *PhD thesis, Hong Kong University*

of Science and Technology.

Zhou, C. and Chen, R. (2021). Modelling the water retention behaviour of anisotropic soils. *Journal of Hydrology* **599**:126361.

Zhou, C. and Ng, C. W. W. (2014). A new and simple stress-dependent water retention model for unsaturated soil. *Computers and Geotechnics* **62**:216-222.

Zhou, C. and Ng, C. W. W. (2015). A thermomechanical model for saturated soil at small and large strains. *Canadian Geotechnical Journal* **52(8)**:1101-1110.

Zhou, C. and Ng, C. W. W. (2018). A new thermo-mechanical model for structured soil. *Géotechnique* **68(12)**:1109-1115.

Zhou, C., Ng, C. W. W. and Chen, R. (2015). A bounding surface plasticity model for unsaturated soil at small strains. *International Journal for Numerical and Analytical Methods in Geomechanics* **39(11)**:1141-1164.

Zhou, Z. W., Ma, W., Zhang, S. J., Du, H. M., Mu, Y. H. and Li, G. Y. (2016). Multiaxial creep of frozen loess. *Mechanics of Materials* **95**:172-191.

Zhou, Z. W., Ma, W., Zhang, S. J., Mu, Y. H. and Li, G. Y. (2020). Experimental investigation of the path-dependent strength and deformation behaviours of frozen loess. *Engineering Geology* **265**:105449.

Zuo, L., Xu, L., Baudet, B. A., Gao, C. Y. and Huang, C. (2024). Small-strain shear stiffness anisotropy of a saturated clayey loess. *Géotechnique* **74(4)**:325-336.

APPENDIX A CONSTITUTIVE MODEL FOR THE MECHANICAL BEHAVIOUR OF SATURATED FROZEN SOILS

Loess in China is predominantly distributed in the northern regions, where it is commonly subjected to seasonal freeze-thaw cycles due to the prevailing climatic conditions. When the soil temperature drops below the freezing point, a portion of the pore water solidifies into ice. The presence of ice introduces a unique soil structure, which significantly alters the mechanical behaviour compared to the unfrozen state. This appendix presents a constitutive model considering the influence of the ice-induced structure on the mechanical behaviour of saturated frozen soils. Particularly, the model incorporates the dual effects of confining pressure in preventing crack formation within pore ice and initiating ice melting, factors not addressed in earlier models. It should be noted that the physical meanings of the symbols in this appendix may differ slightly from those in other chapters, and are thus defined individually for clarity.

The effects of confining pressure on the shear strength of saturated frozen soils

Frozen soils are widely distributed in the world, with approximately 50% of the exposed land area in the Northern Hemisphere covered by permafrost and seasonally frozen soils (Li and Yin, 2025). The mechanical behaviour of frozen soils under high confining pressure has attracted increasing attention due to advance in deep excavation using the artificial ground freezing method (Chamberlain et al., 1972; Qi and Ma, 2007; Liu et al., 2019b; Li et al., 2024). For example, during the excavation of a coal mining well (over 700 m in depth) in Shandong Province, China, the total in situ stress of frozen soils is up to 20 MPa (Qi and Ma, 2007). Over the past several decades, the variation in shear strength (i.e., peak deviatoric stress q_{max}) of saturated frozen soils with post-freezing total confining pressure (i.e., σ_3) has been extensively investigated using triaxial compression tests (e.g., Chamberlain et al., 1972; Ma et al., 1999; Lai et al., 2016; Wang, 2017; Sun et al., 2022). Parameswaran and Jones (1981) tested saturated frozen Ottawa sand at approximately -10°C, with σ_3 ranging from 0.1 to 75 MPa. Their results

showed that the shear strength increased from 16.5 MPa to 36 MPa as σ_3 increased from 0.1 to 40 MPa, but decreased when σ_3 increased from 40 to 75 MPa. Similarly, Liu et al. (2019c) revealed that, at a given temperature, the shear strength of saturated frozen silt initially increased with increasing σ_3, but decreased as σ_3 further increased. More experimental observations on the effects of σ_3 on the shear strength are summarised in Table A-1, with emphases on soil type, strain rate, temperature range, and pressure range. It can be concluded that the shear strength of saturated frozen soils depends non-monotonically on σ_3. The strength initially increases or remains nearly constant and then decreases as σ_3 increases.

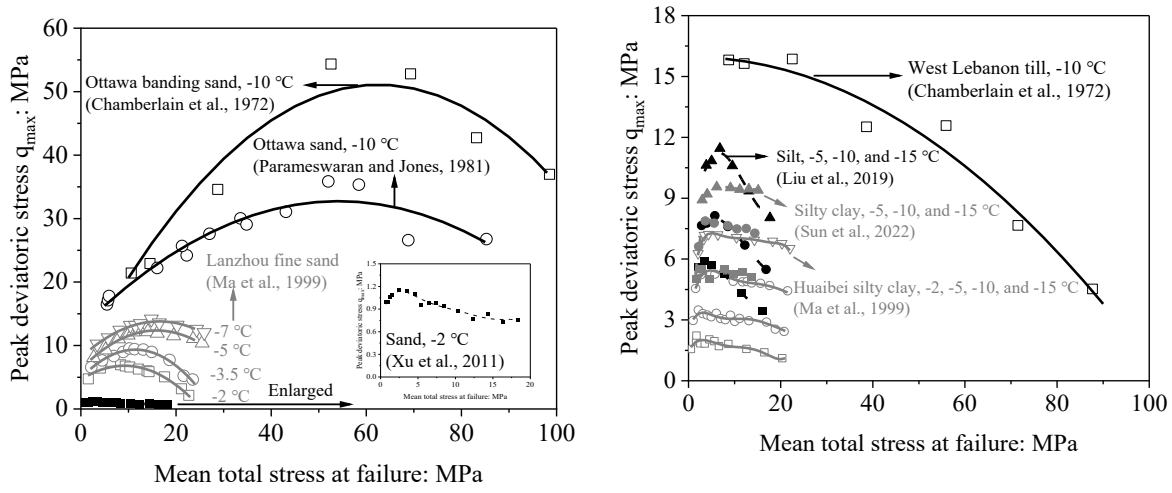

(a) (b)

Figure A-1. Variation of shear strength with mean total stress for saturated frozen soils in the literature: (a) sand; (b) silt and clay

Previous studies have provided some explanations for the variation in shear strength with σ_3. It is widely recognised that the reduction of shear strength with increasing σ_3 is mainly because of pressure-induced ice melting (e.g., Chamberlain et al., 1972; Ma et al., 1999; Lai et al., 2013). Furthermore, a nearly constant shear strength with increasing σ_3 can be observed when ice melting is negligible, such as when σ_3 is within a limited range (e.g., 0.2 - 0.6 MPa in Wang, 2017). However, explanations for the increased shear strength with increasing σ_3 are limited. Note that the isotropic compression of saturated frozen soils is an undrained process because the hydraulic conductivity of soil is very low after freezing, and the increase in σ_3 does not substantially affect the effective soil skeleton stress (Nishimura and Wang, 2019). Recently, Nishimura and Wang (2019) attributed the increase in shear strength with increasing

σ_3 to the dilatancy of saturated dense sands. At low σ_3, the shear process of frozen dense sands is disturbed by the dilatancy-induced tensile failure of pore ice (Ladanyi and Morel, 1990). As σ_3 increases, the higher confinement within the pore ice mitigates tensile failure, increasing shear strength. However, as illustrated in Table A-1 and Figure A-1, the increase in shear strength with increasing σ_3 has also been frequently observed in saturated frozen loose sand (Xu et al., 2011), silt (Liu et al., 2019c) and clay (Sun et al., 2022), whose dilatancy is less significant than that of dense sand. These observations suggest that the increase in shear strength with increasing σ_3 is not fully understood. Confining pressure may influence the shear strength of frozen soils through additional mechanisms that have yet to be explored.

So far, many constitutive models for frozen soils have been developed using multi-phase modelling approaches (e.g., Nishimura et al., 2009; Zhang and Michalowski, 2015; Ghoreishian Amiri et al., 2016; Sun and Zhou, 2021; Amini et al., 2024; Cai and Zhu, 2024), or total stress-based formulations (e.g., Lai et al., 2009; Yang et al., 2010; Liu et al., 2019b; Yu et al., 2022). These multi-phase models commonly adopt two sets of stress variables and a framework similar to the Barcelona Basic model (Alonso et al., 1990). To consider the variation in shear strength with σ_3, some multi-phase models treated the compression of saturated frozen soils as a drained process, resulting in higher effective soil skeleton stress and shear strength at higher σ_3. While this approach effectively captures the increase in shear strength with increasing σ_3, it may contradict the nearly undrained nature of saturated frozen soils. Moreover, total stress-based models typically employ a semi-empirical nonlinear strength criterion to consider the variation in shear strength of saturated frozen soils with σ_3 (e.g., Yang et al., 2010; Liu et al., 2019b). However, these models encounter difficulties in calculating soil responses with variations in temperature and ice content (Amini et al., 2024). Thus, a constitutive model for saturated frozen soils incorporating confining pressure-dependent behaviour is needed.

In this appendix, the influence of confining pressure on the shear behaviour of saturated frozen soils is reviewed and the underlying mechanisms are explored. A constitutive model for saturated frozen soils is developed, with formulations proposed to account for confining pressure-dependent behaviour.

Table A-1. Influence of post-freezing total confining pressure (σ_3) on shear strength (peak deviatoric stress q_{max}) for saturated frozen soils in the literature

Reference	Soil type	Strain rate: s^{-1}	T: ℃	σ_3: MPa	Variation of q_{max} with σ_3 (for σ_3 < 100 MPa[*1])
Sand					
Chamberlain et al. (1972)	Ottawa banding sand	1.0×10^{-3}	-10	3 ~ 276	Increase and then decrease[*2]
Sayles (1974)	Ottawa sand	7.3×10^{-5} ~ 1.1×10^{-2}	-4	0 ~ 8	Increase
Parameswaran and Jones (1981)	Ottawa sand	7.7×10^{-5}	-10	0 ~ 76	Increase and then decrease
Ladanyi and Morel (1990)	Ottawa quartz sand	1.9×10^{-4}	-5	0 ~ 0.3	Increase
Ma et al. (1999)	Lanzhou fine sand	1.1×10^{-3}	-2 ~ -7	0 ~ 22	Increase and then decrease
Qi and Ma (2007)	Lanzhou fine sand	1.1×10^{-3}	-2 ~ -7	2 ~ 22	Increase and then decrease
Zhang et al. (2007)	Sand	1.7×10^{-4}	-4 ~ -6	0 ~ 16	Increase and then decrease
Xu et al. (2011)	Sand	1.7×10^{-4}	-2	0.3 ~ 18	Increase and then decrease
Xu (2014)	Sand	1.7×10^{-4}	-1 ~ -10	0.3 ~ 1	Increase
Lai et al. (2016)	Silty sand	1.7×10^{-4}	-6	1 ~ 16	Increase and then decrease
Ma et al. (2016)	Standard Chinese sand	1.7×10^{-4}	-0.5~ -5	0.5 ~ 10	Increase
Zhang et al. (2017b)	Silty sand	1.7×10^{-4}	-5	0.05 ~ 4	e≤0.62 or e≥3: increase 0.62<e<3: constant
Silt and clay					
Chamberlain et al. (1972)	West Lebanon till	1.0×10^{-3}	-10	3 ~ 276	Constant and then decrease
Ma et al. (1999)	Huaibei silty clay	1.1×10^{-3}	-2 ~ -15	0 ~ 20	Increase and then decrease
Zhang et al. (2007)	Silty clay	1.7×10^{-4}	-4 ~ -6	0 ~ 16	Increase and then decrease
Zhao et al. (2013)	Clay	1.7×10^{-5}	-20	0 ~ 12	Increase and then decrease
Zhou et al. (2016)	Loess	4.0×10^{-4}	-6	1 ~ 15	Increase and then decrease
Wang (2017)	Kasaoka clay	1.7×10^{-6}	-2 ~ -10	0.2 ~ 0.6	Constant
Liu et al. (2019c)	Silt-sand mixture	1.7×10^{-4}	-6 ~ -15	0.3 ~ 15	Increase and then decrease
Xu et al. (2019)	Loess	1.5×10^{-4}	-6	0.5 ~ 9	Constant and then decrease
Zhou et al. (2020)	Loess	2.5×10^{-4}	-6	2 ~ 3	Increase
Sun et al. (2022)	Silty clay	1.7×10^{-4}	-5 ~ -10	0 ~ 12	Increase and then decrease
Wu et al. (2023)	Silty clay	1.7×10^{-4}	-6 ~ -12	0.5 ~ 7	Increase and then decrease
Tang et al. (2024)	Low-plasticity clay	1.1×10^{-4}	-10	0 ~ 1.2	Increase

*Notations:

1. The analysis is limited to results for σ_3 below 100 MPa to maintain relevance to engineering applications.

2. Chamberlain et al. (1972) observed that the shear strength of saturated frozen soils increased again when the confining pressure exceeded 100 MPa. This is probably due to the complete melting of the pore ice, with the subsequent increase in shear strength attributed to the contraction of the pore water, similar to the behaviour of unfrozen soils. This unfrozen soil-like behaviour is not discussed in this study.

Development of a model for the mechanical behaviour of saturated frozen soils

Stress and strain variables

In saturated frozen soils, the current model assumes that the arrangements of soil particles, pore ice, and pore water are identical to those described in Nishimura et al. (2009). The model formulations are presented in the triaxial stress space and the stress variables defined in Nishimura et al. (2009) are adopted:

$$p_n = p - p_i \tag{A-1}$$

$$q = \sigma_1 - \sigma_3 \tag{A-2}$$

$$s = p_i - p_w \tag{A-3}$$

where p_n is the mean net stress; $p = (\sigma_1 + 2\sigma_3)/3$ is the mean total stress; σ_1 and σ_3 are the total major and minor principal stresses, respectively; q is the deviatoric stress; s is the cryogenic suction and is related to the curvature of the pore ice-water interface; p_i is the pore ice pressure; and p_w is the pore water pressure. When the soil is in an unfrozen state, the pore ice pressure p_i is assumed to equal the pore water pressure p_w. Accordingly, the mean effective stress is defined by $p' = p - p_w$, with suction considered to be zero.

The total incremental volumetric strain ($d\varepsilon_v$) and deviatoric strain ($d\varepsilon_q$), which are work-conjugate to the mean stress and deviatoric stress respectively (Sun and Zhou, 2021), are decomposed into elastic and plastic components:

$$d\varepsilon_v = d\varepsilon_v^e + d\varepsilon_v^p \tag{A-4}$$

$$d\varepsilon_q = d\varepsilon_q^e + d\varepsilon_q^p \tag{A-5}$$

where the superscripts ‘e’ and ‘p’ represent elastic and plastic strain components, respectively. The elastic strain increments are calculated as follows:

$$d\varepsilon_v^e = \frac{\kappa dp_n}{(1+e)p_n} \tag{A-6}$$

$$d\varepsilon_q^e = \frac{dq}{3G} \tag{A-7}$$

where κ is the slope of the unloading curve in the $e - \ln p_n$ plane; e is the void ratio; and G is the equivalent elastic shear modulus, which is determined following the methodology proposed by Wang et al. (2019b):

$$G = G_0 + n(1 - S_w)G_i \tag{A-8}$$

where G_0 is the elastic shear modulus at the unfrozen state; n is the porosity; S_w is the degree of saturation of unfrozen water; and G_i is the elastic shear modulus of pore ice.

The plastic strain increments are expressed as follows:

$$d\varepsilon_v^p = D_s\Lambda_s \tag{A-9}$$

$$d\varepsilon_q^p = \Lambda_s \tag{A-10}$$

where $D_s = d\varepsilon_v^p / \left|d\varepsilon_q^p\right|$ is the dilatancy index, determined by the flow rule; and Λ_s is the non-negative loading index, calculated based on the consistency condition of the bounding surface.

Soil freezing characteristic curve

During the freezing process, the equilibrium between the water and ice phases is described by the Clausius-Clapeyron equation:

$$p_w = \frac{\rho_w}{\rho_i}p_i + \rho_w l \ln\frac{T+273.15}{273.15} \tag{A-11}$$

where ρ_w and ρ_i are the densities of pore water and ice, respectively. At 0 °C and atmospheric pressure, ρ_w and ρ_i are taken as 1000 and 910 kg/m^3, respectively (Chamberlain and Hoekstra, 1970). l is the specific latent heat of fusion, taken as 334 kJ/kg, and T is the temperature in degree Celsius. Combining Equations (A-3) and (A-11), the cryogenic suction in the frozen state is correlated with the pore ice pressure as follows:

$$s = \left(1 - \frac{\rho_w}{\rho_i}\right)p_i - \rho_w l \ln\frac{T+273.15}{273.15} \tag{A-12}$$

Noting the analogy between saturated frozen and unsaturated unfrozen soils, the degree of saturation of unfrozen water is correlated with cryogenic suction as follows (Gallipoli et al., 2003b):

$$S_w = \left[1 + \left(\frac{se^{m_1}}{m_2}\right)^{m_3}\right]^{-\frac{1}{m_1 m_3}} \tag{A-13}$$

where m_1, m_2, and m_3 are model parameters. The results of Nishimura et al. (2022) indicate that, at a given temperature, the degree of saturation of unfrozen water was higher for specimens with a lower void ratio. Therefore, in the present study, a soil freezing characteristic curve dependent on the void ratio is employed and its performance is examined in the model validation section. The hysteresis of the soil freezing characteristic curve is not considered in Equation (A-13), as the experimental data used for model validation do not involve freezing-thawing cycles.

Bounding surface and mapping rule

The model is developed within the framework of bounding surface plasticity (Dafalias, 1986b), which allows for plastic deformation when the soil is loaded within the yield (bounding) surface and enables the prediction of gradual yielding. As shown in Figure A-2, the bounding surface is expressed as follows (Yu, 1998):

$$f = \left[\frac{q}{M(p_n + ks)}\right]^N + \frac{1}{\ln R}\ln\left[\frac{p_n + ks}{p_0(s) + ks}\right] \tag{A-14}$$

where M is the slope of the critical state line in the $q - p_n$ plane; N and R are model parameters that define the shape of the bounding surface; k is a parameter describing the increase in apparent cohesion with cryogenic suction; and $p_0(s)$ is the preconsolidation pressure at a given cryogenic suction, which can be determined using the following equation (Nishimura et al., 2009):

$$\frac{p_0(s)}{p_c} = \left[\frac{p_0(0)}{p_c}\right]^{\frac{\lambda(0)-\kappa}{\lambda(s)-\kappa}} \tag{A-15}$$

where p_c is a model parameter; $\lambda(s)$ is the slope of the normal compression line at a given cryogenic suction in the $e - \ln p_n$ plane; $p_0(0)$ and $\lambda(0)$ are the values of $p_0(s)$ and

$\lambda(s)$ in the unfrozen state, respectively. The relationship between $\lambda(s)$ and $\lambda(0)$ is given by the following expression (Alonso et al., 1990; Nishimura et al., 2009):

$$\lambda(s) = \lambda(0)[(1-r)\exp(-\beta s) + r] \tag{A-16}$$

where β and r are model parameters.

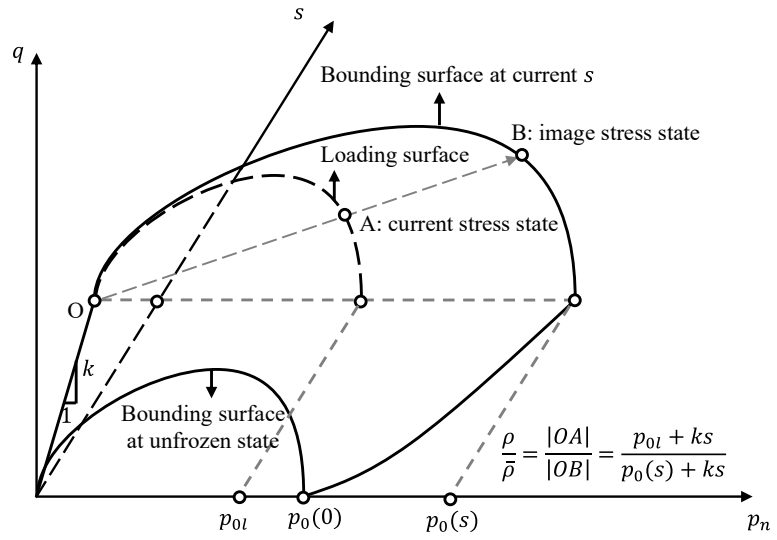

Figure A-2. Illustration of bounding surface and loading surface

The radial mapping rule is adopted to capture the plastic deformation within the bounding surface due to its simplicity and versatility across various stress paths (Dafalias, 1986b). As illustrated in Figure A-2, two Euclidean distances, ρ and $\bar{\rho}$, are defined. ρ represents the distance between the projection centre and the current stress state (i.e., $\rho = |OA|$), while $\bar{\rho}$ denotes the distance between the projection centre and the image stress state (i.e., $\bar{\rho} = |OB|$). The ratio of these two Euclidean distances is calculated as follows:

$$\frac{\rho}{\bar{\rho}} = \frac{p_{0l}+ks}{p_0(s)+ks} \tag{A-17}$$

where p_{0l} represents the size of the loading surface, which is determined on the basis of the current stress state. The ratio $\rho/\bar{\rho}$ is always smaller than one for overconsolidated soil and increases towards one as the soil state moves closer to the bounding surface. This ratio is employed in calculating the plastic strain when the stress state is within the bounding surface, as will be introduced in the sections describing the flow rue and consistency condition.

Flow rule

A non-associated flow rule is employed in this study, and the dilatancy is described as follows (Li and Dafalias, 2000):

$$D_s = \frac{d_1}{\eta}[M\exp(n_d\psi) - \eta] \tag{A-18}$$

where d_1 and n_d are model parameters; η is the stress ratio, defined as $q/(p_n + ks)$; and ψ is a state parameter representing the vertical distance of the soil state from the critical state line in the $e - \ln p_n$ plane, determined as follows:

$$\psi = e - e_c \tag{A-19}$$

where e_c is the critical state void ratio corresponding to the current mean net stress. Based on the equation for bounding surface, e_c is deduced as follows (Ng et al., 2020):

$$e_c = N(s) - [\lambda(s) - \kappa]\ln\left[R + \frac{(R-1)ks}{p_n}\right] - \lambda(s)\ln\left(\frac{p_n}{p_c}\right) \tag{A-20}$$

When the soil is in the unfrozen state and the value of R is set to 2, Equation (A-20) yields the critical state line of the modified Cam-Clay model. The dilatancy in Equation (A-18) is adopted because it has been shown to effectively capture the behaviour of various types of soil, including saturated soils (Li and Dafalias, 2000), unsaturated soils (Chiu and Ng, 2003; Zhou et al., 2015), and methane hydrate-bearing sediments (Ng et al., 2020).

When the stress state is inside the bounding surface, the dilatancy is modified as follows (Ng et al., 2020):

$$D_s = \frac{d_1}{\eta}\left[M\left(\frac{\rho}{\bar{\rho}}\right)^{\alpha}\exp(n_d\psi) - \eta\right] \tag{A-21}$$

The incorporation of the ratio $\rho/\bar{\rho}$ indicates that the soil is more dilative when the overconsolidation ratio (OCR) increases (i.e., $\rho/\bar{\rho}$ is smaller), consistent with previous experimental observations (e.g., Gens, 1982). The exponent α is a model parameter, with a larger value indicating a more dilative response.

Hardening law and consistency condition

The evolution of the bounding surface size at the unfrozen state is related to the plastic volumetric strain as follows (Nishimura et al., 2009):

$$dp_0(0) = \frac{1+e}{\lambda(0)-\kappa} p_0(0) d\varepsilon_v^p \tag{A-22}$$

Thus, the variation of the bounding surface size in the frozen state is given by:

$$dp_0(s) = \frac{\partial p_0(s)}{\partial \lambda(s)} \frac{\partial \lambda(s)}{\partial s} ds + \frac{\partial p_0(s)}{\partial p_0(0)} \frac{\partial p_0(0)}{\partial \varepsilon_v^p} D_s \Lambda_s \tag{A-23}$$

Correspondingly, the consistency condition of the bounding surface suggests:

$$\frac{\partial f}{\partial p_n} dp_n + \frac{\partial f}{\partial q} dq + \frac{\partial f}{\partial s} ds + \frac{\partial f}{\partial p_0(s)} \frac{\partial p_0(s)}{\partial \lambda(s)} \frac{\partial \lambda(s)}{\partial s} ds + \frac{\partial f}{\partial p_0(s)} \frac{\partial p_0(s)}{\partial p_0(0)} \frac{\partial p_0(0)}{\partial \varepsilon_v^p} D_s \Lambda_s = 0 \tag{A-24}$$

According to the dilatancy for normally consolidated soils defined in Equation (A-18), a plastic modulus is introduced and defined as follows:

$$K_p = -\frac{\partial f}{\partial p_0(s)} \frac{\partial p_0(s)}{\partial p_0(0)} \frac{\partial p_0(0)}{\partial \varepsilon_v^p} \frac{d_1}{\eta} [M \exp(n_d \psi) - \eta] \tag{A-25}$$

The plastic modulus is modified to consider the influence of OCR and is expressed as:

$$K_p = -\frac{\partial f}{\partial p_0(s)} \frac{\partial p_0(s)}{\partial p_0(0)} \frac{\partial p_0(0)}{\partial \varepsilon_v^p} \frac{d_1}{\eta} \left[M \left(\frac{\bar{\rho}}{\rho}\right)^{\alpha} \exp(n_d \psi) - \eta\right] \tag{A-26}$$

Note that the ratio of $\bar{\rho}/\rho$ in Equation (A-26) is inverted compared to the ratio of $\rho/\bar{\rho}$ in Equation (A-21). This inversion is because, when the OCR is higher, the inclusion of $\bar{\rho}/\rho$ in Equation (A-26) aims to predict a higher plastic modulus and thus a smaller plastic strain increment, while $\rho/\bar{\rho}$ in Equation (A-21) is used to predict more dilative behaviour. Both are consistent with the experimental results reported in the literature (e.g., Gens, 1982; Zhou et al., 2015). Moreover, a larger value of α leads to a more dilative response and a higher plastic modulus.

Based on Equations (A-24) and (A-26), the loading index Λ_s is determined by:

$$\Lambda_s = \frac{1}{K_p} \left[\frac{\partial f}{\partial p_n} dp_n + \frac{\partial f}{\partial q} dq + \frac{\partial f}{\partial s} ds + \frac{\partial f}{\partial p_0(s)} \frac{\partial p_0(s)}{\partial \lambda(s)} \frac{\partial \lambda(s)}{\partial s} ds\right] \tag{A-27}$$

Investigation on the non-monotonic variation in shear strength with confining pressure

As discussed in the introduction, the shear strength of saturated frozen soils depends non-monotonically on post-freezing total confining pressure. Given that the major difference between frozen and unfrozen soils is the presence of pore ice, it is hypothesised that the confining pressure-dependent shear strength is closely associated with ice properties. Therefore, the variation in the shear strength of pure ice with mean total stress at failure (i.e., the value of p corresponding to q_{max}) reported in the literature (Jones, 1982; Murrell et al., 1991; Rist and Murrell, 1994; Gagnon and Gammon, 1995) is summarised in Figure A-3. The temperature ranges from -40 to -1 ℃, and the strain rate is approximately 5×10^{-3} s^{-1}.

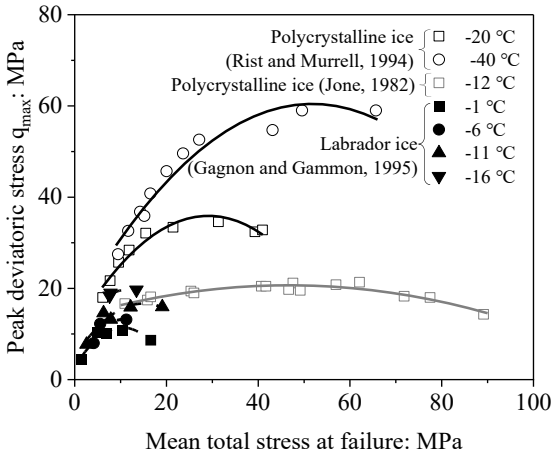

Figure A-3. Variation of shear strength with mean total stress for pure ice in the literature

It is evident that, at a given temperature, the shear strength of pure ice exhibits a two-stage behaviour, initially increasing and then decreasing as mean total stress increases, consistent with the trend identified in saturated frozen soils (see Figure A-1). The initial increase in shear strength is due to higher mean total stress preventing crack growth within pure ice and inhibiting brittle failure, allowing shear stress to rise much higher than in unconfined conditions (Jones, 1982; Murrell et al., 1991; Rist and Murrell, 1994). Furthermore, the reduction in shear strength for pure ice is attributed to the freezing point depression (i.e., ice melting) as mean total stress continues to increase (Gagnon and Gammon, 1995), similar to the behaviour observed in saturated frozen soils. Based on the above considerations, it is postulated that the confining pressure governs the shear strength of saturated frozen soils via two major

mechanisms: (i) prevention of crack formation within the pore ice and (ii) onset of ice melting. Detailed explanations are given below.

On the one hand, the shear process of saturated frozen soils could be disturbed by pore ice cracks caused by dilatancy-induced tensile stress (as in dense sand) (Nishimura and Wang, 2019) or high deviatoric stress (similar to pure ice) (Rist and Murrell, 1994). As the confining pressure increases, the enhanced confinement on the pore ice prevents the formation of ice cracks, increasing the shear strength. This postulation is supported by experimental observations from the literature (e.g., Chamberlain et al., 1972; Wu et al., 2023). For example, Chamberlain et al. (1972) showed that the shear strength of saturated frozen Ottawa banding sand increased as the confining pressure rose from 3 to 34 MPa. Within this range, volumetric expansion was observed due to dilatancy-induced pore ice cracking, but its magnitude became less pronounced at higher confining pressures. When volumetric expansion was completely suppressed at 34 MPa, the maximum shear strength was reached. These findings indicate that the increase in shear strength is strongly correlated with the suppression of pore ice cracks under higher confining pressures, with maximum shear strength achieved when volumetric expansion is fully restrained. Another piece of evidence is provided by Wu et al. (2023), who observed that the shear strength of saturated frozen silty clay increased as the confining pressure increased from 0.5 to 1.5 MPa. Within this pressure range, the failure mode transitions from brittle failure with extensive cracks at 0.5 MPa to ductile deformation with minimal cracks at 1.5 MPa, highlighting the critical role of confinement in mitigating ice fractures and improving shear strength.

On the other hand, confining pressure affects the shear strength of saturated frozen soils through ice melting. As confining pressure increases, ice melting and a corresponding rise in unfrozen water content are observed (e.g., Ma et al., 1999), reducing shear strength. The combined effects of these two mechanisms account for the non-monotonic variation in shear strength with confining pressure, as illustrated in Table A-1 and Figure A-1. In the following section, new formulations are proposed based on these two mechanisms and are incorporated to account for the influence of confining pressure.

Prevention of ice cracks

Since the influence of confining pressure is closely related to the formation of cracks within pore ice, it is assumed that ice cracking occurs when the deviatoric stress of the pore ice satisfies the following equation:

$$q_{i,th} = \chi p_i + q_{ref} \tag{A-28}$$

where $q_{i,th}$ is the ice threshold deviatoric stress at which ice cracks form; χ is a friction coefficient-like parameter that describes the increase in ice threshold deviatoric stress with pore ice pressure p_i; and q_{ref} is a reference deviatoric stress describing the shear strength of pore ice at zero pore ice pressure p_i. Given the challenge of distinguishing the deviatoric stress of pore ice from the total deviatoric stress, the ice threshold deviatoric stress $q_{i,th}$ is substituted with the total threshold deviatoric stress q_{th} in the calculations. This simplification is expected to have limited impacts on the calculation results in most cases, since the presence of pore ice mainly contributes to the shear strength of saturated frozen soils, particularly at low temperatures, as evidenced by the much higher strength in the frozen state than in the unfrozen state (Ladanyi and Morel, 1990; Nishimura and Wang, 2019). Consequently, Equation (A-28) is reformulated as follows:

$$q_{th} = \chi p_i + q_{ref} \tag{A-29}$$

When the deviatoric stress and the pore ice pressure satisfy Equation (A-29), the model predicts the onset of ice cracking and specimen failure. An essential feature of Equation (A-29) is that higher deviatoric stress is required to trigger ice cracking under higher pore ice pressure, consistent with the observed pressure-dependent shear strength. Additionally, Equation (A-29) implies that ice cracking is more likely to occur in dense sand due to the effects of dilatancy, which reduces the pressure of the pore ice. This is well supported by experimental data (e.g., Chamberlain et al., 1972; Parameswaran and Jones, 1981; Qi and Ma, 2007; Zhang et al., 2017b), which show that the increase in shear strength associated with ice cracking is frequently observed in dense sand.

Pressure-induced ice melting

In this study, the influence of pressure-induced ice melting is considered by treating the compression of saturated frozen soils as an undrained process (Nishimura and Wang, 2019). The mass conservation of pore water and pore ice during compression indicates that:

$$e[\rho_w S_w + \rho_i(1 - S_w)] = constant \tag{A-30}$$

The differentiation of Equation (A-30) suggests:

$$(1 + e)(\rho_w S_w - \rho_i S_w + \rho_i)d\varepsilon_v = eS_w \frac{\rho_w}{K_w} dp_w + e(1 - S_w)\frac{\rho_i}{K_i} dp_i + (\rho_w - \rho_i)edS_w \tag{A-31}$$

where K_w and K_i are the bulk moduli of pore water and pore ice, respectively. The bulk modulus of pore water is taken as 2000 MPa (Nishimura and Wang, 2019), and is assumed to be pressure- and temperature-independent for simplicity.

Equation (A-31) reveals that the volumetric strain of saturated frozen soils during isotropic compression (i.e., the left term) is induced by the compression of pore water and pore ice (i.e., the first two terms on the right), as well as the phase transformation between pore water and pore ice (i.e., the last term on the right). Introducing the elastic (Equation (A-6)) and plastic (Equation (A-9)) incremental volumetric strains along with the Clausius-Clapeyron relation (Equation (A-11)) into Equation (A-31), the reformulated expression becomes:

$$\frac{(\rho_w S_w - \rho_i S_w + \rho_i)}{\rho_w}\left[\frac{\kappa dp_n}{(1+e)p_n} + D_s \Lambda_s\right] = \frac{\rho_w e}{(\rho_w - \rho_i)(1+e)}\left[\frac{S_w}{K_w} + \frac{\rho_i^2}{\rho_w^2}\frac{(1-S_w)}{K_i}\right](-ds) + \frac{(\rho_w - \rho_i)e}{\rho_w(1+e)} dS_w \tag{A-32}$$

According to Equation (A-32), it is evident that isotropic compression of saturated frozen soils is associated with a reduction in cryogenic suction and an increase in the degree of saturation of unfrozen water. This reduction in suction will decrease both the shear modulus and the shear strength, as described in Equations (A-14) to (A-26). Consequently, the influence of pressure-induced ice melting is inherently captured by Equation (A-32).

Consequently, the effects of ice cracking and melting are considered by Equations (A-29) and (A-32), respectively. When using the equations introduced in the "Development of a model for the mechanical behaviour of saturated frozen soils" section to simulate soil behaviour, the

plastic modulus defined in Equation (A-26) is set to zero when Equation (A-29) is satisfied, and the current deviatoric stress is taken as the shear strength. Moreover, since Equation (A-32) is derived from the mass conservation condition, it should be incorporated as an additional governing equation for the undrained freezing, compression, and shearing processes.

Model parameters and model validation

The model parameters and their physical meaning are summarised in Table A-2.

Table A-2. Model parameters and corresponding physical meaning

Model parameter	Corresponding physical meaning
Elasticity	
κ	slope of the unloading curve in the $e - \ln p^*$ plane
G_0	elastic shear modulus in the unfrozen state
G_i	elastic shear modulus of pore ice
K_i	bulk modulus of pore ice
Elastoplasticity	
$N(0), \lambda(0), p_c$	definition of the normal compression line (NCL) in the unfrozen state
β, r	definition of the NCL in the frozen state
N, R	definition of the shape of the bounding surface
M	slope of the critical state line in the $q - p_n$ plane
k	definition of the increase in apparent cohesion with cryogenic suction
d_1, n_d	definition of dilatancy
α	definition of the mapping rule
q_{ref}, χ	influence of confining pressure on crack formation in pore ice
Soil freezing characteristic curve	
m_1, m_2, m_3	definition of the soil freezing characteristic curve

Compared to the Modified Cam-Clay model, five new parameters (N, R, d_1, n_d and α) are introduced under the unfrozen state for capturing the behaviour of both clay and sand (Yu, 1998). Additionally, the parameters m_1, m_2, m_3, G_i, K_i, β, r, k, χ and q_{ref} are incorporated to simulate the behaviour of frozen soils. In the subsequent sections, the simulation results are compared with experimental data from the literature (Chamberlain et al., 1972; Ma et al., 1999; Wang, 2017; Sun et al., 2022) to validate the model performance. The effects of temperature, pre-freezing mean effective stress, and post-freezing total confining pressure on the stress-strain curve and shear strength of saturated frozen soils are quantitatively investigated. During model validation, the parameter calibration is briefly introduced with

reference to the experimental results presented by Wang (2017).

Validation under various pre-freezing mean effective stresses and temperatures

Table A-3. Summary of model parameter values

Parameter	Kasaoka clay (Wang, 2017)	West Lebanon till (Chamberlain et al., 1972)	Ottawa banding sand (Chamberlain et al., 1972)	Huaibei silty clay (Ma et al., 1999)	Lanzhou fine sand (Ma et al., 1999)	Silty clay (Sun et al., 2022)
Elasticity						
κ	0.05	0.03	0.01	0.03	0.03	0.03
G_0: MPa	8	8	8	8	8	10
G_i: MPa	400	2000	1800	200	750	1700
K_i: MPa	550	1900	1700	2000	1700	2200
Elastoplasticity						
$N(0)$	2.10	1.35	1.47	1.40	1.45	1.50
$\lambda(0)$	0.21	0.12	0.12	0.13	0.12	0.15
$p_c: kPa$	1.00	1.00	1.00	1.00	1.00	1.00
$\beta: MPa^{-1}$	1.00	0.22	0.30	0.40	0.40	0.40
r	0.90	0.62	0.63	0.70	0.66	0.72
N	1.60	3.00	1.40	1.60	2.50	1.60
R	1.65	1.65	2.00	2.00	2.00	2.00
M	1.08	1.18	1.18	1.20	1.20	1.20
k	0.15	0.40	0.60	0.31	0.80	0.23
d_1	3.00	4.00	0.40	1.00	1.00	3.20
n_d	1.00	0.20	0.30	1.00	3.00	2.00
α	3.00	0.20	5.00	0.30	3.00	0.30
$q_{ref}: MPa$	1.00	25.00	3.00	1.00	4.00	9.50
χ	3.00	3.00	1.80	2.50	1.80	4.00
Soil freezing characteristic curve						
m_1	3.61	3.00	2.00	1.87	2.00	3.50
$m_2: kPa$	125	100	10	510	100	100
m_3	0.81	1.00	1.00	29	29	0.80

Wang (2017) conducted a series of tests on saturated Kasaoka clay, including: (1) isotropic compression and undrained triaxial shear tests under different mean effective stresses and overconsolidation ratios in the unfrozen state; (2) soil freezing characteristic curves under different initial vertical stresses; and (3) triaxial shear tests on frozen specimens at various temperatures and pre-freezing mean effective stresses. The model parameters are summarised in Table A-3, and the parameter calibration is presented based on the dataset from Wang (2017)

as detailed below.

The parameters κ, $N(0)$, $\lambda(0)$ and p_c are determined based on the isotropic compression curve. The parameters G_0, N, R, M, d_1, n_d and α are closely related to the shear behaviour of saturated unfrozen soils. Specifically, G_0 is determined by the initial shear modulus in the stress-strain curve using Equation (A-7). N is determined by the shape of the bounding surface. R is calculated based on the vertical distance between the normal compression line and the critical state line in the $e - \ln p_n$ plane using Equation (A-20). d_1, n_d and α are obtained by fitting the effective stress path during undrained shearing using Equation (A-21). Alternatively, d_1, n_d and α can be obtained by fitting the volumetric strain during drained shearing. Based on these parameters for unfrozen soils, the shear behaviour of saturated unfrozen Kasaoka clay is predicted and compared with the measured data, as shown in Figure A-4. The results show good agreement between the simulated and measured data.

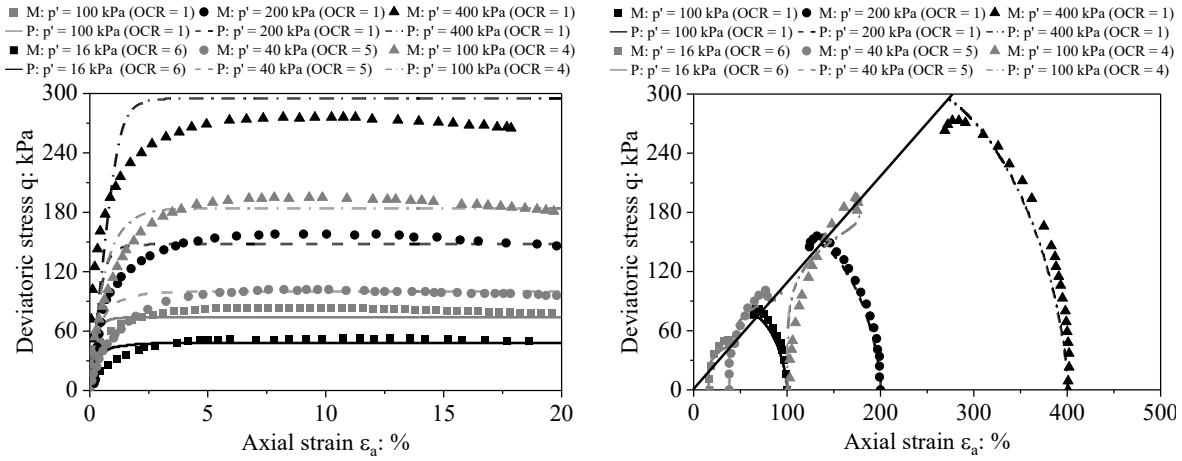

(a) (b)

Figure A-4. Comparison between the measured (M) and predicted (P) results of unfrozen Kasaoka clay from Wang (2017): (a) stress-strain curves; (b) effective stress paths

In the frozen state, m_1, m_2 and m_3 are calculated from the soil freezing characteristic curve using Equation (A-13). G_i is obtained from the initial modulus in the stress-strain curve using Equation (A-7). k, β and r are determined by fitting the stress-strain curve since the compression results and the critical state line of frozen specimens are not available. Finally, K_i, χ and q_{ref} are determined from the variation of shear strength with mean total stress using Equations (A-29) and (A-32). Note that, due to ice morphology and its interaction with

the soil matrix, the shear (G_i) and bulk (K_i) moduli of pore ice are highly dependent on soil properties and cannot be directly derived from those of pure ice.

To examine the model performance, the measured and predicted soil freezing characteristic curves under different initial vertical stresses (i.e., σ_{v0} = 50, 100, and 200 kPa) are presented in Figure A-5. It is evident that the specimen subjected to a higher vertical stress (i.e., a lower initial void ratio) exhibited a higher degree of saturation of unfrozen water at a given temperature, which is well captured by Equation (A-13).

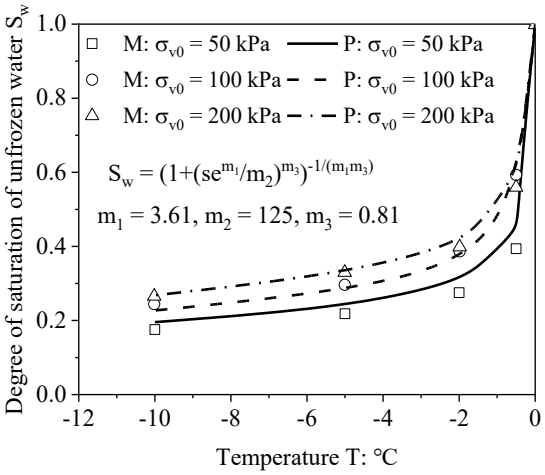

Figure A-5. Comparison between the measured (M) and predicted (P) soil freezing characteristic curves of Kasaoka clay from Wang (2017)

Figure A-6 shows the measured and predicted stress-strain curves of frozen Kasaoka clay under temperatures of -2, -5, and -10 ℃ and pre-freezing mean effective stresses (p'_f) of 100, 200, and 400 kPa. It can be observed that the shear strength increases as temperature decreases due to the higher volumetric ice content and cryogenic suction at lower temperatures. Additionally, the shear strength increases as p'_f increases, mainly due to the higher density at higher p'_f. These essential features are quantitatively captured (see Figure A-6), suggesting a good performance of the proposed model.

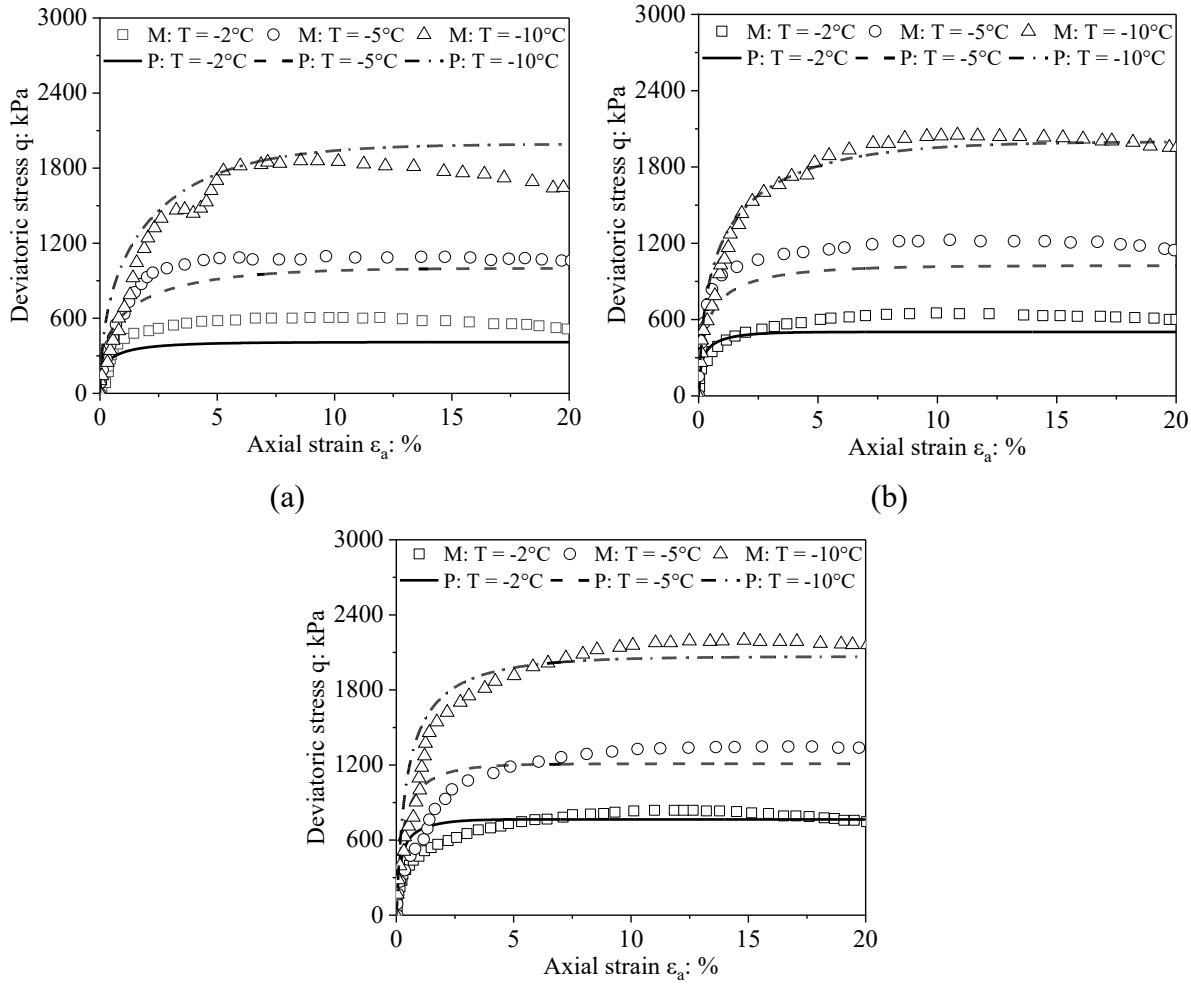

Figure A-6. Comparison between the measured (M) and predicted (P) stress-strain curves of frozen Kasaoka clay from Wang (2017): (a) p'_f = 100 kPa; (b) p'_f = 200 kPa; (c) p'_f = 400 kPa

Validation under various post-freezing total confining pressures and temperatures

Chamberlain et al. (1972) conducted triaxial tests on saturated frozen Ottawa banding sand and West Lebanon till at approximately -10 °C, under confining pressures σ_3 ranging from 3 to 276 MPa. Note that only the results for σ_3 below 100 MPa are investigated to align with practical engineering applications. The model parameters are summarised in Table A-3.

Figure A-7(a) shows the stress-strain curves of West Lebanon till. The shear strength remained nearly constant as σ_3 increased from 3 to 17 MPa and decreased continuously as σ_3 increased to 86 MPa. Figure A-7(b) presents the results of the Ottawa banding sand. At a given axial strain, the deviatoric stress exhibits an increase trend as σ_3 increased from 3 to 34 MPa

but decreases when σ_3 further increased to 86 MPa. More importantly, the predicted results closely align with the experimental data, with differences observed for the Ottawa banding sand. This discrepancy may be attributed to significant particle breakage, as reported by Chamberlain et al. (1972), which is not accounted for in the current model.

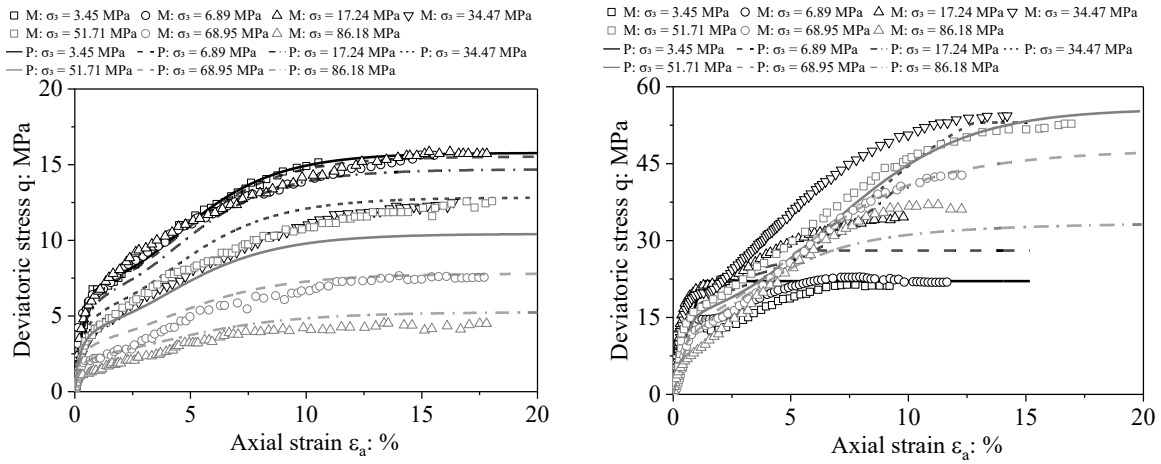

Figure A-7. Comparison between the measured (M) and predicted (P) stress-strain curves for the data presented by Chamberlain et al. (1972) (T = -10 ℃): (a) West Lebanon till; (b) Ottawa banding sand

Figure A-8 illustrates the variation in shear strength with mean total stress. It demonstrates that Equation (A-29) effectively captures the influence of confining pressure by modelling its effects on the prevention of cracks. Meanwhile, Equation (A-32) efficiently accounts for the effects of pressure-induced ice melting on shear strength.

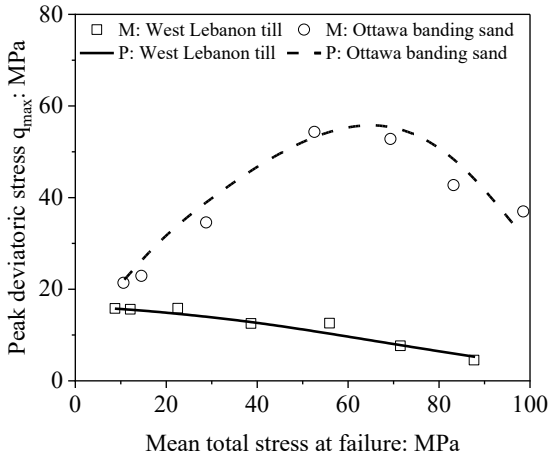

Figure A-8. Variations in shear strength with mean total stress for the data presented by Chamberlain et al. (1972) (T = -10 ℃, M and P stand for measured and predicted results, respectively)

Ma et al. (1999) conducted triaxial shear tests on frozen Huaibei silty clay and Lanzhou fine sand with confining pressures σ_3 varying from 0 to 22 MPa and temperatures between -2 and -15 ℃. Only the stress-strain curves at -5 ℃ were reported, and these data are used for model validation. The model parameters are given in Table A-3.

Figure A-9(a) presents the stress-strain curves of Huaibei silty clay. The results reveal that at axial strains below 10%, the deviatoric stress is higher for specimens under lower σ_3. However, beyond this point, the deviatoric stress for the specimen at σ_3 = 0 MPa remains nearly constant and eventually falls below that at σ_3 = 1 MPa. This behaviour is likely due to specimen failure caused by crack growth at zero σ_3, as discussed in previous sections. Similarly, Figure A-9(b) shows that at axial strains below 1%, the deviatoric stress of Lanzhou fine sand remains nearly identical between specimens with different σ_3 values. As axial strain increases, specimens at σ_3 = 0 and 4 MPa exhibit a reduction in deviatoric stress, which may result from dilatancy-induced tensile failure of the pore ice.

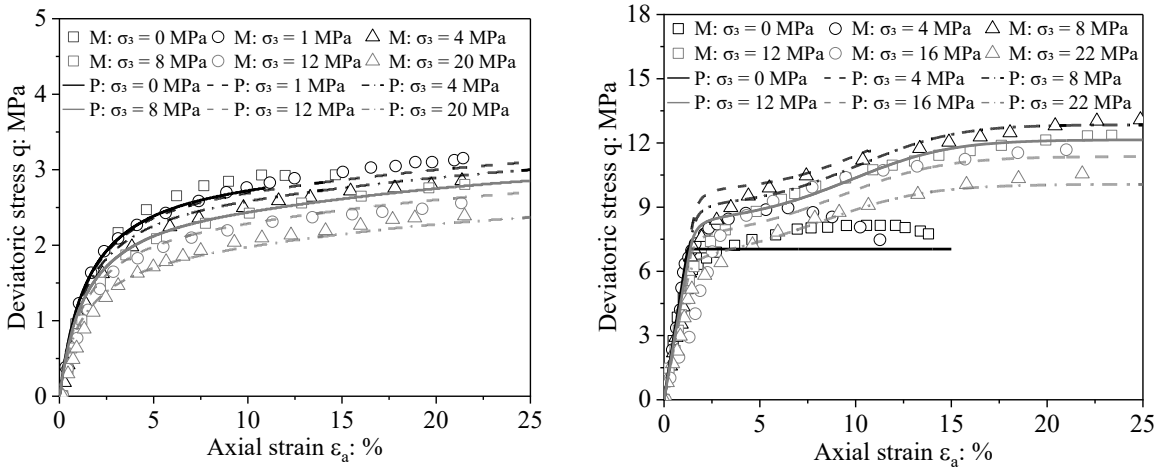

(a) (b)

Figure A-9. Comparison between the measured (M) and predicted (P) stress-strain curves for the data presented by Ma et al. (1999) (T = -5 ℃): (a) Huaibei silty clay; (b) Lanzhou fine sand

The variation of shear strength with mean total stress is shown in Figure A-10, where the predicted results closely align with the experimental data. The results in Figure A-9 and Figure A-10 demonstrate that the proposed explanations for the influence of confining pressure on frozen soil behaviour are consistent with experimental observations, and the proposed

Equations (A-29) and (A-32) effectively capture this behaviour quantitatively.

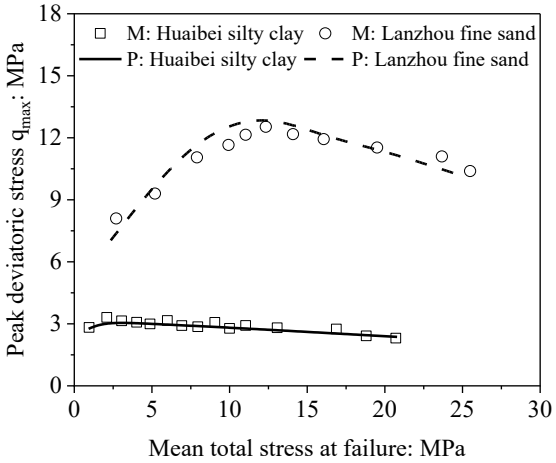

Figure A-10. Variations in shear strength with mean total stress for the data presented by Ma et al. (1999) (T = -5 ℃, M and P stand for measured and predicted results, respectively)

Sun et al. (2022) investigated the shear behaviour of saturated frozen silty clay under confining pressures σ_3 ranging from 0.2 to 12 MPa and temperatures of -5, -10, and -15 ℃. The model parameters are summarised in Table A-3. The stress-strain curves are shown in Figure A-11, where the predicted results exhibit good agreement with the measured data under different σ_3. Note that the stress-strain curves for saturated specimens are not available at -5 and -15 ℃.

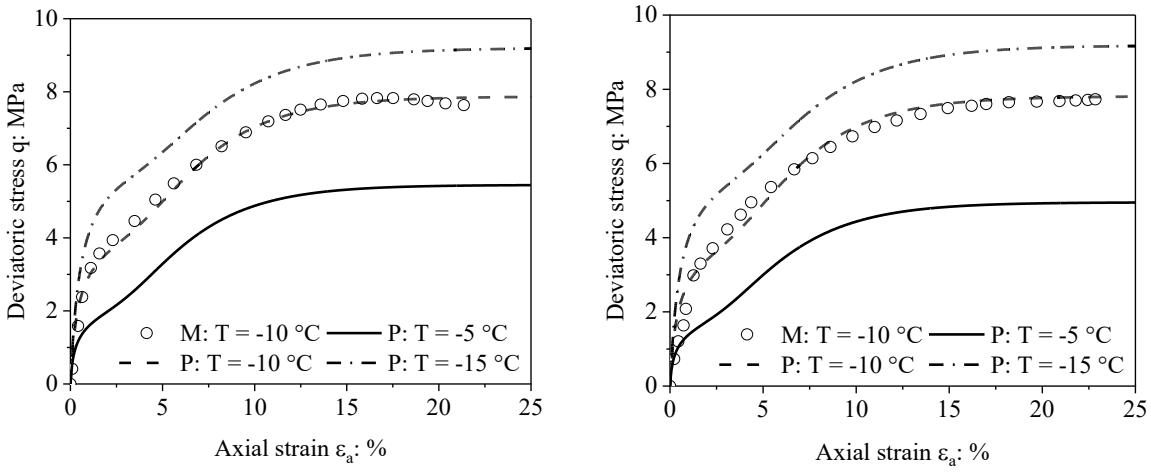

(a) (b)

Figure A-11. Comparison between the measured (M) and predicted (P) stress-strain curves for the data presented by Sun et al. (2022): (a) σ_3 = 1 MPa; (b) σ_3 = 10 MPa (the experimental stress-strain curves at -5 and -15 ℃ are not reported)

Figure A-12 illustrates the variation of the shear strength with the mean total stress. The

comparison between measured and predicted results demonstrates that the proposed model considers well the influence of confining pressure on shear strength under various temperatures.

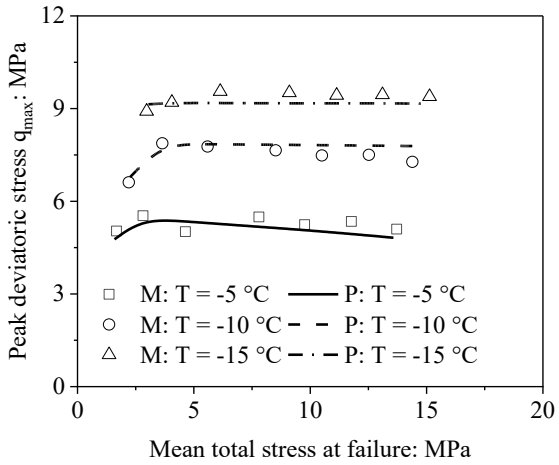

Figure A-12. Variations in shear strength with mean total stress and temperature for the data presented by Sun et al. (2022) (M and P stand for measured and predicted results, respectively)

Based on the results presented in Figure A-7 to Figure A-12, it is evident that the proposed model quantitatively captures the influence of confining pressure on both the stress-strain curve and shear strength under different temperatures. As mentioned in the introduction, the variation in shear strength with confining pressure is considered in some models by treating the compression of saturated frozen soils as a drained process. As a result, the effective soil skeleton stress and associated shear strength would be higher at higher confining pressure. However, this approach is inconsistent with the nearly undrained behaviour of saturated frozen soils. Additionally, while the strength reduction caused by ice melting at high confining pressures is widely recognised, its influence on the stress-strain curve has rarely been incorporated into existing models. Therefore, the incorporating of these new aspects into the proposed model highlights the novel contributions of the present study.

Summary and conclusions

The influence of confining pressure on the shear strength of saturated frozen soils has been reviewed based on extensive data collected from the literature. It is concluded that the shear strength either increases or remains nearly constant at low confining pressures but decreases as the confining pressure continues to increase. In this study, two mechanisms are

proposed to explain the influence of confining pressure on the behaviour of frozen soils: (i) prevention of crack growth within the pore ice and (ii) onset of ice melting. At low confining pressures, the shear process could be disturbed by pore ice cracks, originating from dilatancy-induced tensile stress or high deviatoric stress. As confining pressure increases, the formation of these ice cracks is prevented, resulting in an increase in shear strength. Moreover, pressure-induced ice melting dominates soil behaviour when the confining pressure further increases, leading to a reduction in the shear strength. The combined effects of these two mechanisms account for the non-monotonic variation in shear strength with confining pressure.

A new constitutive model for saturated frozen soils is developed. Formulations are proposed based on the aforementioned mechanisms to incorporate the dual effects of confining pressure. The model is validated against experimental data of saturated frozen soils under different temperatures, pre-freezing mean effective stresses, and post-freezing total confining pressures. The comparisons between measured and predicted data demonstrate that the proposed model quantitatively captures the influence of confining pressure on both the stress-strain curve and shear strength, highlighting the interest of the proposed contributions in modelling the shear behaviour of saturated frozen soils.